IntechOpen

Nanomaterials Based Gas Sensors for SF6 Decomposition Components Detection

Authored by Xiaoxing Zhang, Ju Tang, Song Xiao, Fuping Zeng, Cheng Pan, Yingang Gui

NANOMATERIALS BASED GAS SENSORS FOR SF6 DECOMPOSITION COMPONENTS DETECTION

Authored by **Xiaoxing Zhang, Ju Tang, Song Xiao, Fuping Zeng, Cheng Pan** and **Yingang Gui**

Nanomaterials Based Gas Sensors for SF6 Decomposition Components Detection
http://dx.doi.org/10.5772/67590
Edited by Xiaoxing Zhang, Ju Tang, Song Xiao, Fuping Zeng, Cheng Pan, Yingang Gui

Contributors

Xiaoxing Zhang, Ju Tang, Song Xiao, Fuping Zeng, Cheng Pan, Yingang Gui

Notice

First published in Croatia, 2017 by INTECH d.o.o.
eBook (PDF) Published by IN TECH d.o.o.
Place and year of publication of eBook (PDF): Rijeka, 2019.
IntechOpen is the global imprint of IN TECH d.o.o.
Printed in Croatia

Legal deposit, Croatia: National and University Library in Zagreb

Additional hard and PDF copies can be obtained from orders@intechopen.com

Nanomaterials Based Gas Sensors for SF6 Decomposition Components Detection
Edited by Xiaoxing Zhang, Ju Tang, Song Xiao, Fuping Zeng, Cheng Pan, Yingang Gui

p. cm.

Print ISBN 978-953-51-3257-8

Online ISBN 978-953-51-3258-5

eBook (PDF) ISBN 978-953-51-4809-8

Contents

Preface

This Monograph is a collection of reviewed and relevant research chapters, concerning the developments within the Nanomaterials Based Gas Sensors for SF6 Decomposition Components Detection field of study. The Monograph includes single chapters authored by Xiaoxing Zhang, Fuping Zeng, Song Xiao, Ju Tang, Cheng Pan and Yingang Gui. Each contribution comes as a separate chapter complete in itself but directly related to the book's topics and objectives. This publication aims at providing a thorough overview of the latest research efforts by international authors on Nanomaterials, and open new possible research paths for further novel developments.

InTechOpen

Chapter 1

The SF_6 Decomposition Mechanism: Background and Significance

Xiaoxing Zhang, Ju Tang, Song Xiao and Fuping Zeng

Additional information is available at the end of the chapter

http://dx.doi.org/10.5772/intechopen.68284

Abstract

Gas Insulated Switchgear (GIS) has been widely used in substations. The insulating medium used in GIS is sulfur hexafluoride (SF_6) gas. However, the internal insulation defect existed in GIS would inevitably lead to partial discharge (PD), and cause the composition of SF_6 to SOF_2, $SO2F_2$ and SO_2 and other characteristic component gases. The decomposition phenomenon would greatly reduce the insulation performance of SF_6 insulated equipment, and even paralyze the whole power supply system. In this chapter, we first discuss the objective existence, decomposition mechanism and harmness of insulation defects. Then the methods for insulation defects detection used to avoid the insulation accidents are introduced. Comparing all of the detection methods, diagnosing the insulation defect through analyzing the decomposed gases of SF_6 by chemical gas sensors is the optimal method due to its advantages, such as high detection accuracy and stability, signifying the importance of developing chemical gas sensor used in SF6 insulated equipment. In conclusion, there kinds of gas sensor material, carbon nanotubes, graphene, are chosen as the gas sensing materials to build specific gas sensors for detecting each kind of SF_6 decomposed gases, and then enhance the gas sensitivity and selectivity by material modification.

Keywords: SF_6-insulated equipment, insulation defect, SF_6 decomposition components, detection methods

1. The purpose of study on SF_6 decomposition components

Gas-insulated equipment using SF_6 as insulation and arc extinguishing media such as gas-insulated station (GIS), gas-insulated transformer (GIT), and gas-insulated line (GIL) has been widely used in the field of high voltage and extra-high and ultra-high voltage power systems.

It gradually became the most ideal equipment and one of the important symbols of modern substation because of its high reliability, easy maintenance, less occupied area, and flexible allocation since it was first commissioned in Germany in 1967 [1–3].

However, SF_6 gas-insulated equipment will inevitably have insulation defects. The insulation defects mainly come from the following aspects: (1) residual metal burrs or protrusions on the buses or electrodes during the manufacturing process, (2) loose contacts during the installation or transportation, (3) internal free metal particles, (4) insulation aging, and (5) corrosion and other problems [4, 5]. The positions where the insulation defects existed can occur at the interface or inside of insulators. For the insulation at the surface of insulators, the defect is usually caused by secondary effects of other types of defects, such as the uncleaned remnants, metal powder, partial discharge decomposition components, condensed fluid water on the surface of insulators, and insulator surface air gap [6]. Internal insulation defects are usually small and hard to detect. They are usually formed in the manufacturing processes, such as internal gas gap or delamination caused by the different thermal expansion. Besides, the solid insulators used in GIS are usually made of organic polymer material. The insulation performance of these materials is greatly affected by the strong electric field and thermal field. If small failures occur in the internal equipment, the insulation performance of the solid insulator at fault point would deteriorate significantly due to the continuous strong electric field and thermal field and ultimately would lead to electric breakdown or thermal breakdown. However, the insulation performance of the insulator cannot be self-restored [7–9].

When SF_6 gas-insulated equipment malfunctions, its fully enclosed structure makes it very difficult to carry out the fault location and repairing work. The average power-off overhaul time of the SF_6 gas-insulated equipment after its failure is longer than that of other electrical equipment and it affects a wider range [10]. As the key part of transportation and distribution of electrical energy, the safety and stability of SF_6 gas-insulated equipment play an important role in successful operation of the power system. Once the improper protection appears or timely removal of faults cannot be done, it causes a cascading failure, which will result in an enormous economic loss and even a sudden public safety issue. Therefore, online monitoring of SF_6 gas-insulated equipment becomes a task that must be accomplished by the power grid staff. Analyzing the running status of the equipment by a long-time and reliable data accumulation and studying the characteristic parameters that indicate the state of SF_6 gas-insulated equipment are the major issues for electric power research institutes. The purpose is to find latent or early insulation failure timely by inspecting and identifying key parameters to prevent the development of accidents.

When defects of solid insulation in SF_6 gas-insulated equipment mentioned above occur, these cause the distortion of the electric field in the equipment, which may result in PD or partial overheating (PO) before it completely breaks down [11]. When serious PD or PO appears, it will accelerate the damage of internal insulation, which will ultimately lead to insulation faults and power failure. This is a potential hazard to the running SF_6 gas-insulated equipment, also known as "insulation tumor." On the other hand, PD or PO is one of the key parameters that can represent the internal solid insulation condition of the SF_6 gas-insulated equipment. The insulation defects and their types in SF_6 gas-insulated equipment can

be detected to some extent by detecting PD or PO combined with pattern recognition [12]. Therefore, detecting PD or PO has important significance for ensuring reliable operation of SF_6 gas-insulated equipment and can greatly improve the ability and level of monitoring of the SF_6 gas-insulated equipment.

Based on the existing research results, the continuation of PD and PO will cause SF_6 decomposition. The decomposition products of SF_6 contain some highly active substances, such as F, HF, and SO_2. They will further corrode solid insulation material and metal fasteners and generate substances such as CF_4, COF_2, C_3F_8, C_4F_8, C_4F_{10}, C_5F_{10}, C_6F_{12}, CF_8S, CF_6S_2, CO, CO_2, etc., which will form a vicious cycle and cause further solid insulation deterioration and finally induce sudden failures [13–15]. To sum up, the contents of decomposition components of SF_6 and solid insulating materials and their change rule under continuous PD or PO have a close relationship with the type and severity of internal faults in the equipment. Hence, monitoring the sorts and contents of the decomposition products has become an effective means to determine the cause and the degree of development of thermal and electrical failures. By a theoretical and experimental study of SF_6 decomposition under PD or PO caused by internal faults, the characteristic parameters of decomposition products which can reflect and distinguish different types and severity of faults can be extracted. They can be used to establish fault diagnosis method and comprehensive evaluation system of SF_6 gas-insulated equipment. Thus, the internal insulation failure of SF_6 gas-insulated equipment could be found timely through detection of the decomposition products of SF_6 and the state of insulation could be estimated scientifically, which can reduce the probability of sudden failures of SF_6 gas-insulated equipment and build the first defense system against the sources of large accidents.

2. The current developments of the SF_6 decomposition mechanism and influence factors

So far, researches on SF_6 decomposition under the effect of discharge have mainly been carried out on the decomposition mechanism under arc discharge, spark discharge, and partial discharge, and initial progress has been made. However, a study on the evaluation and fault diagnosis of SF_6 gas-insulated equipment using the characteristics of SF_6 decomposition under different conditions has not yet been reported. As a whole, research about fault diagnosis for equipment evaluation research using the decomposed components analysis (DCA) method is still in the early stage. Most of the results are limited to discussing the influence of partial discharge and the impurity of gas on SF_6 decomposition components, but the content of decomposition gases and gas production characteristics under different insulation flaws has not been studied, and the corresponding mechanism has not been reported so far [16]. As for SF_6 decomposition characteristics and mechanism under overheat conditions, no report exists. Based on the specificity of SF_6 decomposition components under different insulation defects, such as gases types and concentration, it is feasible to develop specific gas sensors to detect corresponding characteristic SF_6 decomposition components, realizing the online evaluation and fault diagnosis of SF_6 gas-insulated equipment.

Pure SF_6 is odorless, colorless, non-toxic, non-combustible, and inert gas, and its chemistry property is very stable under 150°C. Extensive domestic and overseas studies show that when PD occurs in SF_6 gas-insulated equipment, SF_6 will decompose under the effect of electric field energy and generate low fluorine sulfide products such as SF_5, SF_4, SF_3, SF_2, SF, etc. [17]. If PD appears in pure SF_6, these low fluorine sulfur products will recombine into SF_6 after they diffuse out of the local high voltage area. The transient decomposition process of SF_6 has little influence on the insulation performances of SF_6-insulated equipment [18, 19, 20]. However, various impurities, such as trace amounts of air and water, exist in SF_6 gas-insulated equipment inevitably (at present, the content of impurity of SF_6 produced in our country can meet the requirement of International Electrotechnical Commission (IEC) standards and technical conditions in our country). These impurities can react with low fluorine sulfur products mentioned above and generate other oxygen-containing gas components. Some stable decomposition components are shown in **Figure 1**. The decomposition mechanism of SF_6 under corona discharge is shown in **Figure 2**. Therefore, insulation monitoring and fault diagnosis of SF_6 gas-insulated equipment can be achieved by detecting the SF_6 decomposition components and their contents.

The scholars have done a lot of research on the SF_6 decomposition components under arc, spark, and PD conditions, and the decomposition mechanism and decomposition components of SF_6, including SO_2, CF_4, SOF_4, SO_2F_2, HF, SOF_2, and $S_2F_{10}O$ under the PD condition, have also been preliminarily understood. According to an experimental study, S_2F_{10} and $S_2F_{10}O$ are the unique decomposition components under spark discharge, and they cannot be detected under PD. Therefore, S_2F_{10} and $S_2F_{10}O$ can be used as the characteristic gases of spark discharge. However, the decomposition components of SF_6 under PD mainly contain SOF_4, CF_4, SO_2F_2, SOF_2, H_2S, SO_2, and HF. It should be noted that HF is an acid gas, which can easily react with insulation materials, metal connectors, and other equipment components and generate corresponding fluorides, and the content of HF will decrease with the development of PD. For this reason, HF cannot be regarded as the characteristic component of PD [21]. SOF_4 is extremely unstable and can easily react with water to generate SO_2F_2. When the equipment has a certain moisture content inside or a small amount of water infiltrates into the gas during

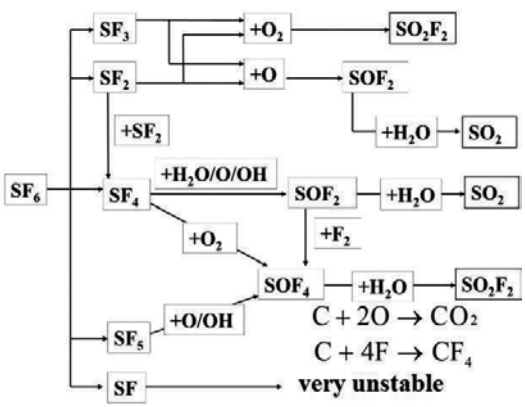

Figure 1. Formation of SF_6 decomposition components.

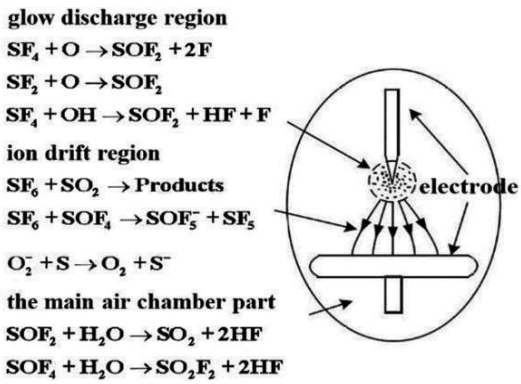

Figure 2. SF_6 decomposition mechanism under corona discharge.

the gas sampling and detecting process, the results will be seriously affected. Therefore, SOF_4 also cannot be used as the characteristic component of PD [22]. Although SOF_2 can be hydrolyzed, it is relatively stable. Based on the above research results, H_2S, SO_2, SOF_2, and SO_2F_2 were chosen as the characteristic components of SF_6 decomposition under PD to conduct the analysis of online monitoring [21, 23].

Up to now, no research scholars have built a unified system for the SF_6 decomposed component analysis method, and gas-insulated equipment insulation online monitoring & fault diagnosis technology. These research areas are not adequate for the electrical equipment online monitoring and fault diagnosis field but have broad prospects. Considering the characteristics of SF_6 decomposition caused by PD or PO with different typical insulation defects in gas-insulated equipment, insulation monitoring and fault diagnosis of gas-insulated equipment can be realized by SF_6 decomposition components and their tendency to change content. The method has become a leading domestic and international detection technology. The progress has attracted wide peer attention worldwide, and some achievements have been used in electric power enterprises. Now, the results of the project have been cited to formulate international standards by the International Council on Large Electric Systems (CIGRE).

3. The detection methods of SF_6 decomposition components

So far, the main methods to detect the decomposition components of SF_6 in GIS are gas chromatography, infrared absorption spectroscopy, photoacoustic spectroscopy, and chemical gas sensor.

3.1. Gas chromatography

The principle of gas chromatography is that the adsorption or dissolving capacity of the stationary phase to various SF_6 decomposition components is different. In other words, the distribution coefficients of different components in the two phases are different. When there is relative motion

between two phases, decomposition components are distributed repeatedly when they move forward in two phases. Different components can be separated because of the different velocities of different components along the column [24–27]. The separated SF_6 decomposition components pass through the detector according to the separation order, and the detector turns the concentrations of components in mobile phase into corresponding electrical signals [28]. This method can measure the concentration of SOF_2, SO_2F_2, SO_2, and CF_4 with high detection sensitivity that can reach 10^{-9}. However, it cannot detect HF and SOF_4. Besides, the testing time is too long for continuous detection. It also demands a high standard of the environment since the separation effect is influenced by the temperature and chromatographic columns need to be washed after using for a period of time. Therefore, this method cannot be used in *in situ* monitoring of GIS [29].

3.2. Photoacoustic spectroscopy

Photoacoustic spectroscopy is the measurement of the effect of absorbed electromagnetic energy (particularly of light) on matter by means of acoustic detection.

The absorbed energy from the light causes local heating and a pressure wave (or sound) is generated through thermal expansion. A photoacoustic spectrum of a sample can be recorded by measuring the sound at different wavelengths of the light. This spectrum can be used to identify the absorbing components of the sample and their concentrations with very high sensitivity. However, this method relies deeply on the experimental environment and is susceptible to external interference [29].

3.3. Infrared absorption spectroscopy

The principle of infrared absorption spectroscopy is that the degree of absorption of infrared light when it passes through the detected gas is linear to the volume fraction of the detected gas. The intensity ratio of the transmitted and incident light and the wavelength form a function, which is the infrared absorption spectrum of the detected gas. During the detection, the gas absorption peak will appear at different detected gases' best absorption wavelength of their infrared spectrum [30]. Based on the above principle, Fourier infrared spectrometer can detect SO_2, SOF_2, SOF_4, SO_2F_2, and CF_4 at the μL/L level. However, the background gas SF_6 will lead to the displacement of the absorption peak of the characteristic gases, and there is also interference among each detected gas. So, the detection results must be corrected when using infrared absorption spectroscopy. In addition, the detection requires large gas volume because the gas pool of infrared absorption spectroscopy is large. The detection sensitivity is also low when detecting trace gases because the difference of the intensity of incident and transmission light is very small. Besides, its accuracy for quantitative detection is easily affected by the reflected and scattered light. In view of the above shortcomings, infrared absorption spectroscopy is not a good option for the online monitoring of GIS. It can only exert its advantage of high detection sensitivity in laboratory studies.

3.4. Gas sensor method

The principle of gas sensor method is that the chemical properties of gas-sensitive materials will change after gas molecules are absorbed on its surface, and this can lead to the change

of electrical properties of the gas-sensitive materials. The gas sensor has the features of high detection speed, high efficiency, and small volume; it can be used with computers to realize automatic online monitoring and diagnosis. However, it can only detect a single gas, so the detection of each gas needs a specific gas sensor [31]. Therefore, a gas sensor array must be developed to detect different SF_6 gas decomposition components. So far, some research results exist on detection of H_2S and SO_2 by gas sensors, but the research about detection of SO_2F_2, SOF_2, CF_4, SF_4, SOF_4, and H_2S using gas sensors is rare.

4. The significance of gas-sensing material on online monitoring SF_6 decomposition components

For the online monitoring of SF_6 gas-insulated equipment, there were no report about suitable online monitoring devices of SF_6 decomposition characteristic components in gas-insulated equipment. Although photoacoustic spectrum method, gas chromatography, infrared absorption spectroscopy, and gas sensors have been used for detecting SF_6 decomposition components at present, there is still lack of fast and low-cost online monitoring means to detect characteristic gases of SF_6 decomposition components in gas-insulated equipment. With the rapid development of nano-sensing technology, the gas sensor method to detect SF_6 decomposition components has become the trend of research hotspot [31–33]. Study of the gas sensor method to detect SF_6 decomposition components not only enriches and develops the new method of online monitoring, but also has important engineering significance and broad application prospects of realizing online monitoring of SF_6 decomposition components in gas-insulated equipment and its condition-based maintenance.

Based on the study of response mechanism and testing experiments of nanometer sensors for detecting SF_6 decomposition components, the first condition for realizing online monitoring SF_6 decomposition components using gas sensor method is to develop nano-sensor technology. Developing composite nanometer sensor technology by various modification methods with a single response for different components of SF_6 decomposition and establishing relationship between a single component of SF_6 decomposition and the intensity of gas-sensitive characteristic signal in order to obtain the sensor array gas-sensitive element are the key technical problems that need to be resolved in order to realize online monitoring of SF_6 decomposition components with the gas sensor method. In this chapter, the following two aspects are investigated about the nanosensors for detecting SF_6 decomposition components. First, for the theoretical simulation, analyzing the characteristics of the mechanism of SF_6 decomposition components absorbing on the surface of nano sensors based on the first principle of density function theory is the theoretical basis of realizing the online monitoring of SF_6 decomposition components. Next, from the aspect of experiments, we need to develop gas sensors of high performance according to the theoretical results and prepare gas sensors with high sensitivity and selectivity to SF_6 decomposition components.

Carbon nanotubes, titanium dioxide nanotubes, and graphene are used for detecting SF_6 decomposition components in this chapter. These three materials are hotspots of new types of functional materials in the field of gas-sensitive sensor. They not only have strong response

sensitivity, selectivity, small size, low working temperature, easy processing, and many other traditional advantages but also have unique atomic structure and excellent electrochemical properties. Hence, gas sensors have great research potential and broad prospects in the field of electrochemistry and gas-sensing technology. Carbon nanotubes have abundant pore structure, large specific surface area, strong surface adsorption ability, good electrical conductivity, and electronic transmission characteristics. These unique physical and chemical properties and excellent gas-sensitive properties make them the hotspots in the field of nanometer gas-sensitive materials [34]. The carbon nanotube gas sensor is featured with high sensitivity, fast response speed, small size, and low power consumption, and it can work at room temperature [35]. It has broad application prospects in the aspect of gas sensor. TiO2 nanotube array (TNTA) has three-dimensional nanopore structure, which results in many virtues: fast gas-sensitive response speed, high sensitivity, possible surface modification, and excellent gas-sensitive selectivity. In order to further improve the gas-sensing properties of TiO_2 nanotubes, domestic and overseas researchers came up with metal doping, nonmetal doping, semiconductor doping, and functional group modification to realize the modification of intrinsic TiO_2 nanotubes [36–39]. Graphene has a unique two-dimensional structure, large specific surface area, excellent conductivity, extremely low Johnson noise and thermal switch noise, and few crystal defects. Theoretical analysis shows that graphene has the ability to detect ultra-low concentration of gas, so it becomes a kind of new functional materials in the field of sensors. In addition, graphene is a material with the best electrical conductivity in room temperature to date. It not only has strong adsorption ability to chemical gas composition, but also has excellent desorption ability. It can reduce the operation temperature of the gas sensors, thereby reducing the energy loss, compared with semiconductor metal oxide sensors of high operating temperature.

Carbon nanotubes, titanium dioxide nanotubes, and graphene materials are applied in the study of detection of SF_6 decomposition characteristic components to explore the practical application in engineering of new gas-sensing nano materials in the field of electrical equipment online monitoring. It can further enrich and develop the online monitoring method of characteristic gases of electrical equipment failure. The achievement of the gas-sensing mechanism based on density functional theory also provides scientific theoretical guidance for developing high-performance sensors.

Author details

Xiaoxing Zhang*, Ju Tang, Song Xiao and Fuping Zeng

*Address all correspondence to: xiaoxing.zhang@outlook.com

School of Electrical Engineering, Wuhan University, Wuhan, China

References

[1] Christophorou LG, Olthoff JK, Van Brunt RJ, et al. Sulfur hexafluoride and electric power industry. IEEE Electrical Insulation Magazine. 1997;**13**(5):20–24

[2] Pearson JS, Farish O, Hampton BF, et al. Partial discharge diagnostics for gas insulated substations. IEEE Transactions on Dielectrics and Electrical Insulation. 1995;**2**(5):893–905

[3] Chu FY. SF_6 decomposition in gas-insulated equipment. IEEE Transactions on Electrical Insulation. 1986;**EI-21**(5):693–725

[4] Gu DX, Xiu MH, Dai M, et al. Study on VFTO of 1000 kV GIS substation. High Voltage Engineering. 2007;**11**(33):27–32

[5] Koch H. Gas insulated transmission lines (GIL). Chichester, UK: John Wiley & Sons; 2011

[6] Joint Working Group 33/23 12. Insulation coordination of GIS: Return of experience, on site tests and diagnostic techniques. Electra; 1998:**176**(2):67297

[7] Kingsbury N. Complex wavelets for shift invariant analysis and filtering of signals. Applied and Computational Harmonic Analysis. 2001;**10**(3):234–253

[8] Qi B, Li CR, Hao Z, et al. Surface discharge initiated by immobilized metallic particles attached to gas insulated substation insulators: Process and features. IEEE Transactions on Dielectrics and Electrical Insulation. 2011;**18**(3):792–800

[9] Li B. Necessity of design for the metal outer rings and shielding inner ring of GIS basin-type insulator. High Voltage Apparatus. 2012; **48**(8):109–113

[10] Si W, Li J, Yuan P, et al. Detection and identification techniques for multi-PD source in GIS. Proceedings of the CSEE. 2009; **29**(16):119–126

[11] Wang Y, Li L, Yao WJ, et al. Analyzing decomposition products in overheat faults simulation to evaluate SF_6 gas insulation device. High Voltage Apparatus. 2011; **47**(1): 62–69

[12] Xin Z, Yuanzhe X. Study on SF_6 breakers micro-water examination device. Engineering & Test. 2009 1:017

[13] Okubo H, Yoshida M, Suzuki A, et al. Discrimination of partial discharge type in SF_6 gas by simultaneous measurement of current waveform and light emission. Conference Record of the 1996 IEEE International Symposium on Electrical Insulation. IEEE. Institute of Electrical and Electronics Engineers, Inc., Piscataway, NJ (United States), 1996;**1**:107–110

[14] Jun-kun Y, Yong-tao P, Xiang-yu TAN, et al. GIS device's discharge type measured by SF_6 decomposition product. Insulating Materials. 2012;**45**(2):61–64

[15] Tang J, Liu F, Meng Q, et al. Partial discharge recognition through an analysis of SF_6 decomposition products part 2: Feature extraction and decision tree-based pattern recognition. IEEE Transactions on Dielectrics and Electrical Insulation. 2012;**19**(1):37–44

[16] Zeng F, Tang J, Fan Q, et al. Decomposition characteristics of SF_6 under thermal fault for temperatures below 400°C. IEEE Transactions on Dielectrics and Electrical Insulation. 2014;**21**(3):995–1004

[17] Bini R, Basse NT, Seeger M. Arc-induced turbulent mixing in an SF_6 circuit breaker model. Journal of Physics D:Applied Physics. 2010;**44**(2):025203

[18] Tang J, Liu F, Zhang X, et al. Partial discharge recognition through an analysis of SF_6 decomposition products part 1: Decomposition characteristics of SF_6 under four different partial discharges. IEEE Transactions on Dielectrics and Electrical Insulation. 2012;**19**(1):29–36

[19] Zhang X, Ren J, Tang J, et al. Kernel statistical uncorrelated optimum discriminant vectors algorithm for GIS PD recognition. IEEE Transactions on Dielectrics and Electrical Insulation. 2009;**16**(1):206–213

[20] Zhang X, Yao YAO, Tang J, et al. Actuamity and perspective of proximate analysis of SF_6 decomposed products under partial discharge. High Voltage Engineering. 2008;**4**(120):37–42

[21] Boeck W. Solutions of essential problems of gas insulated systems for substations (GIS) and lines (GIL). IEEE Proceedings of the 7th International Conference on Properties and Applications of Dielectric Materials. 2003;**1**:1–8

[22] Latham RV, Bayliss KH, Cox BM. Spatially correlated breakdown events initiated by field electron emission in vacuum and high-pressure SF_6. Journal of Physics D: Applied Physics. 1986;**19**(2):219

[23] Tang J, Zeng F, Zhang X, et al. Relationship between decomposition gas ratios and partial discharge energy in GIS, and the influence of residual water and oxygen. IEEE Transactions on Dielectrics and Electrical Insulation. 2014; **21**(3):1226–1234

[24] Brunt RJV and Herron JT. Fundamental processes of SF_6 decomposition and oxidation in glow and corona discharges. IEEE Transactions on Electrical Insulation. 1990;**25**(1):75–99

[25] Siddagangappa MC, Brunt RJ. Mass spectrometric study of SF_6-N_2 plasma during etching of silicon and tungsten. Leeds University: Leeds University Press; 1985

[26] Siddagangappa MC, Brunt RJ, Phelps AV. Influence of Oxygen on the Decomposition Rate of SF_6 in Corona. Springer: NY; 1986

[27] Hergli R, Casanovas J, Derdouri A, et al. Study of the decomposition of SF_6 in the presence of water, subjected to gamma irradiation or corona discharges. IEEE Transactions on Electrical Insulation. 1988;**23**(3):451–465

[28] Brunt RJV, Sauers I. Gas-phase hydrolysis of SOF_2 and SOF_4. Journal of Chemical Physics. 1986;**85**(8):4377–4380

[29] IEC60480 IEC. Guidelines for the checking and treatment of sulfur hexafluoride (SF_6) taken from electrical equipment and specification for its re-use. IEC; 2004

[30] Kurte R, Heise HM, Klockow D. Quantitative infrared spectroscopic analysis of SF_6 decomposition products obtained by electrical partial discharges and sparks using PLS calibrations. Journal of Molecular Structure. 2001;**565**:505–513

[31] Suehiro J, Zhou G, Hara M. Detection of partial discharge in SF_6 gas using a carbon nanotube-based gas sensor. Sensors and Actuators B. 2005;**105**(2):164–169

[32] Ding W, Hayashi R, Suehiro J, et al. Calibration methods of carbon nanotube gas sensor for partial discharge detection in SF_6. IEEE Transactions on Dielectrics and Electrical Insulation. 2006;**13**(2):353–361

[33] Ding W, Hayashi R, Ochi K, et al. Analysis of PD-generated SF_6 decomposition gases adsorbed on carbon nanotubes. IEEE Transactions on Dielectrics and Electrical Insulation. 2006;**13**(6):1200–1207

[34] Li J, Lu Y, Ye Q, et al. Carbon nanotube sensors for gas and organic vapor detection. Nano Letters. 2003;**3**(7):929–933

[35] Du N, Zhang H, Chen BD, et al. Porous indium oxide nanotubes: Layer-by-layer assembly on carbon-nanotube templates and application for room-temperature NH_3 gas sensors. Advanced Materials. 2007;**19**(12):1641–1645

[36] Zaleska A. Doped-TiO2:A review. Recent Patents on Engineering. 2008;**2**(3):157–164

[37] Matsumoto Y, Murakami M, Shono T, et al. Room-temperature ferromagnetism in transparent transition metal-doped titanium dioxide. Science. 2001;**291**(5505):854–856

[38] Wen CZ, Hu QH, Guo YN, et al. From titanium oxydifluoride ($TiOF_2$) to titania (TiO_2): Phase transition and non-metal doping with enhanced photo catalytic hydrogen (H_2) evolution properties. Chemical Communications,.2011;**47**(21):6138–6140

[39] Kumar SG, Devi LG. Review on modified TiO_2 photocatalysis under UV/visible light: Selected results and related mechanisms on interfacial charge carrier transfer dynamics. The Journal of Physical Chemistry A. 2011;**115**(46):13211–13241

Chapter 2

Application of CNTs Gas Sensor in Online Monitoring of SF_6 Insulated Equipment

Xiaoxing Zhang, Song Xiao, Ju Tang and Cheng Pan

Additional information is available at the end of the chapter

http://dx.doi.org/10.5772/intechopen.68325

Abstract

The detection and analysis of SF_6 decomposition components are of great significance in online condition assessment and fault diagnosis of GIS. Considering the shortcomings of general detection methods, carbon nanotubes (CNTs) gas sensor was studied to detect the SF_6 decomposition components because of its advantages in large surface activity and abundant pore structure, et al. The large surface area has a strong adsorption and desorption capacity. In this chapter, SF_6 decomposed gases, namely SO_2F_2, SOF_2, SO_2, H_2S and CF_4 are chosen as probe gases because they are the main by-products in the decomposition of SF_6 under partial density (PD). First, the properties and preparation methods of CNTs are introduced to verify the advantages of CNTs for SF_6 decomposition components detection. Then, both theoretical calculation and sensing experiment were adopted to study the microadsorption mechanism and macrogas-sensing properties. Based on the intrinsic CNTs, study for SF_6 decomposition components adsorption, Pd, Ni, Al, Pt and Au metal doping CNTs and plasma-modified CNTs are discussed in order to enhance the gas sensing and selectivity of CNTs.

Keywords: SF_6 decomposition components, carbon nanotubes, preparation method, density functional theory, metal doping

1. Introduction of carbon nanotubes

1.1. The properties of carbon nanotubes

1.1.1. Structure of carbon nanotubes

Carbon nanotubes (CNTs), which are also called the bucky tube, are a one-dimensional material with special structure. It is one allotrope of carbon, like the diamond, graphite and

fullerene. In January 1991, a Japanese physicist Iijima first found CNTs produced during fabricating Carbon fiber using high-resolution transmission electron microscope [1]. CNTs possess large aspect ratio because of its one-dimensional property. The electron wave function of CNTs exhibits periodic and translational invariance in radial and axial direction. A new strong atomic hybrid orbital is built by sp^2 hybridization of carbon atoms, and CNTs skeleton of a hexagonal honeycomb is combined by σ bonds of carbon atoms. The isolated p electrons of Carbon atoms that did not participate in a hybrid together form conjugated π electron cloud across the entire CNTs. As shown in **Figure 1**, CNTs can be divided into single-wall carbon nanotubes (SWCNTs) and multi-wall carbon nanotubes (MWCNTs). Due to the unique molecular structure, CNTs have some specific properties in mechanics, electricity and heat.

1.1.2. Mechanical properties of carbon nanotubes

Carbon atoms in CNTs show sp^2 hybridization, which have more s orbital compared with sp^3 hybridization, and hence, the formed CNTs possess high modulus and strength. Its hardness is similar to that of diamond, while it also can be stretched due to its good flexibility. Like the reinforced fiber used in industry, the crucial factor that determines the strength of fiber is length to diameter ratio (at least 20:1). And the length to diameter ratio of CNTs has even

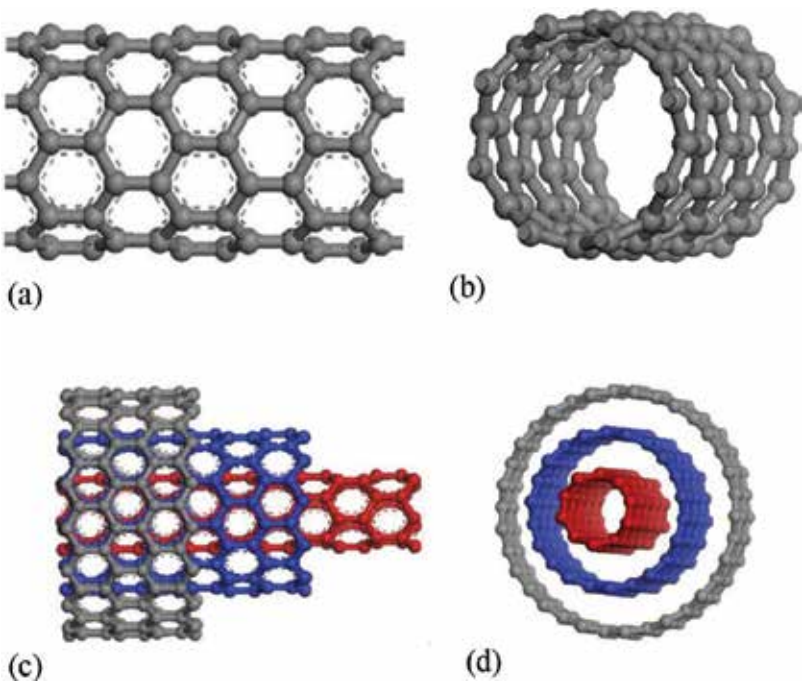

Figure 1. CNTs structural models. (a) SWCNTs (lateral view); (b) SWCNTs (sectional view); (c) MWCNTs (lateral view); (d) MWCNTs (sectional view).

reached 1000:1, making it an ideal fiber material with high strength, while the weight of CNTs is only 1/6–1/7 that of steel [2]. Therefore, CNTs are also called "super fiber". Besides, Krishnan et al. found that the Young's modulus of SWCNTs along radial direction is up to 1 TPa measured by atomic force microscope [3].

1.1.3. The thermal properties of carbon nanotubes

CNTs show heat conduction anisotropy, showing high and low heat exchange in vertical and axial direction, respectively. Therefore, the high anisotropy of heat conduction material can be synthesized by controlling the orientation of the CNTs. The thermal conductivity of composites can be effectively improved by doping trace of CNTs.

1.1.4. The electrical properties of CNTs

The isolated p electrons of C atoms do not participate in a hybridization form a wide range of delocalized π bond due to the significant conjugative effect, making it possesses special electrical properties. As shown in **Figure 2**, C_h represents the arrangement direction of CNTs atom, while a_1 and a_2 represent two basis vectors, respectively, where $C_h = n^*a_1 + m^*a_2$ (noted as (n, m)). (n, m) is closely related to the electrical conductivity of CNTs. For a given (n, m) CNTs, the electrical conductivity of CNTs in this direction is the metallic if $2n + m = 3q$ (q is integer), and otherwise the performance is the semiconductor. For the condition of $n = m$, the electrical conductivity of CNTs is usually 10,000 times as much as that of copper.

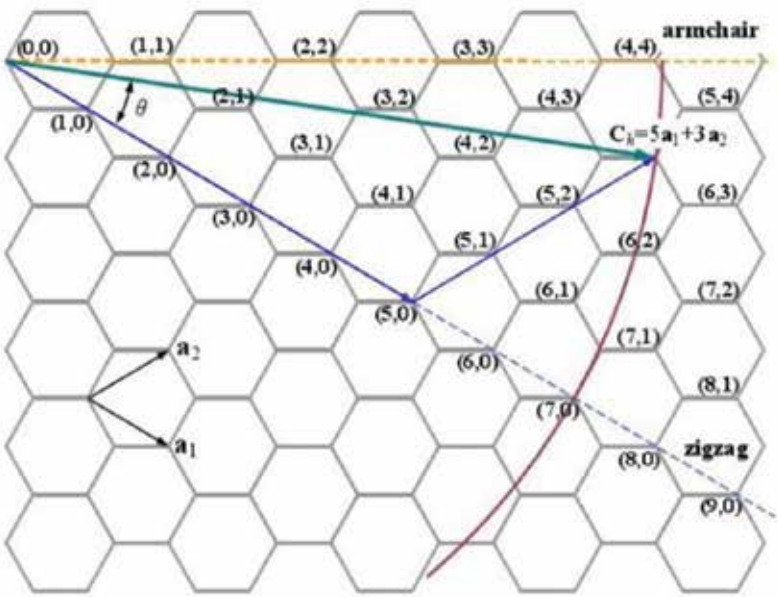

Figure 2. The Chiral vector selection of graphite flake.

1.1.5. The electron emission property of carbon nanotubes

CNTs have a nanometer scale point, which is benefit for to the electrons emission. Hence, scientists predicted and verified that CNTs have an excellent field emission effect.

1.1.6. The adsorption characteristics

CNTs have large surface activity and abundant pore structure. And the large surface area of the gas phase chemical composition has a strong adsorption and desorption capacity.

1.2. Carbon nanotubes preparation methods

1.2.1. Arc discharge method

It is the first and most used method to prepare CNTs. The main process is: (a) keep a certain pressure of inert gas or hydrogen in vacuum vessel, (b) choose graphite (with catalyst: nickel, cobalt and iron) as electrode. The graphite is consumed by evaporation at anode during the arc discharge process, and CNTs are received by depositing at cathode. Ebbesn et al [4]. successfully prepared gram order weight of CNTs under nitrogen gas condition, and then, this method is widely adopted. In 1994, Bethune introduced catalyst for arc reaction, reducing the reaction temperature and enhancing the productivity of CNTs. In 1997, Jounet et al. used catalysts for synthesizing single CNTs under helium condition. Sun Mingliang et al. studied the influence factors to CNTs prepared by DC arc discharge method: (a) inert gas pressure will affect the diameter and length of CNTs; (b) how much the adhesion of particles?; (c) oxygen and water vapor will lead to defects in CNTs, and it is unable to separate and purify after sintering together and (d) current and voltage will affect the yield and production rate of CNTs, but length to diameter ratio of graphite does not affect the generation of CNTs.

1.2.2. Catalytic cracking method

Catalytic cracking method, also known as chemical vapor deposition, prepares CNTs through cracking hydrocarbons or carbon oxides with the help of catalyst. The basic preparation process: (a) mixes the organic gases (such as acetylene and ethylene) with certain proportion of nitrogen gas in quartz tube. (b) CNTs grow on the surface of catalyst under certain temperature when the carbon source flow past and pyrolyze onto the surface of catalyst, and pushing forward the small catalyst particles [4]. (c) The growth of CNTs ends till all of the catalyst particles were coated with graphite layer. The advantages of the method are: easy to control the reaction process, simple equipment, low raw material cost, easy to produce the product in large scale, and the high productivity. The disadvantages are: too much CNTs layers, poor graphitization and exist crystalline defects. These disadvantages have great adverse influence on the physical and chemical properties of CNTs.

1.2.3. Laser evaporation method

Laser evaporation method prepares CNTs by illuminating the graphite target that contains metal catalyst. Then, the vapor mixes with carbon source and deposits on the surface of

substrate and the wall of reaction chamber. Smalley et al. received SWCNTs after adding a certain amount of catalyst to the electrode during preparing C_{60}. After improving the method, Thess et al. successfully fabricated amount of SWCNTs. Under the condition of 1473 K, the graphite target with Ni/Co catalyst particles was irradiated by double pulse laser with 50 ns, receiving the high-quality SWCNTs bundles.

1.2.4. Low-temperature solid-state pyrolysis method

Low-temperature solid-state pyrolysis prepares CNTs through intermediate. First, the nanometer level silicon nitride (Si_2C_2N) ceramic intermediate was prepared. The nanoceramic intermediate is then placed in a boron nitride crucible, which is heated in a graphite resistance furnace to decompose it with nitrogen gas as the protective gas. After 1 h, the nanointermediate powder begins to pyrolyze, and the carbon atoms migrate to the surface. A high proportion of CNTs are obtained with amount of silicon nitride powder in the surface pyrolysis products. The advantage of the low-temperature solid-state pyrolysis method is the repeatable production, which is beneficial for large-scale CNTs production.

1.2.5. Polymer pyrolysis method

The method prepares CNTs by decomposition of hydrocarbons precursor (such as acetylene and benzene) at high temperature. Cho et al. prepared CNTs by heating the polymer obtained from citric acid and glycol after polyesterification under 400°C for 8 h. The CNTs were synthesized by using metal Ni as catalyst in the temperature ranged from 420 to 450°C and under H_2 atmosphere. Under 900°C and Ar-H_2 atmospheric conditions, Sen et al. obtained CNTs by pyrolyzing ferrocene, nickelocene and cobaltocene. These metal compounds not only provide carbon source after pyrolysis, but also provide the catalyst particles. The growth mechanism of the method is similar to the catalytic cracking method.

1.2.6. Ion (electron beam) radiation method

In a vacuum furnace, carbon is evaporated by ion or electron discharge and deposit on the condenser. Chernazatonskii et al. synthesized CNTs with diameter range from 10 to 20 nm and high alignment by evaporating the graphite coated on the surface of substrates. Lin X et al. got CNTs with diameter range from 10 to 15 nm by irradiating amorphous carbon with argon ion beam under high vacuum environment [5].

1.2.7. Flame synthesis method

Flame synthesis method utilizes the heat, produced by burning methane and a small amount of oxygen, and imports hydrocarbons and catalysts at temperature of 600–1300°C to synthesize CNTs. The CNTs prepared by this method have the disadvantages of low crystallinity and large amount of amorphous carbon. There is still no definite explanation for the growth mechanism of CNTs nanostructure by flame method. Richter et al. found SWCNTs that attached with a large amount of amorphous carbon from carbon black after burning the mixture of acetylene, oxygen and argon gases. Daschowdhury et al. found nanometer tubular

CNTs by detecting carbon black after burning the mixture of benzene, acetylene, ethylene and oxygen gases.

1.2.8. Solar energy synthesis method

The CNTs are received from the condensation of high temperature (3000 K) mixture vapor of graphite and metal catalyst that heated by focusing the sunlight. This method is initially used for buckyballs production, then adopted for CNTs synthesis since 1996. Laplaze et al. synthesized the MWCNTs and SWCNTs use this method.

1.2.9. Electrolysis method

The preparation of CNTs by electrochemical method is a novel technique. This method adopts graphite electrode (electrolytic cell as anode), obtained carbon nanomaterials by electrolyzing molten alkali halide salts (such as LiCl) under a certain voltage and current with the protection of air or argon gases at about 600°C. The products include packaged or not packaged CNTs and carbon nanoparticles, and the form of carbon nanomaterials can be controlled by changing the process conditions of electrolysis. Andrei et al. found that CNTs can directly grow on the surface of n-type of (1 0 0) silicon electrode in solution of acetylene/ammonia. Hus et al. synthesized nanotubular and onion like CNTs under argon environment by using molten alkali metal halide as electrolyte and graphite as electrode. Huang Hui et al. successfully synthesized CNTs and carbon nanowires using LiCl and LiCl + $SnCl_2$ as molten salt electrolyte.

1.2.10. Other methods

Stevens et al. got CNTs by using an exothermic reaction between caesium and nanoporous amorphous carbon in the low temperature of 50°C. Chemozatonskii et al. found the fullerene and CNTs at the microholes of Fe_2Ni_2C, Ni_2Fe_2C and $Fe_2Ni_2Co_2C$ alloy prepared by powder metallurgy method [6]. Kyotani et al. first pyrolyze and deposit carbon on the wall of anodic alumina model (with nanometer trench) under 800°C. Then, hollow CNTs with open-end on both sides after removing the anodic alumina membrane by hydrofluoric acid can be obtained. Matveev et al synthesized CNTs using liquid nitrogen solution of acetylene at 233 K by electrochemical method. It is the lowest temperature ever reported to synthesize CNTs.

2. Modification CNTs

2.1. Simulation model build and computation method

This work chooses SWCNTs as a research object to present theoretical simulation for its adsorption of gas decomposition products of SF_6 and then explores its adsorption characteristics and predicts the detectable gas products. Materials Studio (MS) software developed by Accelrys Company is employed in this research, the $Dmol^3$ module of which is used for quantum mechanics stimulation. Generalized gradient approximation (GGA) approach, which

can accurately describe the geometric and electronic structures of CNTs as well as the processes of molecular interaction, is adopted to deal with the interchange and correlation between electrons, and its specific form is Perdew-Burke-Ernzerhof (PBE) [7]. The double-figure basis set (DNP) of polarization function is used in DFT (Density Functional Theory) calculation. In order to avoid the interactions between CNTs, a super grid 20 × 20 × 8.5 $Å^3$ has been designed, working under periodic boundary conditions. The initial distance between SWCNT and gas decomposition products of SF_6 is set as 0.16 nm. All atoms are calculated using full atomic potential, and the convergence value of self-consistent field is set as 10×10^{-5} eV/at [8]. Ref. [9] has shown that accurate results can be achieved by taking two K points in the (8, 0) SWCNTs Brillouin zone. All calculations above are accomplished on Dmol[3] module.

SWCNT, SF_6 as well as its gas decomposition products including SF_6, SO_2F_2, SOF_2, SO_2, H_2S, CF_4 and HF in the superlattices are optimized, respectively, to obtain the most stable structures before each calculation. **Figure 3** presents the stabilized configuration of SWCNT gas molecules (SF_6, SO_2F_2, SOF_2, SO_2, H_2S, CF_4 and HF) after geometrical optimization.

SF_6 and decomposition gas molecules are made to approach the C atom marked on the SWCNT in any possible posture, which is optimized to form a stable molecule-SWCNT system, respectively. Then, stable configurations will be found after a non-restrictive optimization to the molecule-SWCNT systems, and their electron properties will be calculated [8].

To assess the ability to interact between SWCNT and gas molecules, the adsorption energy E_b is calculated. E_b is defined as Eq. (1). E molecule-SWCNT-OH stands for the total energy of the molecule-SWCNT system after geometrical optimization, $E_{SWCNT\text{-}OH}$ and $E_{molecule}$, respectively, stand for the energy of SWCNT and that of an isolated molecule. If $E_b < 0$, it means the adsorption process is exothermic and can occur spontaneously.

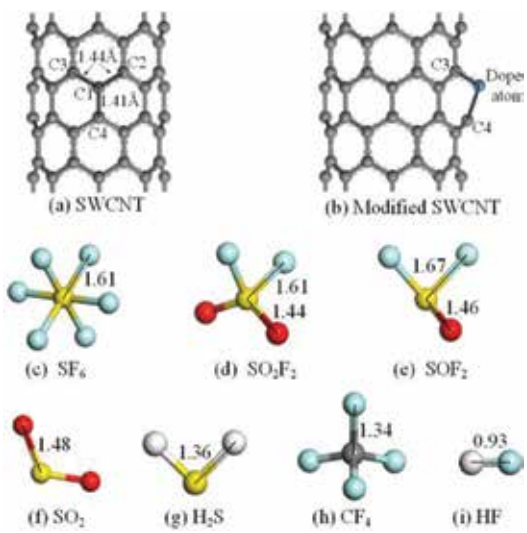

Figure 3. The most stable optimized configurations of SWCNT and gas molecules. The structural parameters are shown in Å. (a) SWCNT; (b) modified SWCNT; (c) SF_6; (d) SO_2F_2; (e) SOF_2; (f) SO_2; (g) H_2S; (h) CF_4; (i) HF.

$$E_b = E_{molecule-SWCNT} - E_{SWCNT} - E_{molecule} \quad (1)$$

The charge transfer Q_T between SWCNT and gas molecules is also computed to indicate the change of electrical conductivity of SWCNT, which can provide important information about electronic responses in the system [8]. The Q_T is calculated through the charge differences between the molecule adsorbed on the SWCNT and an isolated molecule itself as shown in Eq. (2) [8]:

$$Q_T = Q_{adsorped\ molecule} - Q_{isolate\ molecule} \quad (2)$$

Besides, the highest occupied molecular orbital (HOMO) energy level and lowest unoccupied molecular orbital (LUMO) energy level were studied to evaluate the energy needed for electrons to cross the energy barrier based on the frontier molecular orbital analysis [10, 11]. After the adsorption, the energy gap of the adsorption structure can be calculated through the energy levels of E_{HOMO} and E_{LUMO} defined as Eq. (3) [11].

$$E_g = \left| E_{LOMO} - E_{HOMO} \right| \quad (3)$$

2.2. Gas-sensing properties of intrinsic SWCNTs to SOF_2, SO_2F_2, SO_2, H_2S, HF, CF_4 and SF_6

2.2.1. Theoretical study: gas-sensing properties of intrinsic SWCNTs

2.2.1.1. The analysis of gas adsorption structure

We first studied the structure properties of pristine SWCNTs, Ni-SWCNTs, SO_2, SOF_2 and SO_2F_2. As an intrinsic structural beauty, SWCNTs consist of shells of sp^2-hybridized (trivalent) carbon atoms [12] forming a hexagonal network that is itself arranged helically within a tubular motif shown in **Figure 4a**. The bond lengths of zigzag bond C—C2 (C1—C3) and axial bond C1—C4 were 1.44 and 1.41 Å, respectively. **Figure 4** shows the most stable structures after gas molecules adsorb on the surface of intrinsic SWCNT. And the corresponding adsorption data are shown in **Table 1**.

It can be seen from **Figure 4**a, b and e and **Table 1**, the adsorption energy during the interaction of SF_6, HF and CF_4 with SWCNT is rather little, the adsorption energy of HF-SWCNT (−0.16 eV) is an order of magnitude lower than that of SF_6-SWCNT (−2.17 eV), and then, the adsorption energy of CF_4-SWCNT (−0.02 eV) is two orders of magnitude lower than that of SF_6-SWCNT; however, in terms of charge transfer, the number of charge transfer (0.038 au) between SWCNT and HF is an order of magnitude higher than that (0.005 au) between SWCNT and SF_6, while the number (0.003 au) between SWCNT and CF_4 is still lower than that, but in fact, the interacting distance is similar in the interaction of HF and CF_4 with SWCNT. As is shown above that SWCNT is insensitive to HF and CF_4 [8].

From **Figure 4c**, d and f and **Table 1** [8], it is clear that the adsorption energy during the interaction of H_2S, SO_2 and SOF_2 with SWCNT is almost in the same level; the number of charge transfer between SWCNT and H_2S (0.008 au) is a bit higher than that between SWCNT and SF_6 (0.005 au); however, they are in the same order of magnitude, while the number of charge

http://dx.doi.org/10.5772/intechopen.68325

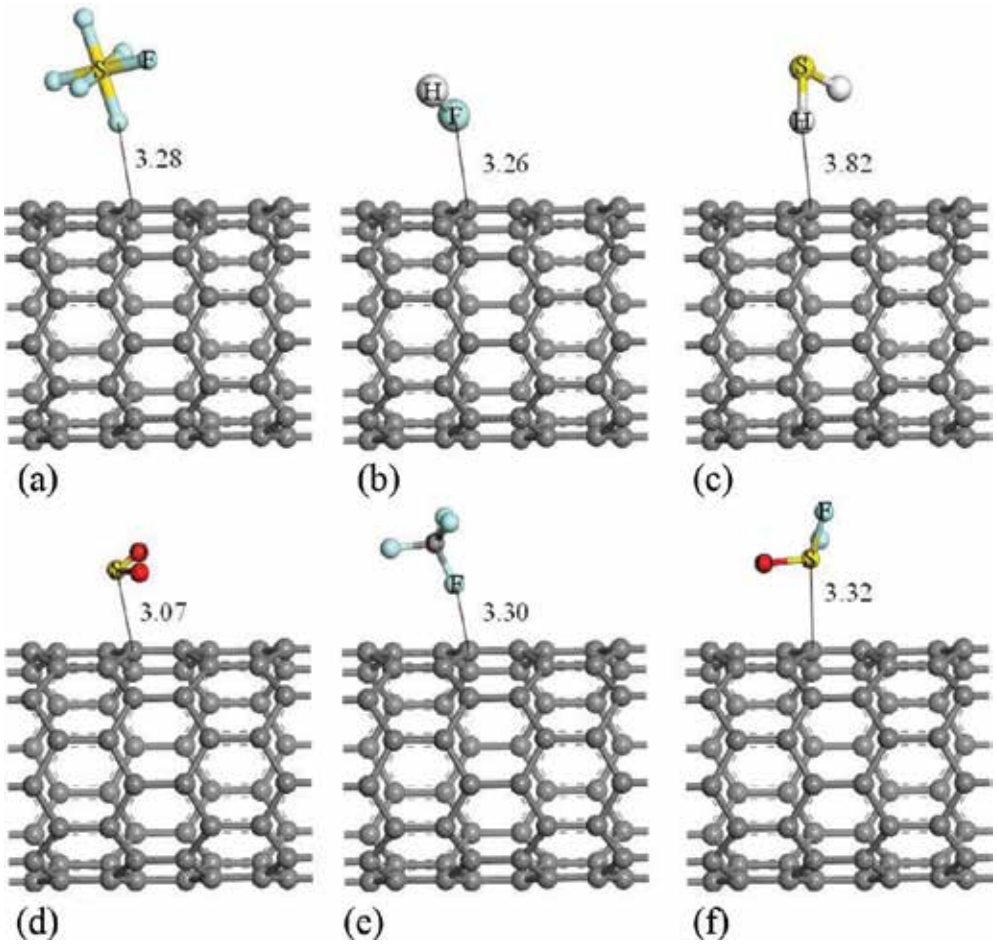

Figure 4. The most stable optimized configurations of gas molecules interacting with SWCNT, respectively. The structural parameters are shown in Å. (a) SF_6-SWCNTs; (b) HF-SWCNTs; (c) H_2S-SWCNTs; (d) SO_2-SWCNTs; (e) CF_4-SWCNTs; (f) SOF_2-SWCNTs.

System	Figure	E_b (eV)	Q_T (au)	D (nm)
SF_6-SWCNT	3a	−2.17	0.005	0.3278
HF-SWCNT	3b	−0.16	0.038	0.3262
H_2S-SWCNT	3c	−2.17	0.008	0.2822
SO_2-SWCNT	3d	−2.23	0.054	0.3071
CF_4-SWCNT	3e	−0.02	0.003	0.3299
SOF_2-SWCNT	3f	−2.21	0.017	0.3320
SO_2F_2-SWCNT	4a, b	−1.19	0.403	0.1943

Table 1. Calculated adsorption energy, charge transfer and interacting distance.

transfer between SWCNT and SO_2, SOF_2 is an order of magnitude higher than that between SWCNT and SF_6. But the interacting distance is similar in the interaction of SO_2, SOF_2, SF_6 with SWCNT. It means the sensitivity of SWCNT to H_2S, SO_2 and SOF_2 is the same as that to SF_6, so there is cross-sensitivity between them. Under the background of the high concentration of SF_6, SWCNT as a gas sensor is unable to accurately detect H_2S, SO_2 and SOF_2.

Figure 5 presents the most stable configurations of SO_2F_2-SWCNT. **Figure 5a** presents the chart whose chemical bond is not displayed; **Figure 5b** gives the chart whose chemical bond is displayed by MS. From **Figure 5b**, it is seen that the S atom in SO_2F_2 has formed the bond with the C atom marked in SWCNT, and the F atom has formed the bond with adjacent C atom yet, which means that the chemisorption between SWCNT and SO_2F_2 occurs. It can be inferred based on the data above that the adsorption energy of SO_2F_2-SWCNT is lower 0.98 eV than that of SF_6-SWCNT, but they are in the same order of magnitude, which shows that there exist differences between them. However, the number of charge transfer (0.403 au) between SWCNT and SO_2F_2 is 80 times higher than that (0.005 au) between SWCNT and SF_6, which shows that the conductivity of SWCNT has changed a lot after adsorbing SO_2F_2. The interacting distance during the interaction of SO_2F_2 with SWCNT is obviously less than that of other molecules. Therefore, it can be concluded that SWCNT is the most sensitive to SO_2F_2 in all the gas decomposition products of SF_6.

2.2.1.2. The analysis of the density of states

From **Figure 6**, it is clear that the density of states curves of SWCNT almost coincides after adsorbing HF, H_2S and CF_4 [8], which reveals that the electronic structures and conductive properties of SWCNT are basically unchanged, so SWCNT is not sensitive to HF, H_2S, and CF_4. However, the density of states curves shifts to the right of Fermi level after SOF_2 and SO_2 are absorbed, which indicates that the electronic structures are changed. There is a short overlap of DOSs between SWCNT and SO_2-SWCNT near Femi level, so the conductive properties change a little. But the DOSs peak of SOF_2-SWCNT is lower than that of SWCNT in the

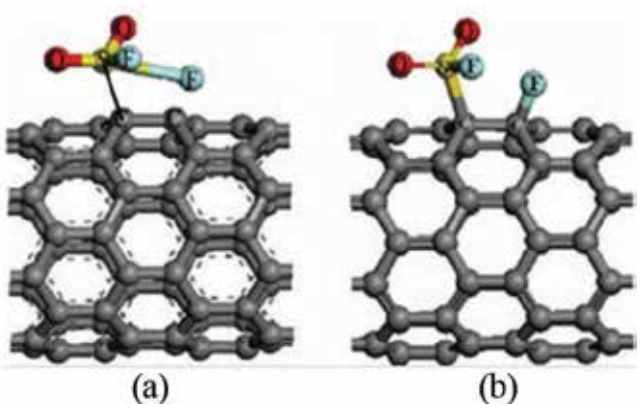

Figure 5. Optimized the most stable configurations of SO_2F_2-SWCNT. (a) Bonds not displayed by MS; (b) bonds displayed by MS.

http://dx.doi.org/10.5772/intechopen.68325

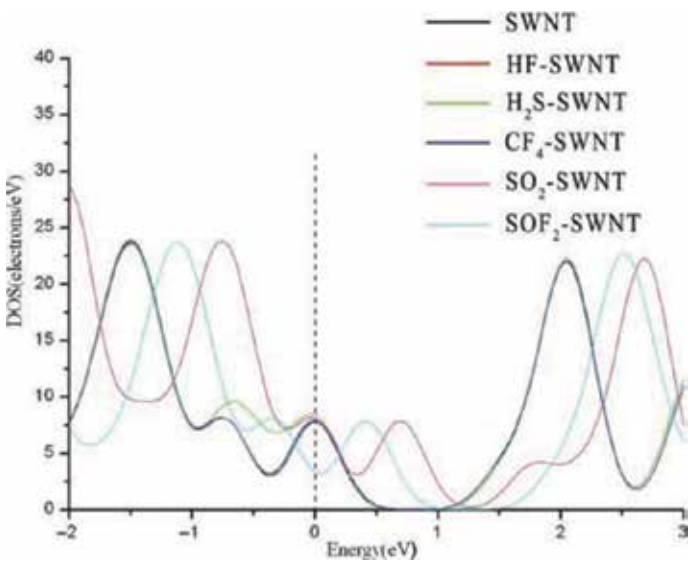

Figure 6. The DOSs of molecules-SWCNT. Dotted line indicates the Fermi level.

Fermi energy level, which means that the number of quantum states occupied by electrons in the Fermi energy level has reduced when SOF_2 molecules adsorbed on SWCNT, causing SWCNT's conductivity decreased. Finally, it can be concluded that the sensitivity of SWCNT to SO_2 is similar to SOF_2 [8].

From the **Figure 7**, it can be derived that DOSs has changed a lot after absorbing SF_6, SO_2F_2 in and near the Fermi level. DOSs curve of SO_2F_2-SWCNT is higher than SWCNT's, while

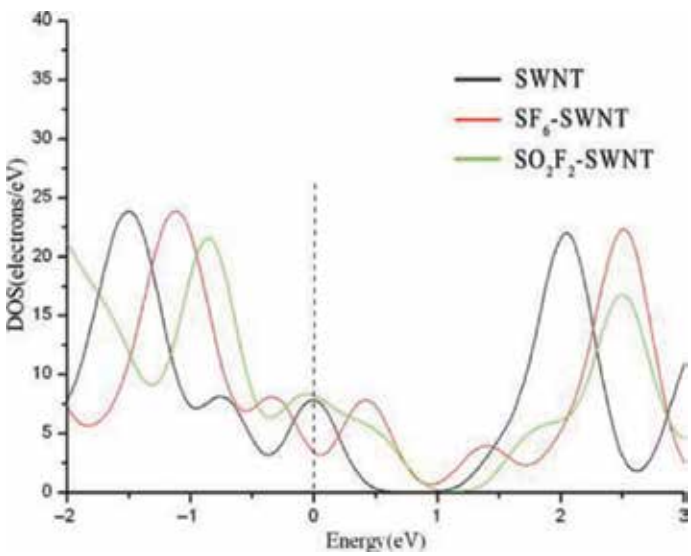

Figure 7. The DOSs of SWCNT, SF_6-SWCNT and SO_2F_2-SWCNT. Dotted line indicates the Fermi level.

DOSs curve of SF_6-SWCNT is lower than SWCNT's. The number of quantum states occupied by electrons near the Fermi energy level has increased after SO_2F_2 adsorbed by SWCNT, the properties of SWCNT becoming more active and conductivity being enhanced, on the contrary, the properties of SWCNT become less active after absorbing SF_6. Based on the analysis above, SWCNT is the most sensitive to SO_2F_2.

Band structures of SWCNT, SF_6-SWCNT and SO_2F_2-SWCNT are given in **Figure 8a–c**, from which we can see that the energy gap (Eg1 of SWCNT is about 0.022 ha (0.60 eV),

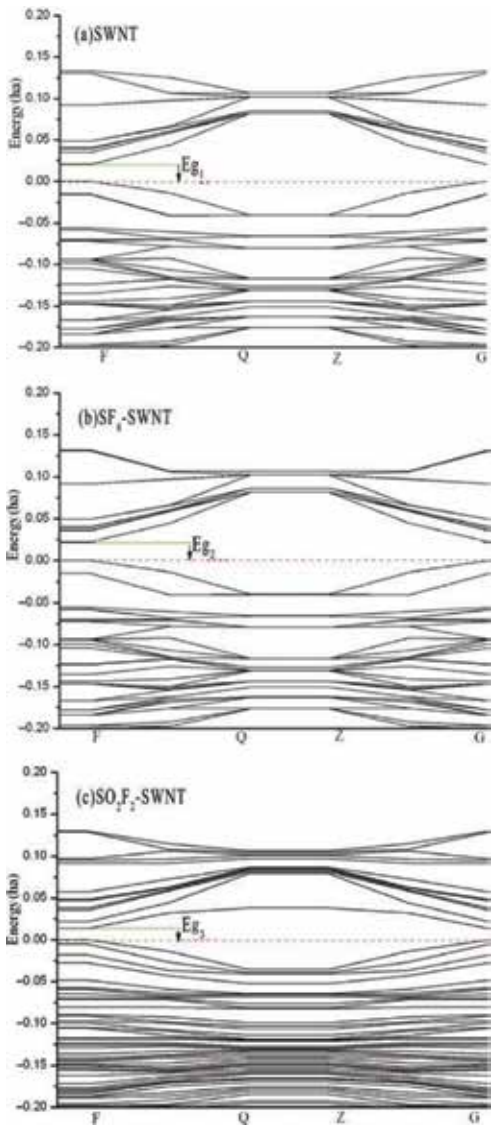

Figure 8. The band structure diagrams of (a) SWCNT, (b) SF_6-SWCNT and (c) SO_2F_2-SWCNT. Dotted line indicates the Fermi level.

SF_6-SWCNT (Eg2 is about 0.022 ha (0.60 eV) and SO_2F_2-SWCNT (Eg3) is about 0.015 ha (0.40 eV), which reveals that the conductivity is unchanged after absorbing SF_6, but the conductivity is increased after absorbing SO_2F_2. Thus, it can be predicted that SWCNT can serve as gas sensors to detect SO_2F_2, one of the decomposing gas products of SF_6, in partial density (PD).

2.2.2. Experimental study: gas-sensing properties of intrinsic SWCNTs

2.2.2.1. Preparation of plasma-modified intrinsic SWCNTs

MWCNTs (tube diameter, 20 to 30 nm; length, 10 to 30 μm; purity, >95%) were grown by chemical vapor deposition (CVD) in black powder and purchased from the Chengdu Institute of Organic Chemistry Chengdu, China. CNTs are one-dimensional (1D) nanomaterials. Hence, appropriate surface processing parameters should be selected. Under strong plasma treatments, high power and long treatment time can destroy the tubular structure and carbonization of CNTs [13, 14]. In this study, a DBD plasma generator was used to modify MWCNTs. **Figure 9** shows the schematic for the test device. Low-temperature plasma experimental power (CTP-2000K) used in this experiment was produced from Nanjing Rongman Electronics Co., Ltd., China. The input voltage of the experimental power is controlled by a voltage regulator. Adjust the voltage to 30 V, which can be reading from the Voltmeter (Power input) in the power device. Adjust output frequency knob in the experimental power until frequency is around 10 kHz. Then, we can get an optimum DBD discharge. Read the input current of 1.96 A from Ammeter in the power device. Using oscilloscope to obtain the output voltage and current waves, and displayed in **Figure 9**. We should point out that there is an attenuator in this experimental power, and the attenuation coefficient is 1000. So the output peak-to-peak voltage is 39.3 kV. The discharge power in DBD plasma reactor can be calculated by Lissajou curve. However, due to the poor laboratory conditions, we do not have enough oscilloscope attenuation probes to protect oscilloscope from breakdown. So other method should be explored, and we try to get in touch with the equipments manufacturers. According to the experience of the manufacturer's data, the plasma treatment power is approximately 0.8 times of the input power at the same experimental conditions. Therefore, we can calculate the discharge power which is 47 W.

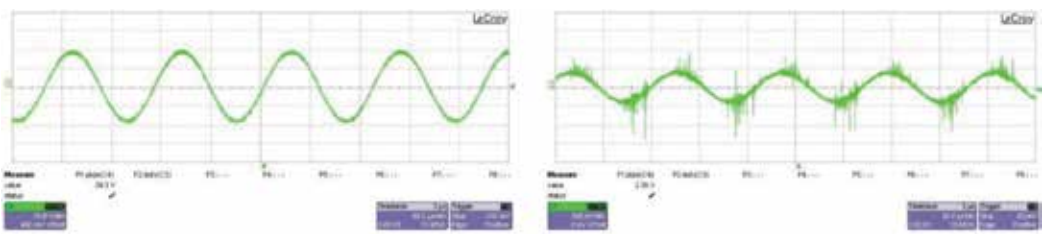

Figure 9. Discharge waveforms (a) output voltage waveform and (b) output current waveform.

Figure 10 reveals that the shape of the reactor is similar to a Petri dish. The reactor electrodes formed a parallel-plate structure and were made of 2-mm thick quartz glass. The upper and bottom electrodes were 8 mm apart. The bottom quartz glass electrode adhered to the reaction kettle, whereas the upper electrode is removable. In the modified experiment, an adequate amount of MWCNTs was placed in a reaction kettle and sealed with silicone to ensure gas tightness. Air was released from the reactor to induce a vacuum state. CF_4 flow rate was controlled at 150 sccm. The parameters of the experimental power were adjusted, and MWCNTs were, respectively, treated for 0.5, 1, 2, 5, 8, 10 and 12 min. The upper quartz glass was removed, and modified MWCNTs were obtained after the treatment.

2.2.2.2. Preparation of plasma-modified MWCNTs-based sensors

MWNT sensors were made of printed circuit board, and the substrate material is epoxy resin. Cu interdigital electrodes were etched in the substrate. The width and spacing of the electrodes are both 0.2 mm. First, MWCNTs were placed into a beaker containing the appropriate ethanol solution. The beaker was placed in an ultrasonic bath for 1 h. Then, the sensor substrate was repeatedly cleaned with deionized water to remove impurities on the electrode surface. Next, the mixed solution was dropped on the substrate surface. Finally, the MWNT-coated substrates were baked in an oven at 80°C for a specific time. This process was repeated several times until uniform MWCNTs films were deposited on the surface. Seven pristine and treated MWCNTs with different modification times were used to fabricate the gas sensors.

2.2.2.3. Characterization of plasma-modified MWCNTs

FTIR spectra are highly useful tools to analyze the characteristics of CNTs. **Figure 11** shows the FTIR spectra of pristine MWCNTs and those generated by CF_4 plasma etching for 1, 5 and 10 min with a Nicolet 5DXCFT-IR spectrometer.

Diverse functional groups and types of bonding were observed in the FTIR spectra of MWCNTs (**Figure 11**). The absorption peaks at 3445 cm^{-1} corresponded to the ─OH groups in pristine and treated nanotubes. The absorption peaks at 1036 and 1151 cm^{-1} were ascribed to the respective C─F and symmetric ─CF_2 stretching vibrations because of the CF_4 plasma treatment.

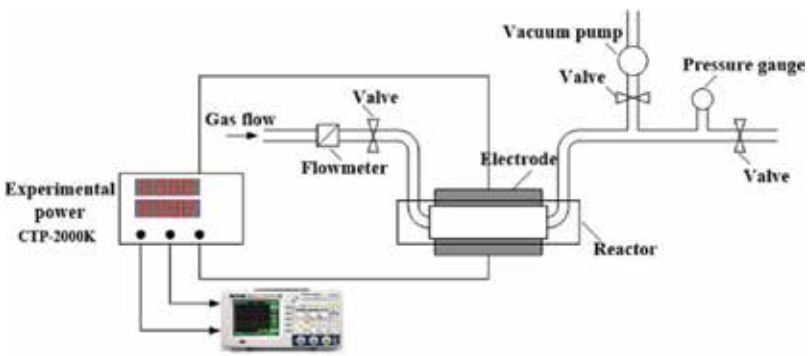

Figure 10. Schematic of the DBD experiment setup.

http://dx.doi.org/10.5772/intechopen.68325

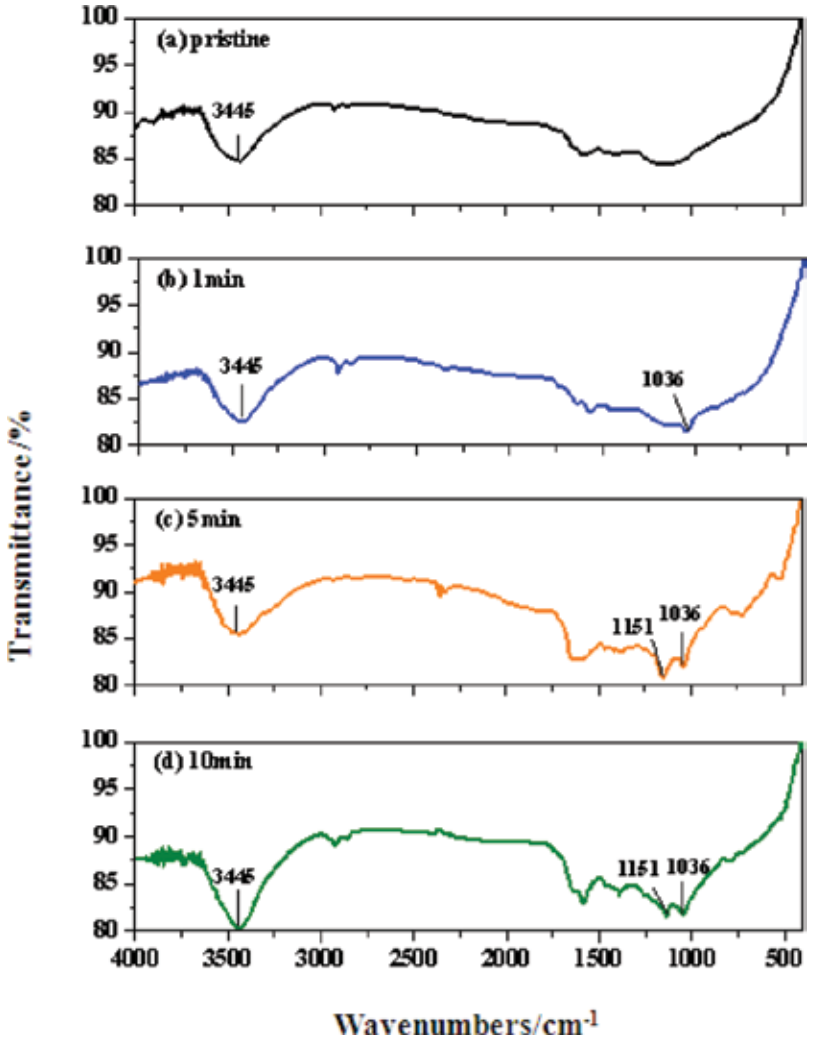

Figure 11. Infrared spectra of pristine and modified MWCNTs. (a) Pristine; (b) 1 min; (c) 5 min; (d) 10 min.

The surface morphologies of the pristine and plasma-treated MWCNTs were analyzed using Zeiss Auriga focused ion beam and double-beam emission scanning electron microscopy (SEM). The SEM images of pristine MWCNTs (**Figure 12a**) indicated the presence of several small particles, which included amorphous carbons and residual catalysts during preparation. **Figure 12b** and **c** shows the SEM images of CF_4 plasma treated for 10 min. The impurities and dopant on the nanotubes surfaces were removed, and MWCNTs became shorter. Plasma treatment retained the nanotubes structures.

2.2.2.4. The analysis of the gas-sensing properties

We used eight kinds of MWCNTs-based gas sensors (pristine MWCNTs and MWCNTs modified by plasma for different time) to detect H_2S and SO_2 whose concentration is both

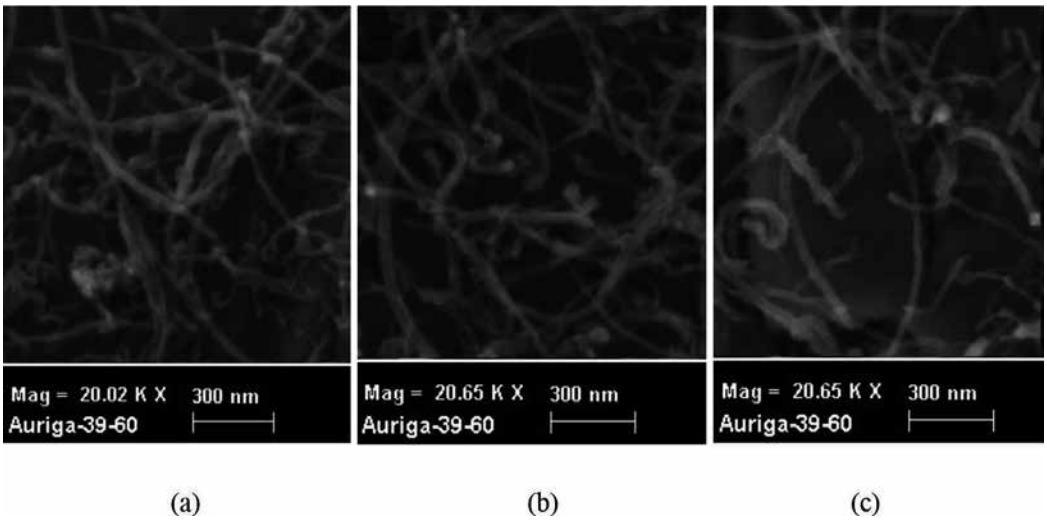

Figure 12. SEM images (a) pristine and (b and c) modified MWCNTs for 10 min.

50 ppm. The gas response curves are shown in **Figure 13**. It can be seen from **Figure 13a** and b that the sensitivity of pristine MWCNTs and those modified by CF_4 plasma for 0.5, 1 and 2 min to H_2S are 3, 3.2, 3.4 and 3.5%, respectively, and to SO_2 are 2.3, 2.4, 2.6 and 2.7%. Obviously, after modification, the gas sensitivities of MWCNTs are not markedly enhanced. Under small discharge power, these phenomena may have been caused by the insufficient treatment time and poorly surface modification. Therefore, if the discharge power remains unchanged, in order to achieve a better surface modification, plasma treatment time should be extended.

In consequence, **Figure 13c** and **d** shows the response curves of pristine MWCNTs and these treated for 5, 8, 10 and 12 min to H_2S and SO_2. We can see that when the treatment time is less than 10 min, the sensitivities of MWCNTs sensors increased with increasing of treatment time. Meanwhile, the MWCNTs modified by CF_4 plasma for 10 min exhibited the best sensitivity both to H_2S and SO_2. However, the sensitivities decreased when the treatment time is over 10 min. Possible reasons may be that after longer treatment time, the structure of the nanotubes was destroyed, and nanotubes were partly carbonized [13] under the bombardment of energetic particles in prolonged plasma treatments, which result in a reduce of active adsorption sites on MWCNTs surface for gas molecules. Hence, the gas-sensing properties of the MWCNTs were affected.

Figure 13 reveals that the response time of CF_4 plasma-modified MWCNTs sensors to H_2S and SO_2 was shorter. For treatment times ranging from 0 to 10 min, the response time decreased with increasing treatment time. Besides, the shortest response times to H_2S and SO_2 are 70 and 150 s, respectively.

Responses of MWCNTs-based sensors to H_2S and SO_2 at different concentrations are studied in this work. MWNT sensors modified by CF_4 plasma for 10 min (Section 3.3) were selected to

http://dx.doi.org/10.5772/intechopen.68325

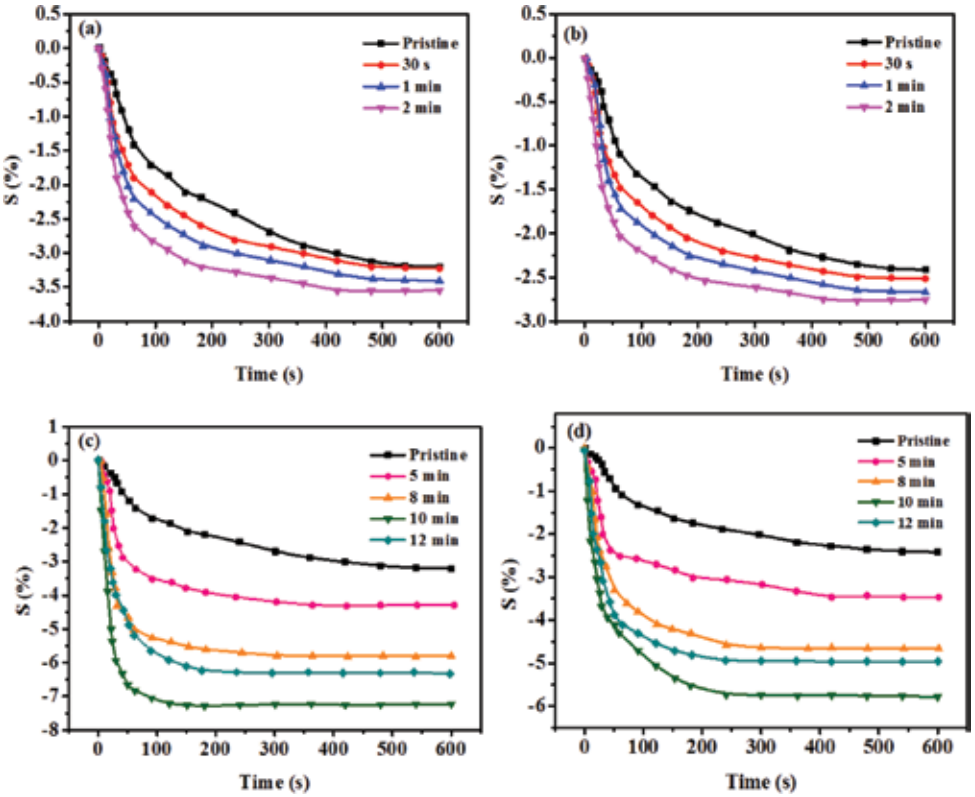

Figure 13. Responses of MWCNTs-based gas sensors (a, c) 50 ppm H_2S and (b, d) 50 ppm SO_2.

detect H_2S and SO_2 at 10, 25, 50 and 100 ppm because these sensors yielded the best sensitivities. **Figure 14a** and **b** indicates that the sensitivity of the sensors increases with the gas concentration.

Figure 15 shows that the gas concentration and sensor sensitivity were linearly correlated for H_2S and SO_2 concentrations of 10–100 ppm with correlation coefficients (R^2) of 0.97183 and 0.9739, respectively.

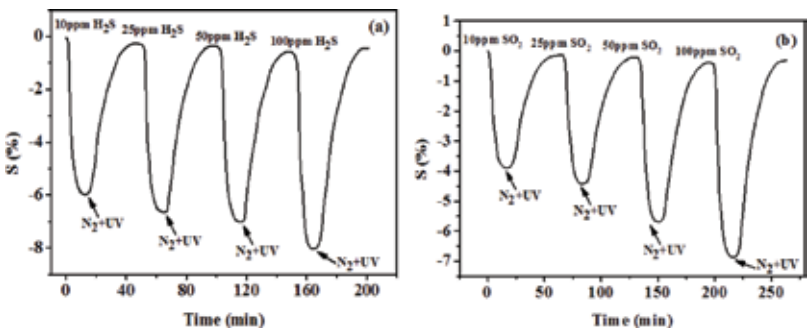

Figure 14. Response curves of MWCNTs-based sensors to different concentrations of (a) H_2S and (b) SO_2.

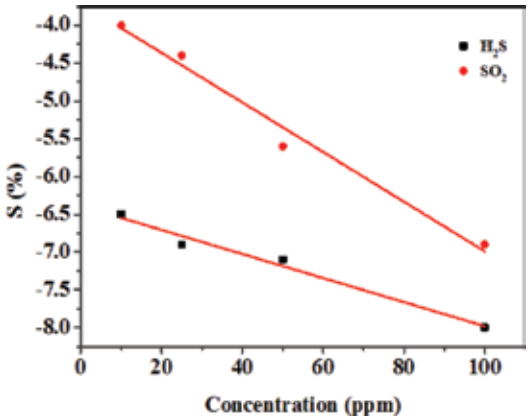

Figure 15. Linear relationship sensitivity of MWNT-based sensors for different concentrations of SO_2 and H_2S.

2.2.2.5. Desorption and repeatability of MWCNTs-based sensors

To analyze the desorption properties of modified MWCNTs gas sensors, these modified by CF_4 plasma for 10 min were chosen to test the recovery curve, as shown in **Figure 16**. The experiment steps are as follows. Firstly, the chamber was pumped into vacuum and standing for a period of time. After resistance of the sensor remains unchanged, in the second minute 50 ppm, H_2S was introduced into the chamber, and the resistance showed a quick decrease. Few minutes later, the resistance of sensor remains stable. Currently, H_2S gas molecules reach adsorption equilibrium at the surface of MWCNTs. In the fifth minute, pure N_2 was injected into the gas chamber, and the sensor resistance can generally recover near the initial value. There still have a small amount of residual gas accumulates on the surface of the sensor which affect the sensitivity. In order to obtain a completely desorption, placed the sensor under UV irradiation. By irradiating with UV light, the residual gas absorbs energy, which enables it to

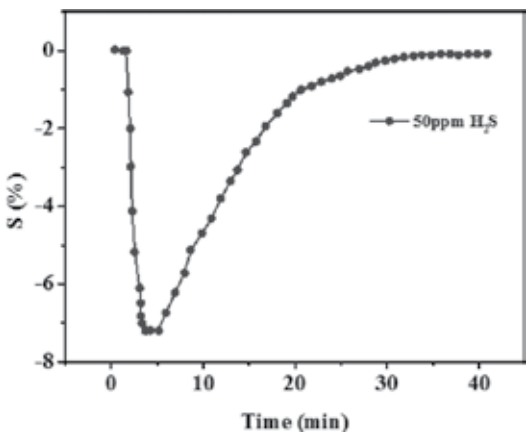

Figure 16. Recovery curve of plasma-modified MWCNTs to H_2S.

"escape" from the "trapped" state where almost no residual gas remains on the surface of the tested sensor. After N_2 and UV treatments, the sensor resistance was gradually restored to its initial value. The recovery time was about 25 min, which was less than that of the pristine MWCNTs sensor to H_2S (40 min; data not shown).

The MWCNTs sensor modified by plasma for 10 min that was most sensitive to SO_2 was selected to illustrate the repeatability process (**Figure 17**). The resistance-change trends remained similar, and the maximum resistance-change rate remained the same and stable. Hence, the gas sensor could be repeatedly used with good response and stability. However, the recovery time was approximately 35 min and was not greatly enhanced in contrast to that of pristine MWNT-based sensors.

2.2.2.6. Gas-sensing mechanism

The CF_4 plasma-modified MWCNTs sensors exhibited high sensitivities to H_2S and SO_2 because of the following reasons: (1) The accelerated electrons, ions and free radicals cleaned the MWNT surface by etching some amorphous carbon and catalyst particles during plasma treatment; (2) the bombardment of energetic particles destroyed some of the nanotubes and increased the defects on their surfaces, which generated effective adsorption sites for gas molecules; and (3) CF_4, a fluorinated gas [14], was ionized to generate fluoride ions in DBD and react with carbon atoms on the MWCNTs surface to yield C—F bonds [15] without destroying the tubular structure. Given the strong polarity and reactivity of F atoms, fluorinated MWCNTs exhibited strong adsorption capacities and high gas-sensing properties.

The response and recovery time of plasma-modified MWNT sensors to H_2S were remarkably reduced, but only the response time to SO_2 decreased, and recovery time was not reduced (Section 3.5). Theoretically, H_2S molecules were physically adsorbed on the surface of MWCNTs through van der Waals interaction. However, some hydroxyls existed on the surfaces of the nanotubes during growth by CVD. F atoms were introduced onto the MWCNTs

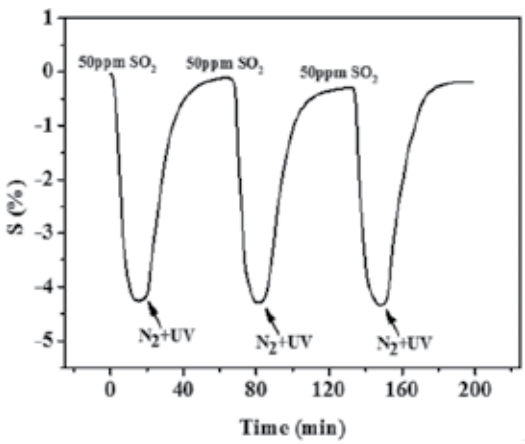

Figure 17. Reversibility curve of modified MWCNTs to 50 ppm SO_2.

surface after fluorination. C—F bonds possessed high polarity because of the strong electro negativity of the F atom, during which —F was essential. Stable hydrogen bonds (C—F…H—S) were formed between H atoms in H_2S molecules and F atoms when H_2S molecules were adsorbed on the surface of modified MWCNTs. Subsequently, the van der Waals forces were replaced, and the adsorption of H_2S molecules was accelerated to reduce the response time (**Figure 18a**). In addition, O atoms in the hydroxyl groups in MWCNTs surfaces exhibited small atomic radii and high electro negativities. Hydrogen bonds (C—O…H—S) were formed between O atoms in hydroxyl and H atoms in H_2S molecules (**Figure 18a**). The recovery time of plasma-based MWCNTs sensors to H_2S decreased possibly because of the effect of UV irradiation that the H—F bond is easier to disintegrate. For SO_2, only O atoms in the SO_2 molecules and H atoms of hydroxyl were combined to form hydrogen bonds [O—H…O—S; **Figure 18b**]. F atoms on the surfaces of modified MWNT increased the number of effective adsorption sites for gas molecules, accelerated the adsorption and reduced the response time. However, the recovery time remained invariant.

2.2.3. Summary: gas adsorption on intrinsic SWCNT

In the theoretical study aspect, the adsorption between SWCNT and SO_2F2 was chemisorption because new covalent bonds were formed. The number of charge transfer between SWCNT and SO_2F_2 was 80 times higher than that of between SWCNT and SF_6, and also higher than that of other gas decomposition products, which show that the adsorption is the strongest. The calculated DOSs indicated that the SO_2F_2 gas molecules adsorbed on SWCNT had changed the electronic structures of SWCNT, chemical properties of SWCNT becoming more active. In fact, the conductivity of SWCNT was also enhanced because the energy gap of SWCNT had decreased from 0.022 ha (0.60 eV) to 0.015 ha (0.40 eV) when the SO_2F_2 gas molecules were adsorbed. However, HF, H_2S and CF_4 molecules adsorbed on SWCNT had little effect on the electronic structures of SWCNT, so SWCNT's properties kept unchanged. Due to the cross-sensitivity of SWCNT to SF_6, SO_2 and SOF_2 molecules, SWCNT cannot detect the SO_2 and SOF_2, respectively. Thus, based on the analysis above, SWCNT can be prepared a gas sensor to detect SO_2F_2 gas among the gas decomposition products of SF_6 in PD.

In the experimental study aspect, MWCNTs grown by the CVD method are initially modified by atmospheric pressure DBD air plasma and are used as gas-sensitive materials. Then,

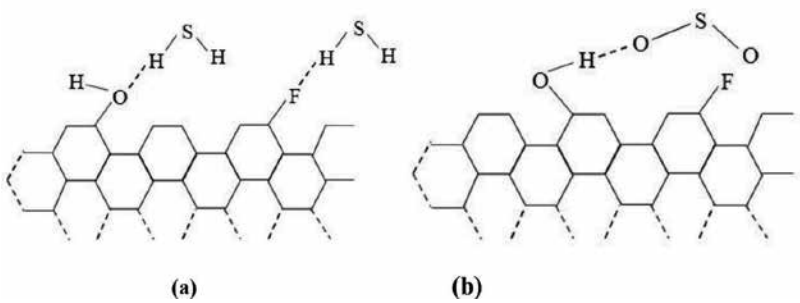

Figure 18. Schematic of the absorption of (a) H_2S and (b) SO_2 in modified MWCNTs.

the gas sensitivity of the unmodified and modified MWCNTs to 50 ppm H_2S and 50 ppm SO_2 is tested, respectively. The results show that the sensitivity of modified MWCNTs to H_2S is enhanced 2.75 times, and the response time to H_2S greatly reduced [16]. However, the sensitivity of modified MWCNTs to SO_2 exhibits the opposite effect. The MWCNTs are almost no longer sensitive to SO_2. Thus, the MWCNTs modified by atmospheric pressure DBD air plasma presented good selectivity to H_2S and have great potential value in the detection of this gas [16].

2.3. Gas-sensing properties of Pd-SWCNTs to SOF_2, SO_2F_2, SO_2, H_2S, HF, CF_4 and SF_6

2.3.1. Structural parameters of intrinsic Pd-SWCNTs

The geometric structure of the SWCNTs is dramatically distorted after substitution as shown in **Figure 19**. The impurity of the Pd atom induces the deformation of the six-membered ring near the doping site to relieve stress, which results in the carbon site substituted by the Pd heteroatom that evidently protrudes out of the tube wall because the radii of the Pd atom are larger than other carbon atoms [17, 18].

2.3.2. The analysis of gas adsorption structure

The SO_2, H_2S, SOF_2, SO_2F_2 and CF_4 gas molecules were made to approach the Pd atom marked on the SWCNTs at any possible posture to find the most stable adsorption system (see **Figure 20**). The adsorption energy E_{ads}, Q_T and interactive distance d are computed to analyze gas response property. All the parameters and configurations are shown in **Table 2** and **Figure 20**, respectively. From **Table 2**, we found that the adsorption energy of all the molecules is negative, so the adsorption reaction is an exothermic process that occurs spontaneously.

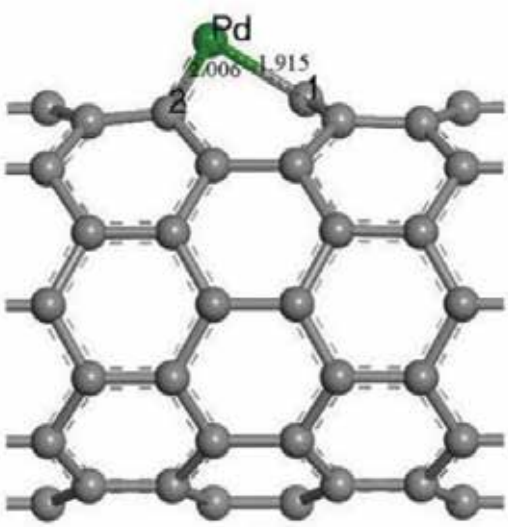

Figure 19. Geometric structures of Pd-doped SWCNTs after optimization. The structural parameters are shown as Å.

Pd acts as the adsorption site in the process of SO_2 adsorption. When one SO_2 molecule approaches the Pd atom and the adsorption structure is optimized to find the steady state (**Figure 20a1**), the two oxygen atoms labeled O1 and O2 are seen close to the Pd atom, whereas the S atom is seen away from the Pd atom, indicating that the Pd and O atoms form a coordinate bond, and the interaction between the Pd and S atoms is weak. The interatomic distance S—O1 changes from 1.480 to 1.565 Å, and the Pd-O1 distance is 2.281 Å in the reaction process, indicating that SO_2 adsorbed on the surface results in the elongation of the S—O bond. The result is agreement with our previous study [19], where the interaction distance between the Pd atom and the SO_2 in our present Pd-doped (8, 0) SWCNTs is generally slightly smaller than that of Pd-doped (5, 5) SWCNTs [20]. The long molecule surface distance 2.281 Å and low banding energy −0.798 eV suggest some kind of physisorption. Upon the adsorption of the second SO_2 molecule on Pd-SWCNTs (**Figure 20a2**), the two molecules become simultaneously close to the Pd atom through the oxygen atom O1' and O2'. The adsorption distance of Pd-O1' and Pd-O2' is 2.231 and 2.236 Å, respectively, which shows no distinct difference to that of single SO_2 adsorption, whereas the interatomic distance of SO_2 becomes slightly elongated compared with the individual molecule causing increased bonding strength between the Pd atom, O1', and O2'.

The optimized structures of H_2S adsorbed on Pd-SWCNTs are shown in **Figure 20b1** and**b2**. The interaction between H atoms of H_2S and Pd is too weak, and thus, adsorption of H_2S through S atom is an appropriate adsorption conformation course for the multiple valence states of the S atom. Upon single molecule adsorption, a quasi-tetrahedron geometry around the Pd center with H_2S forms in one of the apical positions upon adsorption of H_2S. The Pd-S long distance 2.570 Å and the low banding energy −0.802 eV are received in the process of adsorption, which suggests that H_2S undergoes moderate physisorption. After the second H_2S approached the Pd-SWCNTs, both H_2S molecules were situated around the Pd atom in a similar geometrical morphology. The results showed that Pd-SWCNTs had similar adsorption ability with both of the H_2S molecules. The total adsorption energy of the two H_2S molecules has reached −1.361 eV with Pd-S1' and Pd-S2' distance of 2.689 and 2.588 Å, respectively. The adsorption energy has been much enhanced than our previous studied gold doped (8, 0) SWCNT [21]. The H_2S molecules act as electron donor, and the charge transfer QT is 0.481 e. The large adsorption energy and considerable charge transfer made the Pd-SWCNTs a possible sensor material to detect H_2S. Star et al. reported that Pd-Decorated CNTs show good response to 50 ppm H_2S using the experimental method [22].

The adsorption of SOF_2 on the surface of Pd-doped (8, 0) SWCNTs is more stable from the F atom toward the Pd site, as shown in **Figure 20c1** and **c2**. The calculated binding energy for the SOF_2 interacted across the Pd atom of (8, 0) SWCNTs is −0.846 eV, and the adsorption distance between the F1 atom of molecule and the Pd atom of tubes is 2.003 Å, whereas the distance between F1-S bond increased to 2.778 Å. The large binding energy and structure change shown by the SOF_2 molecule presents a strong chemical interaction with the Pd-doped SWCNTs [23]. The Mulliken population analysis showed that the SOF_2 adsorption on Pd-doped (8, 0) SWCNTs leads to 0.572 electron transfer from the tubes to the SOF_2 molecule. Therefore, SOF_2 functions as an electron acceptor, whereas the nanotube functions as an electron donor. From **Figure 20c2**, we found that the adsorption distance between the second SOF_2 and the Pd-SWCNTs was 4.649 Å. Therefore, the adsorption is obviously weaker than

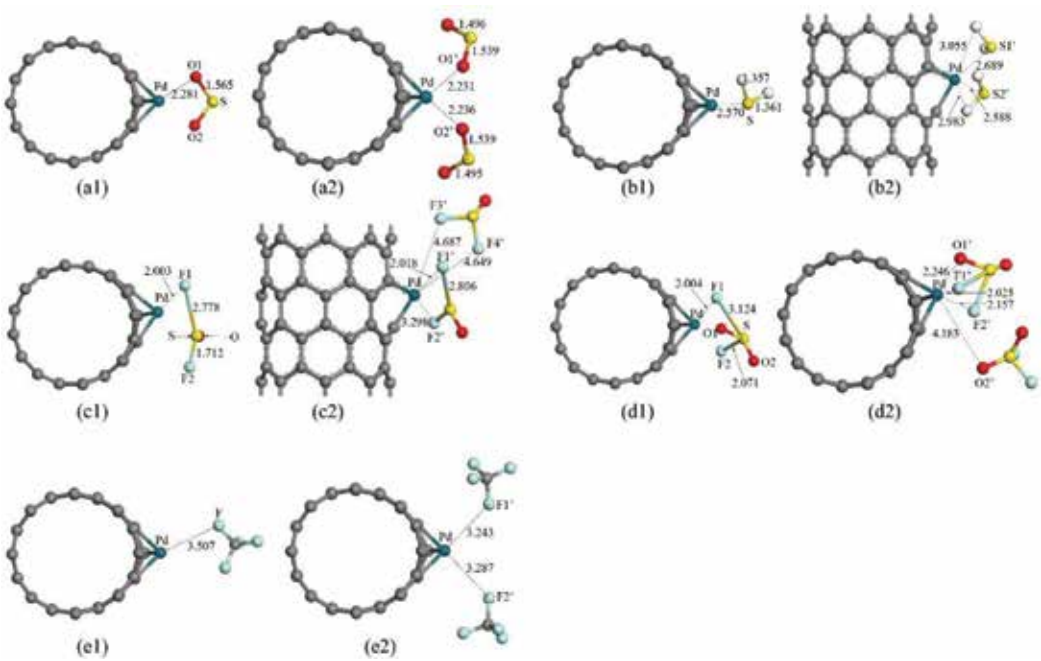

Figure 20. The most stable optimized geometries of gas molecules interacting with Pd-doped SWCNTs. The structural parameters are shown in Å.

the first adsorbed Pd-SWCNTs. The increased adsorption energy induced by the second SOF_2 is only −0.178 eV, which has also confirmed the weak interaction between the second SOF_2 molecule and Pd-SWCNTs. To some extent, the result can be attributed to the strong repulsive force between the SOF_2 molecules. Meanwhile, the charge transfer Q_T is only −0.604 e, which is only 0.032 higher than that of single SOF_2 adsorption.

System	Structure	E_{ads} (eV)	Q_T (e)	d_1 (Å)	d_2 (Å)
SO_2	(a1)	−0.798	−0.304	2.281	/
$2SO_2$	(a2)	−1.120	−0.368	2.231	2.236
H_2S	(b1)	−0.802	0.278	2.570	/
$2H_2S$	(b2)	−1.361	0.481	2.689	2.588
SOF_2	(c1)	−0.846	−0.572	2.003	/
$2SOF_2$	(c2)	−1.024	−0.604	2.018	4.649
SO_2F_2	(d1)	−1.627	−0.991	2.004	/
$2SO_2F_2$	(d2)	−1.735	−0.973	2.025	4.183
CF_4	(e1)	−0.046	−0.001	3.507	/
$2CF_4$	(e2)	−0.097	0.009	3.243	3.287

Table 2. Calculated adsorption energy, charge transfer and the binding distance from Pd atom to the adsorbates.

In the adsorption of SO_2F_2 (**Figure 20d1** and **d2**), although the adsorption energy value of single SO_2F_2 molecule is in the same order of magnitude as SO_2 and SOF_2, the adsorption energy of SO_2F_2 (−1.627 eV) is still almost twice over SO_2 (−0.798 eV), SOF_2 (−0.846 eV), and even reached 20 times more that the value of CF_4 (−0.086 eV). The interatomic distance S-F1 increased from 1.611 to 3.124 Å with an S-Pd distance of 2.004 Å. Therefore, we concluded that Pd doping makes the SWCNTs preferable for SO_2F_2 chemisorption. The adsorption of two SO_2F_2 is similar to SOF_2, which is the first SO_2F_2 near the Pd atom with a binding distance of −2.025 Å. The second molecule from the Pd atom with a distance of 4.183 Å creates the repulsive force between the SO_2F_2 molecules. The total adsorption energy is Pd atom 1.735 eV, and the charge transfer is −0.973 electron, which are almost the same with the values of single SO_2F_2 adsorption.

The adsorption of CF_4 (**Figure 20e1** and **e2**) is only −0.046 eV because of weak van der Waals interaction between two species, and nearly no charge transfer was present [24]. The energy is the least one among all gas molecules adsorption. The interacting distance from Pd atom to the atom F1 is 3.507 Å. Upon the two molecules' adsorption, the Pd-F1' and Pd-F2' are 3.243 and 3.287 Å. The conductivity of Pd-SWCNTs before and after adsorption may change little because of the large interaction distance.

2.3.3. The analysis of the density of states and Frontier molecular orbital

Large charge transfer affects the density of states (DOS) near the Fermi level and brings about significant differences in frontier molecular orbitals [20]. To further elucidate the electronic properties of the Pd-SWCNTs and molecule-Pd-SWCNTs, total electronic density of states (TDOS) and local DOS of a group (Pd or molecule) (LDOS) are depicted to investigate the influence of gas adsorption [25] in **Figure 21**. To further study the electronic structure of the Pd-SWCNTs and molecule-Pd-SWCNTs near the Fermi level, the highest occupied molecular orbital (HOMO) and the lowest unoccupied molecular orbital (LUMO) in the molecule adsorption on the Pd-doped SWCNTs are listed in **Table 3**. The diagrams of HOMO and LUMO are depicted in **Figure 22**.

From **Figure 21**, we found that the LDOS of Pd atom has little contribution to each TDOS and that the changes of TDOS are mainly from the adsorbed molecules. As plotted in **Figure 21a1**, the DOS of Pd-doped SWCNTs is continuous at Fermi level, which suggests that Pd-doped SWCNTs is a conductor. Upon adsorption of SO_2 molecule in **Figure 21b1** and **b2**, the TDOS near Fermi level evidently increased, and the DOS at Fermi level was enhanced when the adsorbed SO_2 molecule increased. In **Figure 22b1**, the HOMO of the SO_2-Pd-SWCNTs was mainly constituted by the Pd and SO_2, and the p orbital of S and O atoms interacted with the d orbitals of the Pt atom. The LUMO is localized on the SWCNTs, as seen in **Figure 22b2**. After the other SO_2 molecule approached the Pd atom in **Figure 22b3** and **b4**, the LUMO significantly transferred to the SO_2 molecules. The HOMO-LUMO energy gap of the SO_2-Pd-SWCNTs is only 0.066 eV, which is 0.279 eV smaller than that of bare Pd-SWCNTs. Although the HOMO-LUMO energy gap of the $2SO_2$-Pd-SWCNTs is slightly bigger than single molecule adsorption, it was still 0.229 eV smaller than individual Pd-SWCNTs. The decrease of HOMO-LUMO energy gap associated with the significantly enhanced in the TDOS near the Fermi level

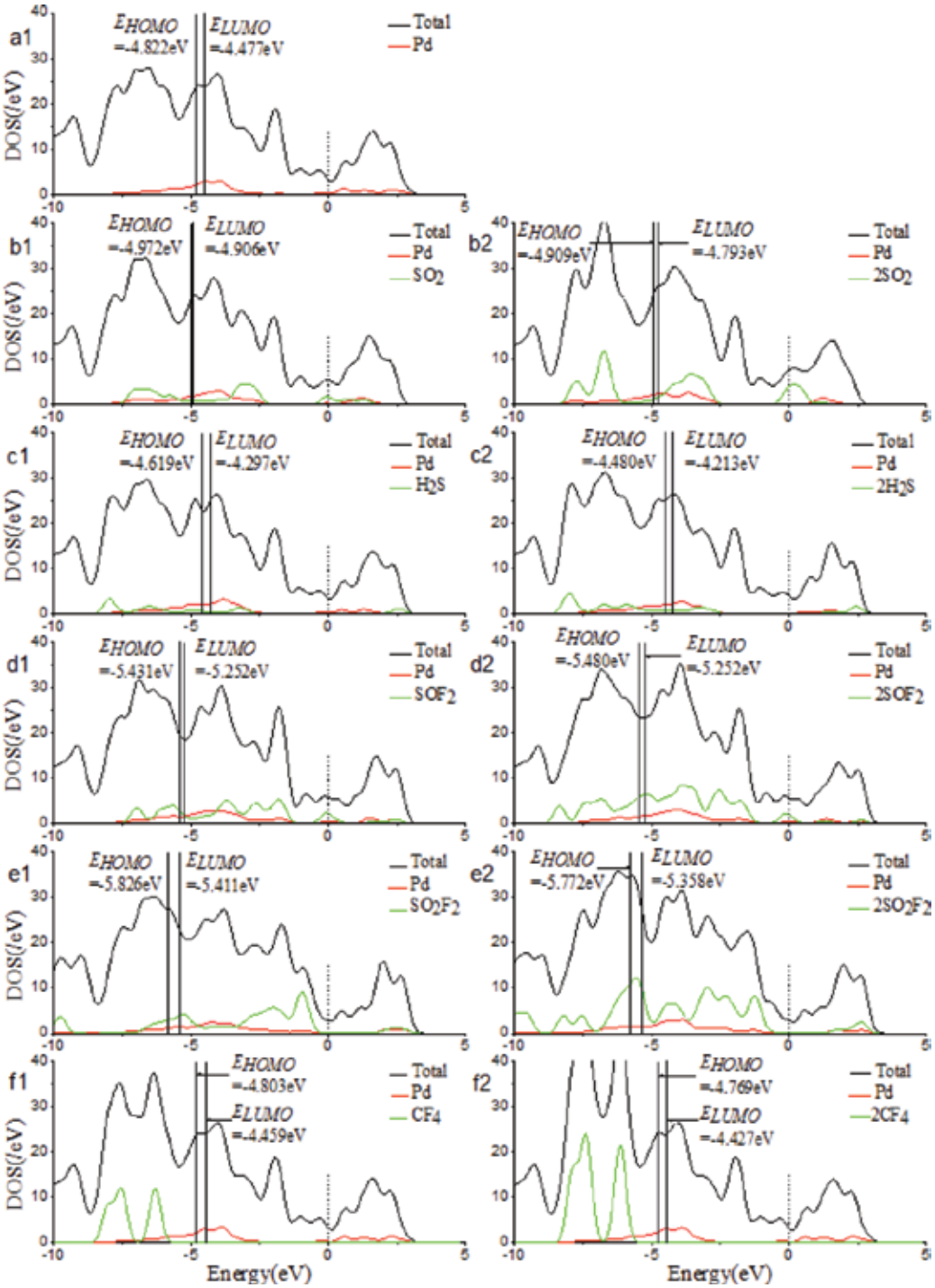

Figure 21. Total electronic density of states and local density of states for the Pd-SWCNTs and molecule-Pd-SWCNTs. Dash and solid lines indicate the Fermi level and HOMO-LUMO, respectively.

System	EHOMO (eV)	ELUMO (eV)	EL-H (eV)
Pd-SWCNTs	−4.822	−4.477	0.345
SO_2-Pd-SWCNTs	−4.972	−4.906	0.066
$2SO_2$-Pd-SWCNTs	−4.909	−4.793	0.116
H_2S-Pd-SWCNTs	−4.619	−4.297	0.322
$2H_2S$-Pd-SWCNTs	−4.480	−4.213	0.267
SOF_2-Pd-SWCNTs	−5.431	−5.252	0.179
$2SOF_2$-Pd-SWCNTs	−5.480	−5.252	0.228
$SO2F_2$-Pd-SWCNTs	−5.826	−5.411	0.415
$2SO2F_2$-Pd-SWCNTs	−5.772	−5.358	0.414
CF_4-Pd-SWCNTs	−4.803	−4.459	0.344
$2CF_4$-Pd-SWCNTs	−4.769	−4.427	0.342

Table 3. The HOMO, LUMO energy and HOMO-LUMO energy gap.

suggests that the adsorption of SO_2 largely increases conductance. According to the results reported by Camilli G et al. [26], using armchair Pd SWCNTs resulted in the reduction in the HOMO-LUMO energy gap of single and dual H_2S molecule adsorption by 0.17 and 0.16 eV, respectively. Meanwhile, the TDOS change introduced by the second SO_2 molecule showed no significant difference. Pd-doped zigzag SWCNTs show preferable sensitivity to SO_2.

According to the H_2S molecules adsorbed on Pd-SWCNTs, the TDOS at Fermi level showed no change whether single or dual H_2S adsorption in **Figure 21c1** and **c2** occurred. In **Figure 22**c1–c4, almost the entire HOMO and LUMO were on Pd-SWCNTs. The HOMO-LUMO energy gap of H_2S-Pd-SWCNTs and $2H_2S$-Pd-SWCNTs is 0.322 and 0.267 eV, respectively, which is slightly decreased compared with the bare Pd-SWCNTs. The results are consistent with the adsorption configurations. Given that the H atoms have formed a covalent bond with the S atom, the H_2S molecules can only interact with Pd-SWCNTs by S atoms. Although S atom forms the interaction with Pd atom, the primary S-H bond makes it hard to build strong interaction with the Pd-SWCNTs. The same result is seen in Pt-doped SWCNTs [27]. The small change at Fermi level in the H_2S adsorption process indicates little change in conductivity, which limits the performance of Pd-SWCNTs to detect the H_2S gas in SF_6 decomposition components.

Upon SOF_2 adsorption, as seen in **Figure 22d1** and **d2**, the p orbital of S atom and d orbital of Pt atom form a δ bonding orbital in the HOMO. In the LUMO, the p orbital of S atom in SOF_2 overlaps with the d orbital of Pt atom. The HOMO and LUMO energies of SOF_2-Pd-SWCNTs are slightly reduced with respect to those of bare Pd-SWCNTs. The HOMO-LUMO energy gap diminished to 0.179 eV. The decrease of the HOMO-LUMO energy gap would result in increased electron transfer to gas molecule. As we have already mentioned, the second SOF_2 molecule is far from the Pd atom. Therefore, the LDOS of the second SOF_2 brings little

http://dx.doi.org/10.5772/intechopen.68325

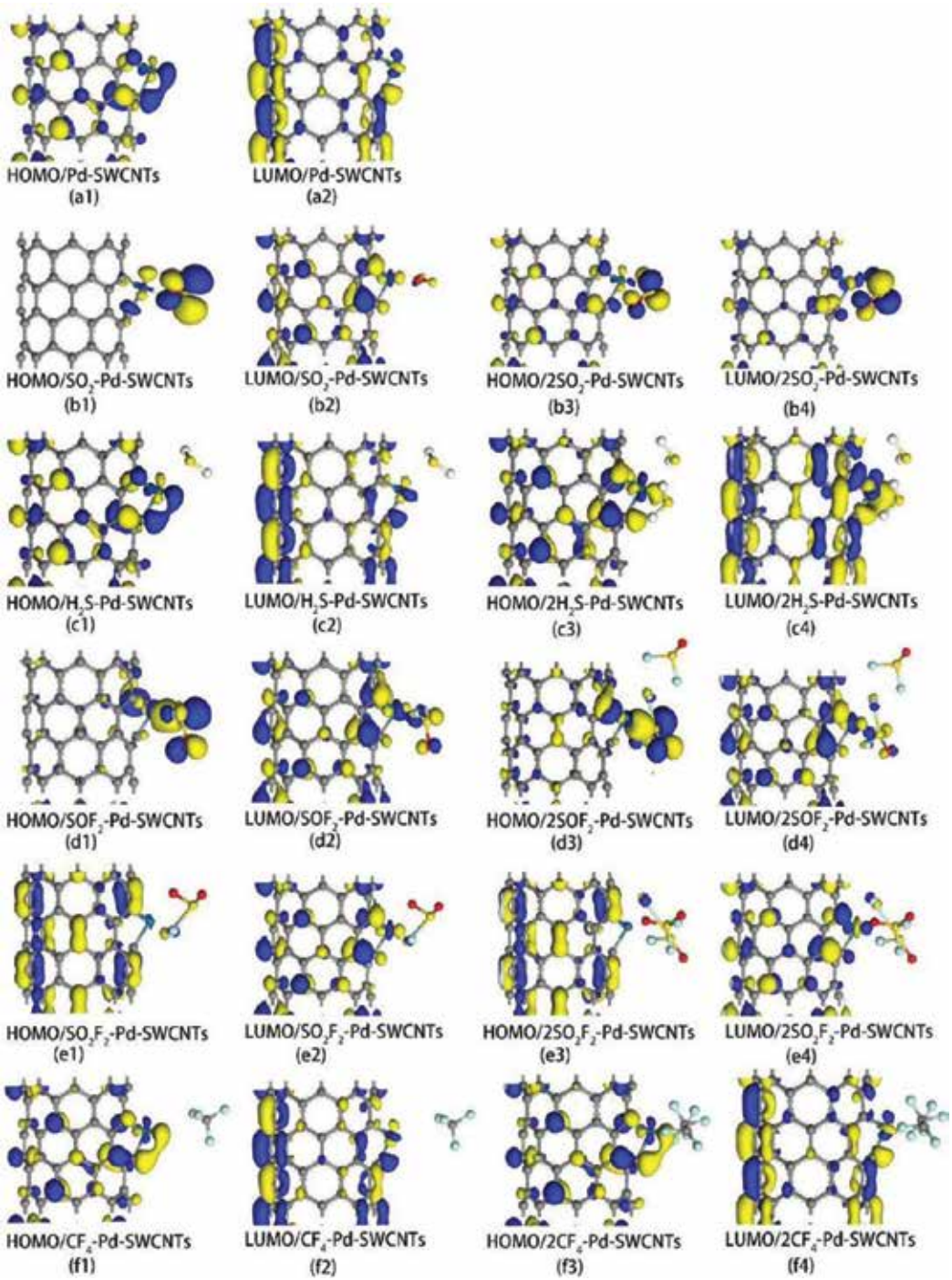

Figure 22. The HOMO and LUMO orbitals on Pd-SWCNTs and molecule-Pd-SWCNTs.

contribution to TDOS of adsorption system (**Figure 21d1** and **d2**). The HOMO and LUMO of 2SOF_2-Pd-SWCNTs in **Figure 22d3** and d4 have also confirmed the analysis results, neither the HOMO nor the LUMO is located on the second SOF_2 molecule. Therefore, conductivity does not increase with the rise of SOF_2 molecule number adsorbed on Pd-SWCNTs.

From the orbital of single SO_2F_2 adsorbed on Pd-SWCNTs in **Figure 22e1**, we can see a weak bond between the molecule and the Pd-SWCNTs. The HOMO-LUMO energy gap is 0.415 eV, which increased with the energy gap in other molecule adsorption. It greatly reduces the electron transition probability between HOMO and LUMO. Similar to the second SOF_2 adsorption, the adsorption system keeps its original characteristics after the second SO_2F_2 adsorbed on Pd-SWCNTs in **Figure 22e2**. In addition, the TDOS of SO_2F_2 adsorbed Pd-SWCNTs at the Fermi level is weaker than individual Pd-SWCNTs. Considering the molecule frontier orbital and TDOS, we assumed that SO_2F_2 adsorption will result in the decrease of conductance.

Upon the adsorption of CF_4, the LDOS introduced by CF_4 mainly under the Fermi level was not significant (**Figure 21f1** and **f2**). Furthermore, the HOMO and LOMO were almost identical to that of Pd-SWCNTs, as shown in **Figure 22f1–f4**. Considering the frontier orbital and TDOS, we predicted that the Pd-SWCNTs are insensitive to CF_4 detection.

2.3.4. Summary: gas adsorption on Pd-SWCNTs

Adsorption of SF_6 decomposed gas molecules (SO_2, H_2S, SOF_2, SO_2F_2 and CF_4) on Pd-doped (8, 0) SWCNTs was explored through density functional theory-based method. The geometrical and electronic structures, density of state and frontier molecular orbital were analyzed to predict the adsorption properties and mechanism of complexes.

In the adsorption of SO_2, strong binding energy between SO_2 and Pd-SWCNTs indicates the nature of chemical adsorption. The adsorption energy increases with the rise of SO_2 molecule number adsorbed on Pd-SWCNTs. The large contribution of SO_2 and the total DOS near the Fermi level is responsible for the conductance increase of SO_2-Pd-SWCNTs. The high adsorption sensitivity of Pd-SWCNTs makes it suitable for SO_2 detection.

For the adsorption SOF_2, F-end adsorption conformation is energetically favorable. The large formation energy and structure change show that the SOF_2 molecule is chemically bonded to Pd-doped SWCNTs. The large enhancement toward the Fermi level induced by the LDOS of SOF_2 implies the increase of conductance for the SO_2-Pd-SWCNTs. However, the strong repulsive force between the SOF_2 molecules limits it is further adsorption, and therefore, the increased conductivity introduced by SOF_2 is smaller than SO_2.

Upon the adsorption of one SO_2F_2 to the Pd-SWCNTs, the HOMO-LUMO energy gap of the SO_2F_2-Pd-SWCNTs increased to 0.415 eV, which is larger than that of the Pd-SWCNTs, whereas the TDOS at Fermi level slightly decreased. The command action of the HOMO-LUMO energy gap and TDOS finally led to the conductivity decrease of the SO_2F_2 adsorbed Pd-SWCNTs.

When CF_4 is adsorbed on Pd-SWCNTs, the HOMO-LUMO energy and TDOS remained unchanged based on our computation. The Pd-CNT showed low sensitivity for CF_4 gas.

Results of the theoretical calculation showed that Pd-SWCNTs had different sensitivity to the SF_6 decomposition gases. After SO_2, H_2S and SOF_2 were adsorbed on Pd-SWCNTs, the conductivity increases in the following order: SO_2 > SOF_2 > H_2S. The conductivity of SO_2F_2 decreased when it was adsorbed by Pd-SWCNTs. Conversely, Pd-SWCNTs are not sensitive to the other gas molecule CF_4. Through changes in conductivity, the Pd-SWCNTs achieved selective detection of five SF_6 decomposition gases: SO_2, H_2S, SOF_2, SO_2F_2 and CF_4.

2.4. Gas-sensing properties of Ni-SWCNTs to SOF_2, SO_2F_2, SO_2, H_2S, HF, CF_4 and SF_6

2.4.1. Structural parameters of intrinsic Ni-SWCNTs

After an individual Ni atom was decorated onto the SWCNTs and relaxed to stable structure, the Ni atom distinctly protruded out of the SWCNTs sidewall due to the large Ni atom radius compared with that of SWCNTs as shown in **Figure 23** [28]. The bond length C3-Ni was stretched to 1.84 Å, and the bond length C4-Ni length along the axial of Ni-SWCNTs increased to 1.76 Å.

2.4.2. The analysis of gas adsorption structure

After the optimization of individual Ni-SWCNT and gas molecules, the gas molecules were relaxed to various sites on the surface of Ni-SWCNTs to get the lowest energy structure [11]. Moreover, in order to fully analyze the influence brought by decomposed products, adsorption of both single and double gas molecules was studied in this work [11]. As seen in **Figure 24**, it was found that all of the gas molecules intended to be adsorbed at the Ni-doped site, which acted as an active site for adsorption [11]. To analyze the adsorption properties, the banding distance D, binding energy E_{ads} and charge transfer Q_t were obtained as shown in **Table 4** [11]. D presented the nearest distance between the adsorbed gas molecules and the surface of Ni-SWCNTs, where D_1 and D_2, respectively, represented the distances for two different

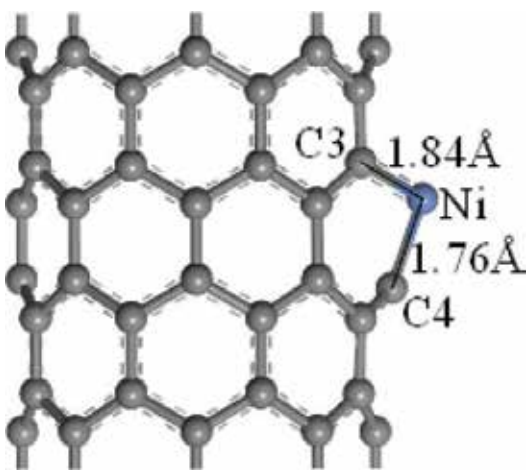

Figure 23. Geometric structures of Ni-doped SWCNTs after optimization. The structural parameters are shown as Å.

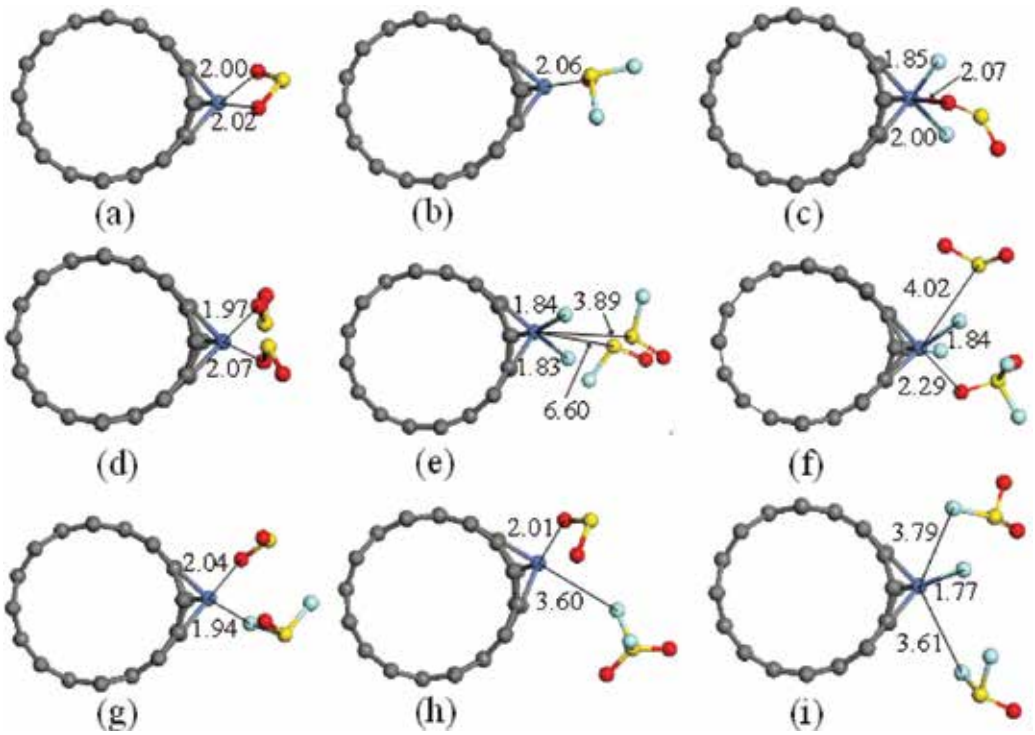

Figure 24. Most stable geometries of gas molecules interacting with Ni-doped SWCNTs (distances in Å).

molecules. Similarly, the charge transferred from gas molecules to Ni-SWCNTs was labeled as Q_t, Q_{t1} and Q_{t2} referred to the charge transfer for these two different molecules. All the negative value of E_{ads} implied that the adsorption was exothermic and occurred spontaneously.

System	D_1 (Å)	D_2 (Å)	Q_{t1} (e)	Q_{t2} (e)	E_{ads} (eV)
SWCNTs/SO_2	2.00	\	−0.35	\	−1.13
SWCNTs/SOF_2	2.06	\	−0.06	\	−0.49
SWCNTs/SO_2F_2	2.07	\	−0.94	\	−1.93
SWCNTs/2SO_2	1.97	2.07	−0.24	−0.08	−1.50
SWCNTs/2SOF_2	3.89	6.60	−0.51	−0.50	−1.79
SWCNTs/2SO_2F_2	2.29	4.02	0.06	−0.83	−2.16
SWCNTs/ SO_2&SOF_2	1.94	2.04	−0.31	−0.09	−0.71
SWCNTs/ SO_2&SO_2F_2	2.01	3.60	−0.35	0	−1.14
SWCNTs/ SOF_2&SO_2F_2	3.61	3.79	0	−0.71	−0.45

Table 4. Adsorption energy E_{ads}, charge transfer Q_t from adsorbed gas molecules to Ni-SWCNTs.

As shown in **Table 4** and **Figure 24a–c,** single SO_2, SOF_2 and SO_2F_2 molecules were adsorbed onto SWCNTs. The oxygen atoms of both SO_2 and SOF_2 were close to the Ni atom with the nearest bond length of 2.00 and 2.06 Å because of the strong electronegativity of oxygen atom [11]. And the sulfur atom was further away from the Ni-SWCNTs sidewall because it built a stable covalent bond with oxygen atoms and fluorine atoms, making it hard to interact with the Ni atom [11]. The structures of SO_2 and SOF_2 were almost kept unchanged in the adsorption process. The low E_{ads} values of SO_2 and SOF_2 indicate that the adsorption of SO_2 and SOF_2 is physisorption, which can also be verified by the long reaction length. However, when one SO_2F_2 molecule was close to Ni-SWCNTs, the S—F bond was broken, resulting in building a new Ni—F bond [11]. The binding distance from the newly formed SO_2 to the surface of the Ni-SWCNTs was 2.07 Å [11]. The E_{ads} reached −1.93 eV, which nearly tripled the E_{ads} value of SOF_2, and doubled that of SO_2. Based on the obvious structure deformation and large E_{ads}, we conclude that the interaction between SO_2F_2 and Ni-SWCNTs is chemisorption.

As to the adsorption of two identical gas molecules, as seen in **Table 4** and **Figure 24d–f**, the double SO_2 adsorption was similar to that of single SO_2 molecule with a nearest bond length of 1.97 Å [11]. Interestingly, the structures of both SOF_2 molecules were deformed with two new SOF molecules produced in the adsorption process, indicating that the Ni-doped metal showed great adsorption ability [11]. According to the SO_2F_2 adsorption, one of the SO_2F_2 molecules deformed to one SO_2 and two fluorine atoms that were adsorbed on Ni atom [11]. And the other SO_2F_2 molecule was close to the Ni atom with a binding distance of 2.29 Å [11]. The E_{ads} of double SO_2, SOF_2 and SO_2F_2 was −1.50, −1.79 and −2.16 eV, respectively, which were increased compared with that of corresponding single molecule adsorption. In general, two SO_2 molecules are physically adsorbed onto Ni-SWCNTs, and the interactions for SOF_2 and SO_2F_2 are chemisorption deducing form the obviously structure changes.

As for the adsorption of two foreign gas molecules on Ni-SWCNTs shown in **Table 4** and **Figure 24g–i**, there was no significant difference in the adsorption length for SO_2 compared with that of single and double SO_2 adsorption in **Figure 24a** and d. It should be noticed that the molecule structures of SOF_2 (**Figure 24g**) and SO_2F_2 (**Figure 24h**) kept unbroken, while in the SOF_2 and SO_2F_2 case in **Figure 24i**, one fluorine broke up from SO_2F_2 and was adsorbed on the Ni atom, and the SOF_2 molecule was away from the sidewall of Ni-SWCNTs with an adsorption length of 3.61 Å.

2.4.3. The analysis of the density of states and frontier molecular orbital

2.4.3.1. Adsorption of single decomposed gas molecule on the surface of Ni-SWCNT

According to the detection mechanism of chemiresistor sensor, the conductivity of gas-sensing materials changes in response to the different gas molecules [11]. Using the density of states (DOS) and frontier molecular orbital theory, the factors influencing the change of conductivity can be found directly [11]. We first analyze the single gas molecule adsorption cases, including SO_2, SOF_2 and SO_2F_2 (**Figure 24a–c**). Along with the charge transfer between the gas molecules and Ni-SWCNTs, the total density of states (TDOS), the highest occupied molecular orbital (HOMO) and the lowest unoccupied molecular orbital (LUMO) were distinctly changed [11]. If the energy gap between HOMO and LUMO narrows down, the charge

carrier transfer becomes easier from HOMO to LUMO. Then, the conductivity of adsorption system increases correspondingly [11].

The continuous TDOS of Ni-SWCNTs shown in **Figure 25a** is consistent with the verified results that intrinsic Ni-SWCNTs possess good conductivity after Ni atom doping. Bak et al. reported that mesoporous nickel/CNTse hybrid material showed high conductivity [29]. Comparing TDOS before (**Figure 25a**) and after (**Figure 25b**) the SO_2 molecule adsorption on the surface of Ni-SWCNTs, there is no significant change of TDOS at the energy levels that are far below or far above the Fermi level, and the main change is located at the energy level that is slightly above the Fermi level, which is attributed to the SO_2 adsorption that increases the number of effective charge. For the case with SOF_2 molecule adsorption, the TDOS almost does not change below the Fermi level as shown in **Figure 25c**. Although the TDOS far above the Fermi level slightly increases, it has no contribution to the change of conductivity, which agrees with the low interaction energy discussed above. For the adsorption of single SO_2F_2 (**Figure 25d**), the TDOS increases below the Fermi level and decreases above the Fermi level due to the chemisorption.

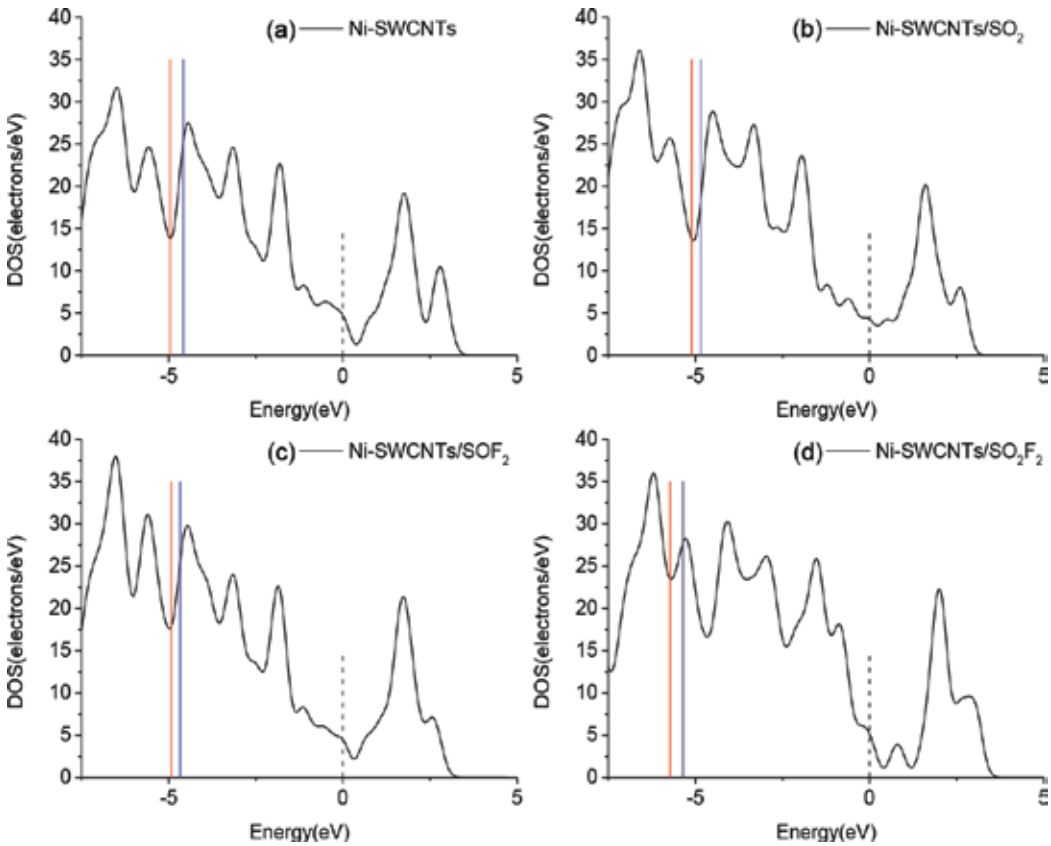

Figure 25. Comparison of the TDOS for (a) intrinsic Ni-SWCNTs, (b) SO_2 adsorbed Ni-SWCNTs, (c) SOF_2 adsorbed Ni-SWCNTs and (d) SOF_2 adsorbed Ni-SWCNTs. The left solid line is HOMO while the right solid line is LUMO, and the dash line is Fermi level.

The HOMO, LUMO, E_g for intrinsic Ni-SWCNTs and the materials with single gas molecule adsorption are reported in **Table 5** [11]. It is found that E_g was reduced at different extent for all gas adsorption process, making the charge easier to transfer for the adsorption system. Before each gas molecule approached to the surface of Ni-SWCNTs, the HOMO and LUMO were mainly distributed on the Ni-doped side and its opposite side (**Figure 26a1** and **a2)** with 0.38 eV E_g. For the physisorption of SO_2, the HOMO and LUMO were slightly transferred to the SO_2 adsorption site as shown in **Figure 26b1** and **b2** and became more uniformly distributed on the surface of Ni-SWCNTs. In addition, the E_g was narrowed down to 0.26 eV. Agreeing with the increase of TDOS, we conclude that the conductivity would increase with the single SO_2 adsorption. The increase result is agree with the conclusion reported by Yu et al. that SO_2 molecules adsorption on the surface of SWCNTs increases the conductivity [30]. When single SOF_2 molecule adsorbed on Ni-SWCNTs, the E_g was reduced to 0.25 eV, which was comparable to the SO_2 adsorption case. Comparing HOMO and LUMO of SOF_2 adsorption system (presented in **Figure 26c1** and **c2**) with that of intrinsic NI-SWCNTs, the HOMO and LUMO were nearly not changed except the slight change of LUMO due to SOF_2 molecule. Considering the weak adsorption energy, unchanged TDOS and frontier molecular orbital comprehensively, single SOF_2 adsorption has no influence on the conductivity of Ni-SWCNTs system. For SO_2F_2 adsorption, the E_g value (0.37 eV) was almost the same as that

System	LUMO	HOMO	E_g (eV)
SWCNTs	−4.58	−4.96	0.38
SWCNTs/SO_2	−4.85	−5.11	0.26
SWCNTs/SOF_2	−4.67	−4.92	0.25
SWCNTs/SO_2F_2	−5.36	−5.73	0.37

Table 5. HOMO, LUMO, E_g of intrinsic Ni-SWCNTs and single gas molecule adsorption.

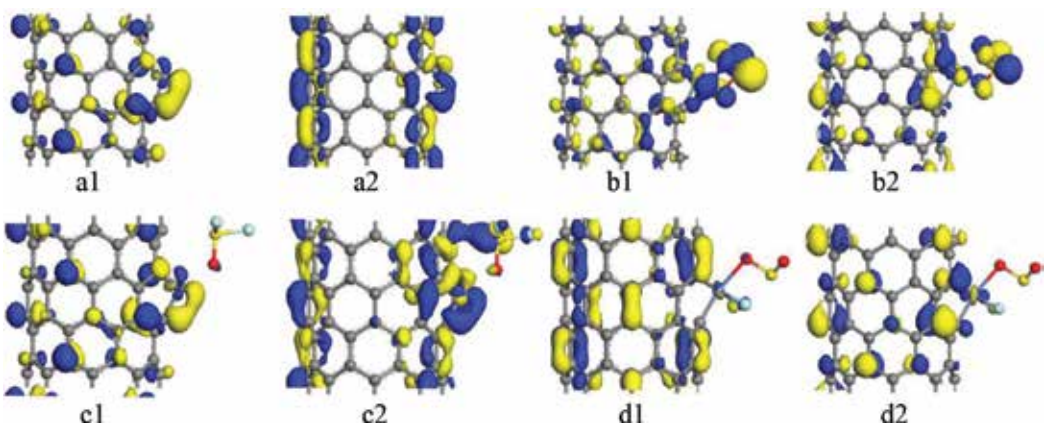

Figure 26. The HOMO and LUMO: (a1) and (a2) intrinsic Ni-SWCNTs; (b1) and (b2) SO_2 adsorbed Ni-SWCNTs; (c1) and (c2) SOF_2 adsorbed Ni-SWCNTs; (d1) and (d2) SO_2F_2 adsorbed Ni-SWCNTs.

of pure Ni-SWCNTs, and the HOMO and LUMO were distinctly reduced as listed in **Table 5**. The configurations of HOMO and LUMO of SO_2F_2 adsorbed Ni-SWCNTs with chemisorption are summarized in **Figure 26d1** and **d2**, and there are few orbital surrounding the adsorbed SO_2F_2. The strong chemical bond between Ni atom and SO_2F_2 impedes the free transportation of charge and reduces the free charge of Ni atom at the same time. In other words, the chemisorption of SO_2F_2 reduces the conductivity, which is consistent with the results of TDOS analysis. The decrease result is also confirmed by our previous research that SO_2 adsorption reduces the conductivity of Pd-doped SWCNTs [31].

2.4.3.2. Adsorption of double identical decomposed gas molecule on the surface of Ni-SWCNT

In practical situation, the insulated SF_6 gas may simultaneously decompose to SO_2, SOF_2 and SO_2F_2, indicating that it is mixed gas in SF_6 insulated equipment. Therefore, the multiple gas molecule adsorption was considered in our study. With the limited adsorption ability of single Ni-doped SWCNTs, double gas molecule adsorption is sufficient to analyze the situation of multiple gas molecule adsorption. The influence on conductivity brought by absorption of double identical decomposed gas molecules is discussed first. Comparison of the TDOS before and after gas molecule adsorption is shown in **Figure 27**. The presence of Ni active site leads to double identical SO_2 simultaneously adsorbed on Ni-SWCNTs, resulting in an enhancement of the communization movement between the Ni-SWCNTs and adsorbed gas molecules. As can be seen form **Figure 27a** and **b**, the TDOS was improved in all energy distribution zone, although the TDOS just above the Fermi level changed little, but that below the Fermi level increased, which means that the major carrier transfer from the valence band and the conduction band is enhanced. When the double identical SOF_2 and SO_2F_2 molecules interacted with Ni-SWCNTs by chemisorption, the TDOS near the Fermi level reduced. It can be seen in **Figure 27c**, the decrease area of TDOS for SOF_2 adsorption is slightly below the Fermi level, while a sharp TDOS reduction occurs above the Fermi level for SO_2F_2 adsorption as shown in **Figure 27d**.

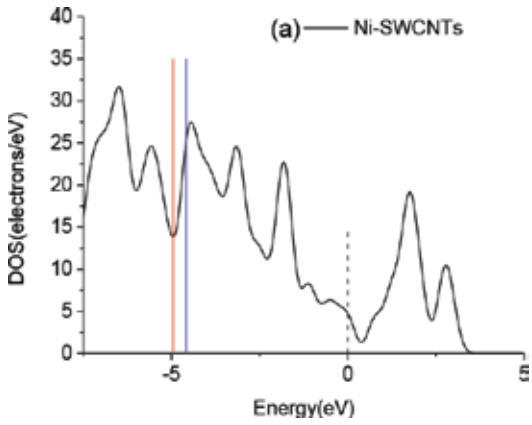

Figure 27. Comparison of the TDOS for double identical molecules: (a) intrinsic Ni-SWCNTs, (b) double SO_2 adsorbed Ni-SWCNTs, (c) double SOF_2 adsorbed Ni-SWCNTs and (d) double SOF_2 adsorbed Ni-SWCNTs. The left solid line is HOMO while the right solid line is LUMO, and the dash line is Fermi level.

Table 6 presents the results of the LUMO and HOMO energies of the double identical SF_6 decomposed products (SO_2, SOF_2 and SO_2F_2) adsorption on the surface of Ni-SWCNTs based on DFT calculation. All of the energy of HOMO and LUMO declined during the adsorption process. Considering the distribution of frontier molecular orbital for double SO_2 physisorption in **Figure 28b1** and **6b2**, the HOMO evenly distributed on the structure of Ni-SWCNTs. In addition, the E_g was declined from 0.38 eV (intrinsic SWCNTs) to 0.26 eV (SWCNTs/2SO_2). The computed TDOS and frontier molecular orbital reveal that the physisorption between double SO_2 and Ni-SWCNTs enhances the conductivity, which is consistent with the result of single SO_2 adsorption. The distribution of HOMO and LUMO for double SOF_2 adsorption signally changed as displayed in **Figure 28c1** and **6c2**. The HOMO has completely transferred to two newly produced SOF molecules. Conversely, the LUMO entirely locates on the surface of Ni-SWCNTs. As we have discussed above, two SOF molecules were far away from the surface of Ni-SWCNTs. So it was hard for charge carrier to transfer between HOMO and LUMO, though the E_g was greatly reduced to 0.08 eV. Comparing with the unchanged conductivity of the single SOF_2 adsorption case, the adsorption of double SOF_2 molecules slightly reduced the conductivity. From **Figure 28d1** and **6d2**, we found neither the HOMO nor the LUMO located around gas adsorption site, because the strong chemical bond interaction prevents the charge carrier from transferring freely. The HOMO evenly distributed on carbon atoms,

System	LUMO	HOMO	E_g (eV)
SWCNTs	−4.58	−4.96	0.38
SWCNTs/2SO_2	−5.03	−5.29	0.26
SWCNTs/2SOF_2	−5.52	−5.60	0.08
SWCNTs/2SO_2F_2	−5.02	−5.48	0.46

Table 6. HOMO, LUMO, E_g of intrinsic Ni-SWCNTs and double identical gas molecules adsorption.

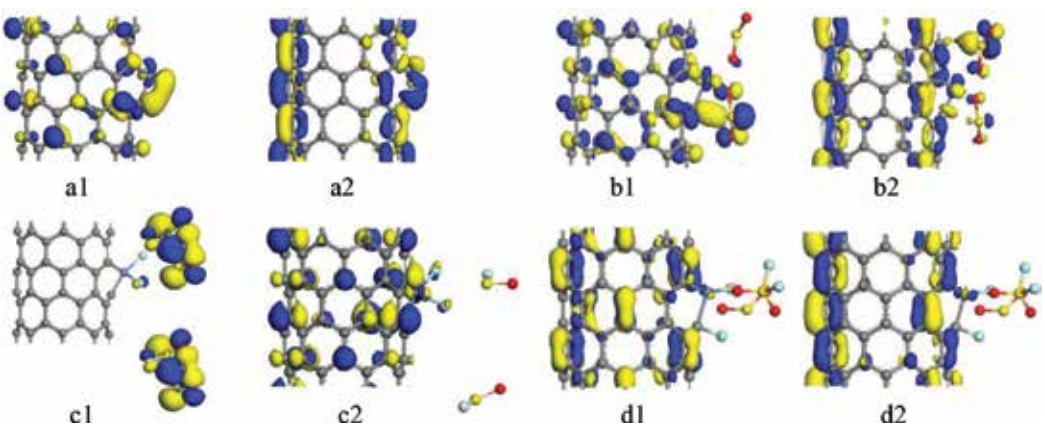

Figure 28. The HOMO and LUMO: (a1) and (a2) intrinsic Ni-SWCNTs; (b1) and (b2) double SO_2 adsorption; (c1) and (c2) double SOF_2 adsorption; (d1) and (d2) double SO_2F_2 adsorption.

and it increased compared with that of intrinsic Ni-SWCNTs. While the distribution of LUMO on carbon atoms kept unaltered. Along with the change of the HOMO and LUMO, the E_g was increased to 0.46 eV. We conclude that the double identical SO_2F_2 adsorption reduces the conductivity of Ni-SWCNTs.

2.4.3.3. Adsorption of double foreign decomposed gas molecule on the surface of Ni-SWCNT

In case of mixed gas decomposed in SF_6 insulated equipment, the mixed gas molecules could also be adsorbed on the surface of Ni-SWCNTs with double foreign gas molecules except the double identical adsorption case discussed above. According to the TDOS shown in **Figure 29**, the change of TDOS presents significant difference comparing with that of single and double identical gas molecules adsorption. All of the TDOS near the Fermi level has increased. As discussed in the geometry analysis for SO_2&SOF_2 adsorption, both gas molecules move close to the surface of Ni-SWCNTs by physisorption. The sharply increased TDOS above the Fermi level (see **Figure 29b**), which is even bigger than that of single SO_2 adsorption implies the prominent improvement of conductivity. And the change of conductivity is agreed with the literature that reported the increase of conductivity during SO_2 gas detection [30]. When SO_2&SOF_2 interacted with Ni-SWCNTs, the SOF_2 molecule was away from the surface of Ni-SWCNTs according to the structure discussed before. Comparing the TDOS of SO_2&SO_2F_2 adsorption (**Figure 29c**) with that of single SO_2, we found that the change of TDOS presents identical increase trend, deriving from the crucial role of SO_2 adsorption. For the adsorption of SOF_2&SO_2F_2, only the broken fluorine atom and one SOF_2 made contribution to the change of conductivity. As the TDOS of SOF_2&SO_2F_2 adsorption depicted in **Figure 29d**, the TDOS near the Fermi level and site of the HOMO and LUMO increased.

All of the increased TDOS for mixed gas molecule adsorption is consistent with the frontier molecular orbital analysis in **Figure 30**. It can be seen obviously that the HOMO and LUMO distribution (see **Figure 30b** and **Table 7**) has extended to the surface of adsorbed SO_2 and SOF_2

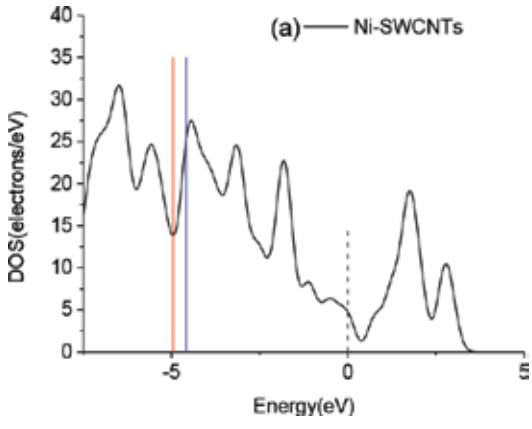

Figure 29. Comparison of the TDOS for double foreign molecules: (a) intrinsic Ni-SWCNTs; (b) SO_2, SOF_2 adsorbed Ni-SWCNTs; (c) SO_2, SO_2F_2 adsorbed Ni-SWCNTs and (d) SOF_2, SO_2F_2 adsorbed Ni-SWCNTs. The left solid line is HOMO while the right solid line is LUMO, and the dash line is Fermi level.

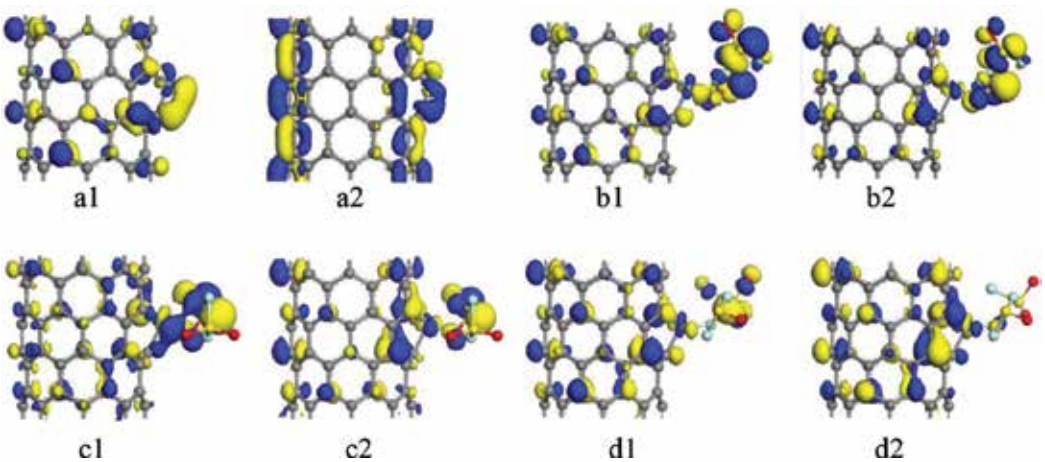

Figure 30. The HOMO and LUMO: (a1) and (a2) intrinsic Ni-SWCNTs; (b1) and (b2) SO_2, SOF_2 adsorption; (c1) and (c2) SO_2, SO_2F_2 adsorption; (d1) and (d2) SOF_2, SO_2F_2 adsorption.

molecules, and the E_g has narrowed to 0.20 eV. So the charge carrier transportation increases correspondingly, which also confirms the enhanced TDOS. Thus, we conclude that the effect of SO_2 and SOF_2 adsorption significantly improves the conductivity of Ni-SWCNTs. Although the SO_2F_2 molecule was too far to affect the frontier molecular orbital (see **Figure 30c**), the adsorbed SO_2 was efficient to enhance the conductivity by reducing the energy barrier E_g (0.26 eV) and increasing the HOMO and LUMO distribution. For the HOMO and LUMO distribution of SOF_2&SO_2F_2 adsorption shown in **Figure 19d**, part of HOMO distributed on the surface of bonded fluorine and one SOF_2 molecule. And the LUMO distribution became uniform on carbon atoms comparing with that of intrinsic Ni-SWCNTs. Besides, the TDOS at site of HOMO and HOMO increased as seen in **Figure 29d** with E_g dropped to 0.21 eV. Taking account of the changed distribution of TDOS and frontier molecular orbital that benefits charge carrier transportation, the adsorption of SOF_2&SO_2F_2 increases the conductivity.

2.4.4. Summary: gas adsorption on Ni-SWCNTs

In summary, the adsorption effects of typical decomposition products: SO_2, SOF_2 and SO_2F_2 in SF_6 insulated equipment toward Ni-doped (8, 0) zigzag SWCNTs have been theoretically investigated using first-principle calculation based on PBE function of DFT. It is found that

System	LUMO	HOMO	E_g (eV)
SWCNTs	−4.58	−4.96	0.38
SWCNTs/SO_2&SOF_2	−4.82	−5.02	0.20
SWCNTs/SO_2&SO_2F_2	−4.85	−5.11	0.26
SWCNTs/SOF_2&SO_2F_2	−5.28	−5.49	0.21

Table 7. HOMO, LUMO, E_g of intrinsic Ni-SWCNTs and double foreign gas molecules adsorption.

the gas molecules tend to approach the surface of Ni-SWCNTs at the Ni-doped active site with the improved adsorption ability to gas molecules. The density of state and frontier molecular orbital were adopted to study the physical properties of Ni-SWCNTs before and after gas molecules adsorption. Comparing the change of conductivity in different adsorption situations, the conductivity of Ni-SWCNTs increases in the following order: SO_2 > SOF_2 after SO_2 and SOF_2 adsorbed onto Ni-SWCNTs. Conversely, SO_2F_2 adsorption onto Ni-SWCNTs slightly decreases conductivity. The following specific conclusion can be drawn.

For single decomposed gas molecule adsorption, SO_2 and SOF_2 interact with Ni-SWCNTs via physisorption, while SO_2F_2 strongly chemisorbed on Ni-SWCNTs. For SO2 adsorption, the TDOS near the Fermi level and the HOMO and LUMO increases with a declined E_g, resulting in the increase of conductivity. Conversely, the conductivity reduces after the SO_2F_2 absorption. And single SOF_2 made little contribution to the change of conductivity.

For the adsorption of double identical gas molecules, the double SO_2 is still physically adsorbed on Ni-SWCNTs, and the chemisorption acts on both SOF_2 and SO_2F_2. Considering the conductivity features, we conclude that the double SO_2 molecules increase the conductivity, while double SOF_2 and double SO_2F_2 adsorption show a decrease effect to conductivity.

The results of gas-sensing properties to mixed gas molecule adsorption have showed that the conductivity increases at different extent, reflecting the sensing specific to different gas molecules. In case of SO_2 and SOF_2 and SO_2 and SO_2F_2 adsorption, the improvement of conductivity is mainly derived from the contribution of SO_2 adsorption, which has also been founded in single and double SO_2 adsorption. For SOF_2 and SO_2F_2 adsorption, the Ni active site bonded with a fluorine broke form SO_2F_2 and the other two SOF_2 molecules away from the surface of Ni-SWCNTs, resulting in the increase of conductivity due to the evenly distributed LUMO.

Taking advantage of the sensing mechanism of Ni-SWCNTs to SF_6 decomposed products: SO_2, SOF_2 and SO_2F_2, the Ni-SWCNTs gas chemiresistor sensor can be prepared to realize the online detection and diagnosis of insulated faults in SF_6 insulated equipment.

2.5. Gas-sensing properties of Al-SWCNTs to SOF_2, SO_2F_2, SO_2, H_2S, HF, CF_4 and SF_6

2.5.1. Structural parameters of intrinsic Al-SWCNTs

When a carbon atom C1 was substituted by an Al atom, significant geometric changes occurred in Al-SWCNTs, as shown in **Figure 31**. Considering that the radius of the Al atom is larger than that of the carbon atom, the Al heteroatom protruded from the Al-SWCNT surface after structural optimization [32]. The bond length between Al—C3 and Al—C4 atoms reached 1.908 and 1.841 Å, respectively. The calculation results were similar to that of other research [17, 32, 33].

2.5.2. The analysis of gas adsorption structure

Following the optimization of each initial structure, all gas molecules were allowed to relax on the surface of Al-doped SWCNTs [32]. Cause the orientational effects play important role on the adsorption results. In addition, in order to receive the global minimum-energy structures

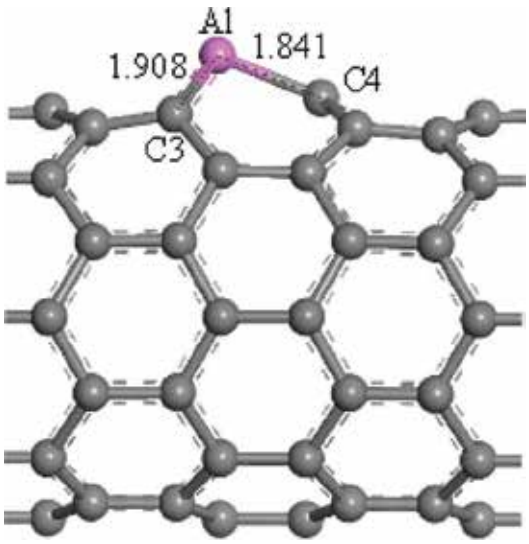

Figure 31. Geometric structures of Al-doped SWCNTs after optimization. The structural parameters are shown as Å.

from the all these minimum-energy structures, which may contain some local minimum-energy structures. Various adsorption sites and approaching ways of decomposition products were calculated to get the most minimum-energy structures, which are used as the most stable structure for each gas molecule adsorption in our study (**Figure 32**) [32]. The results showed that all of the gas molecules tended to adsorb at the site of Al atom, which revealed the stronger adsorption of Al atom than other undoped sites. Given that the electrical properties of SWCNTs could be significantly influenced by gas adsorption [32, 34], the strong adsorption provided an opportunity for the detection of SF_6 decomposition products based on the change of conductivity [32].

The adsorption energy E_{ads}, charge transfer Q_T and interactive distance d were computed to analyze the gas adsorption properties, which are shown in **Table 8**. We determined that all of the molecules have negative adsorption energy, indicating that the adsorption reaction was an exothermic process that occurred spontaneously [35]. In the adsorption process of the SOF_2 and SO_2F_2 gas molecules, the strong interaction decomposed SOF_2 and SO_2F_2 into other gas molecules. Thus, the binding distance from the SOF_2 and SO_2F_2 gas molecules to Al-SWCNTs is not shown in **Table 8**.

As shown in **Figure 32a1** and **a2** and **Table 8** [32], when one SO_2 molecule approached the surface of Al-SWCNTs in a different direction, two oxygen atoms were close to the Al atom. Meanwhile, the sulfur atom is far from the Al atom because the sulfur atom has already built a strong double bond with adjacent oxygen atoms. This steady interaction does not allow the sulfur atom to form another coordinate bond with the Al atom. The bond distance and angle of the SO_2 molecule slightly changed during the adsorption process, which corresponded with the result of a previous study [32, 36]. In the present study, the interaction distance between SO_2 molecule and Al atom was 1.988 Å, which is slightly smaller than that of Pd-doped (8, 0) SWCNTs [37] because the radius of the Al atom is smaller than that of the Pd atom [32]. Long gas

System	Structure	E_{ads} (eV)	Q_T (e)	d_1 (Å)	d_2 (Å)
SO_2	(a1)	−1.606	−0.493	1.988	–
$2SO_2$	(a2)	−2.206	−0.706	1.787	1.868
H_2S	(b1)	−1.051	0.234	2.47	–
$2H_2S$	(b2)	−1.498	0.273	2.425	3.495
SOF_2	(c1)	−2.103	−0.573	–	–
$2SOF_2$	(c2)	−2.974	−1.102	–	–
SO_2F_2	(d1)	−3.408	−1.041	–	–
$2SO_2F_2$	(d2)	−4.952	−3.018	–	–
CF_4	(e1)	−0.033	−0.003	3.27	–
$2CF_4$	(e2)	−0.087	0.019	2.710	3.537

Table 8. Calculated adsorption energy, charge transfer and binding distance from an Al atom to adsorbates.

interaction distance (1.988 Å) and low banding energy (−1.606 eV) indicated that the adsorption was some type of physisorption [32, 38]. When the second SO_2 molecule was adsorbed on Al-SWCNTs, the SO_2 molecules approached the Al atom with only one oxygen atom because of the repulsive interaction between the two gas molecules. The adsorption energy increased to 2.206 eV, with adsorption distances of 1.787 and 1.868 Å to the Al atom [32].

The adsorption structures and parameters of single and double H_2S molecules on Al-SWCNTs are shown in **Figure 32b1** and **b2** and **Table 8** [32]. After the relaxation process, a quasi-tetrahedron geometry around the Al center was observed. The hydrogen atoms and sulfur atom in the H_2S molecule generated strong bond energy [39]. Thus, the interaction between hydrogen atoms and Al was weak. Meanwhile, the sulfur atom could still react with the Al atom because of its multivalent feature. As such, the H_2S molecule approached the Al atom through the sulfur atom. The interaction distance between the S and Al atoms was approximately 2.47 Å, with the H─Al distance of 2.85 Å [32]. Considering the long interaction distance and low binding energy of −1.051 eV, the interaction indicated a moderate physisorption. When double H_2S molecules adsorbed on the surface of Al-SWCNTs, we observed that one molecule was distinctly far from the surface with a distance of 3.495 Å because of the repulsive force between molecules [32]. However, the adsorption site of the other H_2S molecule changed slightly compared with the former single molecule adsorption. The distance from the new added H_2S molecule to the doped Al atom was approximately 2.425 Å. The binding energy between single H_2S and Al-SWCNTs was approximately −1.051 eV, whereas the binding energy between double H_2S and Al-SWCNTs increased to −1.498 eV [32]. The Mulliken population analysis indicated that 0.234 and 0.273 electrons transferred from single and double H_2S molecules to Al-SWCNTs, respectively. In addition, our results were similar to the results of previously studied Au-doped SWCNTs [32, 40], in which the structural parameters, binding energy and charge transfer were also reported. Small difference between our results and than in previous report was found probably because different models were used in the

http://dx.doi.org/10.5772/intechopen.68325

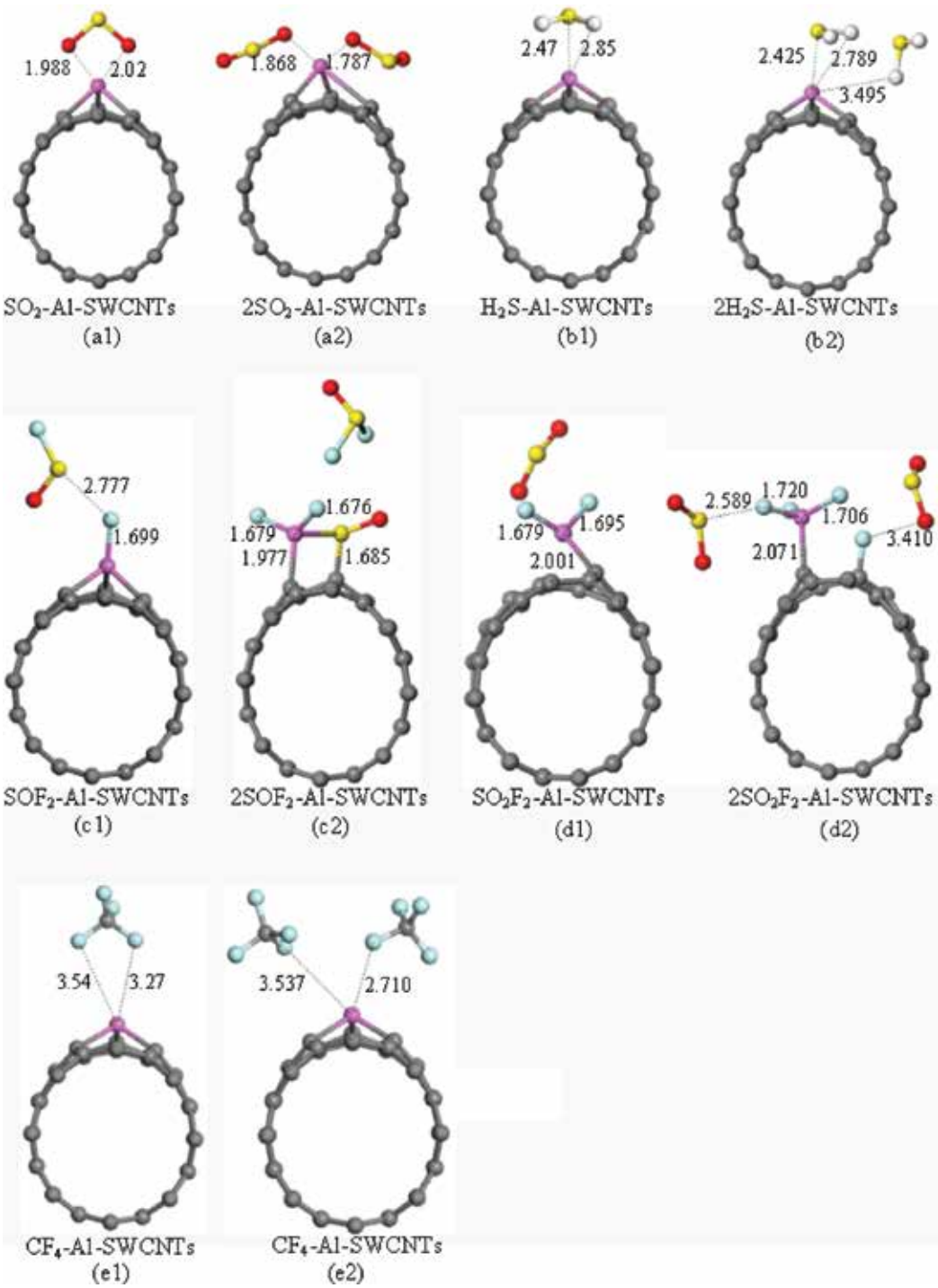

Figure 32. Most stable geometries of gas molecules interacting with Al-doped SWCNTs (distances in Å).

calculations. Al-SWCNTs can be considered a possible sensor material for the detection of H_2S owing to the adsorption energy and considerable charge transfer [32].

Based on the optimized adsorption structures of SOF_2 shown in **Figure 32c1** and **c2** and **Table 8** [32], two types of adsorption, namely single and double SOF_2 molecule adsorption, were outlined to analyze the adsorption capacity. From the relaxed structure of single SOF_2 molecule adsorption, the strong interaction between SOF_2 molecule and Al-SWCNTs decomposed the SOF_2 molecule to one SOF molecule and another fluorine atom [32]. The electronegative fluorine atom bonded to the Al atom through a strong chemical reaction, with the interaction distance of 1.699 Å. Meanwhile, the bond length from the produced SOF molecule to the fluorine atom was 2.777 Å, which indicated the decomposition of SOF_2 [32]. Upon double SOF_2 molecule adsorption, one of the SOF_2 molecules was adsorbed on the surface of Al-SWCNTs by chemisorption [38], whereas the other SOF_2 molecule was found far from the nanotube [32]. Two of the original Al—C bonds broke in the adsorption process. Then, two fluorine atoms of SOF_2 bonded to the Al atom [32].

As shown **Figure 32d1** and **d2** and **Table 8** [32], single and double SO_2F_2 molecules are adsorbed on the surface of Al-SWCNTs. After the structures have relaxed to reach the most steady state, only one original Al—C bond exists after the adsorption process. The other two bonds were broken because of the strong interaction between the F and Al atoms [32, 41]. Upon single SO_2F_2 molecule adsorption, two fluorine atoms separated from SO_2F_2 molecule and bonded to the Al atom, with bond lengths of 1.679 and 1.695 Å, respectively. Meanwhile, the produced SO_2 molecule was far from the surface of Al-SWCNTs. When another SO_2F_2 molecule was added, all of the fluorine atoms separated from the SO_2F_2 molecules. Three of the fluorine atoms bonded to the Al atom. The other fluorine atom bonded to the carbon atom of Al-SWCNTs. Both of the produced SO_2 molecules were far from the surface of Al-SWCNTs, with interactive distances of 2.589 and 3.410 Å, respectively. The weak interaction to the produced SO_2 might be because the Al-SWCNTs have reached saturated adsorption [32].

As shown in **Figure 32e1** and **e2** and **Table 8** [32], the CF_4 molecule was far from the surface of Al-SWCNTs, which was also ineffectively detected by other reported methods [42]. The nearest interaction distances reached 3.27 Å for single CF_4 molecule adsorption and 2.710 and 2.537 Å for double CF_4 molecule adsorption. The long interactions corresponded well with the low adsorption energies of −0.033 and −0.087 eV for single and double CF_4 molecule adsorption, respectively. Furthermore, weak physisorption was consistent with slight charge transfer [32].

2.5.3. The analysis of the density of states and frontier molecular orbital

In the previous section, we discussed the adsorption of single and double SF_6 decomposed gas molecules on Al-SWCNTs. We observed that the Al doping method showed good adsorption capacity for all of the SF_6 decomposed gas molecules, except for the CF_4 molecules, which indicated the possibility of detecting these decomposition components [32]. However, the detecting mechanism of Al-SWCNTs depends on its conductivity change after gas adsorption. The density of states (DOS) and frontier molecular orbitals were investigated to analyze the change of conductivity. The total electron DOS (TDOS) and local DOS (LDOS) were determined to investigate the influence of gas adsorption and to elucidate the electronic properties

of Al-SWCNTs and molecule-Al-SWCNTs [32, 43], as shown in **Figure 33**. The highest occupied molecular orbital (HOMO) and lowest unoccupied molecular orbital (LUMO) upon molecule adsorption on the Al-doped SWCNTs are listed in **Table 9**. The corresponding diagrams of HOMO and LUMO are shown in **Figure 34** [32].

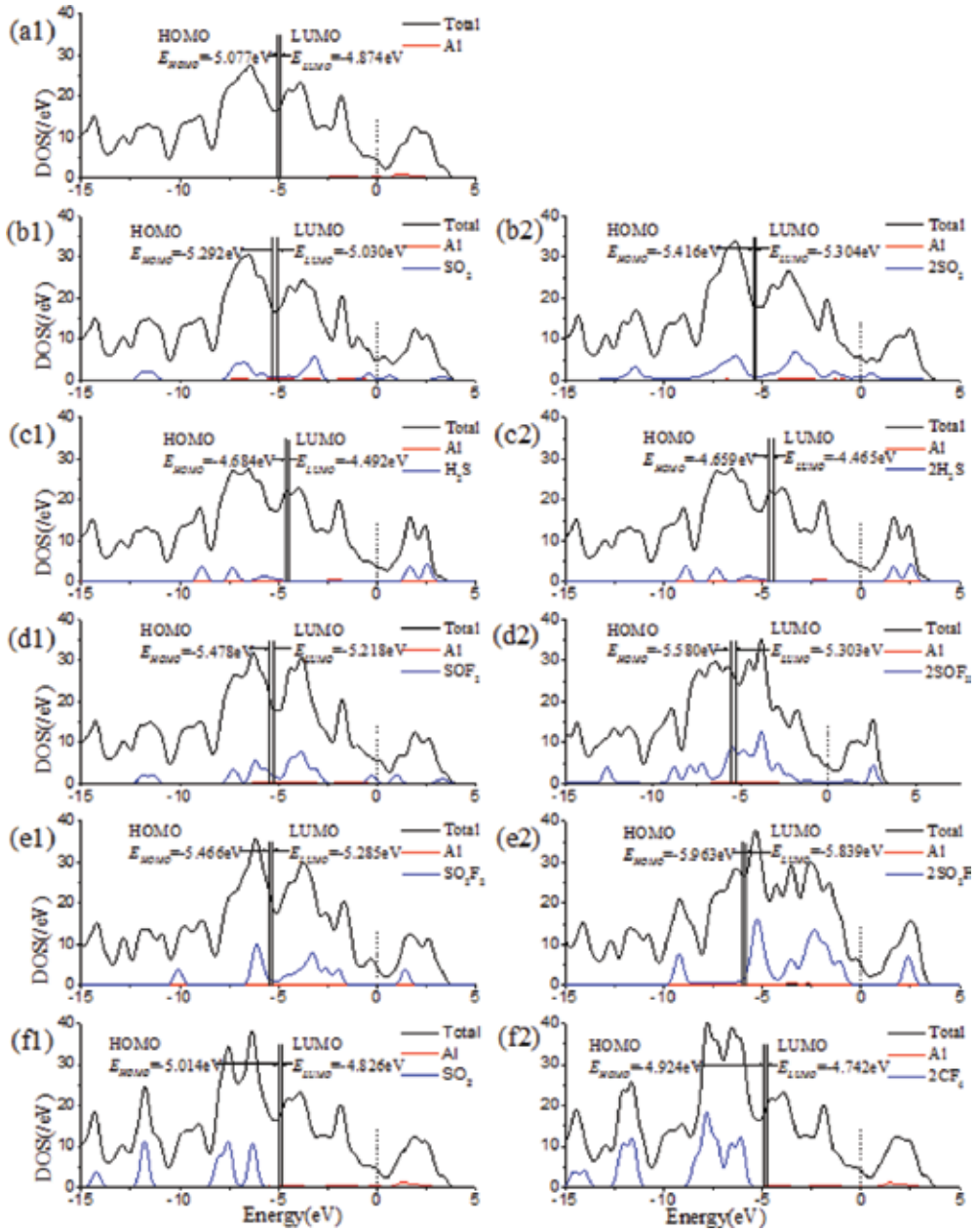

Figure 33. TDOS and LDOS of the Al-SWCNTs and molecule-Al-SWCNTs. Dashed and solid lines indicate the Fermi level and HOMO-LUMO, respectively.

System	EHOMO (eV)	ELUMO (eV)	Eg (eV)
Al-SWCNTs	−5.077	−4.874	0.203
SO_2-Al-SWCNTs	−5.292	−5.030	0.262
$2SO_2$-Al-SWCNTs	−5.416	−5.304	0.112
H_2S-Al-SWCNTs	−4.684	−4.492	0.192
$2H_2S$-Al-SWCNTs	−4.659	−4.465	0.194
SOF_2-Al-SWCNTs	−5.478	−5.218	0.260
$2SOF_2$-Al-SWCNTs	−5.580	−5.303	0.277
SO_2F_2-Al-SWCNTs	−5.466	−5.285	0.181
$2SO_2F_2$-Al-SWCNTs	−5.963	−5.839	0.124
CF_4-Al-SWCNTs	−5.014	−4.826	0.188
$2CF_4$-Al-SWCNTs	−4.924	−4.742	0.182

Table 9. HOMO and LUMO energies (E_{HOMO}, E_{LUMO}) and HOMO-LUMO energy gap (E_g).

Based on the DOS of SF_6 decomposition products before and after adsorption (**Figure 33**) [32], we observed that the LDOS of the Al atom had only a slight contribution to each TDOS. The changes of TDOS were mainly from the adsorbed molecules. Meanwhile, the various changes induced by different adsorbed molecules only provided the chance to detect the SF_6 decomposition products selectively [32].

Based on **Figure 33a1** [32], the TDOS of Al-SWCNTs was apparently distributed to all energy band areas, which reached 4.43 eV at the Fermi level. This finding indicated that Al-SWCNTs are still a good conductor after Al atom doping. The results are in accordance with other experiments on metal-doped materials [44]. **Figure 33a1** and **a2** shows the frontier molecular orbitals of Al-SWCNTs. In addition, the HOMO and LUMO were uniformly located on the Al-SWCNT surface. The HOMO and LUMO of the Al atom were mainly contributed by its *s* orbital. **Table 9** shows that E_{HOMO} and E_{LUMO} of Al-SWCNTs were −5.077 and −4.874 eV, respectively, and E_g was 0.203 eV [32].

The TDOS for SO_2 molecules adsorbed on Al-SWCNTs is shown in **Figure 33b1** and **b2** [32]. When one SO_2 molecule was adsorbed on the surface of Al-SWCNTs, the TDOS slightly increased at and under the Fermi level compared with that of pristine Al-SWCNTs. As shown in **Figures 22b2** and **33b1**, the HOMO and LUMO were entirely located on the carbon atoms upon single SO_2 adsorption. The HOMO energy shifted from −5.077 to −5.292 eV, and the LUMO energy shifted to −5.030 eV in the pristine Al-SWCNTs. E_g was slightly increased to 0.262 eV compared with that of Al-SWCNTs. Upon the second SO_2 molecule adsorption, the TDOS further increased with respect to that of the single molecule adsorption [32]. In addition, E_g decreased to 0.112 eV when the HOMO and LUMO are mainly located on SO_2 molecules and carbon atoms. Considering the increased TDOS and decreased E_g, the conductivity of Al-SWCNTs tended to increase with SO_2 adsorption [20].

http://dx.doi.org/10.5772/intechopen.68325

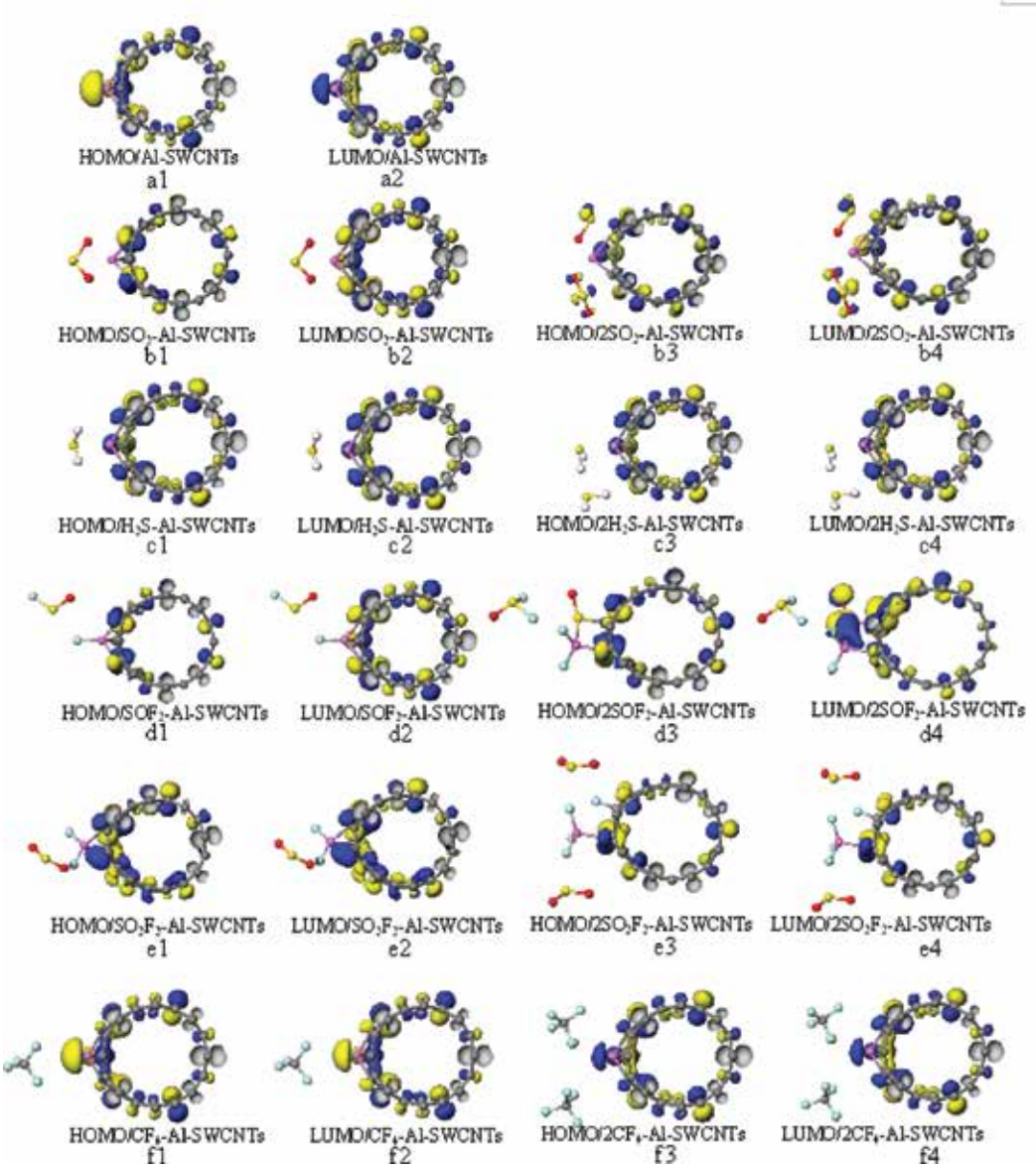

Figure 34. HOMO and LUMO orbitals on Al-SWCNTs and molecule-Al-SWCNTs. From top to bottom: (a1)–(f1) and (b3)–(f3) represent the HOMO orbitals, and (a2)–(f2) and (b4)–(f4) represent the LUMO orbitals.

As shown in **Figure 33c1** and **c2**, the LDOS induced by the H_2S molecules was partly located above the Fermi level, which contributed to the TDOS above the Fermi level. The change of the HOMO and LUMO energies slightly shifted to the right side. E_g for the single and double H_2S molecule adsorption was 0.192and 0.194 eV, respectively, and was smaller than that of pristine Al-SWCNTs. As shown in **Figure 33c1–c4**, the HOMO and LUMO were still

distributed on pristine Al-SWCNTs. In general, the interaction between the H_2S molecules and Al-SWCNTs was favorable and enhanced the conductivity of Al-SWCNTs.

Based on the SOF_2 molecules adsorbed on Al-SWCNTs shown in **Figure 33d1** and **d2**, the LDOS of SOF_2 molecules was mainly below the Fermi level. Herein, the TDOS at the Fermi level was slightly changed compared with that of pristine Al-SWCNTs. However, E_g evidently increased to 0.260 eV for single SOF_2 adsorption and further increased to 0.277 eV when another SOF_2 molecule was adsorbed (**Table 9**). As shown in **Figure 33d1–d4**, the HOMO and LUMO orbitals were distributed on the carbon atoms for single SOF_2 molecule adsorption [32]. Meanwhile, the distribution of the molecular orbital for double SOF_2 molecule adsorption was different, where the HOMO orbital was located on the carbon atoms and the LUMO orbital was located on all of the Al-SWCNTs [32]. Based on the previously presented analysis, conductivity might decrease to a certain extent [32].

When one SO_2F_2 molecule was adsorbed on Al-SWCNTs, the TDOS decreased around the Fermi level (**Figure 33e1**). The LDOS of SO_2F_2 was primarily below the HOMO energy and above the LUMO energy, with the decrease in E_g to 0.181 eV. When the other SO_2F_2 molecule was adsorbed, the TDOS continued to decrease above the Fermi level. With LDOS induced by double SO_2F_2 molecules, we observed that the TDOS distinctly increased above the LUMO energy (see **Figure 33e2**). The value of E_g decreased to 0.124 eV, which facilitated electron conduction between molecular orbitals. As shown in **Figure 33e1–e4**, the HOMO and LUMO orbitals were totally shifted to the carbon atoms after SO_2F_2 adsorption. The strong bond energy between the Al and F atoms seemed to weaken the electron conduction ability among atoms other than carbon [32].

As mentioned previously, the interaction between CF_4 molecules and Al-SWCNTs was weak, resulting in a limited influence of the CF_4 molecules [45]. The LDOS of CF_4 was below the HOMO energy shown in **Figure 33f1** and **f2** [32]. Meanwhile, the TDOS around the Fermi level remains unchanged. E_g (0.188 and 0.182 eV) was slightly smaller than that of pristine Al-SWCNTs. Similarly, the HOMO and LUMO orbitals were almost the same as that of Al-SWCNTs before CF_4 adsorption. Therefore, we conclude that the conductivity of Al-SWCNTs would not change upon CF_4 adsorption.

2.5.4. Summary: gas adsorption on Al-SWCNT

In this study, we analyzed the adsorption of the gases produced by SF_6 decomposition (i.e., SO_2, H_2S, SOF_2, SO_2F_2 and CF_4) on the Al-SWCNT surface using GGA and DFT calculations and considering different sites to determine the most stable structures. In addition, multiple-molecule adsorption was calculated for SF_6 decomposition products to analyze the various changes of conductivity induced by adsorption [32].

The results indicated that the SO_2 molecules were physically adsorbed on Al-SWCNTs. This interaction increased the TDOS and decreased the E_g, which increased the conductivity of the adsorption system [32]. Upon H_2S adsorption, considerable E_{ads} resulted in well-adsorbed H_2S molecules on the surface of Al-SWCNTs. However, the change of conductivity was not evident based on the analyses of DOS and frontier molecular orbital. The SOF_2 and SO_2F_2 molecules were

chemisorbed on the surface of Al-SWCNTs because of the strong interaction between the Al and F atoms. The conductivity of SOF_2 adsorbed on Al-SWCNTs decreased to a certain extent as a result of the increase in E_g and decrease in TDOS around the Fermi level [32]. For SO_2F_2 adsorption, although the TDOS around the Fermi level showed a slight decrease, the evident decrease in E_g indicated that conductivity might be enhanced upon SO_2F_2 adsorption. The calculation results showed that conductivity is unchanged during CF_4 adsorption mainly because the interaction between Al-SWCNTs and CF_4 molecules was weak to induce electron redistribution [32].

In summary, Al atom doping method is potentially an effective technique to adsorb the gases produced by SF_6 decomposition. Through the different changes in conductivity induced by molecule adsorption, the selective detection of each type of SF_6 decomposed gas was achieved. We hope that this innovative study would further accelerate research on the mechanism of metal doping methods in detection of gases from SF_6 decomposition [32].

2.6. Gas-sensing properties of Pt-SWCNTs to SO_2, H_2S

2.6.1. Structural parameters of intrinsic Pt-SWCNT

The radius of Pt atom is 0.183 nm, which is greater than that of C atom (0.070 nm). Thus, Pt is highlighted on the CNT surface as shown in **Figure 35**. The bond lengths between Pt atom and three adjacent C atoms changed from 0.142 nm to 0.199, 0.199 and 0.189 nm for Pt-C1, Pt-C2 and Pt-C3, respectively [16]. These results are consistent with Refs. [16, 46].

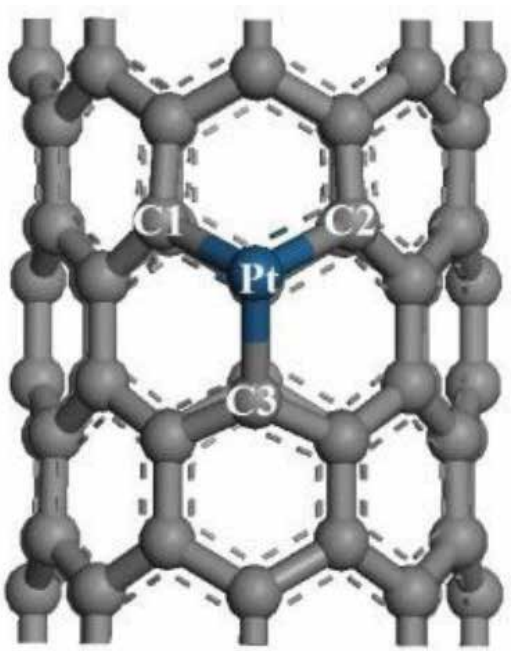

Figure 35. Geometric structures of Pt-doped SWCNTs after optimization. The structural parameters are shown as Å.

2.6.2. The analysis of gas adsorption structure

Pt is not only a sensing element of Pt-SWCNTs, but also an active site. Strong interaction with gas molecules adsorbed on the surface results in deformation of Pt-SWCNTs and elongation of Pt-C bond. The full geometric optimization of the Pt-SWCNTs and SO_2 adsorption model is shown in **Figure 36**. An oxygen atom O1 points to Pt, in which the distances of Pt-O1 and Pt-S are 0.212 and 0.245 nm, respectively.

The reaction adsorption energy for SO_2 adsorption is −1.225 eV, which denotes an exothermic and spontaneous reaction. According to Mulliken charge population analysis shown in **Table 10**, SWCNTs of Pt-SWCNTs have 0.147 positive charge, and Pt has 0.147 negative charge before adsorption. After the adsorption process, SWCNTs have 0.509 positive charge, whereas Pt has 0.116 negative charge. SO_2 obtains 0.301 electrons during the adsorption reaction [16]. Charge variation (ΔQ_{SWCNTs}, ΔQ_{Pt}) of SWCNTs and Pt is 0.362 and 0.031, respectively. Therefore, SO_2 obtains electrons mainly from SWCNTs, whereas Pt exhibits a small charge change.

As shown in **Table 10** [16], Mulliken charge analysis shows that H_2S donates 0.285 electrons. Pt and SWCNTs, respectively, have 0.019 and 0.266 electrons after H_2S is adsorbed on Pt-SWCNTs. A large number of electron transformations convert Pt-SWCNTs from *p*-type to *n*-type.

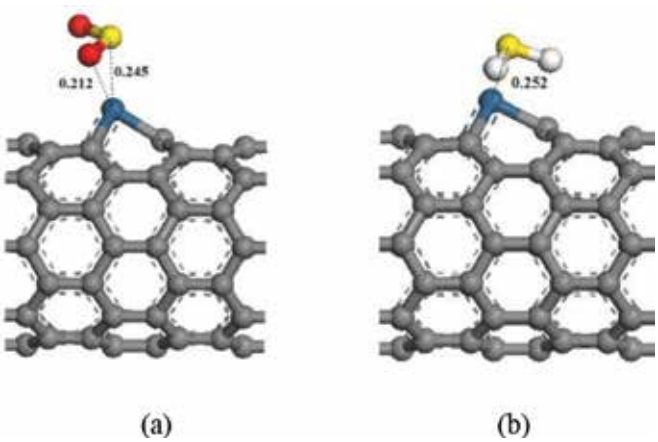

Figure 36. Structural model of the SO_2-Pt-SWCNT adsorptive system. (a) Front view; (b) side view.

System	Q_{SWCNTs}/e	Q_{Pt}/e	Q_{gas}/e	ΔQ_{SWCNTs}/e	ΔQ_{Pt}/e
Pt-SWCNTs	0.147	−0.147			
SO_2-Pt-SWCNTs	0.509	−0.116	-0.393	0.362	0.031
H_2S-Pt-SWCNTs	−0.019	−0.266	0.285	−0.166	−0.119

Table 10. Electrical structure parameters of the adsorption structures.

2.6.3. The analysis of the density of states and frontier molecular orbital

The transfer of a large number of electrons during adsorption causes the redistribution of system charges. The density of states (DOS) near Fermi level appears impure state, and the DOS between HOMO and LUMO changes. **Figure 37** shows that these impure states are caused by SO_2 adsorption. The *p* orbitals of S and O atoms have significant influence on the frontier orbital of the adsorption system, which changes the HOMO and LUMO orbital formation, thereby causing the change in DOS. **Figure 38a** shows that the *p* orbitals of C1 and C3 form σ bond with S, and in **Figure 38b**, the *d* orbitals of Pt and the *p* orbitals of S are hybridized [16]. The frontier orbital energy gap E_g of the system is 0.283 eV after adsorbing SO_2, which is reduced by 0.049 eV compared with the non-adsorbed SO_2 [16]. This observation is beneficial for the transfer of electrons between the HOMO and LUMO, thereby enhancing conductivity [16].

SO_2 adsorption on the surface of Pt-SWCNTs has large adsorption energy and can form a stable structure. The *p*-type Pt-SWCNTs [16, 47] donate electrons and increase hole carriers, thereby reducing the frontier orbital energy, diminishing energy gap E_g and enhancing conductivity. Pt-SWCNTs are highly responsive to SO_2 [16].

The adsorption reaction of Pt-SWCNTs and H_2S is also exothermic, with E_b of −0.977 eV. The frontier orbital energy difference $E_{H\text{-}L}$ = 4.438 eV and $E_{L\text{-}H}$ = 1.519 eV, so H_2S provides electrons to Pt-SWCNTs in this reaction. H_2S-Pt-SWCNT frontier orbitals concentrate on Pt-SWCNTs, and H_2S is not involved in the composition of HOMO and LUMO orbitals shown in **Figure 39**. **Figure 40** shows that DOS of H_2S is not distributed between HOMO and LUMO. DOS near the Fermi level is basically the same with Pt-SWCNTs, which is consistent with the results of frontier orbitals.

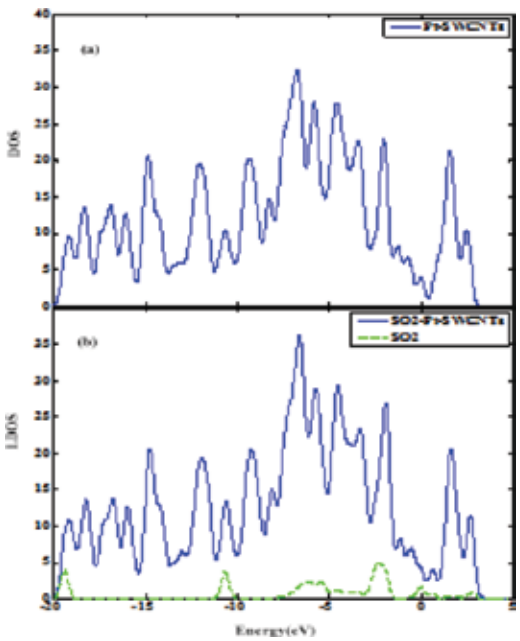

Figure 37. Density of states of Pt-SWCNTs before and after SO_2 adsorption (Fermi level is 0 eV).

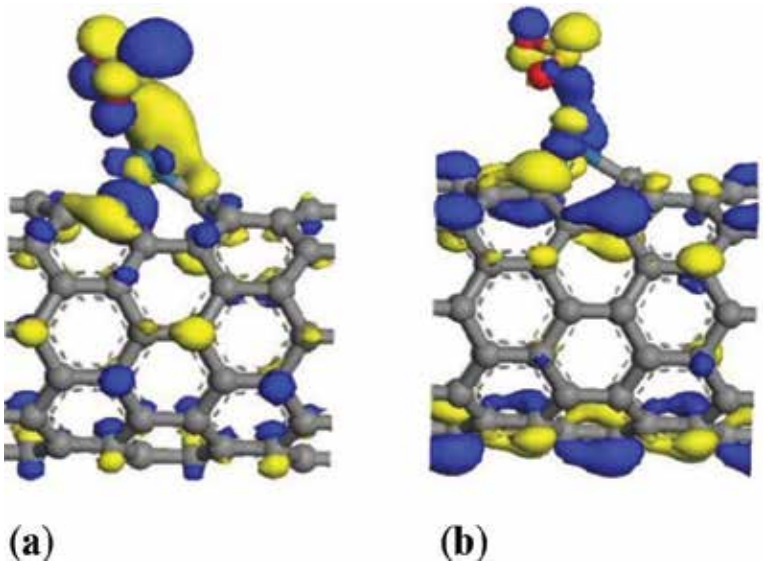

Figure 38. Frontier orbital energy level of SO_2-Pt-SWCNTs. (a) HOMO (−5.208 eV); (b) LUMO (−4.923 eV).

2.6.4. Summary: gas adsorption on Pt-SWCNTs

In this study, adsorptions of three gases on the surface of Pt-SWCNTs were calculated based on DFT [16]. The gas-sensing properties of Pt-SWCNTs were assessed according to the changes in adsorption energy, geometric structure and electronic structure during adsorption. The main conclusions are as follows [16]:

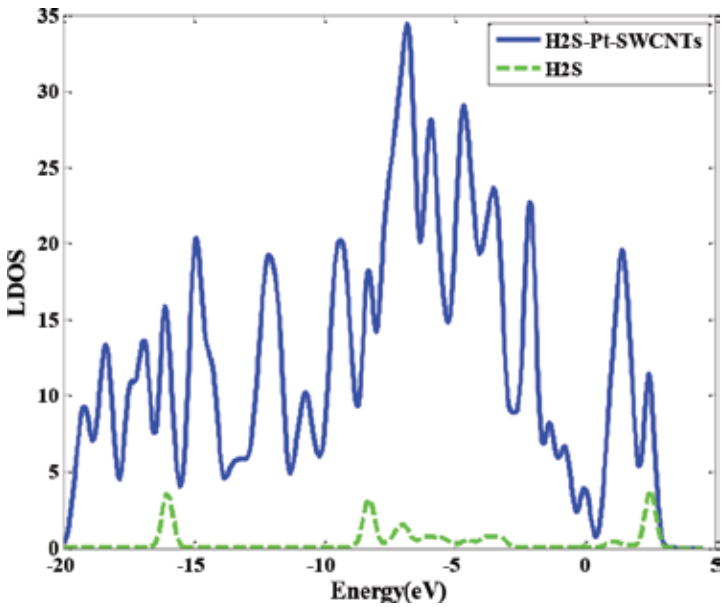

Figure 39. Frontier orbital energy level of H_2S-Pt-SWCNTs. (a) HOMO (−4.425 eV); (b) LUMO (−4.142 eV).

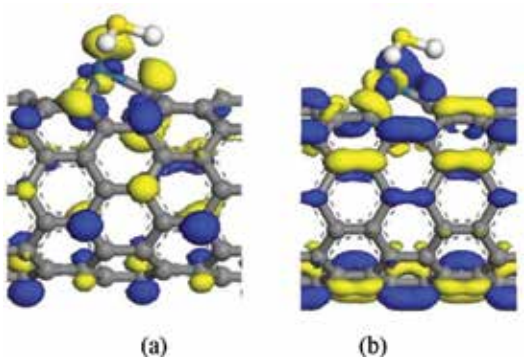

Figure 40. Partial DOS of H_2S-Pt-SWCNTs.

The three adsorption reactions are exothermic and spontaneous.

The adsorption energy of the reaction between Pt-SWCNTs and SO_2 is large, and numerous electrons are transferred from CNTs to the target gases [16]. The frontier orbital energies (E_{HOMO} and E_{LUMO}) and E_g decrease, and the electrical conductivity of Pt-SWCNTs is enhanced. Pt-SWCNTs have high sensitivity to SO_2 [16].

H_2S is reduced when reacted with Pt-SWCNTs and provide a large number of electrons, thereby converting CNTs from *p*-type to *n*-type. The frontier orbital energies increase, whereas E_g decreases, thereby enhancing conductivity [16].

Results of the theoretical calculation show that Pt-SWCNTs can respond to the three gases [16]. The electrical characteristics of Pt-SWCNTs show different degrees of changes after adsorption of the test gases. As SO_2 is adsorbed on Pt-SWCNTs, CNT loses electrons, hole carriers are increased and conductivity is enhanced [16]. As H_2S is adsorbed on the surface of CNTs, Pt-SWCNTs receive a large number of electrons and transforms from *p*-type into *n*-type. The conductivity of Pt-SWCNT is also enhanced [16]. Comparing their adsorption energies and charge transformations, the sensitivity of SO_2 is higher than that of H_2S for Pt-SWCNTs [16]. Therefore, Pt-SWCNTs can be used for fabricating gas sensors in detecting SO_2 and H_2S.

2.7. Gas-sensing properties of Au-SWCNTs to SO_2, H_2S

2.7.1. Structural parameters of intrinsic Au-SWCNTs

The radius of the Au atom is significantly greater than that of the C atom; thus, the Au atom of Au-SWCNT is highlighted on the nanotube surface shown in **Figure 41** [48]. The bond lengths between the Au atom and the three adjacent C atoms are 0.207 (Au—C1), 0.208 (Au—C2) and 0.196 nm (Au—C3). Compared with the C—C bond length of the intrinsic structure, the Au—C bond lengths are elongated by 38, 38 and 46%, respectively [48].

2.7.2. The analysis of gas adsorption structure

The adsorption structures of the gas molecules adsorbed by Au-SWCNT in different initial positions were calculated. We chose two initial positions that are parallel to the nanotube

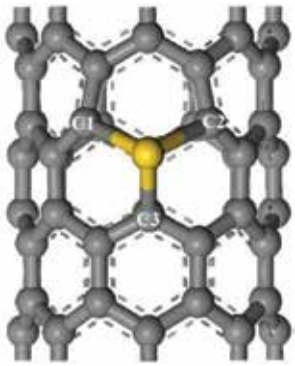

Figure 41. Structural model of Au-SWCNT.

axis and three initial positions that are perpendicular to the nanotube axis. The initial positions were optimized in the geometrical structure [48]. During observation of the optimized structures, the stable adsorption structure of H_2S is the S atom located above the center of the ring that contains Au—C1—C2 [48]. Two main stable adsorption structures of SO_2 exist. One is the S atom located above the Au—C bond and an O atom above the center of the ring that contains Au—C1—C2; another is the S atom located above the center of the ring [48]. SO_2 that is parallel to the axis, and two O atoms above the Au and C atom, respectively. Comparing the two structures, the former is more stable. The most stable adsorption structure is shown in **Figure 42**. **Table 11** lists the adsorption energy and the structural parameter [48].

The adsorption energy of SO_2 is −1.258 eV, which indicates that the adsorption is exothermic and spontaneous. After SO_2 is adsorbed to Au-SWCNT, the structures of Au-SWCNT (**Table 11**) and SO_2 (**Figure 42**) changed [48]. Au—C1 and Au—C2 are elongated by 3.38 and 4.33%, respectively. Moreover, S—O is also elongated. The modified element of CNT is the sensing element and the active site of the modified CNT [48]. The adsorption partially depends

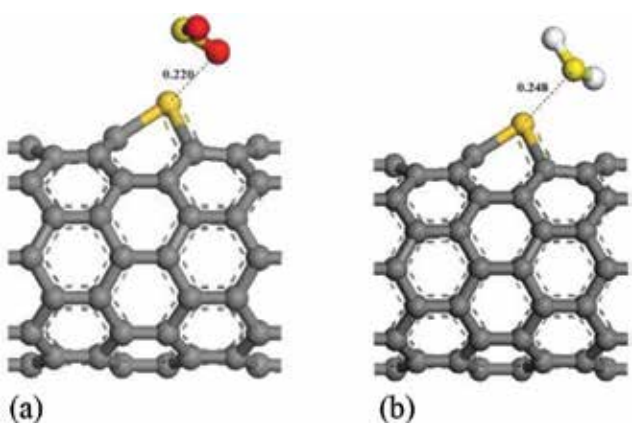

Figure 42. Front and side views of the stable structural model of (a) SO_2-Au-SWCNT and (b) H_2S-Au-SWCNT.

Type	SO_2	H_2S
$d_{Au—C1}$/nm	0.214	0.217
$d_{Au—C2}$/nm	0.217	0.218
$d_{Au—C3}$/nm	0.195	0.195
E_b/eV	−1.258	−1.317

Table 11. Adsorption energy and the structural parameter.

on the interaction between the gas molecule and the sensing element. The strong attraction in the adsorption of SO_2 and Au-SWCNT caused the structural change of Au-SWCNT [48]. The Au—C bond length increased, the bond energy decreased, and the bond activity strengthened. Simultaneously, the electrons are transferred to SO_2, and the excess electrons fill the anti-bonding orbits of SO_2. The increase in repulsion results in a change in the S—O bond length from 0.148 nm to 0.150 and 0.160 nm [48].

The adsorption between H_2S and Au-SWCNT is also exothermic, and the adsorption energy is −1.317 eV. Compared with SO_2, the interaction is slightly stronger. Au—C1 and Au—C2 are elongated by 4.83 and 4.81%, respectively [48].

From the above analysis, Au-SWCNT has a strong adsorption with SO_2 and H_2S, and their adsorption energies are greater than 1 eV. The adsorption reaction can occur at room temperature and the strong interaction changes the geometric structure of the adsorption system [48].

2.7.3. The analysis of the density of states and frontier molecular orbital

In **Table 12** [48], the LUMO of SO_2 was approximated to the HOMO of Au-SWCNT, and the difference of the two orbital energies is only 0.065 eV. The electron of Au-SWCNT only needs to cross a very low energy barrier to transfer to SO_2. In turn, the electron needs to cross a 3.603 eV energy barrier for the electron of SO_2 to transfer to Au-SWCNT, but this process is

System	E_{HOMO}/eV	E_{LUMO}/eV	$E_{L\text{-}H}$/eV	$E_{H\text{-}L}$/eV			
Au-SWCNT	−4.795	−4.585					
SO_2	−8.188	−4.860	3.603	0.065			
H_2S	−5.889	−0.264	1.304	4.531			
System	E_g/eV	Q_{SWCNT}/e	Q_{Au}/e	Q_{gas}/e	ΔE_g/eV	ΔQ_{SWCNT}/e	ΔQ_{Au}/e
Au-SWCNT	0.210	0.070	−0.070				
SO_2-Au-SWCNT	0.183	0.339	−0.038	−0.301	−0.027	0.269	0.032
H_2S-Au-SWCNT	0.245	−0.106	−0.180	0.286	0.035	−0.176	−0.110

Table 12. Electrical structure parameters of the adsorption structures.

more difficult [48]. Thus, the electrons transfer from Au-SWCNT to SO_2 during adsorption. According to Mulliken charge population, SO_2 obtains 0.301 electrons during the adsorption reaction. SWCNT and Au lose 0.269 and 0.032 electrons, respectively. Au has a key role in the adsorption reaction. **Figure 43** shows the three-dimensional plot of the deformation electron density of SO_2-Au-SWCNT [48]. The range is from −0.976 to 0.345 e/nm. The negative value denotes loss of electrons and a decrease in the electron density. The positive value denotes gain of electrons and an increase in the electron density. As seen from the plot, the charge of Au-SWCNT was redistributed after it adsorbed SO_2. SO_2 obtained electrons, whereas Au-SWCNT lost electrons. Correspondingly, the HOMO and LUMO move toward the nuclear and the orbital energy decreases. Au-SWCNT is a p-type semiconductor. The transferred electrons increased the electron holes and simultaneously increased the carriers, enhanced the conductivity, and decreased the frontier orbital energy gap (**Table 12**) [48].

To clarify further the adsorption processes of SO_2, the partial density of states (PDOSs) of the S, O and Au atoms are shown in **Figure 44** [48]. Their PDOSs overlap in the energy region of −10 to −2.5 eV. In this area, the d orbitals of Au, the p orbitals of the S and O atoms are hybridized as the molecular orbitals of the system. In addition, the d orbitals of Au and the p orbitals of S effectively overlap at the Fermi energy (−2.5 eV to 2.5 eV), which strengthens the interaction between the two atoms. The hybridized orbitals at the Fermi level introduce an impurity level and are conducive for the electrons to transfer to SO_2 from Au-SWCNT [48].

Based on the changes in the electronic structure of adsorption system, a significant amount of electrons is transferred in the adsorption process between SO_2 and Au-SWCNT. Au-SWCNT loses electrons, the frontier orbital energy gap decreases, and the conductivity is enhanced. In conclusion, the Au-SWCNT has a good sensitivity to SO_2 and can be used to detect SO_2 gas based on the changes in its conductivity [48].

The S of H_2S is at the lowest valence state. It has a strong reducibility and can provide electrons during the reaction process. In contrast to SO_2, the HOMO of H_2S was approximated to the

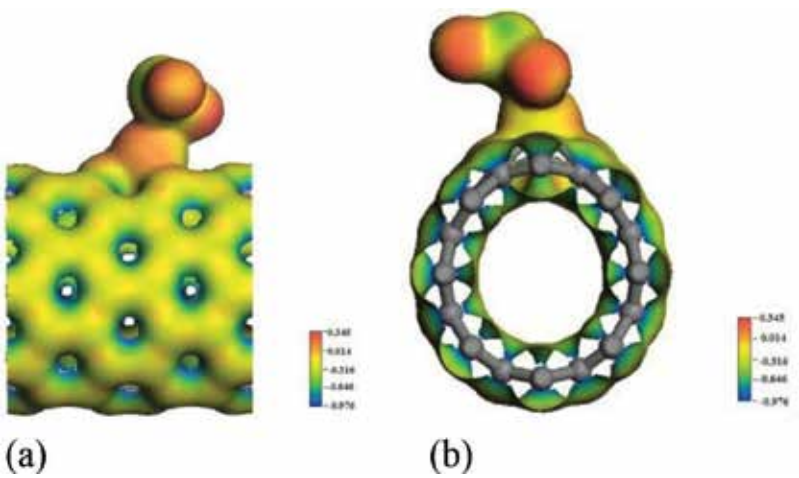

Figure 43. Deformation electron density of SO_2-Au-SWCNT. (a) Front view; (b) side view.

http://dx.doi.org/10.5772/intechopen.68325

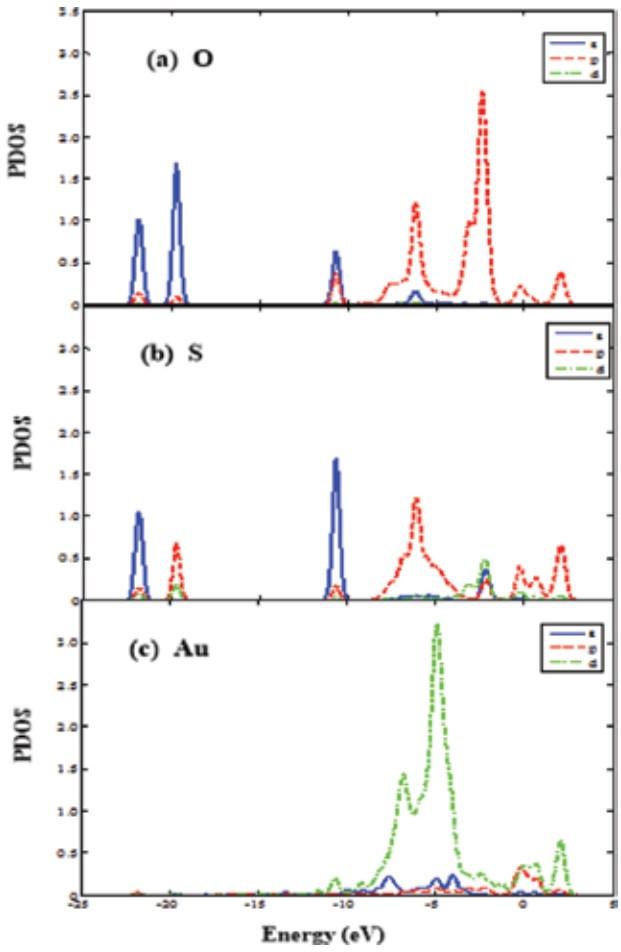

Figure 44. PDOS of SO_2-Au-SWCNT. (a) O; (b) S; (c) Au.

LUMO of Au-SWCNT, and the difference of the energy is only 1.304 eV. Therefore, the electrons of H_2S are easily transferred to Au-SWCNT. Transferring the electrons of Au-SWCNT to H_2S is difficult. Thus, when H_2S was adsorbed to Au-SWCNT, the electrons were transferred from H_2S to Au-SWCNT [48]. According to the Mulliken charge population, the H_2S molecule loses 0.286 electrons. The SWCNT and the Au atom obtain 0.176 and 0.110 electrons, respectively. The three-dimensional plot of the deformation electron density of H_2S-Au-SWCNT is shown on **Figure 45** [48]. The range is −1.172 to 0.320 e/nm. The charges of Au-SWCNT and the adsorbed H_2S are redistributed, H_2S loses electrons and Au-SWCNT gains electrons. Correspondingly, the HOMO and LUMO of Au-SWCNT move away from the nucleus and the orbital energy increases. The transferred electrons decreased the number of electron holes, along with the number of carriers and the conductivity. The frontier orbital energy gap also increased (**Table 12**) [48].

When observing the PDOSs of the adsorption system shown in **Figure 46** [48], which is similar to that of SO_2, the PDOSs of Au in Au-SWCNT and S in H_2S are overlapping. The d orbitals

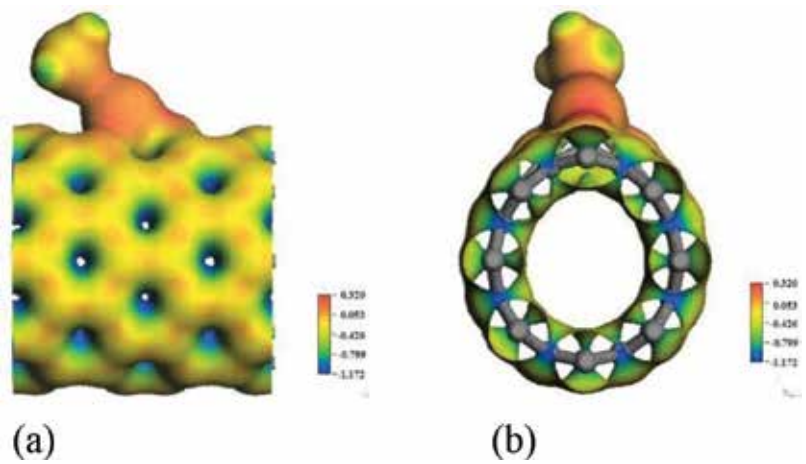

Figure 45. Deformation electron density of H_2S-Au-SWCNT. (a) Front view; (b) side view.

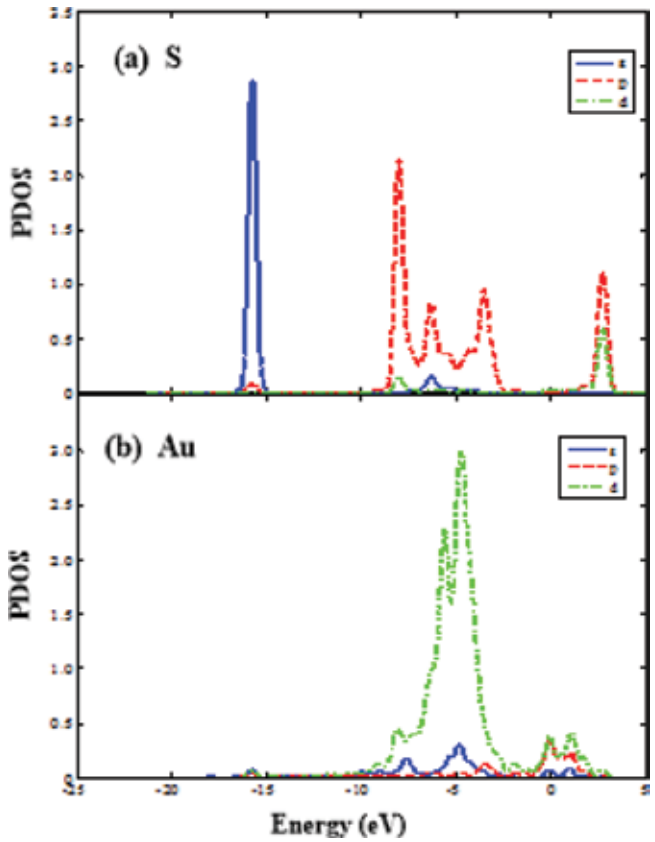

Figure 46. PDOS of H_2S-Au-SWCNT. (a) S; (b) Au.

of Au and the p orbitals of the S atom are hybridized, which is advantageous to the electron transfer and strengthens the interaction between the adsorbed H_2S and Au-SWCNT.

Therefore, Au-SWCNT has a good sensitivity to H_2S, and H_2S can be effectively adsorbed on the surface of Au-SWCNT [48]. When the Au-SWCNT acquired electrons, the frontier orbital energy gap increased, and the conductivity decreased. Hence, Au-SWCNT can be used to detect H_2S [48].

2.7.4. Summary: gas adsorption on Al-SWCNTs

In this study, the adsorption reactions of the two gases on the surface of Au-SWCNT were calculated by DFT, and the sensitivity of Au-SWCNT to the two gases was analyzed [48].

The main conclusions of this study are as follows:

The reactions between the two gases and Au-SWCNT are both exothermic, and the adsorption energies are huge. The interaction between the gas molecule and the nanotubes caused the structure to change, for example, Au—C elongate [48].

During the adsorption process of SO_2, SO_2 acquires electrons and Au-SWCNT loses electrons. The frontier orbital energy gap decreases, and the electrical conductivity of p-type Au-SWCNT is enhanced.

During the adsorption process of H_2S, H_2S loses electrons and Au-SWCNT acquires electrons. The frontier orbital energy gap increases, and the electrical conductivity of p-type Au-SWCNTs decreases.

The theoretical calculation results show that Au-SWCNT has a good sensitivity to both SO_2 and H_2S [48]. The conductivity changes caused by the two gases are inversely proportional. Thus, Au-SWCNT can be used to detect SO_2 and H_2S [48]. This conclusion is helpful to the development of CNT-based gas sensors and provides a theoretical basis for developing Au-SWCNT-based gas sensor [48].

Acknowledgements

Parts of this chapter are reproduced from Refs. [11, 31, 45] with Elsevier's, and from Ref. [32] with Springer's permission.

Author details

Xiaoxing Zhang*, Song Xiao, Ju Tang and Cheng Pan

*Address all correspondence to: xiaoxing.zhang@outlook.com

School of Electrical Engineering, Wuhan University, Wuhan, China

References

[1] Iijima S. Helical microtubules of graphitic carbon. Nature. 1991;**354:**56-58

[2] Hone J, Fischer JE. Quantized phonon spectrum of single-wall carbon nanotubes. Science. 2000;**289**:1730-1733

[3] Krishnan A, Dujardin E, Ebbesen TW, Yianilos PN, Treacy MMJ. Young's modulus of single-walled nanotubes. Physical Review B. 1998;**58**:14013

[4] Ebbesen TW, Ajayan PM. Large-scale synthesis of carbon nanotubes. Nature. 1992;**358**:220-222

[5] Lin X, Wang XK, Dravid VP, Chang RPH, Ketterson J.B. Large scale synthesis of single-shell carbon nanotubes. Applied Physics Letters. 1994;**64:**181-183

[6] Yan Y, Wang WQ, Zhang LX. Dynamical behaviors of fluid-conveyed multi-walled carbon nanotubes. International Journal of Modern Physics B. 2009;**33**:1430-1440

[7] Perdew JP, Burke K, Ernzerhof M. Generalized gradient approximation made simple. [Physical Review Letters 1996;**77:**3865], Physical Review Letters, 1997;**78:**1396

[8] Zhang X, Meng F, Wang Z, Li J. Gas-sensing simulation of single-walled carbon nanotubes applied to detect gas decomposition products of SF6 in PD, In: 2011 Electrical Insulation Conference (EIC). 2011, pp. 132-135

[9] Zhao Q, Nardelli MB, Lu W, Bernholc J. Carbon nanotubes-metal cluster composites: A new road to chemical sensors. Nano Letters. 5:847-851, Nano Letters. 2005;**5:**847-851

[10] Bulat FA, Chamorro E, Fuentealba P, Toro-Labbé A. Condensation of frontier molecular orbital Fukui functions. The Journal of Physical Chemistry A. 2004;**108**:342-349

[11] Zhang X, Gui Y, Xiao H, Zhang Y. Analysis of adsorption properties of typical partial discharge gases on Ni-SWCNTs using density functional theory. Applied Surface Science. 2016;**379:**47-54

[12] Banerjee S, Hemraj-Benny T, Wong S.S. Covalent surface chemistry of single-walled carbon nanotubes. Advanced Materials. 2005;**17:**17-29

[13] Felten A, Bittencourt C, Pireaux JJ, Lier GV, Charlier J.C. Radio-frequency plasma functionalization of carbon nanotubes surface O_2, NH_3, and CF_4 treatments. Journal of Applied Physics. 2005;**98:**074308-074308-074309

[14] Valentini L, Puglia D, Armentano I, Kenny JM. Sidewall functionalization of single-walled carbon nanotubes through CF_4 plasma treatment and subsequent reaction with aliphatic amines. Chemical Physics Letters. 2005;**403:**385-389

[15] Shulga YM, Tien TC, Huang CC, Lo SC, Muradyan VE, Polyakova NV, Ling YC, Loutfy RO, Moravsky AP. XPS study of fluorinated carbon multi-walled nanotubes. Journal of Electron Spectroscopy & Related Phenomena. 2007;**160:**22-28

[16] Zhang X, Dai Z, Wei L, Liang N, Wu X. Theoretical calculation of the gas-sensing properties of Pt-decorated carbon nanotubes. Sensors. 2013;**13:**15159-15171

[17] Wang R, Zhang D, Sun W, Han Z, Liu C. A novel aluminum-doped carbon nanotubes sensor for carbon monoxide. Journal of Molecular Structure: THEOCHEM. 2007;**806:**93-97

[18] Yeung CS, Liu LV, Wang YA. Adsorption of small gas molecules onto Pt-doped single-walled carbon nanotubes. The Journal of Physical Chemistry C. 2008;**112:**7401-7411

[19] Zhang X, Dai Z, Wei L, Liang N, Wu X. Theoretical calculation of the gas-sensing properties of Pt-decorated carbon nanotubes. Sensors. 2013;**13:**15159-15171

[20] Zhou X, Tian WQ, Wang X-L. Adsorption sensitivity of Pd-doped SWCNTs to small gas molecules. Sensors and Actuators B: Chemical. 2010;**151:**56-64

[21] Zhang X, Dai Z, Chen Q, Tang J. A DFT study of SO_2 and H_2S gas adsorption on Au-doped single-walled carbon nanotubes. Physica Scripta. 2014;**89:**065803

[22] Star A, Joshi V, Skarupo S, Thomas D, Gabriel J-CP. Gas sensor array based on metal-decorated carbon nanotubes. The Journal of Physical Chemistry B. 2006;**110:**21014-21020

[23] López-Corral I, Germán E, Volpe MA, Brizuela GP, Juan A. Tight-binding study of hydrogen adsorption on palladium decorated graphene and carbon nanotubes. International Journal of Hydrogen Energy. 2010;**35:**2377-2384

[24] Byl O, Kondratyuk P, Forth ST, FitzGerald SA, Chen L, Johnson JK, Yates JT. Adsorption of CF4 on the internal and external surfaces of opened single-walled carbon nanotubes: A vibrational spectroscopy study. Journal of the American Chemical Society. 2003;**125:**5889-5896

[25] O'Boyle NM, Tenderholt AL, Langner KM. cclib: A library for package-independent computational chemistry algorithms. Journal of Computational Chemistry. 2008;**29:**839-845

[26] Camilli G, Chapman JJ. Gaseous insulation for high-voltage apparatus, American Institute of Electrical Engineers. Transactions of the American Institute of Electrical Engineers. 1947;**66:**1463-1470

[27] Robin-Jouan P, Yousfi M. New breakdown electric field calculation for SF_6 high voltage circuit breaker applications. Plasma Science and Technology. 2007;**9:**690

[28] Pannopard P, Khongpracha P, Probst M, Limtrakul J. Gas sensing properties of platinum derivatives of single-walled carbon nanotubes: A DFT analysis. Journal of Molecular Graphics and Modelling. 2009;**28:**62-69

[29] Bak S-M, Kim K-H, Lee C-W, Kim K-B. Mesoporous nickel/carbon nanotube hybrid material prepared by electroless deposition. Journal of Materials Chemistry. 2011;**21:**1984-1990

[30] Yu S, Yi W. Single-walled carbon nanotubes as a chemical sensor for SO_2 detection. IEEE Transactions on Nanotechnology. 2007;**6;**545-548

[31] Zhang X, Gui Y, Dai Z. A simulation of Pd-doped SWCNTs used to detect SF_6 decomposition components under partial discharge. Applied Surface Science. 2014;**315:**196-202

[32] Zhang X, Gui Y, Dai Z. Adsorption of gases from SF_6 decomposition on aluminum-doped SWCNTs: A density functional theory study. The European Physical Journal D. 2015;**69:**1-8

[33] Azizi K, Karimpanah M. Computational study of Al- or P-doped single-walled carbon nanotubes as NH_3 and NO_2 sensors. Applied Surface Science. 2013;**285:**102-109

[34] Zhang X, Chen Q, Tang J, et al. Adsorption of SF_6 decomposed gas on anatase (101) and (001) surfaces with oxygen defect: a density functional theory study [J]. Scientific Reports, 2014, **4**(4):4762.

[35] Zhang X, Chen Q, Hu W. Zhang J. A DFT study of SF_6 decomposed gas adsorption on an anatase (101) surface. Applied Surface Science. 2013;**286:**47-53

[36] Sammells AF, Schwartz M, Mackay RA, Barton TF, Peterson DR. Catalytic membrane reactors for spontaneous synthesis gas production. Catalysis Today. 2000;**56:**325-328

[37] Zhang X, Gui Y, Dai Z. A simulation of Pd-doped SWCNTs used to detect SF_6 decomposition components under partial discharge. Applied Surface Science. 2014;**315:**196-202

[38] Pan X, Cai Q-x, Chen W-l, Zhuang G-l, Li X-n, Wang J-g. A DFT study of gas molecules adsorption on the anatase (001) nanotube arrays. Computational Materials Science. 2013;**67:**174-181

[39] Reddy EL, Biju VM, Subrahmanyam C. Production of hydrogen from hydrogen sulfide assisted by dielectric barrier discharge. International Journal of Hydrogen Energy. 2012;**37:**2204-2209

[40] Mubeen S, Zhang T, Chartuprayoon N, et al. Sensitive Detection of H2S Using Gold Nanoparticle Decorated Single-Walled Carbon Nanotubes[J]. Analytical Chemistry, 2010, **82**(1):250-7.

[41] Sanderson RT. Electronegativity and bond energy. Journal of the American Chemical Society. 1983;**105:**2259-2261

[42] Casanovas AM, Casanovas J, Dubroca V, Lagarde F, Belarbi A. Optical detection of corona discharges in SF_6, CF_4, and SO_2 under dc and 50-Hz ac voltages. Journal of Applied Physics. 1991;**70:**1220-1226

[43] Kohn W, Becke AD, Parr RG. Density functional theory of electronic structure. The Journal of Physical Chemistry. 1996;**100:**12974-12980

[44] McNicholas TP, Zhao K, Yang C, Hernandez SC, Mulchandani A, Myung NV, Deshusses MA. Sensitive detection of elemental mercury vapor by gold-nanoparticle-decorated carbon nanotube sensors. The Journal of Physical Chemistry C. 2011;**115:**13927-13931

[45] Xiaoxing Z, Fansheng M, Zhen W, Jian L. Gas-sensing simulation of single-walled carbon nanotubes applied to detect gas decomposition products of SF_6 in PD. In: Electrical Insulation Conference (EIC), 2011, Vol. 2011, pp. 132-135

[46] Park Y, Lahaye RJWE, Lee YH. Adsorption of Pt on defective carbon nanotube walls: A DFT approach. Computer Physics Communications. 2007;**177**:46

[47] Pannopard P, Khongpracha P, Probst M, Limtrakul J. Gas sensing properties of platinum derivatives of single-walled carbon nanotubes: A DFT analysis. Journal of Molecular Graphics & Modelling. 2009;**28:**62-69

[48] Zhang X, Dai Z, Chen Q, Tang J. A DFT study of SO_2 and H_2S gas adsorption on Au-doped single-walled carbon nanotubes. Physica Scripta. 2014;**89:**065803

Chapter 3

Application of TiO_2 Nanotubes Gas Sensors in Online Monitoring of SF_6 Insulated Equipment

Ju Tang, Xiaoxing Zhang, Song Xiao and Fuping Zeng

Additional information is available at the end of the chapter

http://dx.doi.org/10.5772/intechopen.68328

Abstract

Titanium dioxide nanotube arrays (TNTAs) are a typical three-dimensional nanomaterial. TNTA has rich chemical and physical properties and low manufacturing costs. Thus, TNTA has broad application prospects. In recent years, research has shown that because of its large specific surface area and nanosize effect, the TNTAs have an enormous potential for development compared with other nanostructure forms in fields such as light catalysis, sensor, and solar batteries. TNTAs have become the hotspot of international nanometer material research. The tiny gas sensor made from TNTA has several advantages, such as fast response, high sensitivity, and small size. Several scholars in this field have achieved significant progress. As a sensitive material, TNTA is used to test O_2, NO_2, H_2, ethanol, and other gases. In this chapter, three SF_6 decomposed gases, namely SO_2, SOF_2 and SO_2F_2, are chosen as probe gases because they are the main by-products in the decomposition of SF_6 under PD. Then, the adsorption behaviors of these gases on different anatase (101) surfaces including intrinsic, Pt-doped and Au-doped, are studied using the first principles density functional theory (DFT) calculations. The simulation results can be used as supplement for gas-sensing experiments of TNTA gas sensors. This work is expected to add insights into the fundamental understanding of interactions between gases and TNTA surfaces for better sensor design.

Keywords: SF_6 decomposed gas, anatase TiO_2 surface, metal doping, adsorption, sensing mechanism, density functional theory

1. Introduction of titanium nanotubes

TiO_2 nanotubes are typically one-dimensional material, which has a wealth of physical and chemical properties and low production cost, and therefore, it bears a broad application

prospects [1, 2]. In particular, recent studies show that, due to large specific surface area and nanosize effect, compared with other forms of nanostructures, TiO_2 nanotubes show great potential for development in photocatalysis, sensors, solar cells and other areas [1, 3, 10]. It has become the research focus of nanomaterials internationally [1, 4–9]. The particular photocatalytic properties of TiO_2 under UV irradiation can degrade pollutants and reduce desorption time, thus extending the lifetime of sensors that based on TiO_2, which provides more opportunity for the development of high-quality new sensors.

1.1. Properties of titanium nanotubes

TiO_2 is one common type of N semiconductor oxide, of which the outer electron distribution is $3d^24s^2$. The molecular structure of TiO_2 belongs to flash zinc crystal lattice. Its structural center, Ti atom, is surrounded by six oxygen atoms, forming an octahedral structure which coordination number is 6. TiO_2 outer layer of 3d electronics is not active and 4 valence electrons of it form a covalent bond with O atom. From the above, we can know that the chemical properties of TiO_2 are very stable. It cannot dissolve in most acid, such as hydrochloric acid, nitric acid and dilute sulfuric acid, except concentrated sulfuric acid and hydrofluoric acid. The band gap of TiO_2 is approximately 3.2 eV. Its electrical conductivity is extremely low at room temperature. Even at high temperature, it only has a small conductivity. So its resistance is very big. We can almost see TiO_2 as an insulator. TiO_2's conductance is achieved by activating the exciting electrons on the additional energy level to the conduction band. The additional level can be introduced from defects and impurities in TiO_2. So the types and quantities of these defects and impurities determine the TiO_2 conductivity type. Therefore, some methods may be employed to form a certain type of defect and impurity level or defect levels in the band gap to change the conductive properties of TiO_2.

There are three TiO_2 polymorphs in nature: rutile, anatase and brookite. Anatase and rutile structures are most widely used. Although rutile and anatase TiO_2 crystalline belong to the same tetragonal, but they have two different lattices. And thus, the X-ray images are different.

Anatase TiO_2 XRD diffraction angle 2θ is located in 25.5°, and rutile TiO_2 XRD diffraction angle 2θ is located in 27.5°. Rutile TiO_2 crystal forms a titanium atom in the lattice center, surrounded by six oxygen atoms which are located in octahedral edges and corners, and a cell composed of two moleculars is the most stable crystal structure. Anatase TiO_2 crystal form is composed of four TiO_2 molecules in a crystal cell, which is stable at low temperature. When the temperature reaches 610°C, it gradually transforms into rutile, and its transformation accelerated rapidly at 730°C, and it can transform into rutile completely at 915°C. Plate titanium ore TiO_2 crystal form, belonging to orthorhombic system, is a cell composed of six TiO_2 moleculars, which is an unstable crystal form that transforms into rutile type when the temperature is higher than 650°C. **Figure 1** is the schematic diagram for the three kinds of morphology of crystalline structure of TiO_2.

Plate titanium ore crystal form belongs to the metastable phase, and thus its structure is unstable, which is therefore rarely used in industrial production. Anatase and rutile belong to the same crystal system, but the atomic arrangement of rutile is compact, so its relative density as

http://dx.doi.org/10.5772/intechopen.68328

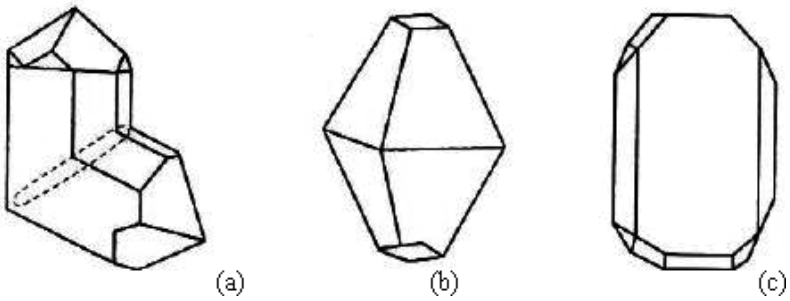

Figure 1. Morphology of crystalline structure of TiO_2 (a) rutile (b) anatase (c) brookite.

well as refractive index is larger, and it has very good properties of scattered light, as well as the shielding effect to UV light, while anatase, with good photocatalytic activity, has a wide application prospect in the aspects of environmental protection and electrochemical sensor.

1.2. Preparation method of titanium nanotubes

Currently, there are three types of the method for preparing TiO_2 nanotubes, namely chemical template method, electrochemical method and hydrothermal method.

1.2.1. Chemical template method

The chemical template method involves assembling nanostructured primitive units into the porous template that forms nanotube structure. In the process of preparation of TiO_2 nanotube template, first, a porous alumina is prepared by anodizing, which is used as a template later, and then impregnates titanium-containing compound into the template by sol-gel method. After turning titanium-containing compound that entered into the porous alumina template into the metal oxide that possesses a template with a similar pore diameter and morphology of nanotube structure by a high temperature annealing process, porous alumina template is then dissolved with concentrated alkali. Since the metal oxide is not dissolved in concentrated alkali, metal oxide nanotubes such as TiO_2 nanotubes can be obtained, which have similar pore morphology to porous alumina template after washing by water. Martin et al. [11–13] successfully prepared nanotubes of TiO_2, Co_3O_4, MnO_2, WO_3 and ZnO and other metal oxides using this method.

1.2.2. Electrochemical method (anodic oxidation method)

Anodic oxidation method uses metal as an anode. Under the influence of applied electric field and electrolyte solution, electrochemical oxidation of the metal appears. Thereby a metal oxide film is produced on the surface of a metal. The formed metal oxide film will gradually dissolve because of the chemical reaction caused by the response plasma in electrolyte solution. The regional of chemical dissolution of metal oxide film is in nanoscale level. Therefore, when the speed of producing metal oxide by electric film dissolution is larger than the rate of chemical

dissolution, the oxide film is ever thickening and accompanied by numerous nanopore deepening constantly caused by chemical dissolution. When the speed of producing metal oxide by electric film dissolution is equal to the rate of chemical dissolution, the thickness of the oxide film and the depth of the nanopores do not change. At this time, a certain thickness oxide film with a metal oxide nanotube structure is ready. With the controlling of the different experimental conditions in certain electrolyte, we can prepare TNTA with different diameters and lengths by anodizing. In 2001, Grimes [14] first reported that the TNTA with ordered arrangement can be obtained at room temperature after directly anodizing for pure titanium sheet in an HF aqueous solution. Grimes [10] studied the growth of the nanotubes changes under different conditions of the anodizing electrolyte. The length of the nanotubes can be increased when the electrolyte exhibits weak acid. In the case of organic phase electrolyte, the tube walls are smoother and the tube length can also reach about a hundred micrometers.

1.2.3. Hydrothermal method

Since the hydrothermal preparation method is simple and cheap, it is widely used in industrial production processes. TiO_2 nanotubes prepared by this way are typically entwined and disorderly: first preparing TiO_2 nanoparticles, and then mixing the nanoparticles with strong alkaline solution. Under conditions of high temperature and pressure, monolayer nanosheets curl of TiO_2 in the alkali solution appears. Its formation mechanism is similar to that of multi-walled carbon nanotubes; it is a combination process from one-dimensional to two-dimensional and three-dimensional. After forming the TiO_2 nanotubes, the product is neutralized by weak acid to neutralize the strong alkaline solution, and centrifuging it to get powdery TiO_2 nanotubes. Using this method, Kasu's team processed the TiO_2 nanoparticles powder and NaOH solution at 110°C, then washed the reactants with water and hydrochloric acid and finally get TiO_2 nanotubes [15].

2. Intrinsic and surface-modified TiO_2 nanotubes gas sensors

2.1. Intrinsic TiO_2 nanotubes gas sensors

2.1.1. Investigation of gas-sensing simulation of intrinsic TiO_2 nanotubes

Three SF_6 decomposed gases, namely SO_2, SOF_2, and SO_2F_2, are chosen as probe gases because they are the main by-products in the decomposition of SF_6 under PD. The adsorption behaviors of these gases on an anatase (101) surface are studied using the first principles density functional theory (DFT) calculations.

2.1.1.1. Adsorption models and calculation methods

The optimal lattice size of bulk anatase given in MS is 3.776 × 3.776 × 9.486 $Å^3$, which is very small compared with the size of a single TiO_2 nanotube. Thus, the gas molecules adsorbed in a small area of the TNTAs surface are simulated, and the nanotube-array structure is not taken into account. The prepared TNTAs are calcined at a high temperature in an oxygen-rich

environment, and oxygen atoms should occupy the oxygen vacancies on the TNTAs surface [16]. The phenomenon is consistent with the findings that many thermodynamically stable (101) facets dominate the surface of most anatase nanocrystals [17]. Therefore, the gas-array interaction can be properly simulated on the anatase (101) surface.

Periodic boundary model is adopted in this work, and the 2 × 2 supercell of the anatase (101) surface is created in MS, as shown in **Figure 2**. The size of the supercell is 10.88 × 7.55 × 17.84 $Å^3$. In order to avoid the interaction between adjacent cells which is induced by the periodic boundary condition, the vacuum layer above surface is about 12 Å. The atoms on the bottom layer are fixed, and the structure of the supercell is optimized.

The generalized gradient approximation (GGA) exchange-correlation function parameterized by Perdew, Burke, and Ernzerhof [18] is employed for the electron-electron exchange and correlation interactions. Moreover, the double numerical basis set plus polarization functions (DNP) [19, 20] are used. All optimized structures are obtained with a precision of 1×10^{-5} Ha for energy, 2×10^{-3} Ha/Å for force, and 5×10^{-3} Å for displacement, the convergence threshold for the electronic self-consistent field is set to 1×10^{-6} Ha. A Fermi smearing of 5×10^{-4} Ha is used. To speed up the convergence and reduce calculation time, the DIIS (direct inversion in an iterative subspace) is used at the same time. The Brillouin zone is sampled at 2 × 3 × 1 *k*-mesh [21]. All spin-unrestricted DFT calculations are performed using the Dmol^3 package [19, 20].

The band gap is 2.16 eV, which is closer to other simulation results [22, 23] but smaller than the experimental gap (3.24 eV [24]). The reason for this is the well-known deficiency of the GGA arithmetic [25] in which DFT maps the problem of N interacting electrons onto a system of N non-interacting fictitious particles. Therefore, the calculation scheme is effective, and the results and conclusions are reasonably reliable.

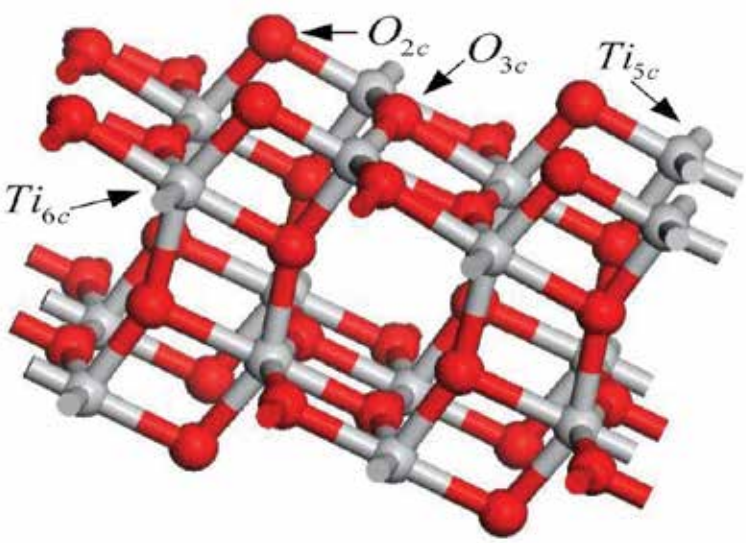

Figure 2. 2 × 2 supercell of the anatase (101) surface.

The active atoms of the anatase (101) surface are Ti_{5c} and O_{2c}, as shown in **Figure 2**. **Figure 3** shows band structure of the optimized supercell. To find the most stable adsorption structures, the three gas molecules should approach the active atoms on the surface in different orientations and behaviors. **Figure 4** shows the most stable adsorption structures of the three gas molecules.

2.1.1.2. Adsorption parameters and analysis

The gas-surface interaction can be described using the adsorption energy E_{ad} defined as $E_{ad} = E_{surf/gas} - E_{gas} - E_{surf}$, where E_{gas} is the energy of one isolated gas molecule in its optimized structure, E_{surf} is the total energy of the TiO_2 structure, and $E_{surf/gas}$ is the total energy of the adsorption structure [1]. $E_{ad} < 0$ means that the adsorption process is exothermic and spontaneous.

The change in charge distribution should be known. Therefore, the charge transfer q is calculated using the Mulliken population analysis and is defined as the charge variation of isolated gas molecules when it is adsorbed [1]. A positive q value means that the charge is transferred from the molecule to the anatase surface. The binding distance d is defined as the nearest distance between the molecule and the surface. The calculated adsorption parameters are shown in **Table 1**.

The adsorption energies are negative, indicating that the adsorptions are exothermic and spontaneous. The values of energy released in the adsorptions are $SO_2 > SOF_2 > SO_2F_2$, and all are small (<0.6 eV). This finding indicates that the molecules of the three gases are physisorbed, not chemisorbed, on the anatase (101) surface. Thus, gas molecules cannot effectively be adsorbed

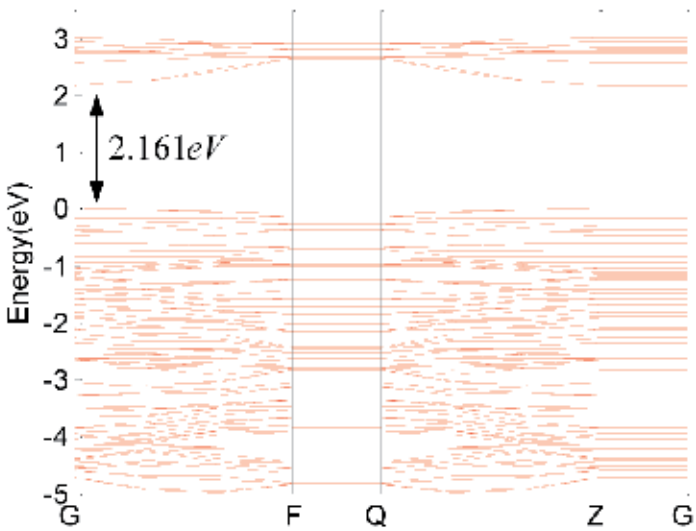

Figure 3. Band structure of the optimized supercell.

http://dx.doi.org/10.5772/intechopen.68328

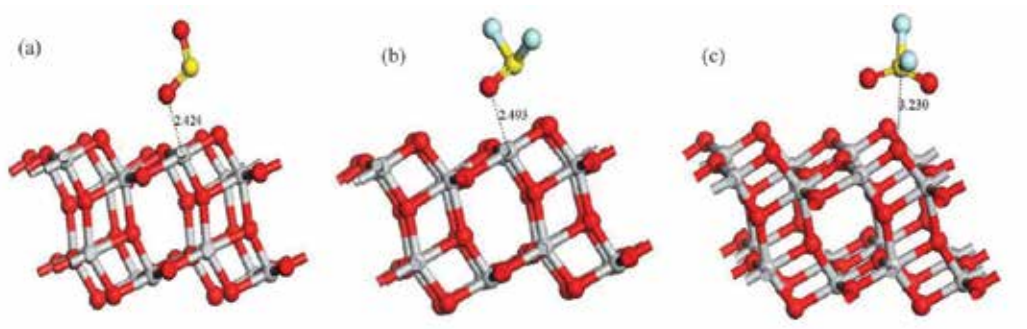

Figure 4. Optimized geometric structures of (a) SO_2, (b) SOF_2, and (c) SO_2F_2 adsorbed on the anatase (101) surface. Ti and O atoms are in gray and red, respectively. Binding distances are in Å.

System	Structure	E_{ad}/eV	q/e	d/Å
SO_2	a	−0.343	0.094	2.424
SOF_2	b	−0.275	0.043	2.493
SO_2F_2	c	−0.186	0.008	3.230

Table 1. Calculated adsorption energy, charge transfer, and binding distance.

on TNTAs at room temperature because of the small adsorption energy, indicating that the experimental responses of the three gases may also be very small at room temperature. When the temperature is high, the Ti_{5c}-O_{2c} bonds will be stretched with the increased temperature, and the interactions between the molecules and surface become stronger. Under this condition, the molecules can be chemisorbed on the surface, which can explain the high responses in the sensing experiment. The adsorption energy of SO_2 is the largest of the three gases, which shows that the adsorption of SO_2 is the strongest; it is firmly absorbed and difficult to desorb.

The three gases all behave as charge donors. The charge transfer of SO_2 is more than twice than that of SOF_2, and for SO_2F_2, it is only 0.008 e. This finding indicates that SO_2 can provide more electrons to the surface and that the surface has a better sensitivity to SO_2.

The highest occupied molecular orbital (HOMO) energy level and lowest unoccupied molecular orbital (LUMO) energy level of the three gas molecules and of the anatase (101) surface are calculated according to molecular orbital theory. By analyzing the HOMO and LUMO, whether the gases easily interact with the anatase (101), surface can be estimated. E_1 and E_2 are defined as follows:

$$\begin{aligned} E_1 &= \left| E_{HOMO(TiO_2)} - E_{LUMO(gas)} \right| \\ E_2 &= \left| E_{LUMO(TiO_2)} - E_{HOMO(gas)} \right| \end{aligned} \tag{1}$$

If E_1 is small, the charge is more easily transferred to the gas molecules from the surface. If E_2 is small, the charge is more easily transferred to the surface from the gas molecules. The calculated E_{HOMO}, E_{LUMO}, E_1, and E_2 are listed in **Table 2**.

System	E_{HOMO}/eV	E_{LUMO}/eV	E_1/eV	E_2/eV
TiO_2	−7.257	−5.093	/	/
SO_2	−8.000	−4.669	2.587	2.917
SOF_2	−8.536	−3.072	4.185	3.453
SO_2F_2	−9.145	−2.628	4.628	4.062

Table 2. Energy frontier molecular orbital and the energy difference.

Both the E_1 and E_2 of SO_2 are smaller than those of the other two gases. This finding shows that SO_2 easily interacts with the anatase (101) surface and that the charge transfer is also the easiest between them. SO_2F_2 interacting with the surface is relatively difficult. Here, we also find that the anatase (101) surface is more sensitive to SO_2 than to SOF_2, and the sensitivity of the surface to SOF_2 is better than that to SO_2F_2.

The energy gap of the adsorption structure can be calculated through the energy levels of the HOMO and LUMO defined as E_g:

$$E_g = \left| E_{HOMO} - E_{LUMO} \right| \tag{2}$$

The energy gap width determines how much energy an electron needs to jump into the LUMO from the HUMO. The wider the gap, the more energy is required and the more difficult it is for electrons to transfer between the valence band (VB) and the conduction band (CB). **Table 3** shows the energy gaps. The adsorption of SO_2 on the anatase (101) surface reduces the energy gap width and improves the electron transfer of the surface. However, the adsorption of SOF_2 and SO_2F_2 cannot do so. Therefore, TNTAs are much more responsive to SO_2 gas than to SOF_2 and SO_2F_2.

The molecular structures of the gases are also analyzed based on valence bond theory (VBT) combined with molecular orbital theory. A three-center four-electron pi bond exists in the SO_2 molecule, and the pi bond contains five orbitals that are hybridized by a 3p orbital, two 3d orbitals in the S atom, and a 3p orbital in each O atom. This finding indicates that the pi bond consists of some 3d orbitals. Four electrons occupy the two lower orbitals (i.e., HOMO and HOMO-1) of the pi bond, and the middle orbital of the pi bond is unoccupied (LUMO). However, the d-p pi bond exists between the S atom and the O atom in the SOF_2 and SO_2F_2 molecules. The S atom in SOF_2 has one lone pair of electrons, but not the SO_2F_2. Therefore, the

System	E_{HOMO}/eV	E_{LUMO}/eV	E_g/eV
TiO_2	−7.257	−5.093	2.164
TiO_2-SO_2	−7.134	−5.607	1.527
TiO_2-SOF_2	−7.208	−5.053	2.155
TiO_2-SO_2F_2	−7.204	−5.047	2.156

Table 3. Energy gaps of the adsorption structures and structures without adsorption.

SO_2F_2 molecule is more stable than the SOF_2 molecule. Moreover, the activities of the gas molecules can be compared by obtaining the difference between E_{HOMO} and E_{LUMO}. **Table 4** shows ΔE, which is defined as $\Delta E = E_{LUMO\ (gas)} - E_{HOMO\ (gas)}$. Based on the VBT analysis and the data in **Table 4**, the pi bond in SO_2 is more active than the d-p pi bond in SOF_2 and SO_2F_2. Moreover, SO_2 is easy to interact with the anatase (101) surface.

To investigate the influence of adsorbed gas molecules on the electronic property of the anatase (101) surface, the total density of states (TDOS) of the adsorption system and the projected density of states (PDOS) of adsorbed gas molecules calculated using MS are given in **Figure 5**. The Fermi level is aligned at zero. As shown in **Figure 5**, when the molecules of the three gases are adsorbed on the surface, the Fermi levels of those still on top of the VB change little. This finding indicates the formation of a depletion region on the surface, and only a few charge carriers are present in this region. Therefore, the surface presents high resistivity.

The TODSs of the SOF_2 and SO_2F_2 adsorption systems remain nearly unchanged compared with the system without adsorption, which indicates that the adsorbed SOF_2 and SO_2F_2 induce little change to the electronic property of the (101) surface. An unapparent density peak of around 2.8 eV exists in the PDOS of SOF_2. On the other hand, the adsorbed SO_2 induces noticeable change to the electronic property of the (101) surface. The SO_2 adsorption introduces an impurity state near the CB, as shown in **Figure 6**, resulting in a narrowing of the band gap (which changes from 2.161 to 1.527 eV). The unoccupied impurity state is a surface state of the anatase (101) surface, which can capture or release electrons or form a composite center, improving the conductive performance of the surface. The PDOSs of p orbitals that contribute to the impurity state and the orbitals that contain the 3p orbital of the S atom and the 2p orbital of the O atom (near the surface in **Figure 4**) are shown in **Figure 7**.

2.1.2. Preparation and surface characterization of intrinsic TiO_2 nanotubes

The present study generated a TNTA by an anodic oxidation method using a two-electrode system [1]. A platinum metal piece was used as cathode, whereas a titanium piece was used as anode. The experimental processes are as follows: first, 0.5-mm-thick Ti foil (area of 0.8 cm × 2.0 cm and purity of 99.94%) was burnished with sandpaper, soaked in 30% HCl solution, and heated to 80°C for 20 min to remove the surface oxidation layer [1]. Then, the Ti pieces were cleaned by washing with deionized water. The clean Ti pieces acted as the anode, whereas the platinum pieces acted as the cathode in the two-electrode electrochemical electrolysis pool. Between the two electrodes, a constant 20 V of anodic oxidation was applied continuously for 2 h. The electrolyte concentration was 0.1 M HF solution, and the electrolyte pH value was tested using a Model 3000 pH meter [1]. Magnetic stirring was applied to ensure the uniformity of the Ti electrode surface electric current and temperature in the oxidation process and

Gas	**SO_2**	**SOF_2**	**SO_2F_2**
ΔE/eV	3.330	5.464	6.517

Table 4. Difference between HOMO and LUMO.

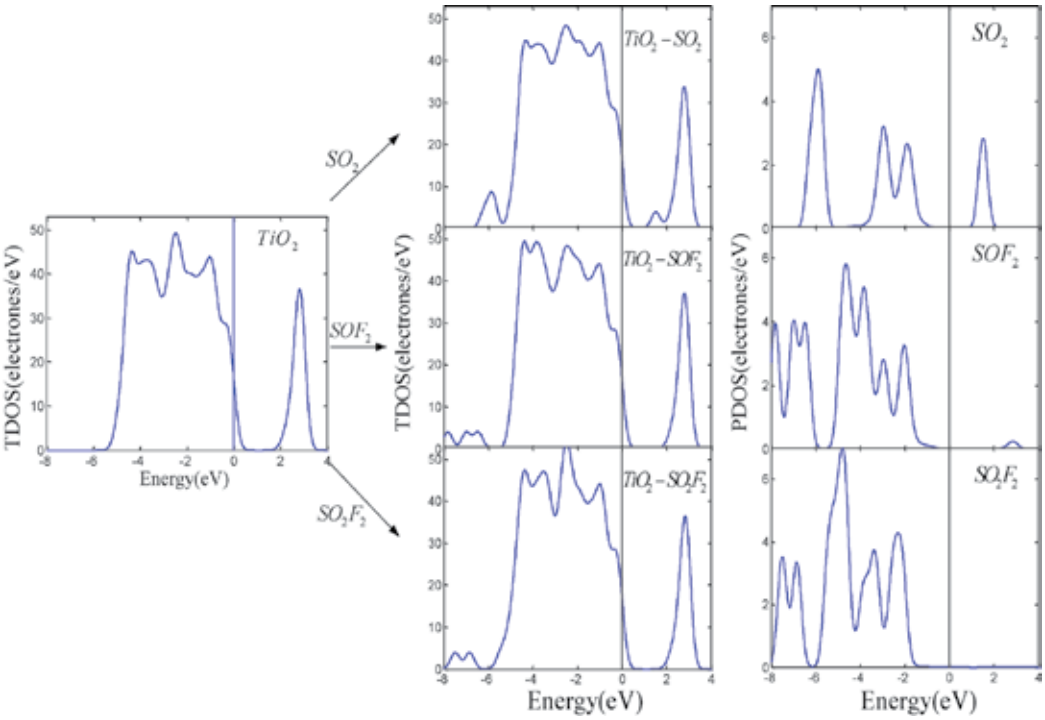

Figure 5. The TDOS of adsorption systems and the PDOS of adsorbed gas molecules.

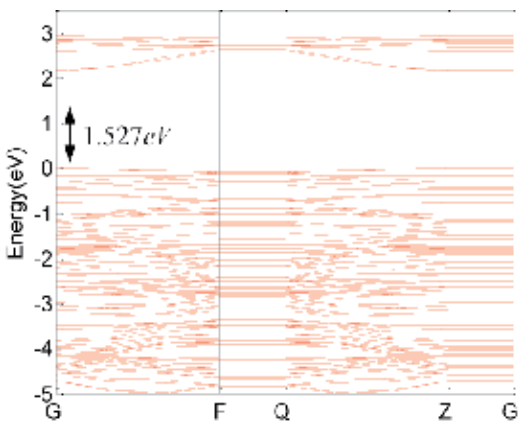

Figure 6. Band structure of the TiO_2-SO_2 adsorption system.

reduce the influence of the double electric layer between the electrolyte and electrode interface [1]. After the reaction, the TNTA was cleaned by washing with deionized water, dried in air heated from 2°C/min to 500°C in a muffle furnace for 1 h, and then removed after the temperature dropped to room temperature [1].

http://dx.doi.org/10.5772/intechopen.68328

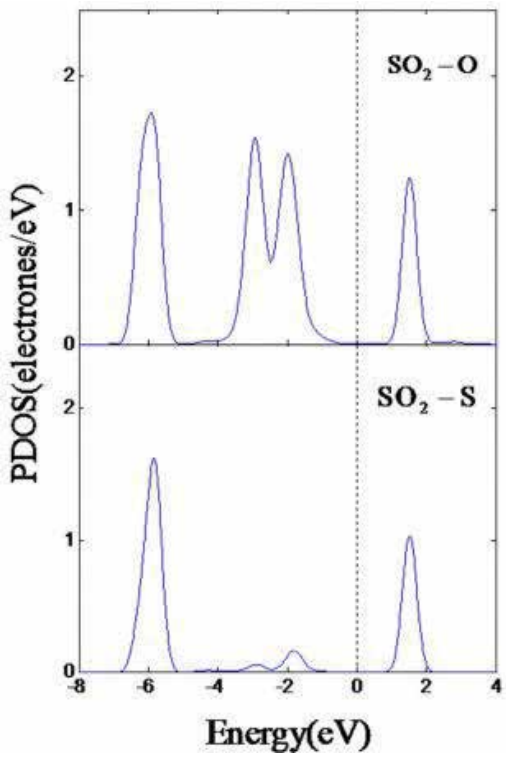

Figure 7. PDOS of the p orbitals of impurity state.

Figure 8 shows the scanning electron microscopy (SEM) images of the TNTAs. As observed from the SEM images, the TNTAs are highly ordered and directionally grown, the pipe diameter of which is about 80 nm, length is about 300 nm, and thickness is about 10 nm. The main effect of having an ordered structure is to further improve the area's effective adsorption area. The schematic diagram of TNTAs is shown in **Figure 9**.

Figure 10 shows the X-ray diffraction spectrum diagram of the TNTAs. The strong (101) facet peak of anatase (A in the figure) exists at $2\theta = 25.3°$, and the weak strong (110) facet peak of rutile exists at $2\theta = 27.4°$ (R in the figure). These findings indicate that TNTAs are mainly anatase, and a small amount of the rutile phase is observed.

2.1.2.1. Gas-sensing experiments of intrinsic TiO_2 nanotubes sensors

Figure 11 presents the detection test device for the TNTA sensor response measurement of the SF_6 decomposition products [1]. Shown in the figure are the following: (1) quartz glass tube; (2) thermal resistance probe; (3) carbon nanotube sensors; (4) ceramic heating slices; (5) vacuum form; (6) vacuum pump; (7) vent ducts; (8) terminals; (9) AC regulator; (10) temperature display apparatus; (11) impedance analyzer; (12) gas flow meter; and (13) inlet ducts [1].

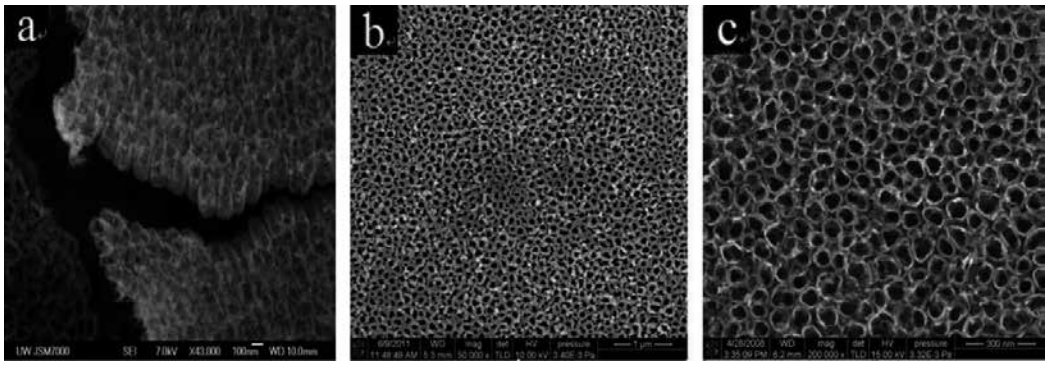

Figure 8. SEM images of TNTAs: (a) side view, (b) front view, (c) front amplification view.

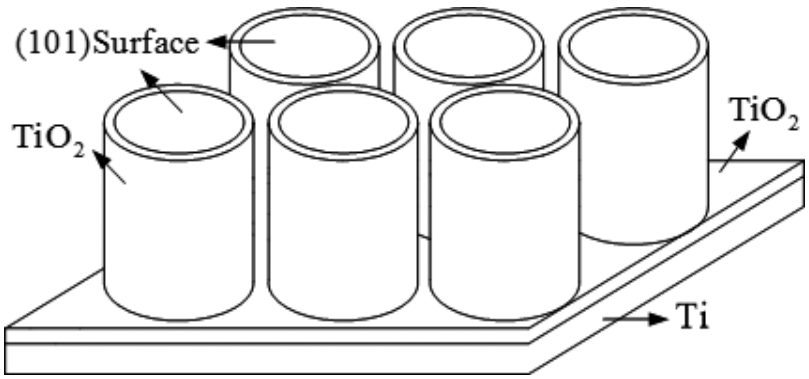

Figure 9. Schematic diagram of TNTAs.

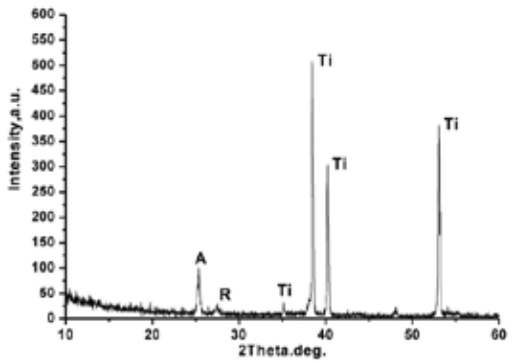

Figure 10. X-ray diffraction pattern of TNTAs.

The tested gases are SO_2, SOF_2, and SO_2F_2, which have a concentration of 50 μL/L, and N_2 is used as the carrier gas [26]. The response R% is defined as the relative variation of the sensor's resistance: $(R_g - R_0)/R_0$, where R_g is the resistance of the sensor to the relevant gas, and R_0 is pure

http://dx.doi.org/10.5772/intechopen.68328

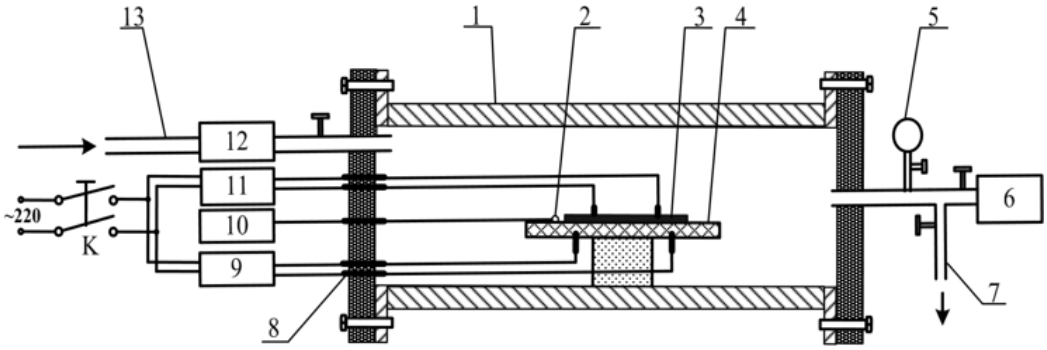

Figure 11. Detection test device for the TNTA sensor response measurement of SF_6 decomposition products.

N_2 [26]. The factors that influenced the response are analyzed comparatively, and the sensing mechanism of the temperature characteristic curves is explained based on the simulation results.

The responses of TNTAs to the 50 μL/L gases are shown in **Figure 12**. At 20°C, the response of SO_2 is slightly higher than that of SOF_2 and SO_2F_2, and the responses of SOF_2 and SO_2F_2 are both small. When the temperature is above 120°C, the response of SO_2 is much higher than that of the two gases. The response of SOF_2 is slightly higher than that of SO_2F_2. This phenomenon matches the simulated findings. Therefore, the study concludes that the response *R*% depends on the impurity state introduced by the adsorbed gas molecule, and the band structure influences by the impurity state.

The sensing mechanism of temperature characteristic curves is analyzed first.

When the temperature is low, the adsorbed gas molecules can provide a number of electrons to the semiconductor surface or reduce the band gap of the semiconductor; the thermal excita-

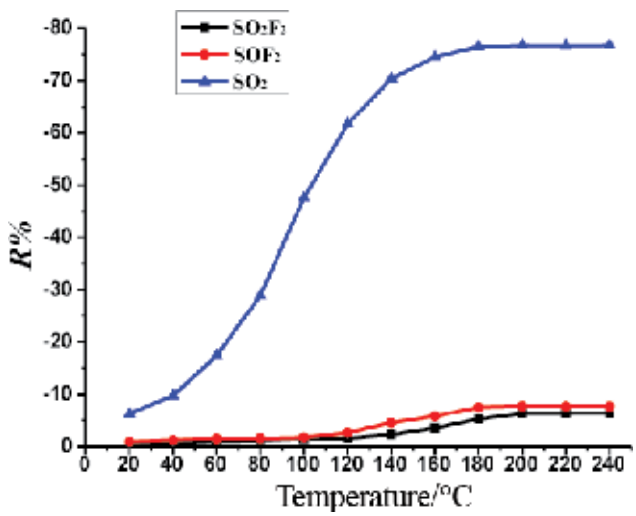

Figure 12. Temperature characteristic curves of the responses of 50 μL/L gases.

tion of the semiconductor remains weak. The electron depletion region of the surface remains, and the electron concentration variation is small. All sensing responses are low when the temperature is low. Conversely, when the temperature increases, thermal excitation begins to play a main role, and more electrons in the valence band exit to the conduction band, producing more hole electron pairs and greatly increasing the electron concentration. The adsorption of the three gases then provides electrons onto the semiconductor surface, introduces the impurity states, and reduces the band gap. Thus, more excited electrons enter into the CB from the VB, and their sensing response becomes higher.

The reason for the changes in the temperature characteristic response of SO_2, as shown in the curve in **Figure 12**, is discussed. The gas response at a high temperature is positively related to the concentration of thermally excited electrons and the adsorption amount of gas molecules. The adsorption amount increases when the temperature increases. However, if the temperature is too high, the thermal motions of the gas molecules become aggressive and a number of adsorbed gas molecules break away from the surface, decreasing the adsorption amount. The electrons produced by thermal excitation grow exponentially with the increasing temperature. Thus, the temperature characteristic response increases with the increasing temperature at first and then remains nearly unchanged.

The responses of SO_2 and SOF_2 are then compared. When the temperature is about 200°C, the response of SOF_2 is much lower than that of SO_2, and it is not sensitive to the varying temperature. The impurity state introduced by SO_2 has a great impact on the band structure and the SO_2 has a higher response because the impurity state introduced by SOF_2 has little effect on the band structure. The thermal excitation is weak, and only a few electrons are exit to the CB through the impurity states under 20°C. Therefore, the impurity states of SO_2 and SOF_2 have little effect on the band structure. However, TSO_2 provides more electrons to the surface, and the response of SO_2 is slightly high.

Finally, the responses of SOF_2 and SO_2F_2 are compared. SOF_2 provides more electrons to the surface than SO_2F_2, but the responses of the two gases are both small because the impurity states induced by the two adsorbed gases have little influence on the band structure. The electron depletion region on the surface also influences the low responses. Considering the comparative analysis of SO_2 and SOF_2, it can be concluded that, if the impurity state introduced by adsorbed gas has a greater impact on the band structure, the electrons provided by adsorbed gas will have a relatively large influence on the response at low temperatures.

When the temperature is high, the response of SOF_2 is slightly higher than that of SO_2F_2. The unapparent density peak around 2.8 eV in the PDOS of SOF_2 has a certain effect on the band structure, and some electrons in the VB exit to the CB, which promotes the response.

The difference between the responses to 50 μL/L SOF_2 and SO_2F_2 is not obvious in **Figure 12**; thus, we discuss the concentration response curves of SOF_2 and SO_2F_2 at 200°C in **Figure 13**. In **Figure 13**, with increased concentration, the increase in SO_2F_2 response is relatively larger than that of the SOF_2 response because the impurity state introduced by the increase in SOF_2 has a greater impact on the band structure.

http://dx.doi.org/10.5772/intechopen.68328

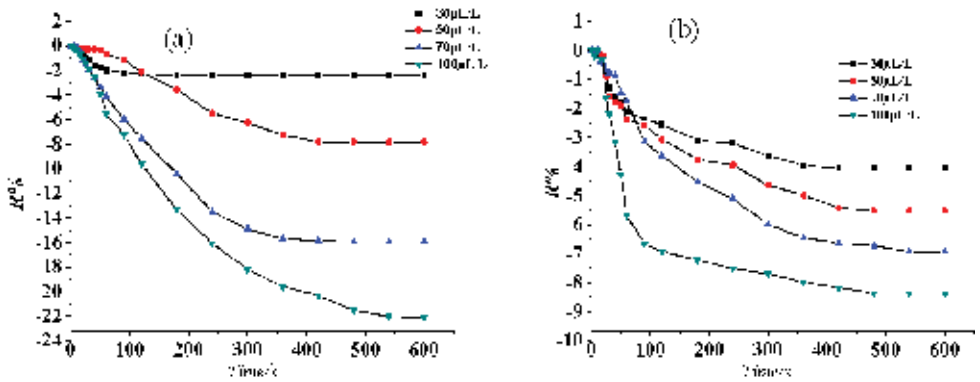

Figure 13. Response curves of SOF_2 (a) and SO_2F_2 (b) when the concentration varies at 200°C.

2.2. Pt-doped TiO_2 nanotubes sensors

The adsorptions of SO_2, SOF_2, and SO_2F_2 on Pt-modified anatase (101) surface are calculated, the effect of modified Pt on the adsorption behavior of gas molecules is analyzed, and the sensing mechanism of Pt-modified TNTA is also explained clearly [27]. In this study, we improve the sensing mechanism of Pt-modified TNTA and provide a theoretical basis for the detection of SF_6 decomposition components using the TNTA gas sensor [1, 28].

2.2.1. Investigation of gas-sensing simulation of Pt-doped TiO_2 nanotubes

2.2.1.1. Adsorption models and calculation methods

Figure 14 shows the adsorption structures of SO_2, SOF_2, and SO_2F_2 on the perfect (101) surface of Pt-modified anatase [1]. The adsorption parameters are shown in **Table 5**. Comparing the parameters in **Table 5** [1] with the parameters in references [29, 30], we observed that the modified

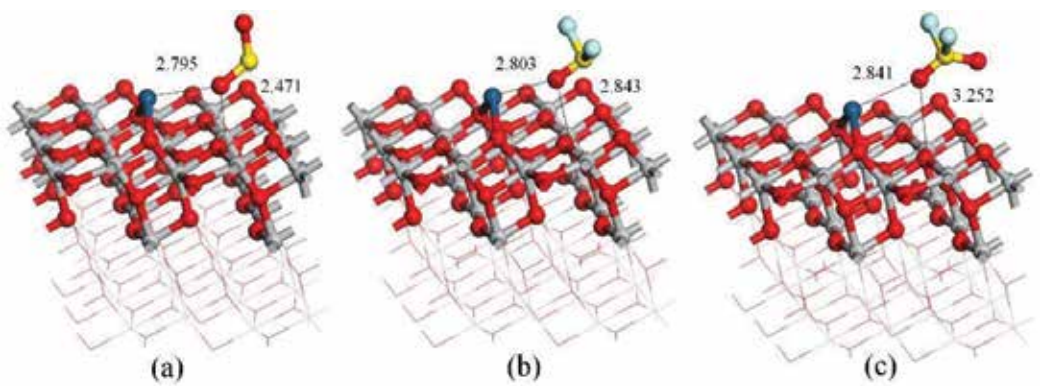

Figure 14. Adsorption structures of SO_2, SOF_2, and SO_2F_2 on the perfect (101) surface of Pt-modified anatase.

Adsorption site	Structure	Adsorption energy	Charge transfer	Bond distance
Perfect surface of the Pt-modified anatase surface	SO_2–TiO_2(a)	−0.3606	0.0920	2.471
	SOF_2–TiO_2(b)	−0.2811	0.0470	2.803
	SO_2F_2–TiO_2(c)	−0.0692	0.0110	2.841

Table 5. Adsorption parameters of the three gases adsorbed on the perfect (101) surface of Pt-modified anatase.

Pt atom has a slight influence on the adsorptions of the three gases on the perfect surface near the Pt atom [1]. The energy values of the three gases adsorbed on the anatase perfect surface are all still <0.6 eV. The charges in the adsorptions are still transferred from the molecules to the surface, which reveals that the three adsorptions are physisorptions [1]. This finding indicates that the adsorption performance of the perfect (101) surface of the Pt-modified anatase to the three gases is nearly unchanged [1]. **Figure 15** shows the DOS of the three adsorption structures [1]. We observed that the DOS is also nearly unchanged, and the state density near the Fermi level is mainly determined by the modified Pt atom. However, when the three gas molecules adsorb on the perfect (101) surface of the Pt-modified anatase, the conductivity of the surface is improved [1, 29].

2.2.1.2. Adsorption parameters and analysis

Figure 16 shows the adsorption structures of SO_2, SOF_2, and SO_2F_2 on the modified Pt atom [1]. The adsorption parameters are shown in **Table 6** [1]. When SO_2 is adsorbed, two situations, which depend on the initial structure, occur. One is the physisorption structure shown

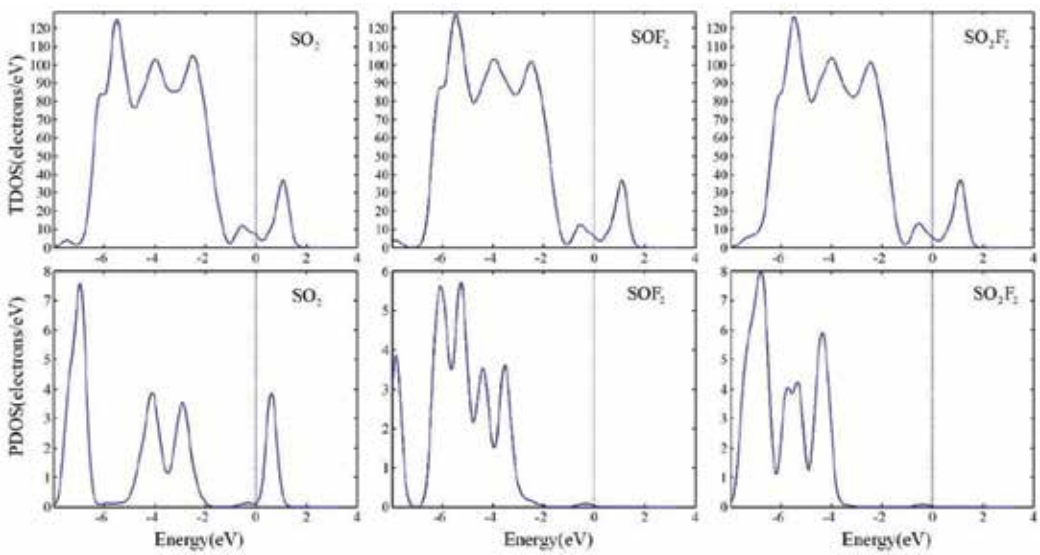

Figure 15. TDOSs of the adsorption structures of SO_2, SOF_2, and SO_2F_2 on the perfect (101) surface of Pt-modified anatase and PDOSs of the three gases in these structures.

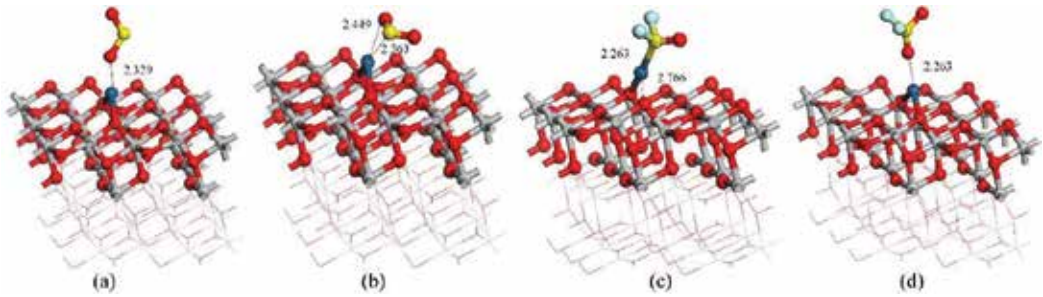

Figure 16. Adsorption structures of SO_2, SOF_2, and SO_2F_2 on the modified Pt atom of Pt-modified anatase.

in **Figure 16a** whose adsorption energy is −0.2394 eV. The other is the chemisorption structure shown in **Figure 16b** whose adsorption energy is −1.1009 eV. When SOF_2 is adsorbed, the physisorption and chemisorption situations occur. The chemisorption structure is shown in **Figure 16c** The Pt atom has a stronger adsorption to the S atom in SOF_2 than the O or F atom [1]. Thus, the SOF_2 molecule is more easily chemisorbed on the Pt atom with the S atom, rather than physisorbed with the O or F atom [1].

When SO_2F_2 is adsorbed, the adsorptions are mainly physisorptions, such as the structure shown in **Figure 16d** In addition, in a few initial structures, one S–F bond of SO_2F_2 may break and SO_2F_2 would be chemisorbed on the Pt atom. **Figure 17** shows the DOS of the three gases adsorbed on the Pt atom [1]. The adsorbed gas molecules contributed to the state density near the Fermi level, which changes the electronic distribution of the area around the modified Pt atom and influences the conductivity of this area [1].

Considering that the actual size of the modified Pt nanoparticle is larger than a single gas atom, and the conductivity of the nanoparticle is good and stable, we assume that the adsorptions of the gas molecules on the surface of the nanoparticle have a slight influence on the conductivity of the nanoparticle [1]. The main effect of the nanoparticle is the catalytic decomposition of some gas molecules [1]. We also calculated the adsorptions of SO_2, SOF_2, and SO_2F_2 on the Pt (200) surface to verify this finding. The adsorption structures are shown in **Figure 18** [1]. In **Figure 18a** and **b** [1], we observed that SO_2 and SOF_2 form stable adsorption structures on the Pt (200) surface with the S atoms, which are similar to the structures on the single Pt atom of the anatase (101) surface. **Figure 18c** [1] is the stable adsorption structure of SO_2F_2 on the Pt (200) surface, which is different from the structure shown in **Figure 17d** [1], in that one

Adsorption site	Structure	Adsorption energy	Charge transfer	Bond distance
Adsorbed on the modified Pt atom	SO_2–TiO_2(a)	−0.2394	−0.115	2.329
	SO_2–TiO_2(b)	−1.1009	−0.292	2.363
	SOF_2–TiO_2(c)	−0.9416	−0.075	2.263
	SO_2F_2–TiO_2(d)	−0.0630	0.020	2.425

Table 6. Adsorption parameters of the three gases adsorbed on the modified Pt atom of Pt-modified anatase.

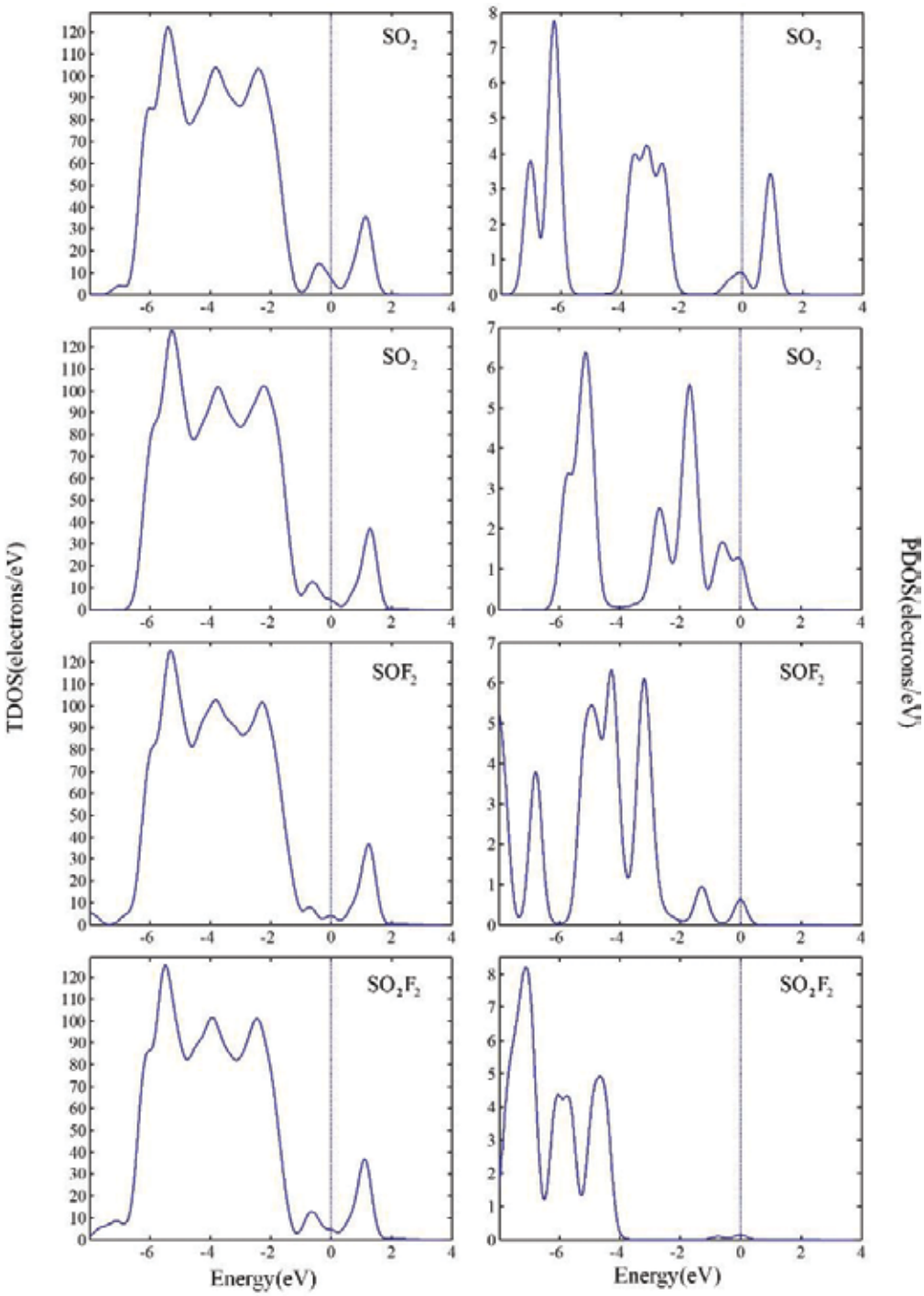

Figure 17. TDOSs of the adsorption structures of SO_2, SOF_2, and SO_2F_2 on the modified Pt atom of Pt-modified anatase and PDOSs of the three gases in these structures.

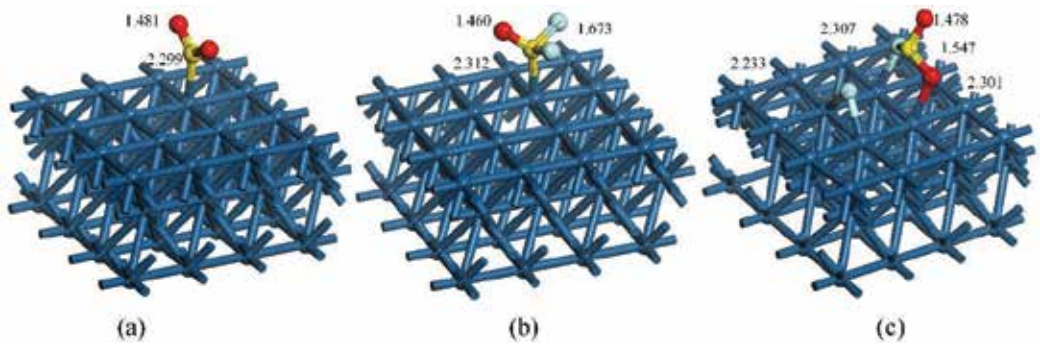

Figure 18. Adsorption structures of SO_2, SOF_2, and SO_2F_2 on the Pt (200) surface.

S–F bond of SO_2F_2 breaks, as shown in **Figure 18c** [1], and SO_2F_2 is chemisorbed on the Pt (200) surface. The Pt (200) surface supplies more electrons than a single Pt atom of the anatase (101) surface and the S–F bond more easily breaks. Thus, we conclude that, when adsorbed on the Pt nanoparticles of the TNTA surface, the SO_2F_2 gas molecules are more easily catalytically decomposed by the Pt nanoparticles than the SOF_2 molecules.

Figure 19 [1] shows the adsorption structures of SO_2, SOF_2, and SO_2F_2 on Pt and anatase. The adsorption parameters are shown in **Table 7**. From **Table 7** [1], we observed that the values of the adsorption energies of the three gases adsorbed on this site are relatively large, which indicates chemisorption [1]. The adsorption energy of SO_2F_2 is the largest and that of SOF_2 is the smallest. When SO_2 is adsorbed, the S atom of the SO_2 molecule bonds with the Pt atom, and one O atom of the SO_2 molecule bonds with the titanium (Ti) atom, as shown in **Figure 19a** [1]. When SOF_2 is adsorbed, the S atom of the SO_2 molecule also bonds with the Pt atom and one O atom of the SO_2 molecule bonds with the Ti atom, as shown in **Figure 19b** [1]. When SO_2F_2 is adsorbed, one S–F bond of SO_2F_2 breaks down. The S and F atoms bond with the Pt atom, with one O atom of the SO_2F_2 molecule bonding with the Ti atom, as shown in **Figure 19c**.

Figure 20 [1] shows the DOS of the three gases adsorbed on Pt and anatase. We observed that the adsorbed gas molecules contributed to the state density near the Fermi level, which also changes the electronic distribution of the area around this adsorption site. Considering the actual effect of Pt nanoparticles, we assume that this adsorption site is more active and the adsorptions of gas molecules on this site effectively connects the Pt nanoparticle surface and the anatase (101) surface, which may improve the conductivity performance of this area [1].

2.2.2. Preparation and surface characterization of Pt-doped TiO_2 nanotubes

The Pt-doped TiO_2NTs based on intrinsic TiO_2NTs were prepared using constant current method to deposit the Pt nanoparticles onto the TiO_2NT surface. Intrinsic TiO_2NTs were prepared through anodic oxidation [31], and a conventional three-electrode system with constant potential method is used to dope Pt nanoparticles into TiO_2NTs. In the three-electrode system, the intrinsic TiO_2NTs serve as the working electrode with a geometric area of 4.0 cm^2. The

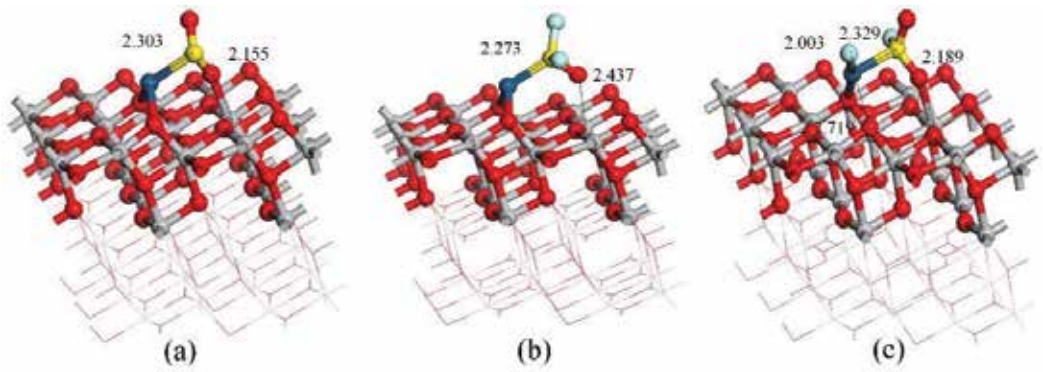

Figure 19. Adsorption structures of SO_2, SOF_2, and SO_2F_2 on both Pt and anatase.

Adsorption site	Structure	Adsorption energy	Charge transfer	Bond distance
Adsorbed on Pt and anatase	SO_2–Pt–TiO_2(a)	−1.4215	−0.2700	2.155
	SOF_2–Pt–TiO_2(b)	−0.8405	−0.1930	2.273
	SO_2F_2–Pt–TiO_2(c)	−1.6862	−0.7110	2.003

Table 7. Adsorption parameters of the three gases adsorbed on both of Pt and anatase.

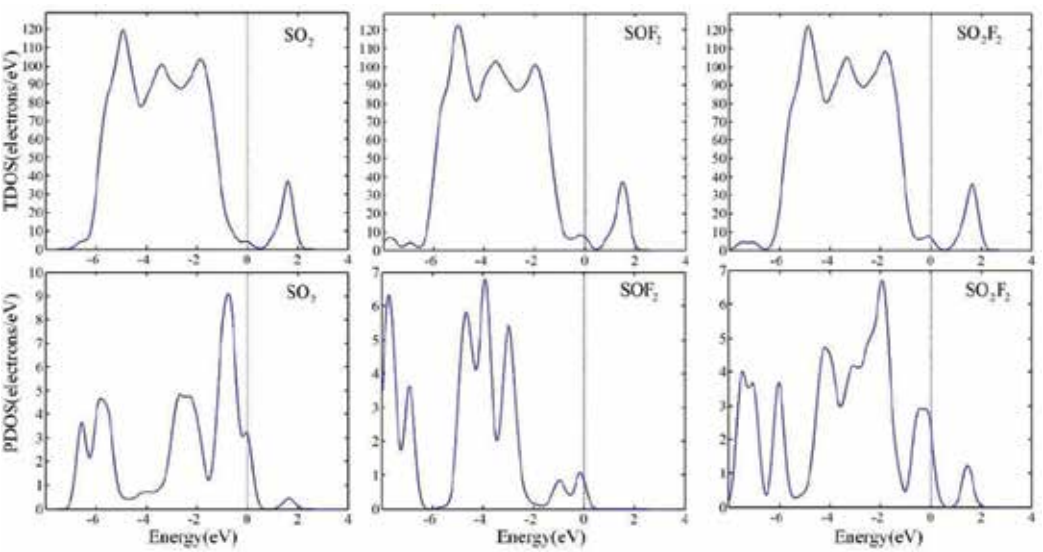

Figure 20. TDOSs of the adsorption structures of SO_2, SOF_2, and SO_2F_2 on both of Pt and anatase and PDOSs of the three gases in these structures.

http://dx.doi.org/10.5772/intechopen.68328

Ag/AgCl electrode is the reference electrode, and platinum electrode functions as the counter electrode. An electronic pulse signal was produced in the constant current control mode of the Shanghai Chen Hua CHI660D electrochemical analyzer. The electrolyte was an aqueous solution of $H_2PtCl_6 \cdot 6H_2O$ (1 g/L) and H_3BO_3 (20 g/L) at 50°C (pH = 4.4). After numerous exploratory experiments, the optimal parameters determined for the constant current method are as follows: current density of 0.1 mA/cm^2, and doping times of 10, 20, 30, and 40 s. In the deposition process, a magnetic stirrer is used to ensure that the liquid has a stable metal ion concentration.

Figure 21 shows the cyclic voltammetry curve of the four types of sensors with different amounts of doped Pt in 1.0 mol/L NaOH solution. Curves (a) to (d) correspond to the doping times of 10, 20, 30, and 40 s, respectively. During electrochemical deposition, Pt^{4+} in the electrolyte is reduced to Pt, as described in [32]; the sizes of the curve areas were compared to determine the amount of deposited Pt metal. The humps between −1.0 and 0.8 V in the four curves shown in **Figure 21** correspond to the hydrogen absorption and dehydrogenation processes of the Pt ions in NaOH solution [33]. The hump in curve (a) is not evident, and the humps in curves (b) to (d) are significant. Based on the size of each curve surrounding the area, we concluded that the amount of deposited Pt nanoparticles on the TiO_2NT surface is proportional to deposition time.

Figure 22 shows the SEM images of intrinsic and Pt-doped TiO_2NTs. **Figure 22a** shows the intrinsic TiO_2NTs, and **Figure 22b–e** presents the Pt-doped TiO_2NTs with deposition times of 10, 20, 30, and 40 s. The white objects around or above the tube wall in **Figure 22** are Pt nanoparticles. The SEM images show that the amount of Pt deposition increases with the deposition time. At 10 s, less Pt nanoparticles are deposited, and at 30 s, the Pt nanoparticles have moderate

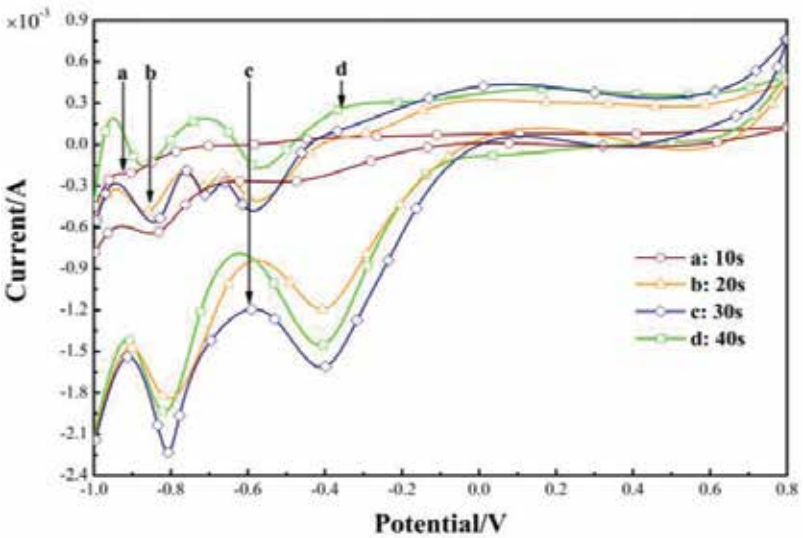

Figure 21. Cyclic voltammetry curve of sensors with different amounts of doped Pt in 1.0 mol/L NaOH.

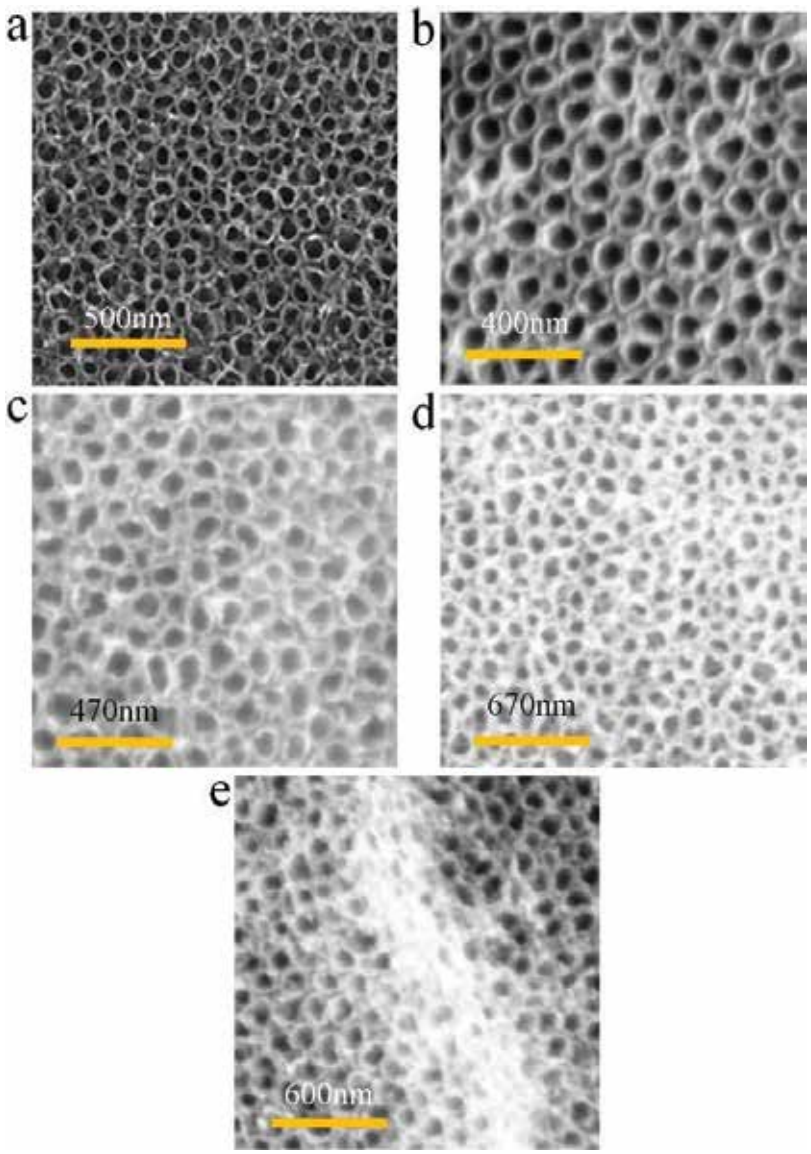

Figure 22. SEM images of intrinsic and Pt-doped TiO_2NTs.

sizes and are uniformly distributed. At 40 s, more Pt nanoparticles are deposited, and large tracts of these nanoparticles block the mouth of TiO_2NTs, as shown in **Figure 22e**.

Figure 23 shows that the intrinsic and Pt-doped TiO_2 NTs have strong anatase (101) crystal plane peak at $2\theta = 25.3°$ (A in **Figure 23**). Pt (111) and (200) crystal surface peaks at $2\theta = 40.5$ and 46° were observed in the XRD patterns of the Pt-doped TiO_2 NTs.

However, no such peaks are found for the intrinsic TiO_2 NTs. This result shows that the constant potential method is useful when Pt nanoparticles are doped on TiO_2 NTs.

http://dx.doi.org/10.5772/intechopen.68328

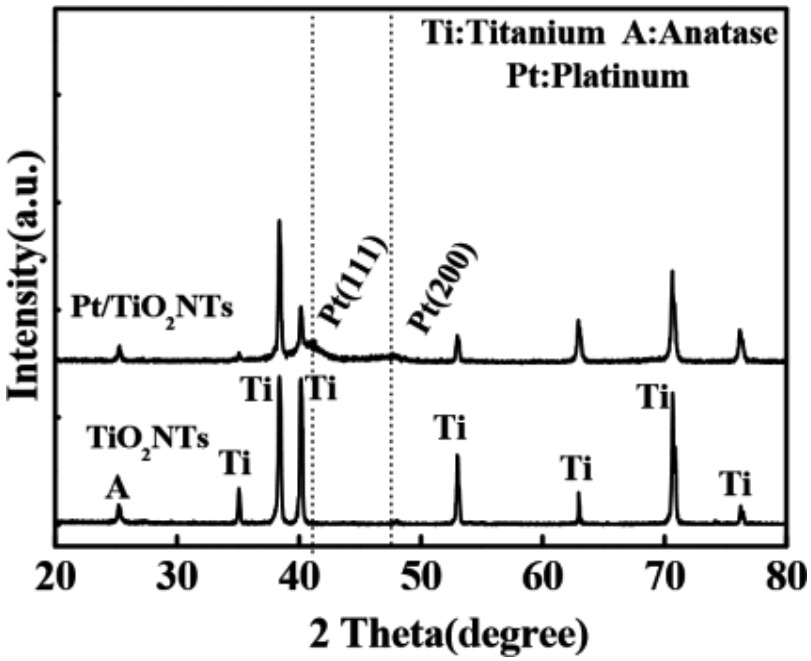

Figure 23. XRD patterns of Pt-doped TiO_2NTs.

2.2.3. Gas-sensing experiments of Pt-doped TiO_2 nanotubes sensors

The performance of gas-sensitive metal oxide material is significantly influenced by working temperature. Therefore, the gas-sensing responses of the sensors with different amounts of doped Pt were investigated under different operating temperatures for SOF_2, SO_2F_2, and SO_2 gases. The optimal operating temperatures of the sensors were also determined.

The prepared Pt-doped sensors were placed into the test device (**Figure 11**). The sensor surface was then controllably heated. In this experiment, the sensor gas-sensing characteristics of the sensors for SOF_2, SO_2F_2, and SO_2 gases at 100 ppm from 20 to 220°C were examined. The results are shown in **Figure 24**.

Figure 24 shows the resistance sensitivity curves of the sensors with different amounts of doped Pt for SOF_2, SO_2F_2, and SO_2. The figure shows that the gas response value of the sensor (i.e., resistance change rate, *R*%) increases with increasing sensor surface temperature. The optimal sensor operating temperature is approximately 160°C. When the temperature reaches 100–160°C, the largest response value is observed. As the temperature increases, the sensor response value begins to dramatically decrease. When the temperature reaches 200°C, the response value becomes small. The optimal operating temperatures and selectivity of the four sensors for the three decomposition component gases vary, as shown in **Table 8**.

The optimal operating temperature is 160, 150, 130, and 100°C at 10, 20, 30, and 40 s doping time, respectively. These results show that with increasing doping time, the optimal working

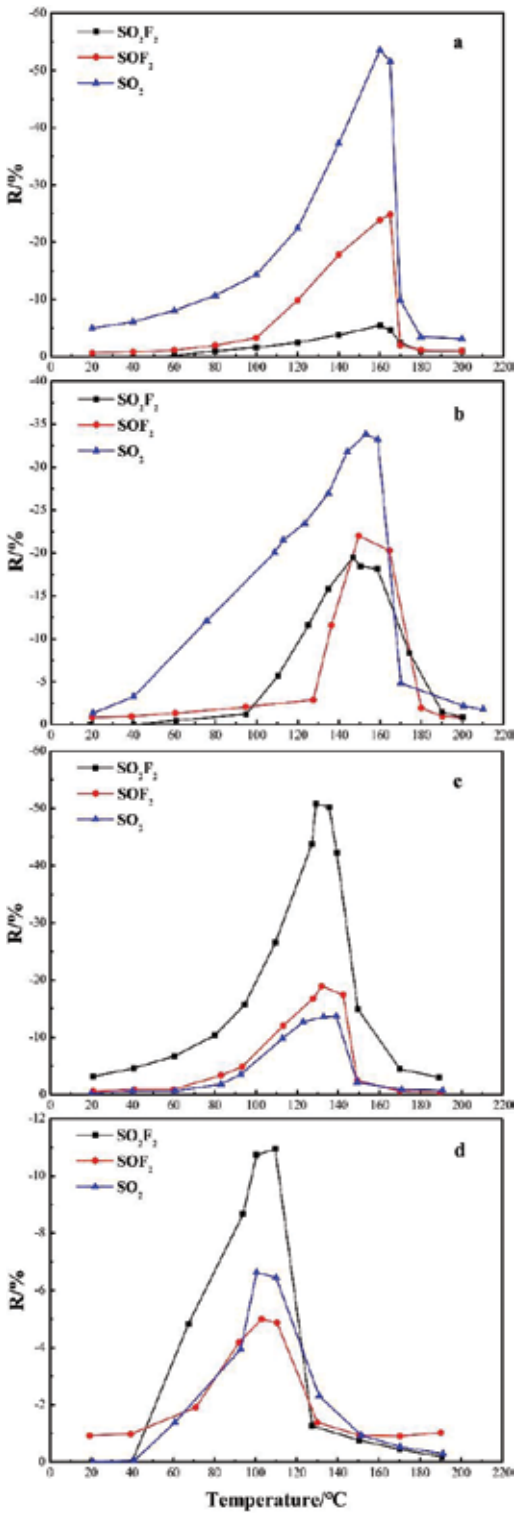

Figure 24. Sensitivity of sensors with different amounts of doped Pt with varying working temperatures.

Doping time	Optimal temperature	Sensitivity		
		SO_2	SOF_2	SO_2F_2
10 s	160°C	−53.3%	−24.2%	−5.4%
20 s	150°C	−33.9%	−22.1%	−19.2%
30 s	130°C	−13.8%	−19.1%	−50.6%
40 s	100°C	−6.7%	−5.1%	−10.7%

Table 8. Sensitivity of Pt-doped sensors for 100 ppm SO_2, SOF_2, and SO_2F_2 at their optimum temperatures.

temperature of the sensor decreases. In addition, at the optimal temperature, the sensor with 10 s of doping time is the most sensitive to SO_2 at −53.3% but has the weakest response to SO_2F_2 at −5.4%. The sensor with 20 s of doping time is most sensitive to SO_2 at −33.9% but has weakest response to SO_2F_2 at −19.2%. The sensor with 30 s of doping time is most sensitive to SO_2F_2 at −50.6% but has weakest response to SO_2 at −13.7%. The SOF_2 gas response values of these three sensors remained almost unchanged. The sensor with 40 s of doping of time has significantly low responses for the three gases.

Compared with the intrinsic TiO_2NT sensor, the doped Pt nanoparticles alter the sensor surface microstructure and charge distribution. When the sensor surface temperature is higher than its optimum working temperature, the Pt nanoparticles improve the chemical desorption rate on the sensor surface. This result indicates that the desorption rate of a gas molecule is higher than its adsorption rate, and that the density of the gas molecule adsorbed onto the surface decreases, such that the response value of the sensor rapidly decreases. However, most parts of the tube mouth of the 40 s sensor are blocked by Pt nanoparticles; thus, the gas-sensing response value is highly reduced.

According to the experimental methods and procedures mentioned above, the four kinds of sensors function at their optimal operating temperatures. Their gas-sensing property curves are tested under SO_2, SOF_2, and SO_2F_2 gases at 25, 50, 75, and 100 ppm. The change rate of the sensor resistance (gas-sensing response value) was calculated at various concentrations. The linear relationship between the change rate of the sensor resistance and gas concentration was examined. Using the linear fit curve, we can also estimate the concentration of the gas using the sensor response value. After multiple experiments, the gas-sensing response values of the four sensors were found to increase with the experiment gas concentration, but for one kind of gas. Therefore, in the following section, only the 30 s sensor is considered, and its gas-sensing response curves were obtained at different gas concentrations. The experimental data of the remaining three sensors were obtained using the linear fit curve.

2.2.3.1. Gas-sensing properties of sensors with different amounts of doped Pt to SO_2 gas

Figure 25a shows that sensor with 30 s of doping time has resistance change rates of −2.0, −7.0, −10.0, and −13.8% for the SO_2 gas at 25, 50, 75, and 100 ppm, respectively. **Figure 25b** shows that sensor with 10 s doping time has response values of −10.7, −25.6, −36.0, and −53.2% for the four SO_2 concentrations. For the sensor with 20 s of doping time, the response values

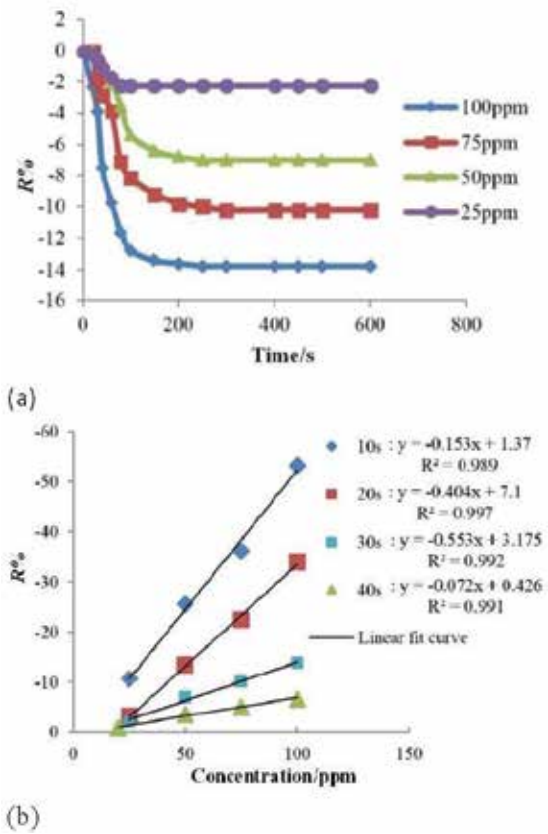

Figure 25. Response of four sensors with different amounts of doped Pt to varying concentrations of SO_2. (a) Gas-sensing response curves of 30 s sensor for different concentrations of SO_2 gas at 130°C. (b) Linear relationship between sensor response and gas concentration.

are −3.2, −13.4, −22.3, and −33.9% for the four SO_2 concentrations. Meanwhile, for the sensors with 40 s of doping time, response values are −0.8, −3.5, −5.0, and −6.7% for the four SO_2 concentrations. The sensitivities are shown in **Table 9**. The linear fit function and linear correlation coefficient are shown in **Figure 25b**.

Concentration	SO_2			
	10 s	**20 s**	**30 s**	**40 s**
100 ppm	−53.2%	−33.9%	−13.8%	−6.7%
75 ppm	−36.0%	−22.3%	−10.0%	−5.0%
50 ppm	−25.6%	−13.4%	−7.0%	−3.5%
25 ppm	−10.7%	−3.2%	−2.0%	−0.8%

Table 9. Sensitivity of Pt-doped 30 s sensor to different concentrations of SO_2 at optimal working temperature.

2.2.3.2. Gas-sensing properties of sensors with different amounts of doped Pt for SO_2F_2 gas

Figure 26a shows the gas-sensing response curve of the sensor with 30 s doping time for SO_2F_2 at 25, 50, 75, and 100 ppm and 130°C. The resistance change rate is −3.5, −16.1, −32.1, and −50.6% for the different tested SO_2F_2 concentrations. **Figure 26b** shows that sensor with 10 s of doping time has response values of −0.9, −2.1, −3.9, and −5.4% for the different SO_2F_2 concentrations. The sensor with 20 s of doping time has response values of −1.1, −7.8, −11.5, and −19.1% for the different SO_2F_2 concentrations. The sensor with 40 s doping time has response values for −0.9, −3.0, −7.2, and −10.9% to the different SO_2F_2 concentrations. The sensor sensitivities are shown in **Table 10**. The linear fit function and linear correlation coefficient are shown in **Figure 26b**.

2.2.3.3. Gas-sensing properties of sensors with different amounts of doped Pt for SOF_2 gas

Figure 27 shows that the sensor with 30 s of doping time has a resistance change rates of −1.1, −6.3, −10.0, and −19.1% for SOF_2 gas at 25, 50, 75, and 100 ppm, respectively. **Figure 27b** shows that the sensor with 10 s doping time has response values of −3.2, −8.7, −15.8, and −24.9% for the four SOF_2 concentrations. The sensor with 20 s doping time has response values of −2.0, −8.2, −14.2, and −22.3% for the four SOF_2 concentrations. The sensor with 40 s doping time has response values of −0.8, −2.0, −3.9, and −5.3% to four SOF_2 concentrations. The linear fit function and linear correlation coefficient are shown in **Figure 27b**.

Figure 28 shows a comparison chart for the gas-sensing responses of the four sensors for SO_2, SOF_2, and SO_2F_2 gases at 100 ppm and at their optimal working temperatures. The responses of the intrinsic TiO_2NT sensor for these decomposition gases are discussed in Ref. [30]. With increasing doping amount, the sensor response for SO_2 decreases and follows the trend: intrinsic (−73.5%) > 10 s (−53.3%) > 20 s (−33.9%) > 30 s (−13.8%) > 40 s (−6.7%). When the doping amount increases, the sensor response for SO_2F_2 increases and follows the trend: intrinsic (−4.1%) < 10 s (−5.4%) < 20 s (−19.2%) < 30 s (−50.6%) >> 40 s (−10.9%). The responses of the 10, 20, and 30 s sensors for SOF_2 gas are nearly identical; however, response of the 40 s sensor for SOF_2 dramatically decreases.

Figure 28 shows that the *R*% values of the Pt-doped TiO_2 nanotube for the three SF_6 decomposition gases are negative. This result indicates that the resistance of the Pt-doped TiO_2 nanotube sensor tends to decrease. Based on a known response mechanism, the three measured gases serve as reducing gases or as electron-donating gases. The reaction occurs as follows:

$$R+O_{ads}^{-} \rightarrow RO_{ads}+e^{-}$$

where R is the SF_6 decomposition component gas (i.e., SO_2, SOF_2, and SO_2F_2), and O_{ads}^{-} is the adsorbed oxygen ion on the sensor surface.

The results show that the reducing function and electron donating effect of SO_2 gas are the most prominent in the micro-oxidation reduction reaction (i.e., most likely to lose electrons). SO_2 is followed by SOF_2, while SO_2F_2 is the weakest. The selectivity of the sensor is highest for SO_2 gas. Therefore, the order of gas-sensing response of the intrinsic sensor for the three tested gases follows: SO_2 (−74.6%) > SOF_2 (−7.8%) > SO_2F_2 (−5.5%) [34].

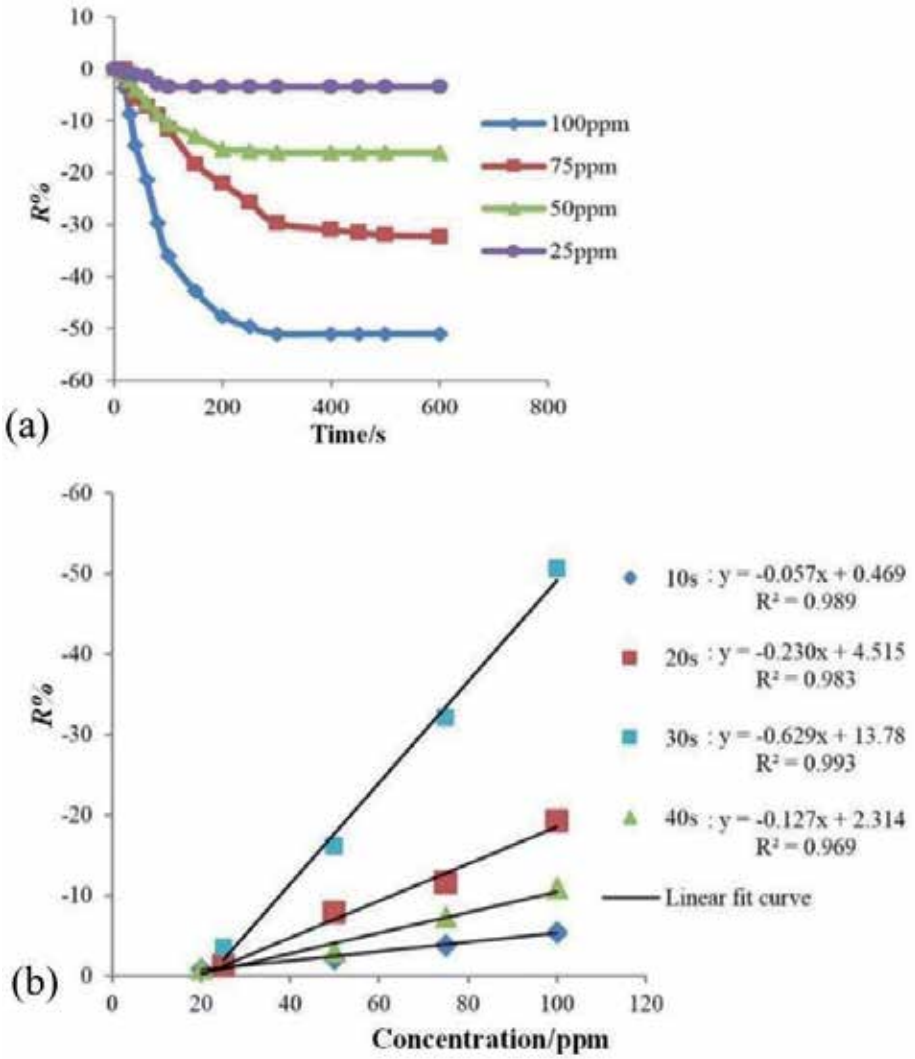

Figure 26. Response of four sensors with different amounts of doped Pt to varying concentrations of SO_2F_2. (a) Gas-sensing response curves of 30 s sensor for different concentrations of SO_2F_2 gas at 130°C. (b) Linear relationship between sensor response and gas concentration.

Concentration	SO_2F_2			
	10 s	**20 s**	**30 s**	**40 s**
100 ppm	−5.4%	−19.1%	−50.6%	−10.9%
75 ppm	−3.8%	−11.5%	−32.1%	−7.2%
50 ppm	−2.1%	−7.8%	−16.1%	−3.0%
25 ppm	−0.9%	−1.1%	−3.5%	−0.9%

Table 10. Sensitivity of Pt-doped 30 s sensor to different concentrations of SO_2F_2 at optimal working temperature.

http://dx.doi.org/10.5772/intechopen.68328

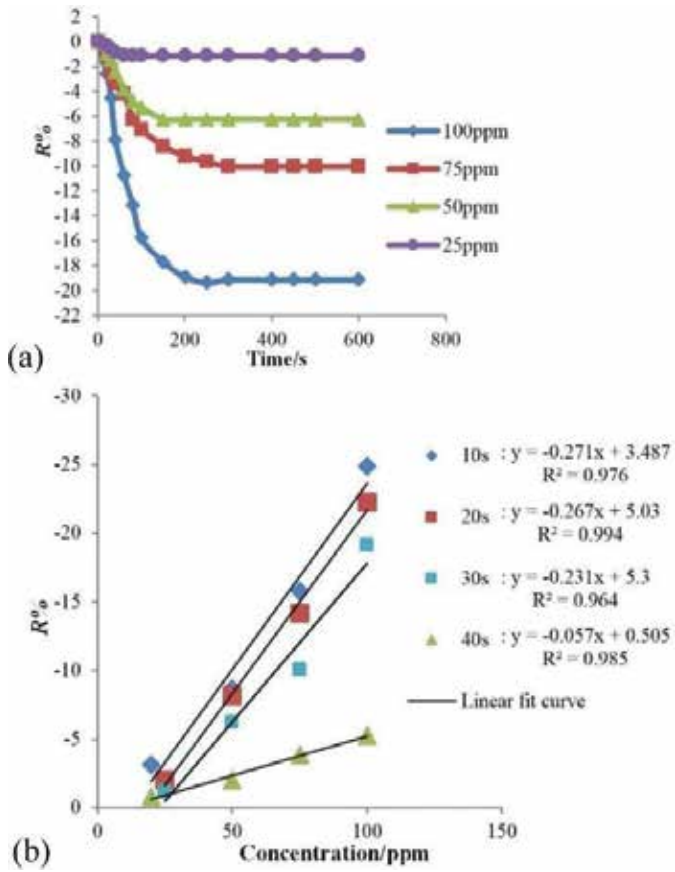

Figure 27. Responses of sensors doped with different amounts of Pt to varying concentrations of SOF_2. (a) Gas-sensing response curves of 30 s sensor for different concentrations SOF_2 gas at 130°C. (b) Linear relationship between sensor response and gas concentration.

The doped Pt significantly affects the gas-sensing response of the TiO_2NT sensor for the SO_2, SOF_2, and SO_2F_2 gases, and thus, the selectivity of the sensor changes.

Pt serves as an oxygen storage point by constantly providing O_{ads}^- to the TiO_2NT sensor surface. The noble metal doping specifically reduced the activation energy of the reaction $O_2+2e^-\rightarrow 2O^-$. Thus, the optimal working temperature also decreases, and the reaction rate and gas sensitive effects are enhanced. Meanwhile, the catalyst particles existing on the surface of the TiO_2-sensitive body has better affinity interactions with the target gases. Therefore, these gases will be more attached to the sensor surface at a lower temperature. The catalyst particles are embedded on the surface of the sensitive body. When the adhesion concentration of the measured gas on the catalyst particles surface reaches a certain value, these gases will "overflow" from the catalyst particles toward the surface of the sensitive body, and further react with the adsorbed oxygen ions. Ultimately, the sensitivity of this gas sensor increases, and the sensor response accelerates.

SO_2, SOF_2, and SO_2F_2 gases are specifically discussed. Sulfides have a certain degree of toxicity to noble metal catalysts, and the level of toxicity is associated with the valence elements and

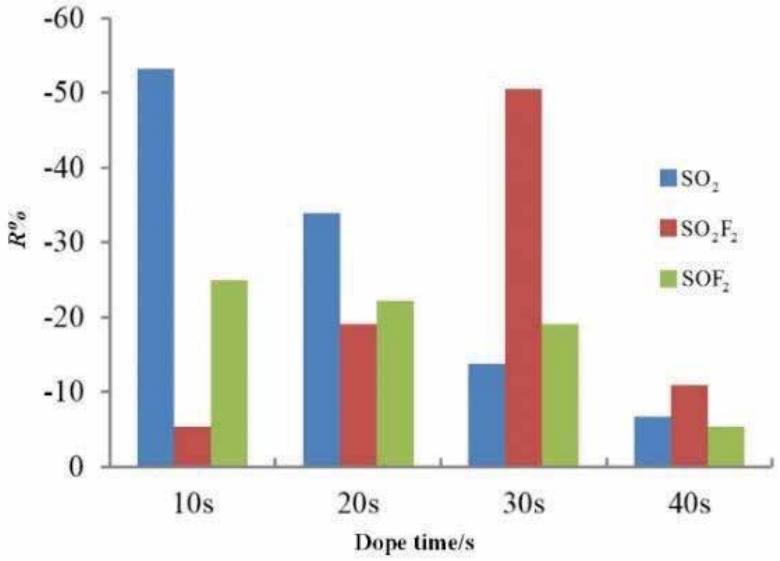

Figure 28. Gas-sensing response of sensor with different amounts of doped Pt to SF_6 decomposition components.

molecular structure. The decreasing toxicity of the three experimental gases follows the order of SO_2 > SOF_2 > SO_2F_2; S^{6+} within a certain range is non-toxic [35]. Therefore, once the strong toxicity of SO_2 accumulates, the Pt-doped sensor would be poisoned. The sensor poisoning follows a specific process. First, SO_2 is physically adsorbed on the active center of the catalyst, and then, redox reaction occurs between SO_2 and the active ingredient. Ultimately, the reaction produces alkylene sulfide and other sulfides, which block the active sites. In this complex series of processes, the activity of the catalyst decreases [35]; in addition, the sensitivity of the sensor is significantly improved with the nearly non-toxic SO_2F_2 gas.

2.3. Au-doped TiO_2 nanotubes

2.3.1. Investigation of gas-sensing simulation of Au-doped TiO_2 nanotubes

Intrinsic anatase TiO_2 (101) surface model was optimized in $Dmol^3$ module shown in **Figure 29a**, **b** while Au-doped anatase TiO_2 (101) surface model after optimization was exhibited in **Figure 29c** and **d**.

In **Figure 30** [1], density of states (DOS) of intrinsic and Au-doped anatase (101) surfaces as well as the doped Au atom was compared. As can be concluded, Au-doping could reduce band gap of TiO_2, to some extent [1]. To obtain more precise values, highest occupied molecular orbital (HOMO) and lowest unoccupied molecular orbital (LUMO) were calculated, and band gap of Au-doped anatase (101) surface was 1.906 eV, less than 1.932 eV, band gap of intrinsic anatase (101) surface [1]. The decrease of band gap made it easier for electrons to transfer from valence band to conduction band. In addition, Au-doping enhanced the DOS below Fermi level and increased density of electrons, providing more electrons which were possible to transfer to conduction band [1].

http://dx.doi.org/10.5772/intechopen.68328

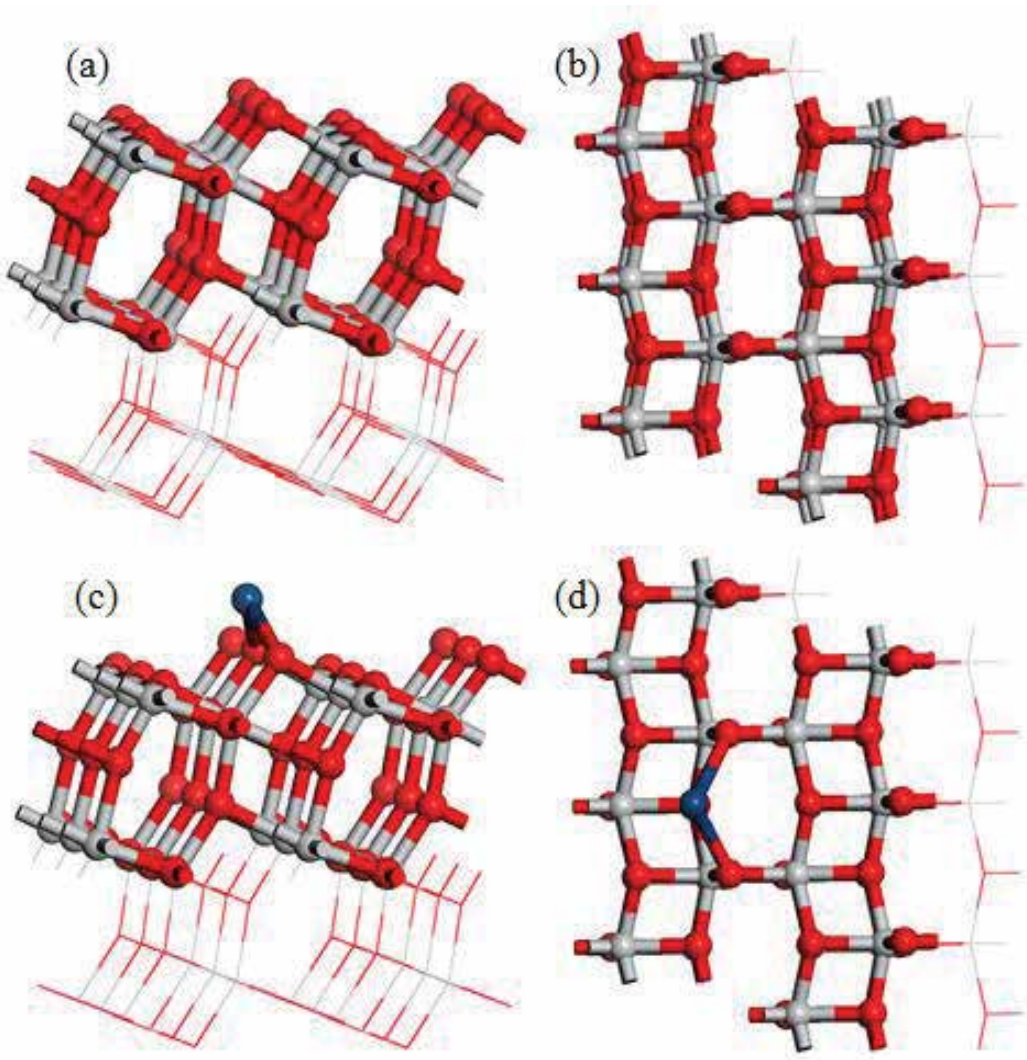

Figure 29. Views of intrinsic and Au-doped anatase TiO_2 (101) surface models from different angles.

Gas molecules approach Au-doped anatase TiO_2 (101) surface by different atoms, shown in **Figure 31**. Considering structure features of SO_2F_2 that S atom is inside the tetrahedron made of O and F atoms, two conditions that SO_2F_2 approaches Au-doped anatase TiO_2 (101) surface by O and F atoms were taken into consideration.

Table 11 [1] shows adsorption parameters of gases adsorbed on Au-doped anatase TiO_2 (101) surface. As can be found, when SO_2 molecule approaches Au atom by O or S atoms, adsorption parameters are close to each other, while similar condition occurs when SOF_2 approaches Au atom. When SO_2F_2 approaches Au atom by O atom, the adsorption energy and charge transfer are obviously smaller than those of the other condition that SO_2F_2 approaches Au atom by F atom, which indicates that it is easier for SO_2F_2 to adsorb on Au atom by F atom.

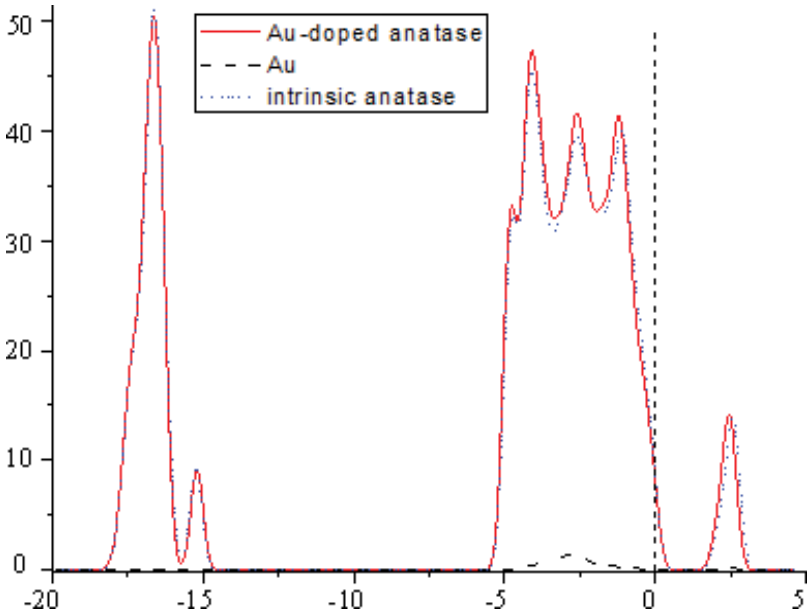

Figure 30. DOS of intrinsic and Au-doped anatase TiO_2 (101) surface.

By comparison of adsorption energy, it can be concluded that, whatever figure gas molecules approach adsorption surface by, adsorption energy of SO_2 is the largest, about 2–3 times that of SOF_2 and SO_2F_2 [1]. It can also be found from the view of charge transfer that, electrons transfer from adsorption surface to SO_2 molecule, the opposite direction of electron transfer in SOF_2 and SO_2F_2 adsorption processes [1]. The phenomenon can be explained by the strong oxidizing ability of SO_2. In addition, SO_2 adsorption possesses larger absolute value of charge transfer in adsorption process than SOF_2 and SO_2F_2 adsorption processes.

Figures 32–34 showed the total density of states (TDOS) of adsorption system and partial density of states (PDOS) of adsorbed gas molecules, SO_2, SOF_2, and SO_2F_2, respectively. "SO_2-O-TiO_2" represents that SO_2 approaches anatase TiO_2 (101) surface by O atom, and the like.

In order to investigate the effect of Au-doping on gas-sensing properties of TiO_2 (101) surface, simulation results were compared with those of gas molecules adsorbed on intrinsic TiO_2 (101) surface [1]. Detailed calculation and results of adsorption on intrinsic TiO_2 (101) surface were included in the published reference [1, 36–39]. It should be noted that, in reference [32], SO_2 and SOF_2 molecules were adsorbed on intrinsic anatase TiO_2 (101) surface by O atom, while SO_2F_2 approached adsorption surface by F atom [1]. Therefore, the comparisons of adsorption parameters are mainly based on calculation results when gas molecules approached surface by the same atom [1]. In this paper, more approaching figures of gas molecules adsorbed on TiO_2 (101) surface are involved [1].

As can be concluded from the adsorption parameters, adsorption energy and charge transfer increased obviously after SO_2 molecule was adsorbed on Au-doped anatase TiO_2 (101) surface

http://dx.doi.org/10.5772/intechopen.68328

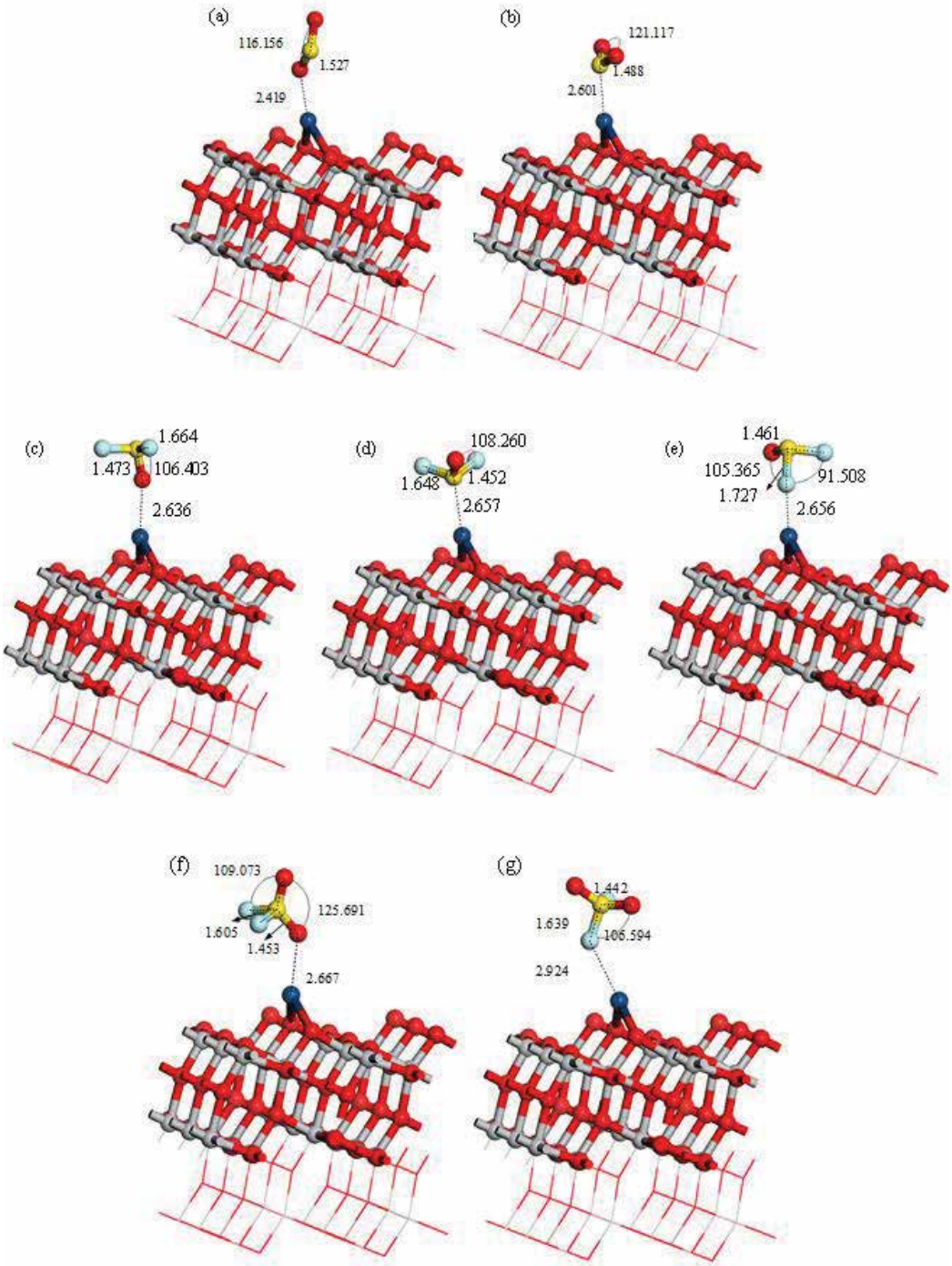

Figure 31. Adsorption structures of three gas molecules on Au-doped anatase TiO_2 (101) surface.

Gas molecules	Adsorption structure	Adsorption energy E_a/eV	Charge transfer Q/e	Adsorption distance d/Å
SO_2	-S	−0.657	−0.156	2.601
	-O	−0.571	−0.182	2.419
SOF_2	-S	−0.238	0.067	2.657
	-O	−0.363	0.042	2.636
	-F	−0.593	−0.006	2.656
SO_2F_2	-O	−0.071	0.009	2.667
	-F	−0.200	0.039	2.924

Table 11. Adsorption parameters of gases adsorbed on Au-doped anatase TiO_2 (101) surface "-S", "-O" and "-F" represent that gas molecules approach adsorption surface by S, O and F atoms, respectively.

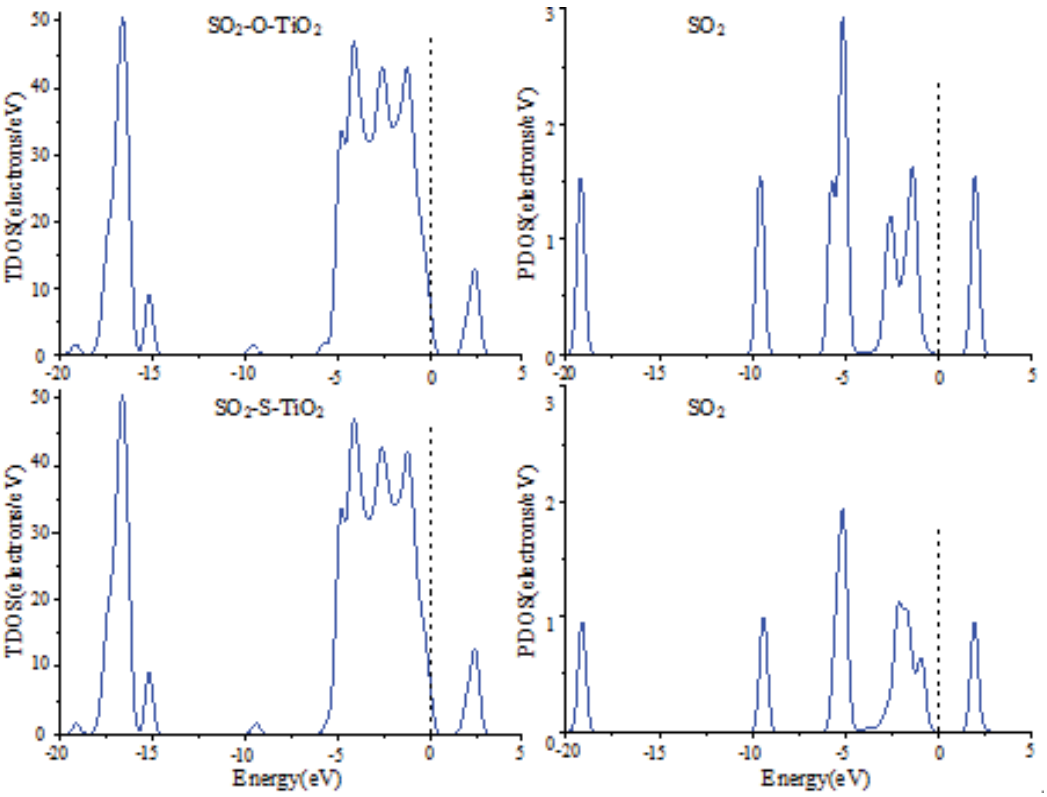

Figure 32. TDOS of adsorption systems and PDOS of adsorbed SO_2.

than intrinsic anatase TiO_2 (101) surface, while adsorption distance changed slightly [1]. More importantly, Au-doping changed the direction of charge transfer, causing the resistivity of adsorption system changing from decrease to increase [1]. As for SOF_2, adsorption energy increased by one-third while charge transfer and adsorption distance kept almost unchanged [1]. It can be judged that adsorption ability of SOF_2 on Au-doped surface slightly increased

http://dx.doi.org/10.5772/intechopen.68328

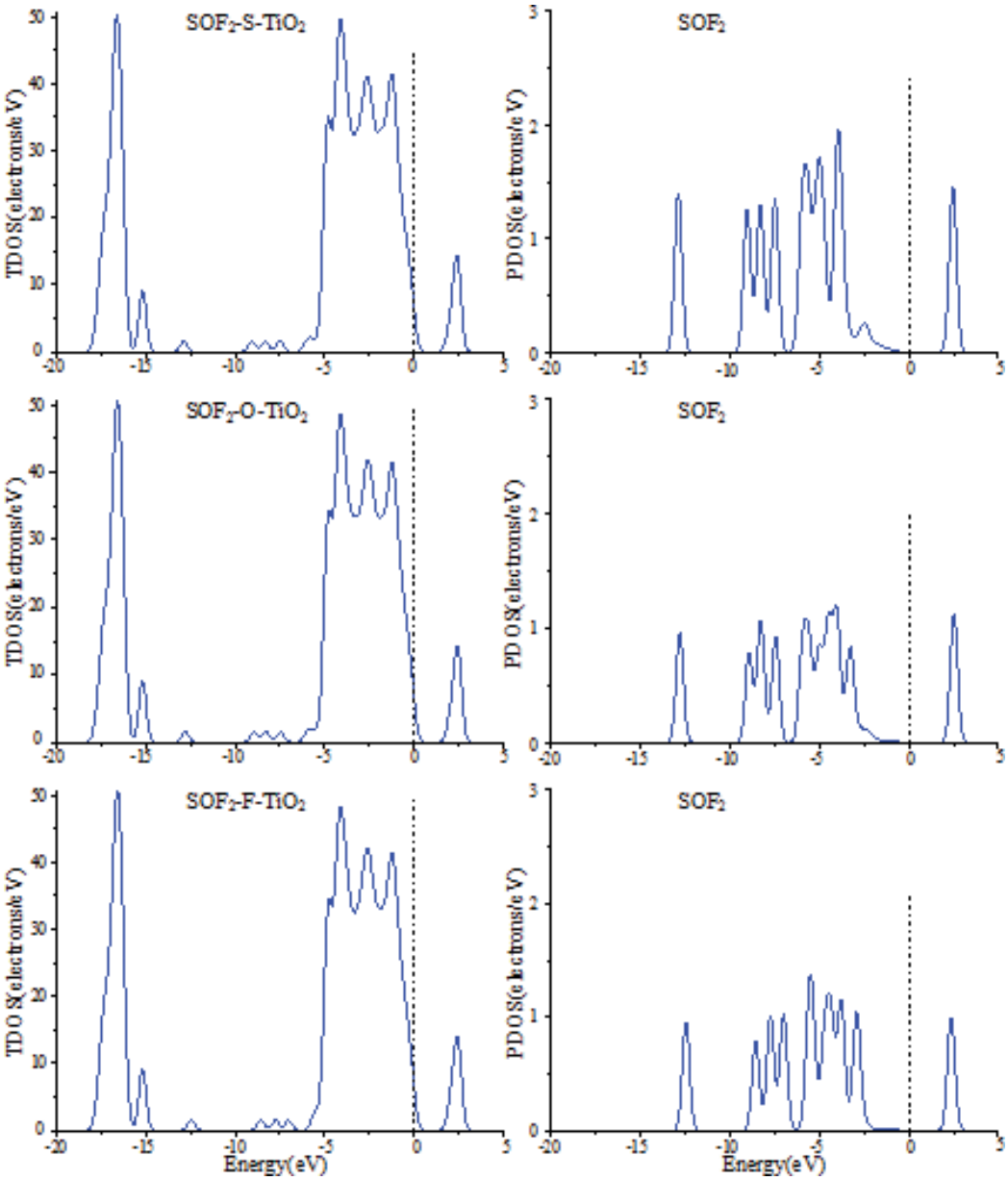

Figure 33. TDOS of adsorption systems and PDOS of adsorbed SOF_2.

compared with that of SOF_2 on intrinsic surface [1]. After SO_2F_2 was adsorbed on Au-doped anatase TiO_2 (101) surface, adsorption distance became smaller, while adsorption energy and charge transfer became larger compared with the adsorption on intrinsic anatase TiO_2 (101) surface. It can also be found that absolute values of adsorption energy and charge transfer became larger when three molecules were adsorbed on Au-doped TiO_2 (101) surface with

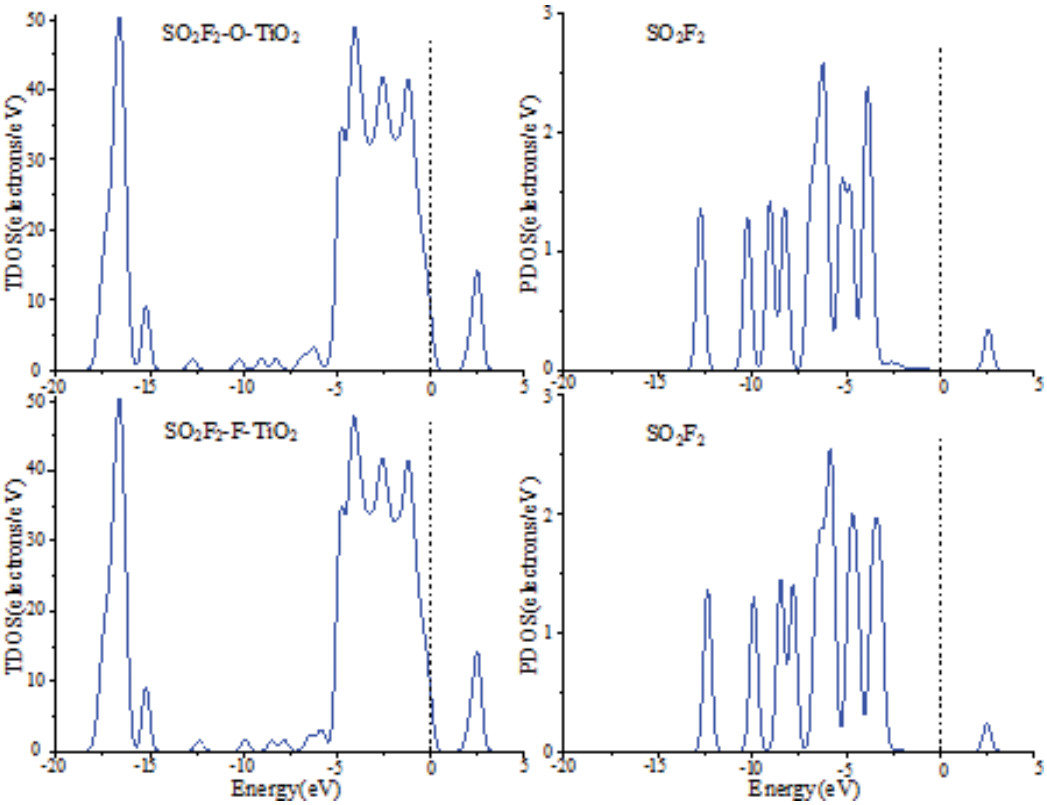

Figure 34. TDOS of adsorption systems and PDOS of adsorbed SO_2F_2.

adsorption distance almost unchanged compared with the adsorption on intrinsic surface. That is to say, Au-doping improved adsorption performance of intrinsic anatase TiO_2 (101) surface to SO_2, SOF_2, and SO_2F_2 [1]. When SO_2 molecule was adsorbed on Au-doped adsorption surface by S atom, adsorption energy was 0.657 > 0.6 eV, so the process belonged to chemical adsorption, while adsorption energy was 0.571 eV when SO_2 molecule was adsorbed by O atom, slightly smaller than 0.6 eV, which can be considered close to chemical adsorption. Adsorption energies of SOF_2 and SO_2F_2 molecules adsorbed on Au-doped adsorption surface were much smaller than 0.6 eV, belonging to physical adsorption [1].

TDOS of adsorption systems and gas molecules was compared, too [1]. Reference [41] shows TDOS of adsorption systems and PDOS of gas molecules adsorbed on intrinsic anatase TiO_2 (101) surface. By comparing with adsorption on intrinsic anatase TiO_2 (101) surface, an obvious TDOS peak did not appear above Fermi level when SO_2 was adsorbed on Au-doped anatase TiO_2 (101) surface [1]. As can be concluded, SO_2 molecule contributed less electrons to conduction band, leading to increase of adsorption system's resistivity, which is consistent with the above analysis based on adsorption parameters. Au-doping changed variation tendency of adsorption system's resistivity when SO_2 was adsorbed on anatase TiO_2 (101) surface [1].

Compared with adsorption of SOF_2 on intrinsic anatase TiO_2 (101) surface, SOF_2 made obvious contribution to DOS near Fermi level when it was adsorbed on Au-doped anatase TiO_2 (101) surface, which increased the amount of electrons in conduction band. From macroscopic view, resistivity of adsorption system dropped more severely and resistance declined more wildly as well in the adsorption process [1]. That is to say, Au-doping improved the sensitivity of anatase TiO_2 (101) surface to SOF_2, to some extent.

As far as SO_2F_2, adsorption of SO_2F_2 molecule did not contribute much to the DOS near Fermi level when SO_2F_2 was adsorbed on intrinsic anatase TiO_2 (101) surface, that is, SO_2F_2 provided almost no electrons for conduction band of adsorption system [1]. When SO_2F_2 was adsorbed on Au-doped anatase TiO_2 (101) surface, however, obvious DOS peaks appeared above Fermi level, and SO_2F_2 supplied more electrons to conduction band of adsorption system. Macroscopically, sensitivity of Au-doped anatase TiO_2 (101) surface to SO_2F_2 increased obviously compared with intrinsic anatase TiO_2 (101) surface [1].

Based on the above analysis of adsorption parameters and density of states, it can be concluded that, resistance's variation tendency of Au-doped anatase TiO_2 (101) surface after the adsorption of SO_2 is decreasing, different from intrinsic anatase TiO_2 (101) surface [1]. Resistance of Au-doped anatase TiO_2 (101) surface dropped more, and the sensitivity increased slightly after SOF_2 adsorption, while resistance of Au-doped anatase TiO_2 (101) surface dropped severely, and the sensitivity increased obviously after SO_2F_2 adsorption [1].

2.3.2. Preparation and surface characterization of Au-doped TiO_2 nanotubes

To prepare the Au-TNTA, the intrinsic TiO_2 nanotubes were first fabricated, and then, Au was deposited onto the TiO_2 nanotubes using the deposition-precipitation method. The intrinsic TNTAs used in this paper were prepared by the anodic oxidation method [1, 38], and NaOH was selected as the precipitating agent. Firstly, the pH of the 1.01×10^{-3} mol/L $HAuCl_4$ solution was adjusted to 9 using NaOH solution [1]. Then, the intrinsic TiO_2 nanotubes were subsequently added to the above solution, resulting in the pH value decreasing. At the moment, a little more NaOH solution was needed to maintain the pH value at 9. Next, the resulting suspension was stirred for 2 h at 70°C to allow the Au to be supported on the carrier sufficiently. During the process, the suspension became pale purple gradually, and the pH value remained at 9 after cooling. TiO_2 nanotubes were picked out, washed, filtered, dried at room temperature and calcined for 4 h at 100°C to finally obtain the Au-TiO_2 nanotube sensors [1, 39].

As for the reasons for keeping the pH at 9, the selection of a pH value of 8–9 is in agreement with several previous experimental investigations [1, 40–45]. A number of groups have proven that the selection of pH leads to different geometries of TiO_2 [1, 45], and the pH of an aqueous solution dramatically affects the particle size of Au [1, 43]. Though a finite value for the size cannot be deduced from the activity, since the electronic factors depend on the interaction with the support, the morphology of the particle or the chemical state of the gold, there is general agreement that the activity increases as the particle size decreases [1, 44]. Hence, the pH value of the solution has significant influence on the catalytic activity.

A low pH causes a big Au particle, while a high pH causes a low Au deposition amount. The optimum pH aims to not only cause Au to be completely precipitated, but also leads to an appropriate diameter [1, 45]. Ivanova et al. have proven that when the pH value is above 8, the main species of Au in the solution is transformed from $AuCl_4^-$ to $Au(OH)_4$, leading to a smaller particle diameter. In order to remove Cl^- ions completely [1, 46], we chose a pH of 9.

The sample morphology was analyzed by scanning electron microscopy (SEM). The SEM images were obtained by JEOLJSM7000 field emission SEM equipment operated at 10 kV [1].

Figure 35 [1] shows SEM images of the pore size distribution of films composed of (a) intrinsic TiO_2 nanotubes and aggregates and (b) the Au nanoparticles distribution of Au-TiO_2 prepared by the deposition-precipitation method. The surfaces of the films were observed before and after Au deposition [1]. It is obvious that the morphology of the TiO_2 films is significantly changed after the Au nanoparticle modification. The adopted fabrication method results in the formation of tubular TiO_2 of 25 nm in diameter [1]. After the Au deposition treatment, the diameter of the tubes remains about the same. However, on the Au-TiO_2 surface, the pipes are covered with Au nanoparticles of a dozen nanometers in size, aggregating at the pipe orifices [1]. The SEM images confirm that the formed films, whether composed of intrinsic or Au-TiO_2, are homogeneous with a uniform distribution of pores or Au nanoparticles, respectively, as expected [1].

The crystal structures of the obtained intrinsic TiO_2 and Au-TiO_2 nanotubes were analyzed by X-ray diffraction, measured on an X'pert Pro (PANalytical, The Netherland) using Cu Kα radiation (λ = 0.15405 nm) at 40 kV, 35 mA. The wide-angle XRD patterns were collected at a scanning speed of 10°/min over the 2θ range of 20°–100°. **Figure 36** [1] gives the XRD patterns of the products prepared by the deposition-precipitation treatment. Previously, Varghese et al. observed both the anatase and rutile phases of TiO_2 by annealing treatment in ambient oxygen [1, 47, 48]. In our study, the labels A at 25.3° are observed in intrinsic, as well as in Au-doped

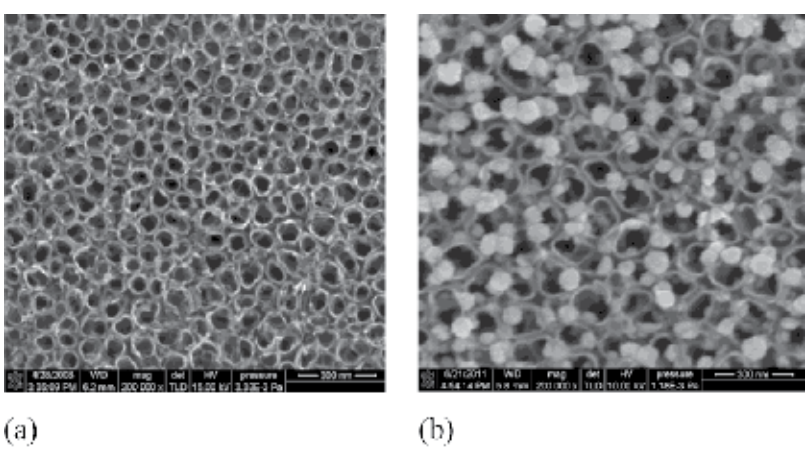

Figure 35. (a) SEM image of the intrinsic TiO_2 nanotubes. (b) SEM image of the Au-TiO_2 nanotubes.

http://dx.doi.org/10.5772/intechopen.68328

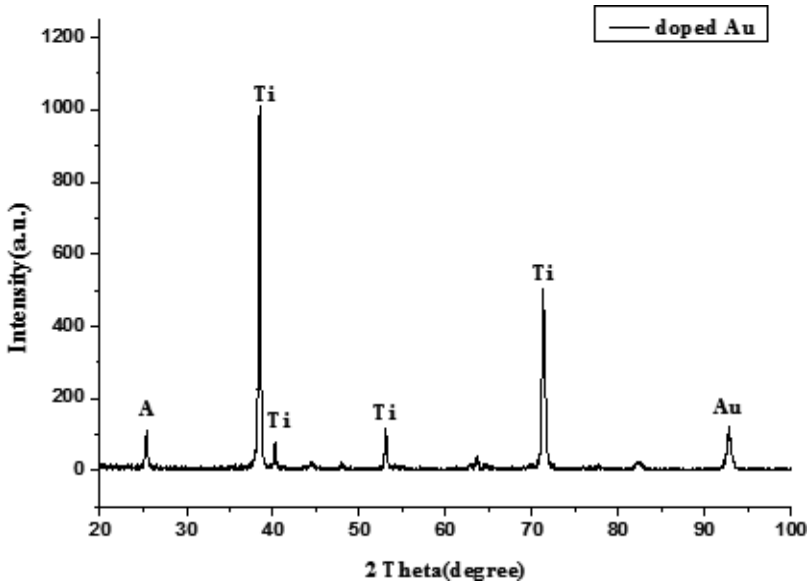

Figure 36. XRD of Au-TiO_2 nanotubes.

TiO_2, indicating that the crystal phases of TiO_2 are both anatase according to previous structural characterizations [1, 49], for which it can be confirmed that, in these preparation conditions, the TiO_2 nanotubes adopt an anatase crystal structure, while a rutile structure is not observed. The labels T and Au represent the reflections from the titanium substrate and different Au crystallographic forms. It is clearly seen from **Figure 36** [1] that characteristic gold peaks come into existence in XRD analysis observed at 38.2° (111), 44.2° (200), 64.3° (220) and 98.1° (400), respectively. The main Au (111) characteristic peak suggests that approximately 10-nm gold nanoparticles are coated onto the anodized TiO_2 nanotubes on the basis of the Scherer formula [1, 50].

Meanwhile, a certain amount of 200, 220 and 400 Au particle crystal forms do exist [1]. There is a popular belief that the characteristics of a metal oxide semiconductor are greatly affected by the doped metal or metalloid, which would also influence the operating temperature in a sensing application further. Therefore, it is necessary to investigate the gas-sensing response of Au-TiO_2 NTAs to SF_6 decomposed components (i.e., 50 ppm SOF_2, SO_2F_2 and SO_2) in an operating range of 20–200°C in order to find out the optimum operating temperature [1].

2.3.3. Gas-sensing experiments of Au-doped TiO_2 nanotubes sensors

Figure 37 [1] depicts the curves of the resistance changes' rate (i.e., the response value) of Au-doped and intrinsic TiO_2 NTAs to SO_2, SOF_2 and SO_2F_2 at different operating temperatures. The response value of the intrinsic TiO_2 nanotubes to SF_6 decomposed components increases as the surface temperature rises, reaching saturation around 180°C, which is considered the optimum operating temperature. In the case of Au-TiO_2, the resistance response

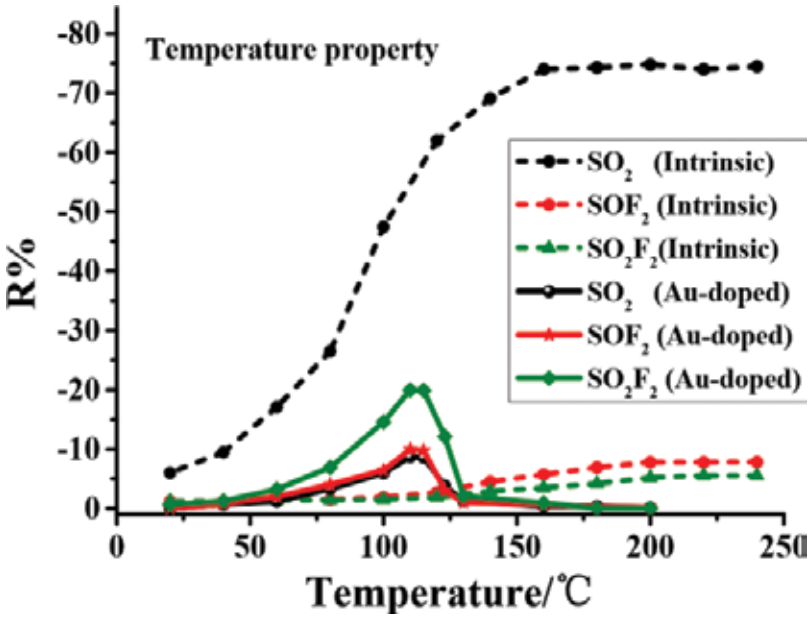

Figure 37. Sensor responses for 50 ppm SO_2 (black dots), SOF_2 (red dots) and SO_2F_2 (green dots), respectively, for the intrinsic (short dashed lines, in the range of 20–240°C) and Au-doped TiO_2 (solid lines, in the range of 20–200°C) nanotubular films at different working temperatures.

increases with increasing operating temperature before 110°C, following the typical behavior of an oxide semiconductor [1]. However, the resistance response dramatically drops down when the temperature exceeds 110°C. Hence, the optimum operating temperature of the Au-TiO_2 nanotubes sensor is taken as 110°C. A comparison of Au-doped and intrinsic TiO_2 indicates that Au-doping reduces the working temperature of TiO_2 NTAs along with obvious changes in the temperature characteristic curve [1].

The performance of the intrinsic TiO_2 nanotube sensors maintaining its response value after it reaches 180°C might be attributed to the dynamic equilibrium of the gas adsorption and desorption rate on the sensor's surface in the meantime [1]. As for Au-TiO_2, the Au nanoparticles change the microscopic structure and charge distribution of the surface, and the doped Au results in a promoted chemical desorption rate when the temperature surpasses 110°C, causing the oxygen desorption rate to be faster than its adsorption rate [1]. As a result, the oxygen chemisorption density on the surface decreases, leading to a rapid drop of the response value [1, 51].

The gas-sensing response curves of SO_2, SOF_2 and SO_2F_2 for Au-TiO_2 NTAs were recorded at different concentrations (i.e., 25, 50, 75, 100 ppm) under the optimal operating temperature (110°C) [1]. The results were linearly fit to investigate the linear relationship between the sensor's resistance change and the gas concentration. Therefore, the concentration of target gases in real power equipment could be estimated through the linear relationship acquired by these sample gases [1].

http://dx.doi.org/10.5772/intechopen.68328

2.3.3.1. Sensing performances of Au-TiO_2 NTAs for SO_2

As **Figure 38** [1] shows, the resistance change rates of the Au-TiO_2 nanotube gas sensor for SO_2 at 25, 50, 75 and 100 ppm are −2.14, −8.73, −15.76 and −23.75%, respectively. The linear

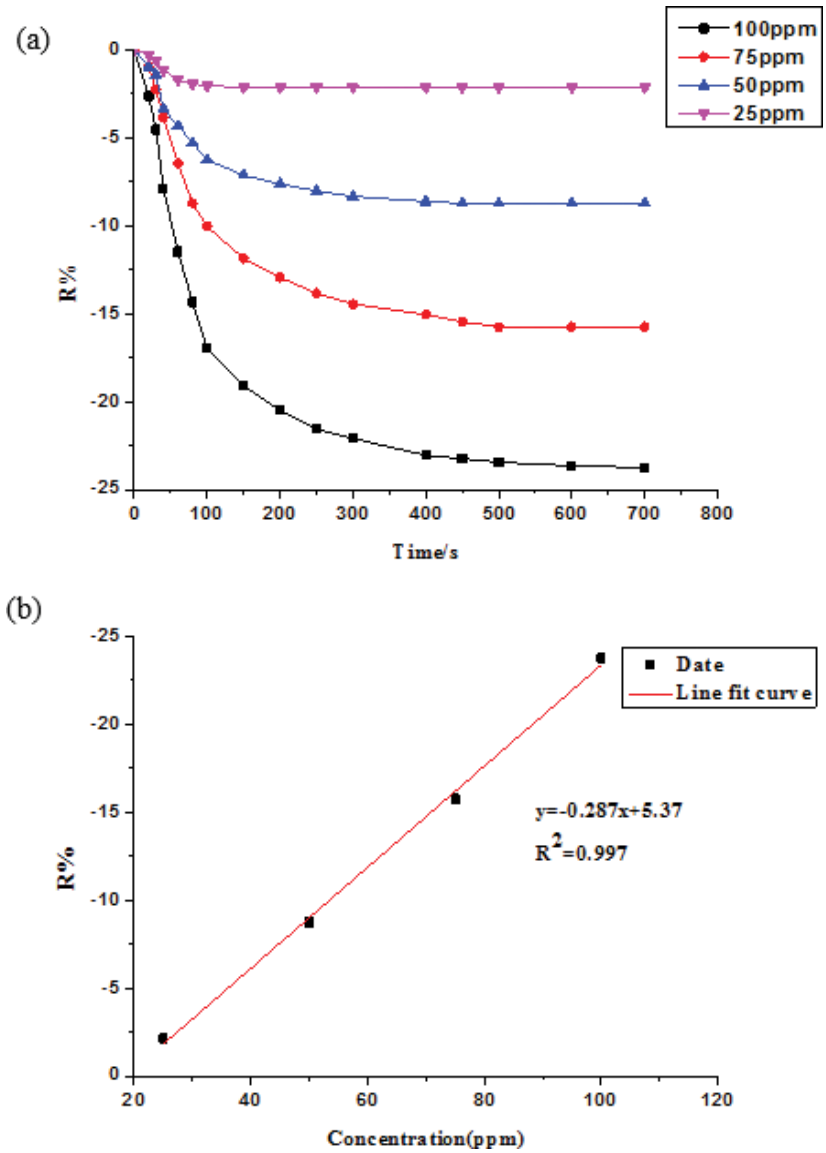

Figure 38. (a) Au-TiO_2 NTAs' response to different concentrations of SO_2 at the 110°C working temperature. (b) Linear relationship between the sensor's response value and the SO_2 concentration.

relationship between the sensor's resistance change rate and the SO_2 concentration is fitted as y = −0.287x + 5.37 with a linear correlation coefficient (R^2) of 0.997 [1].

2.3.3.2. Sensing performances of Au-TiO_2 NTAs for SOF_2

Figure 39 [1] exhibits the sensing response curves of the Au-TiO_2 nanotube sensor for SOF_2 at different concentrations under 110°C. From **Figure 39a**, the resistance change rates that correspond to 25, 50, 75 and 100 ppm of SOF_2 are separately −3.00, −9.97, −18.42 and −28.37%. After linear fitting, the linear function is calculated to be y = −0.338x + 6.197, as shown in **Figure 39b**,

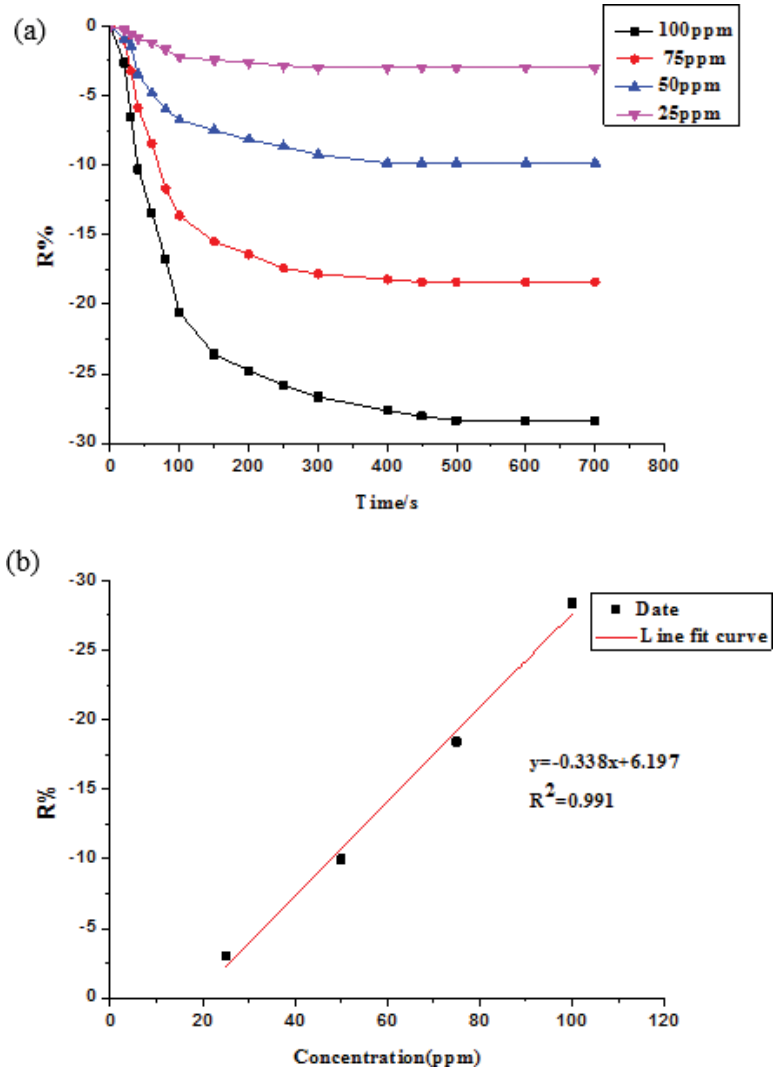

Figure 39. (a) Au-doped TiO_2 NTAs' response to different concentrations of SOF_2 at the 110°C working temperature. (b) Linear relationship between the sensor's response value and the SOF_2 concentration.

http://dx.doi.org/10.5772/intechopen.68328

with R^2 equaling 0.991. It can be concluded that, within a certain range of concentrations, a linear relationship between the resistance change rate of the Au-TiO_2 nanotube sensor and the SOF_2 concentration is also displayed [1].

2.3.3.3. Sensing performances of Au-TiO_2 NTAs for SO_2F_2

Resistance change rates of Au-TiO_2 nanotube gas sensor for SOF_2 with different concentrations at 25, 50, 75 and 100 ppm are, respectively, −4.04, −19.58, −30.93 and −42.31%, as shown in **Figure 40a**. The linear fitting relationship is y = −0.503x + 7.138 and the linear correlation coefficient R^2 equals 0.991 [1].

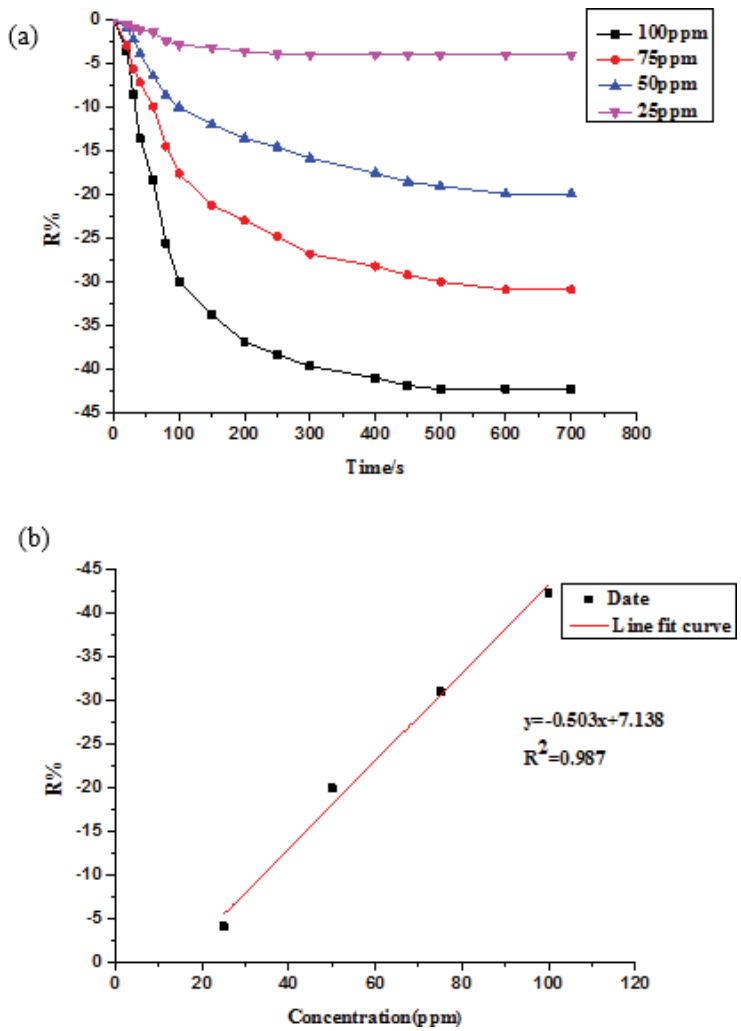

Figure 40. (a) Au-doped TiO_2 NTAs response to different concentrations of SO_2F_2 at the 110°C working temperature. (b) Linear relationship between the sensor's response value and the SO_2F_2 concentration.

Figure 41 [1] shows the gas-sensing response comparison chart of intrinsic and Au-doped TiO_2 NTAs at their optimum operating temperatures for 50 ppm SF_6 decomposed gases, that is, SO_2, SOF_2 and SO_2F_2, where the gas-sensing properties of intrinsic TiO_2 NTAs have been discussed in [1, 52]. The responses of intrinsic and Au-doped TiO_2 NTAs both exhibit a negative behavior, that is, the resistances of intrinsic and Au-doped TiO_2 NTAs decrease after introducing these gases.

The gas-sensing response values of the intrinsic TiO_2 nanotube sensor are SO_2 (−74.6%) > SOF_2 (−7.82%) > SO_2F_2 (−5.52%), while for the Au-TiO_2 nanotube sensor is SO_2F_2 (−19.95%) > SOF_2 (−9.97%) > SO_2 (−8.73%). It is worth noting that the experimental results in our study are statistically significant, the values of which are at the average level according to dozens of experiments [1]. Obviously, the response value of SO_2F_2 dramatically increases, while SO_2 is reduced, and the response of SOF_2 remains constant. The selective detection of SO_2F_2 was actually achieved in our experimental research by the modification of Au nanoparticles at the appropriate operation temperature [1]. Hence, the Au-TiO_2 NTAs are potential substrates for the SO_2F_2 detection application. Furthermore, combined Au-doped and intrinsic TiO_2 arrays are promising substrates for SF_6 decomposition component detection [1].

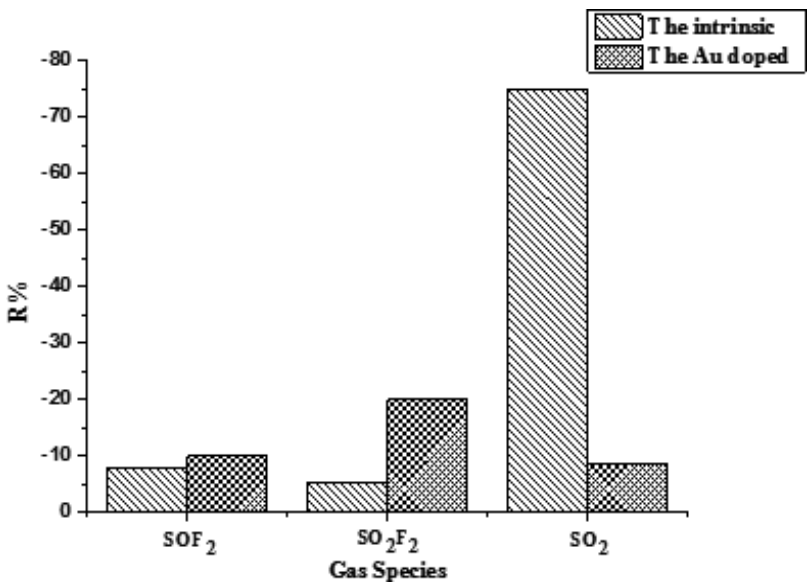

Figure 41. Sensor responses of Au-doped and intrinsic TNTA for SF_6 decomposition components.

Acknowledgements

Parts of this chapter are reproduced from Refs. [27–28] with Elsevier's permission and from Refs. [1, 37] under the terms of their respective Creative Commons licenses.

http://dx.doi.org/10.5772/intechopen.68328

Author details

Ju Tang, Xiaoxing Zhang*, Song Xiao and Fuping Zeng

*Address all correspondence to: xiaoxing.zhang@outlook.com

School of Electrical Engineering, Wuhan University, Wuhan, China

References

[1] Xiaoxing Zhang JZ, Yichao Jia, Peng Xiao, Ju Tang. TiO2 Nanotube Array Sensor for Detecting the SF6 Decomposition Product SO2. Sensors. 2012;**12:**3302–3313

[2] Beyer C, Jenett H, Klockow D. Influence of reactive SFx gases on electrode surfaces after electrical discharges under SF_6 atmosphere. IEEE Transactions on Dielectrics and Electrical Insulation. 2000;**7**:234–240

[3] Mor GK, Shankar K, Paulose M, Varghese OK, Grimes CA. Enhanced photocleavage of water using Titania nanotube arrays. Nano Letters. 2005;**5**:191–195

[4] Grimes CA, Mor GK. TiO_2 NT Arrays Synthesis, Properties, and Applications. Norwell, MA: Springer; 2009

[5] Seo M-H, Yuasa M, Kida T, Huh J-S, Yamazoe N, Shimanoe K. Detection of organic gases using TiO_2 nanotube-based gas sensors. Procedia Chemistry. 2009;**1**:192–195

[6] Lin S, Li D, Wu J, Li X, Akbar SA. A selective room temperature formaldehyde gas sensor using TNTA. Sensors and Actuators B. 2011;**156**:505–509

[7] Yun H. Preparation of NO_2 Gas Sensor Based on TiO_2 Nanotubes. [thesis], Dalian, China: Dalian University of Technology; 2005

[8] Varghese OK, Gong D, Paulose M, Ong KG, Grimes CA. Hydrogen sensing using Titania nanotubes. Sensors and Actuators B. 2003;**93**:338–344

[9] Mor GK, Varghese OK, Paulose M, Shankar K, Grimes CA. A review on highly ordered, vertically oriented TNTA: Fabrication, material properties, and solar energy applications. Solar Energy Materials and Solar Cells. 2006;**90**:2011–2075

[10] Mor GK, Varghese OK, Paulose M, et al. A review on highly ordered, vertically oriented TNTA: Fabrication, material properties, and solar energy applications. Solar Energy Materials & Solar Cells. 2006;**90**(14):2011–2075

[11] Hulteen JC, Martin CR. A general template-based method for the preparation of nanomaterials. Journal of Materials Chemistry. 1997;**7**(7):1075–1087

[12] Lakshmi BB, Dorhout PK, Martin CR. Sol-gel template synthesis of semiconductor nanostructures. Chemistry of Materials. 199**7**:857–862

[13] Lakshmi BB, Patrissi CJ, Martin CR. Sol-gel template synthesis of semiconductor oxide micro-and nanostructures. Chemistry of Materials. 1997, **9**:2544–2550.

[14] Gong D, Grimes CA, Varghese OK, et al. Titanium oxide nanotube arrays prepared by anodic oxidation. Journal of Materials Research. 2001;**16**:3331

[15] Kasu G, Hirama T, Hoson A, et al. Formation of titanium oxide nanotube. Langmuir. 1998;**14**:3160

[16] Cheng ZJ, Liu TY, Yang CX, Gan HX, Chen JY, Zhang FW. Ab initio atomic thermodynamics investigation on oxygen defects in the anatase TiO_2. Journal of Alloys and Compounds. 2013;**546**:246–252

[17] Vittadini A, Casarin M, Selloni A. Chenmistry of and on TiO_2-anatase surfaces by DFT calcutions: A partial review. Theoretical Chemistry Accounts. 2007;**117:**663–671

[18] Perdew JP, Burke K, Ernzerhof M. Generalized gradient approximation made simple. Physical Review Letters. 1996;**77**:3865

[19] Delley B. An all-electron numerical method for solving the local density functional for polyatomic molecules. The Journal of Chemical Physics. 1990;**92:**508–517

[20] Delley B. From molecules to solids with the DMol approach. The Journal of Chemical Physics. 2000;**113:**7756–7764

[21] Monkhorst H, Pack JD. Special points for Brillouin-zone integrations. Physical Review B. 1976;**13**:5188–5192

[22] Long R, Dai Y, Huang B.B. Energetic and electronic properties of X-(Si, Ge, Sn, Pb) doped TiO_2 from first-principles. Computational Materials Science. 2009;**45:**223–228

[23] Yen CC, Wang DY, Chang LS, Shih HC. Characterization and photocatalytic activity of Fe-and N-co-deposited TiO_2 and first-principles study for electronic structure. Journal of Solid State Chemistry. 2011;**184:**2053–2060

[24] Burdett JK, Hughbanks T, Miller GJ, Richardson JW Jr, Smith JV. Structural-electronic relationships in inorganic solids: powder neutron diffraction studies of the rutile and anatase polymorphs of titanium dioxide at 15 and 295K. Journal of the American Chemical Society. 1987;**109:**3639–3646

[25] Valentin CD, Pacchioni G, Selloni A, Livraghi S, Giamello E. Characterization of paramagnetic species in N-doped TiO_2 powers by EPR spectroscopy and DFT calculations. The Journal of Physical Chemistry B. 2005;**109:**11414–11419

[26] Zhang X, Chen Q, Tang J, Hu W, Zhang J. Adsorption of SF6 decomposed gas on anatase (101) and (001) surfaces with oxygen defect: a density functional theory study. Scientific Reports. 2014;**4:**4762

[27] Zhang X, Chen Q, Hu W, Zhang J. Adsorptions of SO 2, SOF 2, and SO 2 F 2 on Pt-modified anatase (1 0 1) surface: sensing mechanism study. Applied Surface Science. 2015;**353:**662–669

[28] Zhang X, Dong X, Gui Y. Theoretical and experimental study on competitive adsorption of SF 6 decomposed components on Au-modified anatase (101) surface. Applied Surface Science.2016;**387:**437–445

[29] Zhang X, Chen Q, Hu W, Zhang J. A DFT study of SF_6 decomposed gas adsorption on an anatase (101) surface. Applied Surface Science. 2013;**286:**47–53

[30] Zhang X, Chen Q, Tang J, Hu W, Zhang J. Adsorption of SF_6 decomposed gas on anatase (101) and (001) surfaces with oxygen defect: a density functional theory study. Scientific Reports. 2014;**4:**1–11

[31] Gong D, Grimes CA, Varghese OK, Hu WC, Singh RS, Chen Z, Dickey EC. Titanium oxide nanotube arrays prepared by anodic oxidation. Journal of Materials Research. 2001;**16:**3331–3334

[32] Zhou WQ, Zhai CY, Du YK, Xu JK, Yang P. Electrochemical fabrication of novel platinum-poly(5-nitroindole) composite catalyst and its application for methanol oxidation in alkaline medium. International Journal of Hydrogen Energy. 2009;**34**:9316–9323

[33] Gangal ND, Gupta NM, Lyer RM. Microcalorimetric study of the interaction of CO, O_2, and CO + O_2 with Pt/SnO_2 and SO_2 catalysts. Journal of Catalysis. 1990;**11:**13–25

[34] Zhang XX, Zhang JB, Jia YC, Xiao P, Tang J. TiO_2 nanotube array sensor for detecting the SF6 decomposition product SO_2. Sensors. 2012;**12**:3302–3313

[35] Okazaki K, Ichikawa S, Maeda Y, Haruta M, Kohyama M. Electronic structures of Au supported on TiO_2. Applied Catalysis A General. 2005;**291:**45–54

[36] Zhang X, Chen Q, Hu W, et al. A DFT study of SF_6 decomposed gas adsorption on an anatase (101) surface. Applied Surface Science. 2013;**286**(12):47–53

[37] Zhang X, Yu L, Jing T, Dong X. Gas sensitivity and sensing mechanism studies on Au-doped TiO2 nanotube arrays for detecting SF6 decomposed components. Sensors. 2013;**14:**19517–19532

[38] Xing XZ, Bin JZ, Jia Y, Peng X, Ju T. TiO_2 nanotube array sensor for detecting the SF_6 decomposition product SO_2. Sensors. 2012;**12**:3302–3313

[39] Zhu B, Guo Q, Huang X, Wang S, Zhang S, Wu S, Huang W. Characterization and catalytic performance of TiO_2 nanotubes-supported gold and copper particles. Journal of Molecular Catalysis A: Chemical. 2006;**249**:211–217

[40] Cunningham DAH, Vogel W, Kageyama H, Tsubota S, Haruta M. The relationship between the structure and activity of nanometer size gold when supported on $Mg(OH)_2$. Journal of Catalysis. 1998;**177**:1–10

[41] Dekkers MAP, Lippits MJ, Nieuwenhuys BE. Supported gold/MO_x catalysts for NO/H_2 and CO/O_2 reactions. Catalysis Today. 1999;**54**:381–390

[42] Macak JM, Schmuki P. Anodic growth of self-organized anodic TiO_2 nanotubes in viscous electrolytes. Electrochimica Acta. 2006;**52**:1258–1264

[43] Xu Q, Kharas KC, Datye AK. The preparation of highly dispersed Au/Al_2O_3 by aqueous impregnation. Catalysis Letters. 2003;**85**:229–235

[44] Guczi L, Beck A, Pászti Z. Gold catalysis: effect of particle size on reactivity towards various substrates. Catalysis Today. 2012;**181**;26–32

[45] Ivanova S, Petit C, Pitchon V. A new preparation method for the formation of gold nanoparticles on an oxide support. Applied Catalysis A: General. 2004;**267**:191–201

[46] Haruta M, Ueda A, Tsubota S, Torres Sanchez RM. Low-temperature catalytic combustion of methanol and its decomposed derivatives over supported gold catalysts. Catalysis Today. 1996;**29**:443–447

[47] Şennik E, Çolak Z, Kılınç N, Öztürk ZZ. Synthesis of highly-ordered TiO_2 nanotubes for a hydrogen sensor. International Journal of Hydrogen Energy. 2010;**35**:4420–4427

[48] Sun XM, Yadong L. Synthesis and characterization of ion-exchangeable titanate nanotubes. Chemistry - A European Journal. 2003;**9**:2229–2238

[49] Varghese OK, Gong D, Paulose M, Ong KG, Grimes CA. Hydrogen sensing using titania nanotubes. Sensors and Actuators B: Chemical. 2003;**93**:338–344

[50] Patterson AL. The Scherrer formula for X-ray particle size determination. Physical Review. 1939;**56**:978

[51] Xing XZ, Jing T, Bin JZ. A Pt-doped TNTA sensor for detecting SF_6 decomposition products. Sensors. 2013;**13**:14764–14776

[52] Xing XZ, Bin JZ, Jia Y, Peng X, Ju T. TiO_2 Nanotube array sensor for detecting the SF_6 decomposition product SO_2. Sensors. 2012;**12**:3302–3313

Chapter 4

Application of Graphene Gas Sensors in Online Monitoring of SF_6 Insulated Equipment

Xiaoxing Zhang, Ju Tang, Song Xiao and Cheng Pan

Additional information is available at the end of the chapter

http://dx.doi.org/10.5772/intechopen.68329

Abstract

Graphene is an allotrope of carbon apart from graphite, diamond, fullerene and carbon nanotubes. Because graphene has unique mechanical, structural, thermal and electrochemical properties and can present the stability characteristics of these features, it becomes two-dimensional (2-d) materials which can alter three-dimensional (3-d) carbon nanotubes composite materials and has important research value. Pristine graphene and graphene films doped with Au nanoparticles were synthesized by the chemical reduction method. Their corresponding gas sensors were both fabricated by the traditional drop coating method and then used as an adsorbent for the detection of H_2S, SO_2, SOF_2 and SO_2F_2 at room temperature. Theoretical simulation was also investigated when the decomposed gaseous components of sulfur hexafluoride (SF_6), namely, H_2S, SO_2, SOF_2 and SO_2F_2, were adsorbed on pristine and Au-embedded graphene based on DFT. In order to interpret the adsorption processes between Au-doped graphene and gas molecules, this chapter discussed the charge transfer mechanism on the adsorption surface for further investigation.

Keywords: graphene, properties, preparation methods, characterization analysis, Au-decorated graphene, experimental response

1. Introduction of graphene

1.1. Properties of graphene

Graphene is an allotrope of carbon apart from graphite, diamond, fullerene and carbon nanotubes, and it is also a kind of atomic crystal with two-dimensional laminar nano-structure materials. It was first prepared by Professor Geim in the University of Manchester by the micro-mechanical

stripping method [1]. The discovery of the new material confirmed that a strict two-dimensional material existed in the nature. The research group of Professor Geim found that the new materials had unique, excellent physical and chemical properties and had great development potential and application space in super capacitor, biochemical, fuel cell, etc. after carrying out system characterization on electrical properties of graphene. Professor Geim and Dr Novoselov won the Nobel Prize for physics in 2010 for a groundbreaking research. This raised a hot wave of graphene research.

The thickness of the monolayer graphene is only 0.34 nm, that is, the thickness of the layer of carbon atoms [2]. The outer electron distribution of C-atoms is $2s^2 2p^2$, two 2s electrons and one 2p electron form two-dimensional hexagonal honeycomb structure by sp^2 hybridization. **Figure 1** is the diagram of graphene configuration and **Figure 2** is the band structure of graphene. The strong C-C bonds making the graphene layer has excellent structural rigidity. Each carbon atom

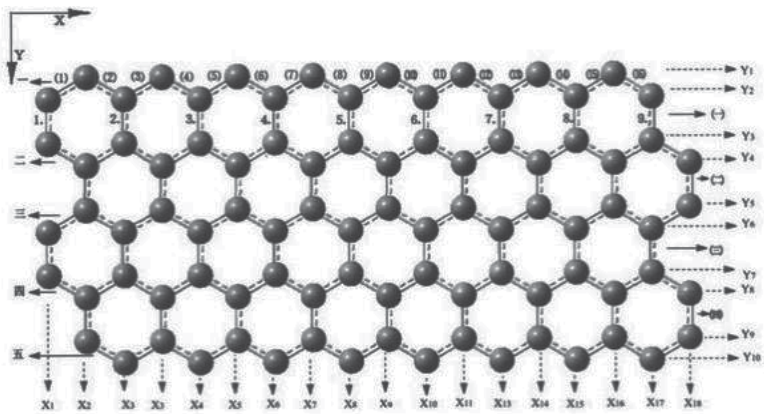

Figure 1. Graphene configuration diagram.

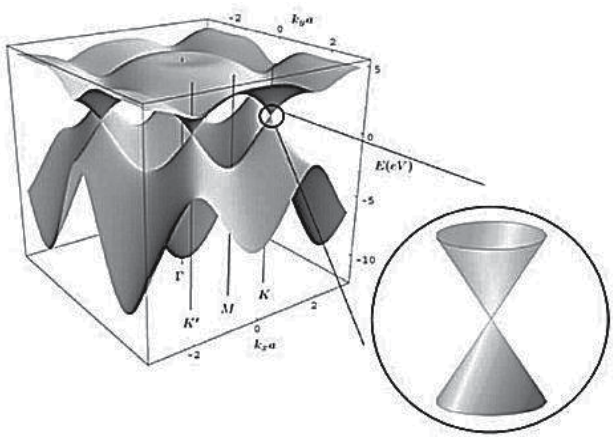

Figure 2. Graphene band structure.

has a non-binding 2p free electron. These electrons process free motion in delocalized π-orbitals which were formed in the vertical direction of carbon atoms plane. Thus, graphene has good electrical conductivity [3]. By analyzing the energy band structure of graphene and brillouin zone map, we can find that the conduction band and valence band are like cone-shaped valleys [4, 5]. They are highly symmetrical in the brillouin zone and form a double cone. There is a linear relationship between amplitude of the momentum and the change of the energy. The conduction band and valence band just intersect at six points of Fermi level. The state density is 0 at these six points. Because of the unique structure of graphene [4], it has incomparable excellent properties compared with other materials. At present, the physical properties which have been confirmed include:

- The carrier concentration of graphene is $10^{12}/cm^2$ and the electrical resistivity is 10^{-6} Ω/cm^3. It has been found that graphene is the best conductor at room temperature [6].
- Single layer graphene has ultra-high carrier mobility at room temperature, which can reach 2×10^5 cm^2/Vs [7].
- Each carbon atom can act as the surface atom on graphene, as all carbon atoms are exposed. Therefore, graphene has a large specific surface area, which has a theoretical value of 2630 m^2/g [8].
- Graphene has extremely low Johnson noise under the condition of small carries amount. Therefore, a very small change of carrier concentration will cause significant change in the conductivity [9].
- The typical electronic conduction velocity of graphene is 8×10^5 m/s, nearly 1/400 of the propagation velocity of light in vacuum and much larger than electrical conduction rate of general semiconductor materials [10].

1.2. Preparation methods of graphene

Because graphene has unique mechanical, structural, thermal and electrochemical properties and can present the stability characteristics of these features, it becomes 2-d materials which can alter 3-d carbon nanotubes composite materials and has important research value. These superior properties, however, depend largely on the process of separating graphite substrate into the nano-sized level of the graphene layer. As carbon nanotubes and other nano-composite materials, the first problem before graphene materials that can be widely used is how to synthesis single layer or fewer layers of high-quality graphene. How to get complete structure and disperse graphene evenly in a solution becomes the second biggest problem among scholars around the world. In addition, due to the interaction of van der Waals force, graphene may irreversibly stack and accumulate unless graphene layers completely separate. But the majority of superior physical and chemical properties of graphene materials only exists in single-layer graphene. Therefore, the synthesis of graphene has a vital influence in its application in various fields. Effectively preventing it from stacking and accumulating is particularly important. If one summarizes achievements in the field of graphene synthesis in recent years, scholars mainly found the exfoliation method, several synthetic methods, etc. Different synthetic methods can be chosen according to different applications:

1.2.1. Mechanical exfoliation method

The mechanical exfoliation method is the simplest way of preparation of graphene [11, 12]. Research group of Geim first got single-layer graphene by this method [8]. This was only a 0.34 nm of two-dimensional layered nanostructures atomic crystal. The significance of this study was that it confirmed that the perfect two-dimensional crystal can also stably exist in finite temperature and corrected the fallacy that a two-dimensional crystal cannot exist in finite temperature stability in material science field. This method uses high orientation pyrolysis graphite (HOPG) as raw materials, and the specific steps are: make HOPG of 1 mm deep from a square platform of 5-μm deep after oxygen plasma etching and adhere the square platform on the photoresist and extrude properly. Repeatedly strip off the graphene sheets from square HOPG piece using transparent tape. At last, dissolve the graphene which adheres on the photoresist in acetone and transfer it to the silicon substrate and process ultrasonic treatment. Remove the thicker sheet and get the graphene of less than 10 nm thick. It is generally believed that this type of method for preparing graphene layers can get single layer and fewer layers of graphene which have relatively good crystal structure, least structure defects and excellent physical and chemical properties. But this method is time consuming and cannot effectively control the thickness of graphene layer. It is also vulnerable to tape pollution and the yield is very low. So, this method cannot realize large-scale preparation of graphene synthesis.

In general, the mechanical exfoliation method is still the most effective method for preparation of single layer or fewer layer of high-quality graphene. This method is suitable for the laboratory basic theory research.

1.2.2. Chemical stripping method

Chemical stripping method is the method that by using oxidizing graphite, remove the oxygen-containing functional groups between the graphite layers so as to get a large area of graphene [12, 13]. At present, there are mainly three methods (Brodie, Staudenmaier and Hummers) for graphite oxidation treatment. Among them, Hummers is most commonly used because preparation process parameters can be easily modified and effectively reduce emissions of poison. After oxidation treatment, the flake graphite layers interact mainly by weak van der Waals force, effectively improving the graphite layer spacing. Removing oxygen-containing functional groups between graphite layers includes both chemical reduction and thermal reduction method. The main reducers used in chemical reduction method are hydrazine, vitamin C, etc. Hydrazine is a kind of strong polarity toxic compounds. Research has confirmed that environmental vitamin C can also obtain good reduction effect. No matter what kind of reducing agent is chosen, chemical reduction process will inevitably leave a certain amount of oxygen, resulting in lower conductivity of graphene by the chemical reduction method compared with the mechanical stripping method. Heat treatment is also an effective method for reducing oxidized graphite, which works effectively in alkaline environment or in microwave conditions. At present, there is research that combined the chemical reduction and thermal reduction methods to reduce oxidized graphite. Overall, chemical stripping method is an effective method to realize the large-scale preparation of graphene, which has the advantages of fewer layers, high yield, and is easy to operate, but the graphene

prepared by the method is easily polluted by the addition of dispersion solvent; the crystal structure has some defects and is somewhat mixed and disorderly. Therefore, this method is suitable for sensor and catalytic applications where the conductivity requirements are not rigorous.

1.2.3. Chemical vapor deposition (CVD) method

Chemical vapor deposition method is the most accepted method for preparation of large size monolayer or fewer layers of high-quality graphene [14–16]. Graphene is the first compound prepared by Somani research team using this method. In CVD method, graphene growth needs the high temperature of around 1000°C and must have a fast cooling process. Hydrocarbon gases such as methane, methanol act as carbon source, interact with foil catalytic media like nickel, drill or copper. Under the suitable growth temperature, the carbon element inside the gas will effectively dissolve in metal foil, similar to the carburizing process. Then, in the rapid quenching process, the carbon dissolved in the metal foil separate out of the surface, thus forming a layer of uniform, a relatively perfect and large size of crystal structure of graphene films. From growth mechanism, the thickness and crystalline sequence of the graphene by this method are decided mainly by the quenching rate, thickness of metal foil and the carbon content dissolved in the metal foil. Graphene prepared by the CVD method can be easily transferred to other basement, such as SiC, SiO_2 substrate, and can also be cut to suitable size according to its uses which provides convenience for the subsequent application. In any case, the CVD method provides graphene synthesis method for a layer of controllable size, regular crystal of monolayer or fewer layers of high-quality graphene, which makes it possible to have large production of thin film electrode in volume. The disadvantages of this method include complexity of process and relatively high cost.

1.2.4. Epitaxial method

Ultrahigh vacuum thermal treatment of SiC is an effective way to obtain high-quality graphene layers [17, 18], especially in semiconductor manufacturing industry. The graphene prepared by this method is widely used because it is directly used with insulating properties of SiC for substrate without any complex substrate transfer process which can be directly assembled. When 6H-SiC single crystal in ultra-high vacuum conditions is heated to a certain temperature, Si atoms on the surface will sublimate from the basal surface because of its higher vapor pressure, and the C atom not sublimated will stay on the basal surface rearranged to form honeycomb stable structure, which becomes the graphene layer. The thickness of the graphene layers depends on the annealing time and heating temperature. The study shows that the condition for the preparation of fewer layers of graphene is treated with the high temperature of 1200–1600°C after 1 hour, and then have a few minutes of SiC annealing treatment. According to a study, the high temperature of 1600°C on SiC substrate is more advantageous to form a uniform fewer layer graphene. Despite the epitaxial method, it is worth looking forward to, but there are a few questions that need to be resolved. First of all, how to precisely control the thickness of the large size graphene film in the actual production is the first challenge to face. Second, epitaxial graphene layers grown on different surfaces in SiC (Si, C surface) differ in structure, thickness, even some physical properties and electrical properties,

and the mechanism of above differences has not obtained any breakthrough. The relationship of structure and electron properties between two layers, between lamella and substrate, is the third challenge for further study. Anyhow, graphene prepared by epitaxial method only bases on SiC and cannot be transferred to other substrate, which limits its application in other areas.

1.2.5. Other synthetic methods

In addition to several commonly used preparation methods introduced above, there are other methods like organic synthesis method, cracking carbon nanotube method, arc discharge method [19]. Organic synthesis is mainly used to form graphene-like hydrocarbons polymer (PAHs) by organic reactions. Although this method can realize diversity of synthesis, grafting boundary, changing solubility and many other advantages, the biggest question is how to stably store, spread and form a large area of two-dimensional plane PAHs. Cracking the carbon nanotube method mainly depends on carbon nanotubes, these contain curling graphene layers. The advantage of this method is that the preparation methods of different size carbon nanotubes have ease of application, so the size of the graphene layer can be controlled effectively by etching and cracking of hydrogen plasma. For amorphous carbon, the arc discharge method is used to obtain perfect lattice and stable graphene by high temperature plasma modification of amorphous carbon and H: etching. Studies have demonstrated that the arc discharge process is actually a fast thermal reduction process, which prepares high conductivity and stable graphene after liquid phase separation and centrifugation.

2. Decorated graphene

2.1. Gas sensing properties of pristine graphene and Au-decorated graphene to SOF_2, SO_2F_2, SO_2 and H_2S through simulation

We investigated the adsorption effects of gaseous molecules on pristine graphene and Au-graphene. **Figure 3(a)–(h)** shows the most stable adsorption configurations of H_2S, SO_2, SO_2F_2 and SOF_2 on pristine graphene and Au-graphene. All presented stable configurations have the lowest energies of various adsorption sites with different gas molecular orientations. We focused on the adsorption of H_2S, SO_2, SOF_2 and SO_2F_2 [20].

2.1.1. H_2S adsorption

We mainly considered eight possible configurations for an H_2S molecule on pristine graphene: four different orientations for H atoms close to the C plane, three different configurations for S atoms close to the C plane and a configuration for an H_2S molecule parallel with the C plane. Comparing these binding energies, two H atoms perpendicular to the graphene surface on the hollow site, shown in **Figure 3(a)**, is the most thermodynamically stable configuration. **Table 1** details the calculated results for adsorption distance, E_{ad}, bond length, charge transfer (CT) and magnetic moment for the entire system of H_2S adsorbed on pristine graphene and Au-graphene. The results show that the geometric structure of H_2S (1.356 Å for H-S bond length and 91.076 for H-S-H bond angle) practically remains the same as in the gas phase. The

http://dx.doi.org/10.5772/intechopen.68329

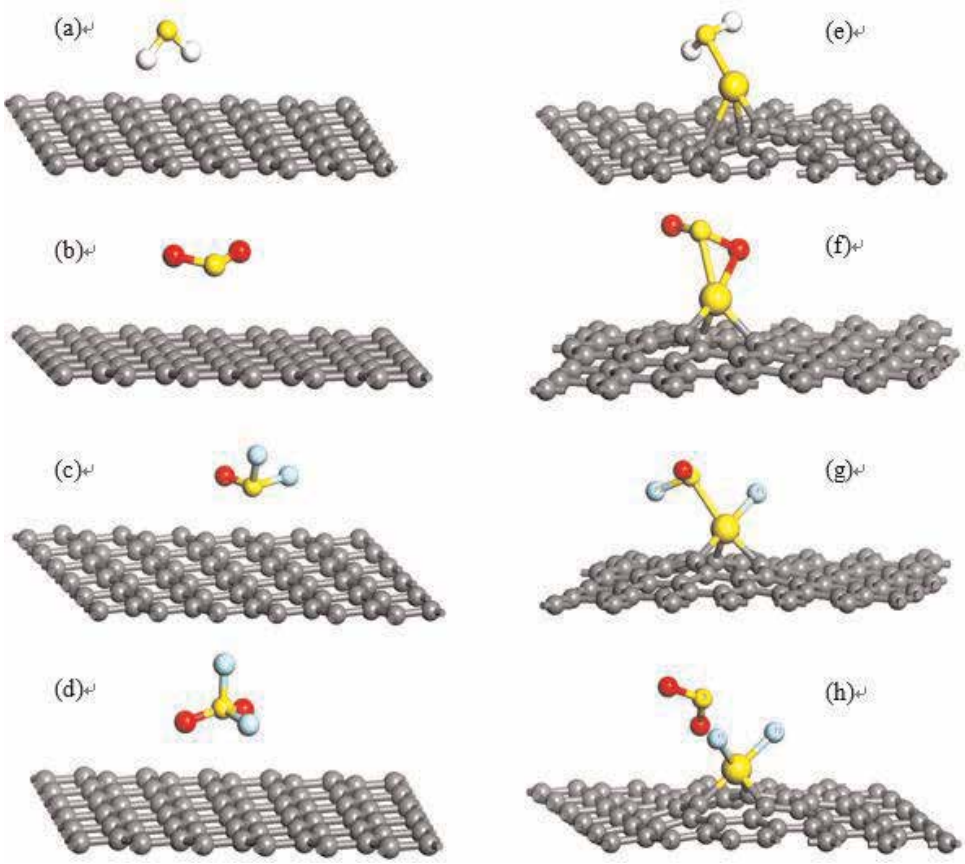

Figure 3. (a)–(d) Optimized configurations for H_2S, SO_2, SOF_2 and SO_2F_2 adsorbed on pristine graphene; (e)–(h) optimized configurations for H_2S, SO_2, SOF_2 and SO_2F_2 adsorbed on Au-graphene. Various configurations were considered; only the most stable ones were presented.

Configuration	d (Å)	E_{ad} (eV)	Bond length (Å)	Q_t (e)	M (μ_B)
Au-graphene	\	\	\	\	−1.005
H_2S	\	\	1.356 (S-H)	\	0
H_2S on graphene	3.108	−0. 717	1.356 (S-H)	+0.011	0
H_2S on Au-graphene	2.401	−0.900	1.360 (S-H_1), 1.362 (S-H_2)	+0.348	0.999

Table 1. H_2S adsorption on pristine graphene and Au-graphene: adsorption distance (d), adsorption energy (E_{ad}), bond length, charge transfer from H_2S to the substrate (Q_t), and magnetic moment of the entire system (M).

Mulliken population analysis demonstrates that fewer than 0.011 electrons are transferred from the H_2S molecule to the pristine graphene. The E_{ad} (−0.717 eV) is a relatively strong intermediate between physisorption and chemisorption, which indicates that van der Waals acts as a main factor.

Figure 3(e) shows that H_2S is adsorbed parallel to the graphene surface with the S atom closest to the Au-graphene plane in all original positions of Au-graphene. The geometric structure of H_2S changed only slightly; the H-S-H bond angle became 91.719, while each H-S bond length became 1.360 and 1.362 Å, respectively. However, adsorption distance decreased to 2.401 Å, and E_{ad} significantly increased to 0.90 eV. A total of 0.348 electrons got transferred from the H_2S molecule to Au-graphene, which leads to electron enrichment of the Au-graphene surface. These results reveal a stronger interaction in the Au-graphene adsorption system than in the pristine one.

The calculated density of states (DOS) for pristine graphene and Au-graphene, with and without a single H_2S molecule, are plotted in **Figure 4(a)** to further understand H_2S interaction with the Au-graphene surface. A slight difference was observed near the Fermi level, which indicates a decrease in the surrounding DOS and a magnetism alteration of the magnetic moment to 0.999 μ_B is obtained. **Figure 4(b)** shows an analysis of partial DOS (PDOS) for the H_2S molecule and Au atom. **Table 2** lists orbital CTs. The 3p of S in H_2S and 5-d orbital of Au are hybridized between −9 and −1.1 eV in a valence band with a certain filling rate degree in PDOS peaks. A comparison between **Figure 4(b)** and **Table 2** shows that the electrons in the 5-d orbital of Au that are populated to initially empty spin-down π^* are obtained, which leads to a strong interaction between Au and H_2S.

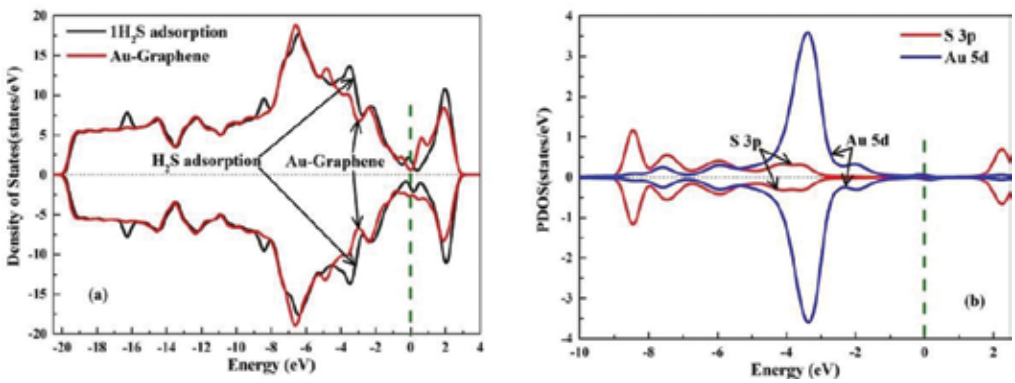

Figure 4. (a) Spin-polarized total DOS for Au-graphene with and without single H_2S adsorption; (b) PDOS projected on the 3p of S in H_2S and 5d orbital of Au. Fermi energy is set to $E-E_f$.

Element	s (e)	p (e)	d (e)	Charge (e)	Spin (μ_B)
Au	−0.28	−0.336	+0.432	−0.184	0.049
S	+0.237	−0.178	−0.202	−0.141	−0.005
H_1	+0.272	−0.03	\	0.241	0.000
H_2	+0.279	−0.03	\	0.248	0.001

Table 2. H_2S adsorption on Au-graphene: charges transfer in s, p and d orbitals, and total charge, spin magnetic moment of a single atom.

2.1.2. SO_2 adsorption

Figure 3(b) shows that the most energetically favorable configuration for SO_2 adsorption on pristine graphene is the S atom on top of the T site carbon atom, with SO_2 lying nearly parallel to the surface and the S atom, tilting slightly toward it. Three configurations for the S atom initially approached the graphene plane because of the different orientations on the carbon ring. These configurations include three positions for two O atoms close to it and one configuration for the SO_2 molecule parallel to it; they are all studied. The calculated E_{ad} and d are 0.302 eV and 3.335 Å, respectively. S-O bond length and bond angle are at 1.482 Å and 119.550, respectively; they remain almost the same as in the gas phase (1.480 Å and 119.916). A total of 0.012 electrons transfer from the pristine graphene to the SO_2 molecule. Consequently, SO_2 undergoes van der Waals interaction on pristine graphene.

Figure 3(f) shows that SO_2 is adsorbed with one S-O bond approaching Au in the Au-graphene substrate; a significant increase in E_{ad} and CT and a notable decrease in adsorption distance are observed. **Table 3** details all these values. The close S-O bond is expanded from 1.480 Å in the gas phase to 1.609 Å in the adsorption system, with the bond angle (O-S-O) changing from 119.550 to 114.944. This stable configuration exhibits a 0.351 eV charge flow from Au-graphene to the SO_2 molecule, which indicates that SO_2 has a charge acceptor nature. These findings indicate that a stronger interaction occurred on Au-graphene (−0.587 eV) compared with pristine graphene (−0.302 eV). However, chemisorption with a binding energy above 0.8 eV was not observed.

Figure 5(a) shows the DOS for Au-graphene with and without single SO_2 molecule adsorption. The PDOS for Au and SO_2 were also plotted in **Figure 5(b)**. Asymmetrical spin-up and spin-down channels maintain metallicity. The spin-up channel of SO_2 adsorption on Au-graphene is obviously altered near the Fermi level, which leads to a magnetic moment of 0.948 μ_B for the entire system. The 5-d electrons of Au are hybridized with π states of S and O at −6.5eV in the valence band, which is indicated in the atomic population analysis results (**Table 4**). This hybridization results in a strong E_{ad} to SO_2.

2.1.3. SOF_2 adsorption

Adsorption of an uncommon SOF_2 is more complicated than that of H_2S or SO_2. SOF_2 and SO_2F_2 adsorption on graphene-based materials has not been studied. We thoroughly investigate two kinds of gases. For SOF_2 on pristine graphene, we considered the S atom down to the graphene surface with three positions (H, T and B sites) and the F and O parallel atoms down to the plane with two different orientations. **Figure 3(c)** shows that the configuration of

Configuration	d (Å)	E_{ad} (eV)	Bond length (Å)	Q_t (e)	M (μ_B)
SO_2	\	\	1.480 (S-O)	\	0
SO_2 on graphene	3.335	−0.302	1.482 (S-O)	−0.012	0
SO_2 on Au-graphene	2.176	−0.587	1.609 (O_1-S), 1.501 (O_2-S)	−0.351	0.948

Table 3. SO_2 adsorption on pristine graphene and Au graphene: adsorption distance (d), adsorption energy (E_{ad}), bond length, charge transfer from the substrate to SO_2 (Q_t), and magnetic moment of the entire system (M).

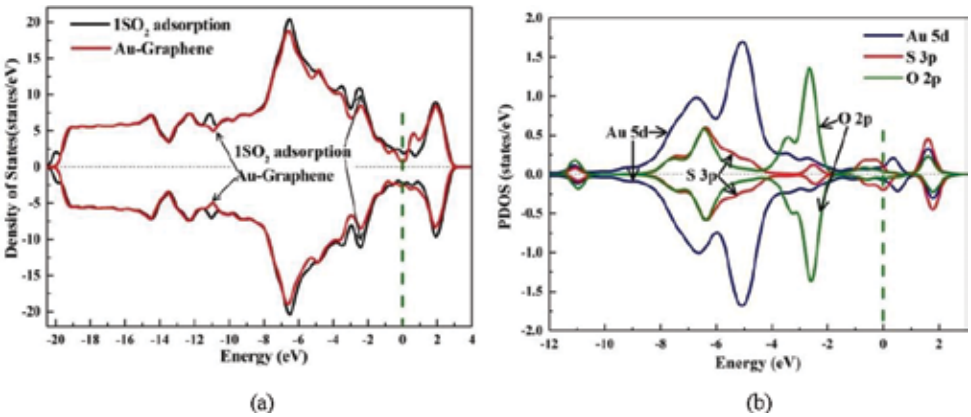

Figure 5. (a) Spin-polarized total DOS for Au-graphene with and without single SO_2 adsorption; (b) PDOS projected on the 3p of S, 2p of O in SO_2 and 5d orbital of Au. Fermi energy is set to E-E_f.

Element	s (e)	p (e)	d (e)	Charge (e)	Spin (μ_B)
Au	−0.057	−0.763	+0.794	−0.023	0.044
S	+0.217	+0.908	−0.776	0.350	0.107
O_1	+0.119	−0.481	−0.037	−0.397	0.022
O_2	+0.163	−0.427	−0.038	−0.304	0.111

Table 4. SO_2 adsorption on Au-graphene: charge transfer in s, p and d orbitals, and total charge spin magnetic moment of a single atom.

S close to the graphene plane top on the bridge (B) site, is the most stable one according to the calculated adsorption energies, with E_{ad} of −0.467 eV. **Table 5** details the adsorption parameters. The Mulliken population analysis indicates that 0.002 electrons shifted from graphene to SOF_2, which is not considered an apparent interaction with the pristine surface, and the charges shift value is meaningless for chemical interaction. SOF_2 bond lengths and bond angles substantially remain the same. Therefore, the electron interaction between SOF_2 and the pristine surface is negligible, and the van der Waals interaction plays a significant role in this case.

Configuration	*d* (Å)	E_{ad} (eV)	Bond length (Å)	Q_t (e)	*M* (μ_B)
SOF_2	\	\	1.459 (S-O), 1.668 (S-F)	\	0
SOF_2 on graphene	3.526	−0.467	1.461 Á (S-O), 1.670 Á (S-F)	−0.002	0
SOF_2 on Au-graphene	2.039	−0.961	2.894 (S-F_1), 1.72 (S-F_2)		
1.501 (O-S)	−0.624	0			

Table 5. SOF_2 adsorption on pristine graphene and Au-graphene: adsorption distance (*d*), adsorption energy (E_{ad}), bond length, charge transfer from the substrate to SOF_2 (Q_t), and magnetic moment of the entire system (*M*).

The situation was different for Au-graphene. **Figure 3(g)** shows that SOF_2 preferred the configuration with the S atom on top of the H site and the S-F bond extended to 2.894 Å, which is likely to rupture. One F atom is possibly bonded to Au, which is indicated by the distance between F and Au (2.039 Å). The preferred adsorption configuration is a stable geometric configuration where the electron-rich F and Au interact. A similar situation occurred between the Au and S. **Table 5** shows a large electron transfer and SOF_2 exhibits a charge acceptor-like feature.

Figure 6(a) shows that the DOS for Au-graphene with a single SOF_2 molecule significantly changed near the Fermi level unlike with H_2S and SO_2. The spin-up and spin-down channels are shifted toward a high-energy direction. The SOF_2 adsorption turns magnetic Au-graphene into a non-magnetic system. However, this phenomenon has not been observed in the H_2S and SO_2 adsorption systems. Combining **Figure 6(b)** and **Table 6**, the electrons in the π states of F are transferred from the 5-d orbital of metal Au on adsorption. The electrons are strongly hybridized at −2.25 eV in the valence band. The occupied 3p orbital of S is broadened and shifted far below the Fermi level, which is hybridized with the 5-d orbital of Au. The original empty d orbital of S also participates in hybridization, which

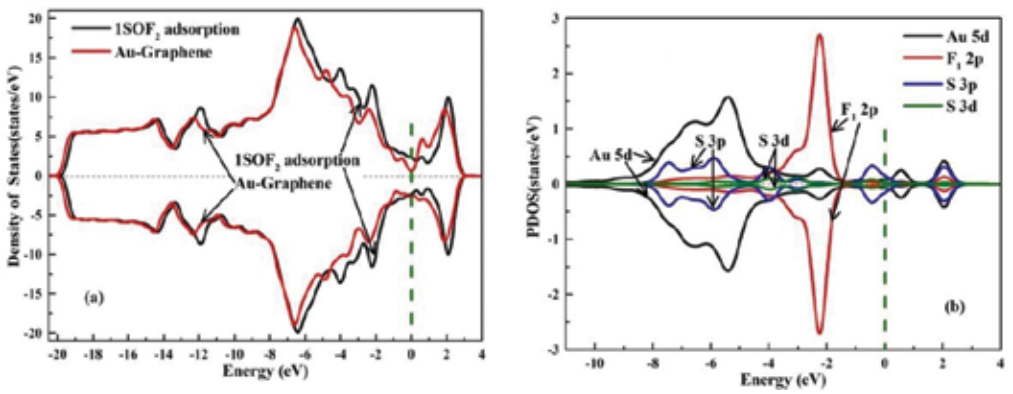

Figure 6. (a) Spin-polarized total DOS for Au-graphene with and without single SOF_2 adsorption; (b) PDOS projected on 3p and 3d of S, 2p orbital of F1 in SOF_2 and 5d orbital of Au. Fermi energy is set to $E\text{-}E_f$.

Element	s (e)	p (e)	d (e)	Charge (e)	Spin (μ_B)
Au	−0.032	−0.852	+0.898	0.014	0.000
S	+0.22	+0.914	−0.636	0.500	0.000
O	+0.164	−0.424	−0.04	−0.300	0.000
F_1	+0.032	−0.530	−0.01	−0.508	0.000
F_2	+0.044	−0.342	−0.016	−0.317	0.000

Table 6. SOF_2 adsorption on Au-graphene: charges transfer in s, p and d orbitals, and total charge spin magnetic moment of a single atom.

leads to accumulation of electrons. These findings suggest the strong influence of Au-graphene on the chemical reactivity of SOF_2 adsorption.

2.1.4. SO_2F_2 adsorption

Figure 3(d) and **(h)** reveal the lowest-energy configurations for SO_2F_2 adsorption on pristine graphene and Au-graphene, respectively. Only six original configurations were considered on the pristine graphene because of the highly symmetrical structure of SO_2F_2. These configurations include one orientation with two F atoms and one O atom close to the graphene substrate and another orientation with two O atoms and one F atom close to the plane. The two orientations must consider the relative locations on the plane (H, B and T sites). The most stable configuration is ultimately with two F, one S and two O atoms directly on every close-in C atom, which leaves the S atom on top of the T site carbon. The geometry of SO_2F_2 remains unchanged, which indicates rare interaction on the pristine one. This finding is consistent with the generally accepted idea that pristine graphene has weak interaction with common small gaseous molecules (excluding NO_2 and NH_3) because of its dangling bond shortage [21, 22].

A strong interaction is observed on Au-graphene. **Table 7** details the adsorption parameters. SO_2F_2 is adsorbed with the two F atoms bonded to Au in the substrate, while the bond lengths of S-F significantly increased. SO_2F_2 has a good chance of dissociating into SO_2 because electron-rich F atoms play a vital role in the adsorption process. The SO_2F_2 molecule pulls electrons away from Au-graphene. Unlike cases for H_2S, SO_2 and SOF_2 adsorbates, a significantly large electron shift occurs in SO_2F_2 due to adsorption on Au-graphene. This electron shift affects the local distribution of the adsorption system and significantly changes electron properties.

Therefore, we observe the DOS for Au-graphene with SO_2F_2 molecule adsorption. **Figure 7(a)** shows that magnetism disappears because of SO_2F_2; a similar case for SOF_2 is observed. SO_2F_2 causes a finite DOS within a band at a certain degree below Fermi level. A significant conductance change is expected because of the notable DOS change obtained from the Fermi level, which is highly consistent with the electron shift analysis. **Figure 7(b)** and **Table 8** show a strong interaction between Au and F atoms that occurred with an orbital mixing according to calculated PDOS and the atomic population analysis results for each atom, respectively. The accumulated electrons that occupied the π orbital of the two F atoms are mainly derived from

Configuration	d (Å)	E_{ad} (eV)	Bond length (Å)	Q_t (e)	M (μ_B)
SO_2F_2	\	\	1.609 Å (S-F), 1.441 Å (S-O)	\	0
SO_2F_2 on graphene	3.472	−0.472	1.609 (S-F_2), 1.610 (S-F_2)	−0.004	0
			1.442 (O_2-S), 1.441 (O_1-S)		
SO_2F_2 on Au-graphene	2.035	−1.790	3.145 (S-F_2), 2.095 (S-F_2)	−0.967	0
			1.477 (O_2-S), 1.545 (O_1-S)		

Table 7. SO_2F_2 adsorption on pristine graphene and Au-graphene: adsorption distance (d), adsorption energy (E_{ad}), bond length, charge transfer from the substrate to SO_2F_2 (Q_t), and magnetic moment of the entire system (M).

http://dx.doi.org/10.5772/intechopen.68329

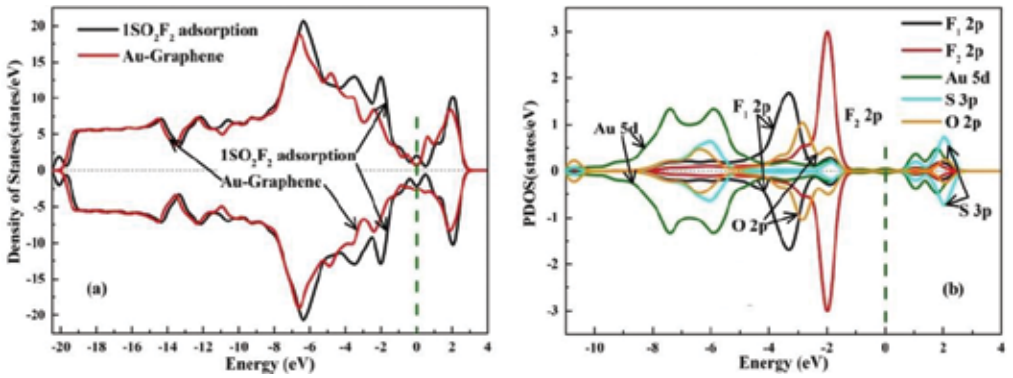

Figure 7. (a) Spin-polarized total DOS for Au-graphene with and without single SO_2F_2 adsorption; (b) PDOS projected on the 3p of S, 2p of O, 2p orbital of F1 and F2 in SO_2F_2 and 5d orbital of Au. Fermi energy is set to E-E_f.

Element	s (e)	p (e)	d (e)	Charge (e)	Spin (μ_B)
Au	+0.05	−0.876	+1.023	0.197	0.000
S	+0.204	+1.21	−0.836	0.577	0.000
O_1	+0.172	−0.388	−0.04	−0.256	0.000
O_2	+0.156	−0.488	−0.036	−0.367	0.000
F_1	+0.032	−0.532	−0.012	−0.506	0.000
F_2	+0.034	−0.438	−0.01	−0.415	0.000

Table 8. SO_2F_2 adsorption on Au-graphene: charges transfer in s, p and d orbitals, and total charge spin magnetic moment of a single atom.

the 5-d orbital of Au. They appear with a certain hybridization degree in the valence band not far from the Fermi level. This condition provides a valuable reason for S-F bond breakage and formation of Au-F bonds.

2.2. Preparation methods of Au-decorated graphene

Au-decorated Graphene films (GrF) was synthesized through the following chemical reduction procedure [23]: carboxyl functionalized graphene (1 mg) was dispersed in 5 mL $HAuCl_4$ (1 mM) solution as precursor under constant sonication for 40 min to reach a stable colloid state; 5 mL $NaBH_4$ (40 mM) solution was added dropwise to the above colloid mixed solution with vigorous stirring for 30 min; centrifugal separation step was then followed; the resulting products were collected and washed with distilled water for several times; and were finally dried in a vacuum oven at 60°C for 12 h to obtain the Au-doped GrF. Au-doped GrF powders (5 mg) were dispersed ultrasonically in 200 mL DMF solution for 30 min to reach a relatively good dispersibility.

Then, we describe the methods of sensors fabrication and sensing performance. The sensors based on Au-doped GrF were fabricated by layer-by-layer (LBL) deposition method [24]. Then, the responses were measured by monitoring surface resistance change in a pressure-tight system. As to the planar sensor, depicted in **Figure 8**, copper electrodes were interdigitally etched on epoxy resin with approximately 30-μm foil thickness and 0.2-mm electrode gap. Quantitative prepared and dispersed Au-doped GrF solution was continuously dropped on the substrate with accompanied drying treatment to the substrate until the initial surface resistance values met the needs. In short, uniform, dense and smooth deposited films were the destination [25]. Thus, an expected Au-doped GrF sensor was ready for detection. Then, the sensing element was placed in the autonomous sealed chamber and connected to an electrochemical analyzer. Here, it is worth noting that initial vacuum resistance stability is a prerequisite for the following gas detection. Response measurements were all carried out at room temperature and repeated several times to obtain reliable results.

2.3. Characterization analysis of Au-decorated graphene

Analyses of material are basically required. Preliminary, **Figure 9(a)** exhibits X-ray diffraction (XRD) patterns of the Au-doped GrF and reduced graphene oxide (rGO). The Au characteristic peaks in Au-doped GrF are observed at 38.1 (111), 44.3 (200), 64.5 (220), 77.55 (311) and 81.65 (222), as compared with the standard Au peaks at 38.184 (111), 44.392 (200), 64.576 (220), 77.547 (311) and 81.721 (222), respectively. The main Au (111) peak suggests the crystal phase formed and the broad Au peaks imply that highly dispersed Au nanoparticals (AuNPs) exist in the sample [20]. Particle size estimated from the main peak width of Au (111) suggests 14 nm according to the Scherer formula. Meanwhile, broad diffraction peaks at 24.63 and 23.77 for Au-doped GrF and rGO samples exhibit the carbon structure of graphene.

Then, Raman spectra were introduced for structural characterization [26]. Typical post-subtraction Raman spectra recorded directly on the sensor substrate are exhibited in **Figure 9**. Note that, for the epoxy layers underlying the films are insulating, the effect on the electron distribution is not considered here. A comparison of the Raman spectra between Au-doped GrF and pure rGO films concludes that the presence of low amount doped AuNPs does not seriously change the formation of in-plane sp^2 domains of graphene. The Raman spectra for the films indicate representative peaks at 1358/cm (D), 1591/cm (G) along with broad bands

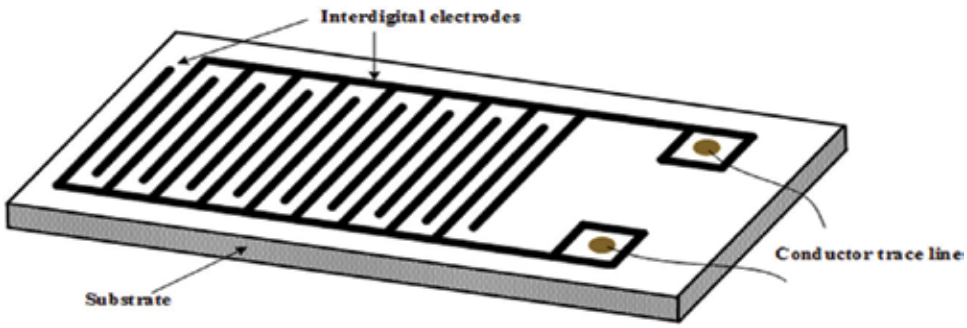

Figure 8. Schematic structural view of the planar sensor.

http://dx.doi.org/10.5772/intechopen.68329

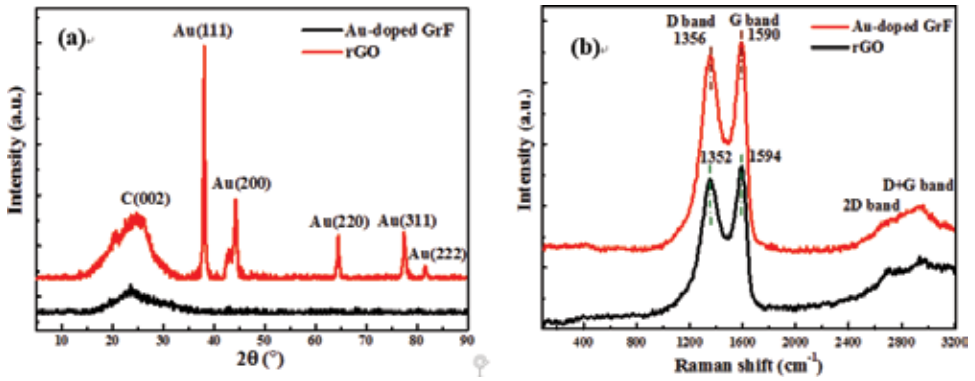

Figure 9. (a) XRD patterns of rGO and Au-doped GrF; (b) Raman spectra of rGO and Au-doped GrF.

between 2400/cm and 3200/cm. The ratio of intensities of the D and G peaks is highly sensitive to the quality of material [27], from which we speculate that the graphene-based materials are multilayers. Furthermore, the D-peak is quite obvious, indicative of a significant number of defects and a degree of confusion structure, which is caused by deprivation of parts of oxygen functionalities during the hydrogen reduction [28]. A size of tens to hundreds nanometers are concluded for these sample flakes according to the D/G ratio of 0.85 and the G peak position. This observation is roughly in accordance with the XRD analysis.

The morphological structure, particle size and metal dispersion of Au-doped GrF films are examined by SEM, as shown in **Figure 10(b)**. The enhanced area caused by the highly dispersed AuNPs enables more available active sites on the sensing surface. From these results, AuNPs are uniformly embedded in and covered on the rGO. After analyzing numerous images, the average diameter of AuNPs is tens of nanometers, in agreement with the XRD and Raman studies [20]. The TEM morphologies of Au-doped GrF are shown in **Figure 10(c)–(d)**. The TEM images also prove that AuNPs with dozens of nanometers sizes are homogenously dispersed on rGO sheets surface. A close observation of high-resolution TEM images in **Figure 3(d)** inset indicates well-defined lattice fringes of Au (111) with the clear lattice distance ($d_{111} = 0.235$ nm), showing that the AuNPs exist and are highly crystalline. Moreover, the EDS spectrum verifies again the Au element successfully doped in graphene.

As is well known, XPS spectra play a significant role in valence analysis. The XPS signatures of rGO and Au-doped GrF are shown in **Figure 11**. In accordance with XRD, SEM and TEM, the XPS results reveal that approximately 6% AuNPs have successfully doped on the graphene surface. The high-resolution C 1s XPS spectrum of rGO indicates a plenty of heteroatom defects existing on the plane and edges, in which the C 1s spectrum can be fitted into four peaks, corresponding to C atom in four different kinds of functional groups: the nonoxygenated ring C at 284.8 eV, the C in C-N bond at 285.8 eV, the hydroxyl C at 286.8 eV and the carbonyl C at 288.6 eV. After Au was introduced, the new peak at 284.2 eV appears, which is attributed to the C-N-Au bond [29]. After peak-differentiation-imitating, Au 4f doublet deconvolutes into two pair of peaks, corresponding to the reduced Au (0) at 84.27 eV in Au $4f_{7/2}$ and 87.94 eV in Au $4f_{5/2}$; the Au (III) ions at 85.02 eV in Au $4f_{7/2}$ and the Au (I) ions at

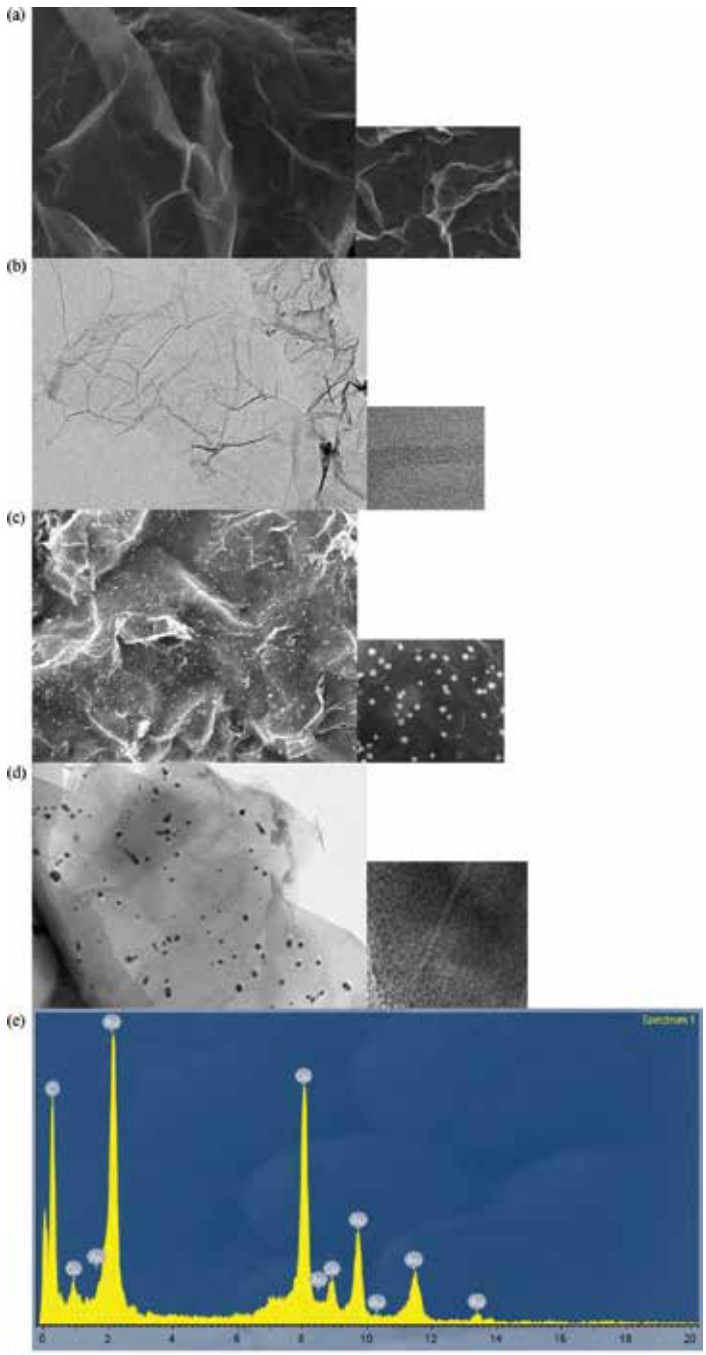

Figure 10. (a) rGO SEM image; (b) Au-doped GrF SEM image; (c) rGO TEM and HRTEM image inset; (d) Au-doped GrF TEM and HRTEM image inset; (e) EDS spectrum of Au-doped GrF.

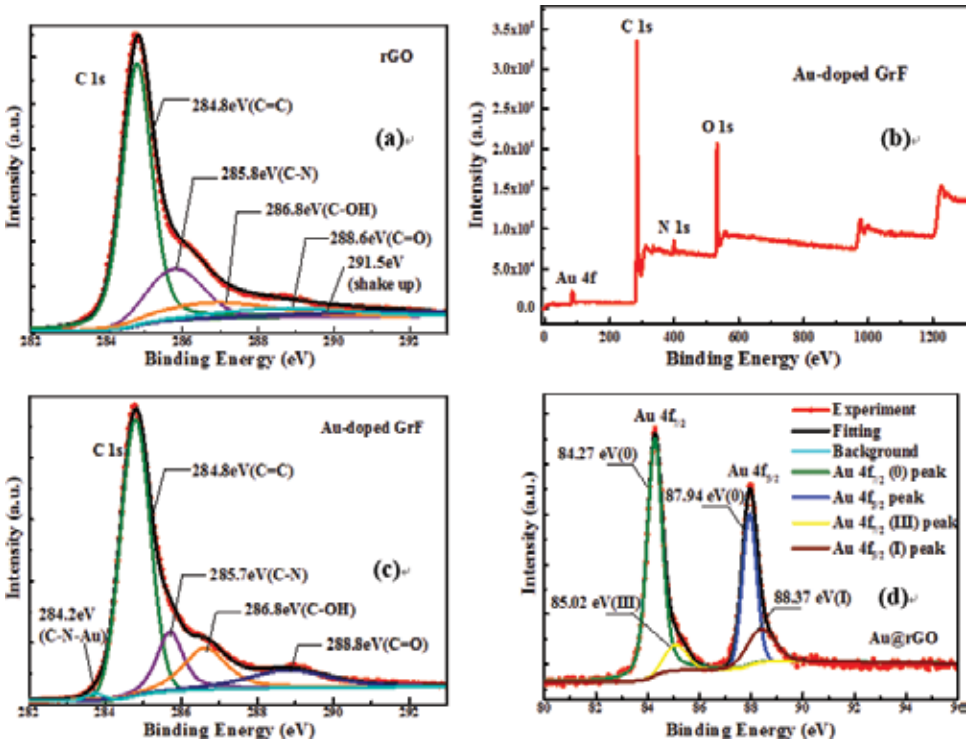

Figure 11. XPS spectra of the (a) C 1s region of rGO; (b) survey spectrum of Au-doped GrF; (c) C 1s region of Au-doped GrF; and (d) Au 4f region of Au-doped GrF.

88.37 eV in Au $4f_{5/2}$, respectively. Compared with the XPS of bulk Au (83.7 eV), there exists a nearly 0.6 eV red shift of XPS peak of Au (0) ions in Au $4f_{7/2}$. Such shift in the bonding energy may be ascribed to the underlying substrate and the reduced core-hole screening in metal particles. Furthermore, a dynamic electron transfer from the doped AuNPs to the support graphene films is proved by the existence of positively charged Au (III) and Au (I) ions according to the electrostatic balance principle [20], which is also confirmed by the following theoretical calculation in our density functional theory (DFT) study.

2.4. Experimental response of Au-decorated graphene

Figure 12(a)–(b) gives the rGO and Au-doped GrF sensor responses in terms of change in resistance obtained during the varied concentrations of target gases exposure in the autonomous sealed chamber. The change of resistance is defined as

$$\Delta R = R_F - R_I \tag{1}$$

where R_F represents the sensor resistance at the final target gas exposure and R_I represents the initial vacuum resistance at the previous rest period. Here, the sensor response is universally defined as [30]:

$$\text{Sensitivity} = \frac{\Delta R}{R_I} \times 100\% \tag{2}$$

Though humidity and temperature have a significant effect on the sensor response, the specific operating conditions in electrical equipment will reduce this variation. **Figure 12(a)–(d)** shows the sensor responses after exposure to 50 and 100 ppm of H_2S and SOF_2, respectively. For the purpose of exploring the sensing mechanism, here we only present the responses at this two-concentration atmosphere. In ambient conditions, for rGO, 100 ppm H_2S causes 15.78% reduction in resistance as much as 10.53% for lower concentration of 50 ppm. And then, SOF_2 is found to be insensitive to rGO. As illustrated in **Figure 5(d)**, 100 ppm SOF_2 results in 23.83% reduction to Au-doped GrF and the change is 15.36% for 50 ppm SOF_2, which indicates a larger sensitivity of Au-doped GrF to SOF_2 in comparison to rGO. Also, Au-doped GrF is tested to be sensitive to H_2S, but the opposite resistance change is observed. Note that 100 ppm H_2S increases the resistance by 28.15% and 50 ppm makes 18.73% addition. The sensing performance of Au-doped GrF and bare rGO may be of value in selective detection application. Therefore, the sensing behaviors are required to be analyzed in much more detail [20, 31].

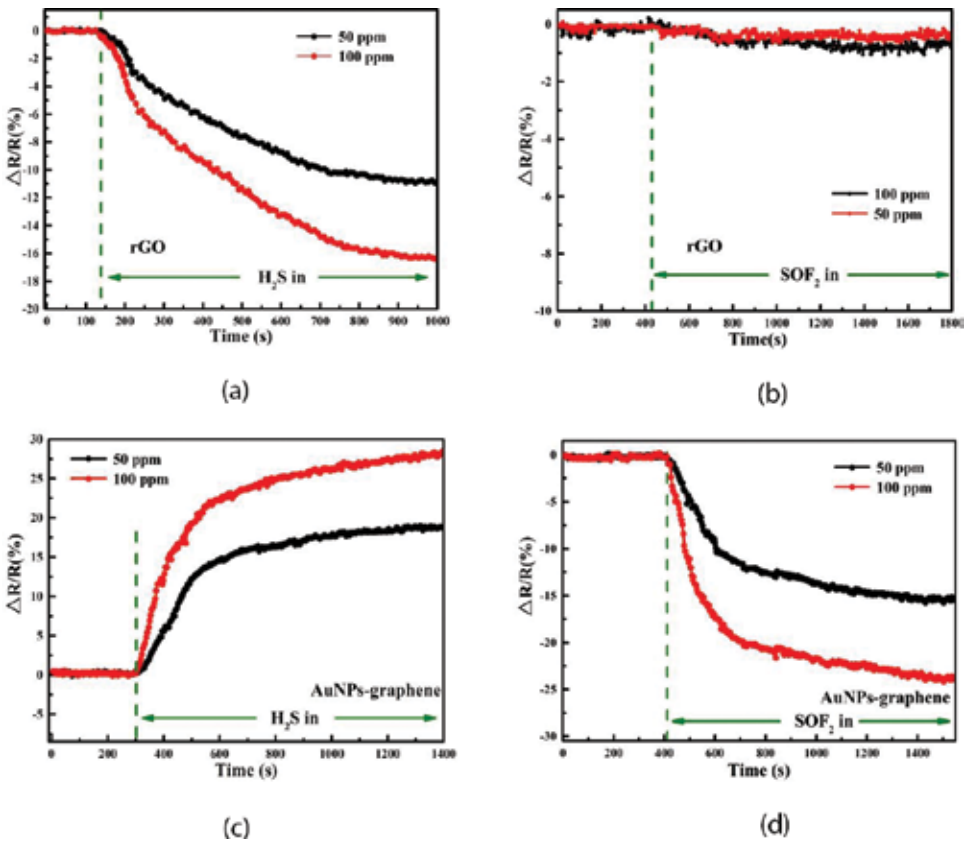

Figure 12. Experimental response transients of rGO sensors to (a) H_2S, (b) SOF_2; Au-doped GrF sensors to (c) H_2S, (d) SOF_2.

Acknowledgements

Parts of this chapter are reproduced from Ref. [31] with Elsevier's permission.

Author details

Xiaoxing Zhang*, Ju Tang, Song Xiao and Cheng Pan

*Address all correspondence to: xiaoxing.zhang@outlook.com

School of Electrical Engineering, Wuhan University, Wuhan, China

References

[1] Novoselov KS, Geim AK, Morozov SV, et al. Electric field effect in atomically thin carbonfilms. Science. 2004;**306**(5696):666–669

[2] Lee C, Wei X, Kysar JW, et al. Measurement of the elastic properties and intrinsic strength of monolayer graphene. Science. 2008;**321**(5887):385–388

[3] Neto AHC, Guinea F, Peres NMR, et al. The electronic properties of graphene. Reviews of Modern Physics. 2009;**81**(1):109

[4] Geim AK. Graphene: Status and prospects. Science. 2009;**324**(5934):1530–1534

[5] Wakabayashi K. Graphene and its Fascinating Attributes. World Scientific Publishing Company; 2011

[6] Dragoman M, Dragoman D. Graphene-based quantum electronics. Progress in Quantum Electronics. 2009;**33**(6):165–214

[7] Verma R, Bhattacharya S, Mahapatra S. Modeling of temperature and field-dependent electron mobility in a single-layer graphene sheet. IEEE Transactions on Electron Devices. 2013;**60**(8):2695–2698

[8] Wang C, Li Z, Guo Z, et al. A novel hydrazine electrochemical sensor based on the high specific surface area graphene. Microchimica Acta. 2010;**169**(1):1–6

[9] Karasik BS, Mckitterick CB, Prober DE. Prospective performance of graphene HEB for ultrasensitive detection of sub-mm radiation. Journal of Low Temperature Physics. 2014;**176**(3–4):249–254

[10] Ptitsin VE. Electron beam ablation phenomenon--theoretical model and applications. Applied Optics. 1987;**26**(19):4036–4038

[11] Lotya M, Hernandez Y, King PJ, et al. Liquid phase production of graphene by exfoliationof graphite in surfactant/water solutions. Journal of the American Chemical Society. 2009;**131**(10):3611–3620

[12] Stankovich S, Dikin DA, Piner RD, et al. Synthesis of graphene-based nanosheets via chemical reduction of exfoliated graphite oxide. Carbon. 2007;**45**(7):1558–1565

[13] Eda G, Fanchini G, Chhowalla M. Large-area ultrathin films of reduced graphene oxide as a transparent and flexible electronic material. Nature Nanotechnology. 2008;**3**(5):270–274

[14] Bhaviripudi S, Jia X, Dresselhaus MS, et al. Role of kinetic factors in chemical vapor deposition synthesis of uniform large area graphene using copper catalyst. Nano Letters. 2010;**10**(10):4128–4133

[15] Li X, Cai W, An J, et al. Large-area synthesis of high-quality and uniform graphene films on copper foils. Science. 2009;**324**(5932):1312–1314

[16] Chae SJ, Günes F, Kim KK, et al. Synthesis of large-area graphene layers on poly-nickel substrate by chemical vapor deposition: wrinkle formation. Advanced Materials. 2009;**21**(22):2328–2333

[17] Forbeaux I, Themlin JM, Debever JM. Heteroepitaxial graphite on 6H-SiC (0001): Interface formation through conduction-band electronic structure. Physical Review B. 1998; **7658**(24):16396

[18] Emtsev KV, Bostwick A, Horn K, et al. Towards wafer-size graphene layers by atmospheric pressure graphitization of silicon carbide. Nature Materials. 2009;**8**(3):203–207

[19] Singh V, Joung D, Zhai L, et al. Graphene based materials: past, present and future. Progress in Materials Science. 2011;**56**(8):1178–1271

[20] Zhang X, Yu L, Wu X, Hu W. Experimental sensing and density functional theory study of H_2S and SOF_2 adsorption on Au-doped graphene. Advanced Science. 2015;**2**(11):612–612

[21] Ran Q, Gao M, Guan X, Wang Y, Yu Z. First-principles investigation on bonding formation and electronic structure of metal-graphene contacts. Applied Physics Letters. 2009;**94**:103511

[22] Geng W, Liu H, Yao X. Enhanced photocatalytic properties of titania-graphene nanocomposites: A density functional theory study. Physical Chemistry Chemical Physics. 2013;**15**:6025–6033

[23] Hu Y, Xue Z, He H, Ai R, Liu X, Lu X. Photoelectrochemical sensing for hydroquinone based on porphyrin-functionalized Au nanoparticles on graphene. Biosensors & Bioelectronics. 2013;**47**:45–49

[24] Qureshi SS, Zheng Z, Sarwar MI, Félix O, Decher G. Nanoprotective Layer-by-Layer coatings with epoxy components for enhancing abrasion resistance: Toward robust multimaterial nanoscale films. ACS Nano. 2013;7:9336–9344

[25] Lei Y, Zhang X, Tang J. The sensitive characteristics study of SF_6, decomposed gases using a graphene sensor. In: International Conference on High Voltage Engineering and Application (ICHVE); IEEE; 2014. 1–4

[26] Wang G, Yang J, Park J, Gou X, Wang B, Liu H, Yao J. Facile synthesis and characterization of graphene nanosheets. Journal of Physical Chemistry C. 2008;**112**:8192–8195

[27] Cançado LG, Jorio A, Martins Ferreira EH, et al. Quantifying defects in graphene via Raman spectroscopy at different excitation energies. Nano Letters. 2011;**11**(8):3190–3196

[28] Li Y, Yu Y, Wang JG, Song J, Li Q, Dong M, Liu CJ. CO oxidation over graphene supported palladium catalyst. Applied Catalysis B: Environmental. 2012;**125**:189–196

[29] Yin H, Tang H, Wang D, Gao Y, Tang Z. Facile synthesis of surfactant-free Au cluster/graphene hybrids for high-performance oxygen reduction reaction. Acs Nano. 2012;**6**:8288–8297

[30] Bai S, Guo T, Zhao Y, Sun J, Li D, Chen A, Liu CC. Sensing performance and mechanism of Fe-doped ZnO microflowers. Applied Catalysis B: Environmental. 2014;**195**:657–666

[31] Zhang X, Yu L, Gui Y, et al. First-principles study of SF_6 decomposed gas adsorbed on Au-decorated graphene. Applied Surface Science. 2016;**367**:259–269

Chapter 5

Comparative Study of Materials to SF_6 Decomposition Components

Song Xiao, Xiaoxing Zhang, Ju Tang, Fuping Zeng,
Cheng Pan and Yingang Gui

Additional information is available at the end of the chapter

http://dx.doi.org/10.5772/intechopen.68322

Abstract

In order to judge the inside insulation fault of SF_6 insulated equipment, the gas-sensing properties to a series of characteristic SF_6 decomposition components, SOF_2, SO_2F_2, SO_2, H_2S, CF_4, HF, and SF_6, have been studied. In this study, a comparative study of these gas-sensing materials has been made in theoretical and experimental fields to find the optimal gas-sensing material, and put forward the effective approaches to improve the gas-sensing properties of materials.

Keywords: SF_6 decomposed gases, carbon nanotubes, TiO_2 nanotubes, graphene gas sensor, gas-sensing comparison

1. Theoretical study comparison

To detect, evaluate, and diagnose the insulation status of SF_6 gas insulated equipment using the characteristics of SF_6 decomposition, a series of characteristic SF_6 decomposition components, SOF_2, SO_2F_2, SO_2, H_2S, CF_4, HF, and SF_6, are detected by gas sensors, including metal functionalized single wall carbon nanotubes (SWCNTs) [1–6], TiO_2 nanotubes [7–9], and graphene gas sensors [10, 11], as shown in **Table 1**. According to the theoretical calculation results, these three kinds of gas-sensing materials are not sensitive to the background gas SF_6 and decomposition component CF_4. And the concentration of HF in decomposition components is less than the concentration of the other typical gases. Therefore, we compare the adsorption properties four types of SF_6 decomposition components: SOF_2, SO_2F_2, SO_2, and H_2S, under the detection of metal functionalized SWCNTs, TiO_2 nanotubes, and graphene gas sensors.

Material	Dopant	Typical decomposition components						
SWCNTs	/	SOF_2	SO_2F_2	SO_2	H_2S	CF_4	HF	SF_6
	Pd	SOF_2	SO_2F_2	SO_2	H_2S	CF_4	/	/
	Ni	SOF_2	SO_2F_2	SO_2	/	/	/	/
	Al	SOF_2	SO_2F_2	SO_2	H_2S	CF_4	/	/
	Pt	/	/	SO_2	H_2S	/	/	/
	Au	/	/	SO_2	H_2S	/	/	/
TiO_2	/	SOF_2	SO_2F_2	SO_2	/	/	/	/
	Pt	SOF_2	SO_2F_2	SO_2	/	/	/	/
	Au	SOF_2	SO_2F_2	SO_2	/	/	/	/
Graphene	/	SOF_2	SO_2F_2	SO_2	H_2S	/	/	/
	Au	SOF_2	SO_2F_2	SO_2	H_2S	/	/	/

Table 1. The typical decomposition components of SF_6 detected by gas sensor.

Metal atom modification not only greatly improves the gas-sensing properties to SF_6 decomposition components, but also enhances the gas-sensing selectivity of sensors to different gas molecules. Upon SOF_2 and SO_2F_2 detection, intrinsic gas sensors show weak sensitivity to SOF_2 because of the weak interaction between gas molecules and the surface of gas-sensing materials. After metal atoms modification, which acts as the active sites, SOF_2 molecule tends to approaches the adsorption site by fluorine atom due the its strong chemical activity. Generally, the strong activity breaks the chemical bonds of SOF_2. Similarly, SO_2F_2 interacts with the metal atom-doped gas-sensing material by chemisorption, reflecting in aspect that the fluorine atom breaks from SO_2F_2 to build new bond with metal atoms. Upon SO_2 and H_2S detection, these two small gas molecules are generally adsorbed on the surface of gas sensors by physisorption, which was benefit to gas desorption process. SO_2 and H_2S get approach to the surrounding of metal dopant by oxygen and sulfur atom, respectively, because of its polyvalency property.

Comparing the gas-sensing properties of different sensor materials, the regular porous structure of TiO_2 nanotubes contributes to gas desorption and reusability. In addition, its big specific surface area helps the metal dopant modification and gas-sensing sites. But, TiO_2 nanotubes sensor usually needs high work temperature, and its high resistance hinders the transmission of detection signals. In comparison, metal atom-doped SWCNT and graphene sensor can work effectively at room temperature, and its low resistance helps to transfer detection signals, resulting in reducing gas-sensing time.

2. Experimental study comparison

Using the own design platform which is used to test the performance of TiO_2 nanotubes sensor, the gas response characteristics and temperature characteristics of the intrinsic TiO_2 nanotubes sensor to three main SF_6 gas decomposition compositions SO_2, SOF_2, and SO_2F_2 were studied. The same sensing experiments were also carried out on Pt and Au-doped TiO_2

nanotubes sensors. The results are compared as shown in **Table 2** for TiO_2 nanotubes gas sensor and **Table 3** for graphene gas sensor.

It is concluded that the Au-doped TiO_2 nanotubes sensor has better selectivity to SO_2F_2 gas. Pt nanoparticles doping changes gas selectivity of TiO_2 nanotubes sensor to SO_2, SOF_2, and SO_2F_2. Compared with the intrinsic sensor, Au nanoparticles doped significantly changed the selectively of sensor to SO_2, SOF_2, and SO_2F_2 (**Table 3**).

Pristine graphene is considered a promising adsorbent for H_2S selective detection. Compared with the performance on pristine graphene films, Au-doped graphene emerges significant response to H_2S, SOF_2, and SO_2F_2 but weak interaction to SO_2, with the sequence of $SO_2F_2 > H_2S > SOF_2 > SO_2$. Among them, only H_2S shows the opposite response with its resistance increase, while SO_2, SOF_2, and SO_2F_2 decrease the resistance of Au-doped graphene.

Doping metal	Doping time	Gas-sensing parameters to typical decomposition components		
		SO_2	SOF_2	SO_2F_2
/	0 s	−74.6%	−7.82%	−5.52%
Pt	10 s	−53.3%	−24.2%	−5.4%
	20 s	−33.9%	−22.1%	−19.2%
	30 s	−13.8%	−19.1%	−50.6%
	40 s	−6.7%	−5.1%	−10.7%
Au	–	−23.75%	−28.37%	−42.31%

Table 2. The typical decomposition components of SF_6 detected by TiO_2 nanotubes gas sensor.

Doping metal	Gas-sensing parameters to typical decomposition components			
	H_2S	SO_2	SOF_2	SO_2F_2
/	−15.78%	−1.5%	−0.8%	−0.3%
Au	28.15%	−6.98%	−23.83%	−33.91%

Table 3. The typical decomposition components of SF_6 detected by graphene gas sensor.

3. Conclusions

In order to evaluate and diagnose the insulation status of SF_6 insulated equipment, gas sensor detection becomes an effective new method to realize the function by detecting the decomposition components of SF_6. Theoretical simulations are performed to understand the adsorption process of gas sensors and typical components of SF_6. And using carbon nanotubes (CNTs) based as novel kind of sensors show high sensitivity and quick responses to target gases. For TiO_2-based gas sensor, the adsorption of typical components of SF_6 on different surfaces of TiO_2 is reviewed in this section. It is found that the metal decoration improves the sensitivity

and selectivity to SO_2 and SOF_2, and SO_2F_2 also reduces the working temperature for gas detection. Pristine graphene exhibits weak adsorption and absence of charge transfer, which indicates barely satisfactory sensing for decomposed components. SOF_2 and SO_2F_2 exhibit a strong chemisorption interaction with Au-graphene, while H_2S and SO_2 exhibit quasi-molecular binding effects. Only H_2S exhibits n-type doping to Au-graphene, whereas the rest gases exhibit p-type doping. In general, the sensors array composed of modified gas sensors can be used in the GIS to realize the highly precise detection of related gases, thus accurately deducing the related insulation faults.

Author details

Song Xiao[1], Xiaoxing Zhang[1]*, Ju Tang[1], Fuping Zeng[1], Cheng Pan[1] and Yingang Gui[2]

*Address all correspondence to: xiaoxing.zhang@outlook.com

1 School of Electrical Engineering, Wuhan University, Wuhan, China

2 College of engineering and technology, Southwest Universit, Chongqing, China

References

[1] Xiaoxing Zhang, Yingang Gui, Ziqiang Dai. A simulation of Pd-doped SWCNTs used to detect SF_6 decomposition components under partial discharge. Applied Surface Science. 2014;**315**(10):196-202

[2] Xiaoxing Zhang, Yingang Gui, Hanyan Xiao, Ying Zhang. Analysis of adsorption properties of typical partial discharge gases on Ni-SWCNTs using density functional theory. Applied Surface Science. 2016;**379**:47-54

[3] Xiaoxing Zhang, Ziqiang Dai, Qinchuan Chen, Ju Tang. A DFT study of SO_2 and H_2S gas adsorption on Au-doped single-walled carbon nanotubes. Physica Scripta. 2014;**89**(6):065803

[4] Zhang X, Dai Z, Wei L, Liang N, Wu X. Theoretical calculation of the gas-sensing properties of Pt-decorated carbon nanotubes. Sensors. 2013;**13**(11):15159

[5] Xiaoxing Zhang, Yingang Gui, Ziqiang Dai. Adsorption of gases from SF_6 decomposition on aluminum-doped SWCNTs: A density functional theory study. The European Physical Journal D. 2015;**69**(7):1-8

[6] Xiaoxing Zhang, Jinbin Zhang, Ju Tang, Bing Yang. Gas-sensing simulation of single-walled carbon nanotubes applied to detect gas decomposition products of SF_6. Journal of Computational & Theoretical Nanoscience. 2012;**9**(8):1096-1100

[7] Zhang X, Tie J, Zhang J. A Pt-doped TiO_2 nanotube arrays sensor for detecting SF_6 decomposition products. Sensors. 2013;**13**(11):14764

[8] Xiaoxing Zhang, Lei Yu, Jing Tie, Xingchen Dong. Gas sensitivity and sensing mechanism studies on Au-doped TiO_2 nanotube arrays for detecting SF_6 decomposed components. Sensors. 2014;**14**(10):19517

[9] Xiaoxing Zhang, Jinbin Zhang, Yichao Jia, Peng Xiao, Ju Tang. TiO_2 nanotube array sensor for detecting the SF_6 decomposition product SO_2. Sensors. 2012;**12**(3):3302

[10] Xiaoxing Zhang, Lei Yu, Yingang Gui, Weihua Hu. First-principles study of SF_6 decomposed gas adsorbed on Au-decorated graphene. Applied Surface Science. 2016;**367**:259-269

[11] Zhang X, Yu L, Wu X, Hu W. Experimental sensing and density functional theory study of H_2S and SOF_2 adsorption on Au-modified graphene. Advanced Science. 2015;**2**(11):612-612

Authored by Xiaoxing Zhang, Ju Tang, Song Xiao, Fuping Zeng, Cheng Pan, Yingang Gui

The insulating medium used in gas-insulated switchgear is SF6 gas, which has been widely used in substations. Energy generated by discharge will cause the composition of SF6 and generate characteristic component gases. Diagnosing the insulation defect through analyzing the decomposed gases of SF6 by chemical gas sensors is the optimal method due to its advantages. Carbon nanotubes, TiO_2 nanotubes and graphene are chosen as the gas-sensing materials to build specific gas sensors for detecting each kind of SF6 decomposed gases and then enhance the gas sensitivity and selectivity by material modification. The properties and preparation methods are introduced in this book. The author studied the micro-adsorption mechanism and macro-gas sensing properties by theoretical calculation and sensing experiment.

ISBN 978-953-51-4809-8

IntechOpen